UNIVERSITY OF CALIFORNIA
RIVERSIDE

A Modeling Perspective on Carbon Cycling and the Impacts of Astronomical Forcing

A Dissertation submitted in partial satisfaction
of the requirements for the degree of

Doctor of Philosophy

in

Earth and Planetary Sciences

by

Pam Vervoort

December 2022

Dissertation Committee:

Dr. Sandra Kirtland Turner, Chairperson
Dr. Stephen Kane
Dr. Andy Ridgwell

The Dissertation of Pam Vervoort is approved:

Committee Chairperson

University of California, Riverside

Acknowledgments

I am forever grateful to those who have helped and accompanied me along the way toward obtaining my PhD degree. There are many people to acknowledge here but first and foremost, I could not have wished for better advisors than those on my dissertation committee: Sandy Kirtland Turner, Andy Ridgwell, and Stephen Kane.

Sandy, thank you. Not only did you introduce me to Earth system modelling during my masters, you went as far as inviting me to start a PhD program with you, and accepting this offer was one of the best decisions I could have made. I will never stop being amazed by the amount of knowledge you have and I feel lucky I can carry some of that with me onto future ventures. But, of course, a great advisor is more than just knowledgeable. You have always been so supportive, allowing me to explore many different research avenues, and whenever I felt a little lost, conversations with you have been incredibly helpful in moving forward. You have been a fantastic teacher and mentor. I truly appreciate your guidance and I am excited to see where future collaborations will take us.

Andy, thank you. I am privileged to have been around the cGENIE genius while exploring the applications and capabilities of cGENIE during my PhD. You have taught me how to best use the model and get the most meaningful results through your expertise. You may not know this but your advise and help have saved me from throwing my computer our of the window in our windowless office on several occasions, so a special thanks is in order here. And of course, thank you for opening up your beautiful mountain home for the occasional party, and for the delicious baked goods during all our Matlab teaching sessions on the way too early Monday mornings.

Stephen, thank you. Never could I have imagined to dive into the world of exoplanet research and yet, here we are. Both you and Jonti Horner have been instrumental in a large part of the work in this dissertation. You sparked my interest during the exoplanet science classes and taught me how knowledge on the Earth system can be used to inform the search of habitable planets beyond the Solar System. Thank you for welcoming me in your research group, for your patience while I learned the new ropes, and for your always kind and encouraging words.

And of course, many thanks to all with whom I shared the best office in the building. Dominik, Yoshi, Sebastiaan, Rebecca, Carlye, Alexandre, always ready with wise (and not so wise) postdoc advise. Allison, Michelle, and Gayarti, former and current labmates who have been or currently are on the same journey. And lab visitors, Fiona and Markus, with whom I have had great conversations that have led to fruitful collaborations.

Finally, I cannot go without thanking all the amazing friends I met along the way. Thank you for your moral support, for listening, for the many pizzas at the Getaway Cafe, and for the unforgettable camping trips across some of the most beautiful places the US has to offer. You have made this incredible 5-year adventure a little easier and without you, it would not have been the same.

ABSTRACT OF THE DISSERTATION

A Modeling Perspective on Carbon Cycling and the Impacts of Astronomical Forcing

by

Pam Vervoort

Doctor of Philosophy, Graduate Program in Earth and Planetary Sciences
University of California, Riverside, December 2022
Dr. Sandra Kirtland Turner, Chairperson

Planetary climates are controlled by the delicate radiative balance between incoming and outgoing energy. Any perturbation to either side of the equation disrupts the surface temperature with implications for the physical environment and (bio)geochemical processes that in their turn impose additional alterations to the radiative energy balance. In this dissertation, I use numerical approaches to investigate the role of changing greenhouse gas concentrations and astronomical forcing (quasi-periodic variations in solar radiation via gradual changes in Earth's orbit and tilt) on the surface climate, carbon cycling, and the environmental consequences of associated feedback processes, on Earth and beyond.

First, I address the impact of carbon dioxide release to the atmosphere on geological timescales. Past carbon release events and episodes of global warming that are preserved in paleoclimate records are compared to an ensemble of Earth system model simulations to estimate the carbon input and output fluxes during past events and determine how the Earth responded to such perturbations. Next, I provide the reader with a thorough analysis of the impact of astronomical forcing and its imprint on the marine environment as simu-

lated in an Earth system model. The transient modeling approach allows direct comparison between time-varying model output and multi-million-year-long paleoclimate records and thereby provides an opportunity to determine from model-data (mis)matches what feedback processes are the main drivers for variations in the climate-carbon system on astronomical timescales across tens of thousand to millions of years. Lastly, I examine with the use of orbital and obliquity simulations how the frequency and amplitude of astronomical cycles change as a function of planetary architecture and assess their impact on surface conditions and planetary habitability across million-year timescales. This research contributes to identifying exoplanets in other systems that may have been able to maintain habitable conditions over prolonged periods of time required for the development and evolution of life elsewhere in the universe.

Contents

List of Figures

List of Tables

Chapter 1

Introduction

1.1 Background

The need to improve our understanding of climate dynamics and the intricate processes involved, such as those related to the carbon cycle, is continuously growing. First and foremost so the future climate trajectory of Earth under the influence of anthropogenic perturbations can be predicted more accurately, but also to advance interpretation of paleoclimate records that ultimately inform future climate projections. Moreover, research toward fundamental climate behaviour on planets beyond the Solar System is becoming increasingly important as we enter a new era of exoplanet characterization and embark on the search for habitable planets elsewhere in the universe with the launch of the James Webb Space Telescope, just a few months prior to the time of writing.

Planetary climates are controlled by the delicate radiative balance between incoming and outgoing energy. Stellar irradiation, downward radiation emitted by greenhouse gasses, geothermal energy, and tidal heating are the main sources of incoming energy al-

though on Earth today, tidal and geothermal heating are negligible forces. Energy is lost to space through the direct reflection of stellar energy, particularly on bright surfaces such as clouds and snow, and upward infrared radiation emitted by the surface and atmosphere.

The sensitivity of the climate system to perturbations to the radiative equation is perhaps best exemplified by the modern climate crisis. Since the industrial revolution, we have increased carbon dioxide (CO_2) concentrations in our atmosphere from 280 to almost 420 ppm, resulting in the absorption of more energy by the atmosphere while lowering the outgoing energy, thereby raising the global temperature by more than 1°C (Hawkins et al., 2017). The Intergovernmental Panel on Climate Change advises to limit the rise in global temperature to 1.5-2.0°C to prevent extreme environmental disruption. Yet, translating this to an upper limit for allowed CO_2 emissions is complicated by large uncertainties in the relation between carbon release-uptake rates, atmospheric CO_2 concentration, and global temperature. Many intricate climate-CO_2 feedback processes that redistribute carbon between the atmosphere, ocean, biosphere, and geological reservoirs need to be considered and each process responds on different timescales while their strength often changes over time along with the changing environmental conditions.

Paleoclimate records provide us with a unique window into the past to study how the Earth has responded previously to natural carbon release events. The magnitude and rates of carbon fluxes can be constrained from carbon isotope ($\delta^{13}C$) data and indicators for carbonate chemistry whereas paleo-temperature proxies are a measure for the climatic consequences. In combination with advanced numerical models, the various feedbacks affecting the climate response and carbon cycle, and their relative contributions can be explored in

more detail. One problem, however, is that geological archives such as (marine) sediments that contain paleoenvironmental information are limited by their resolution. Sediments often experience chemical, physical, or biological distortions after deposition, meaning they do not preserve the original magnitude and duration of past events with consequences for their interpretation and reconstruction of the events.

The paleorecord also shows evidence of perpetual radiative imbalance due to quasi-periodic changes in the amount and distribution of the incoming solar energy. Earth's orbit and tilt gradually change over time as a result of gravitational forces between our planet and other bodies in our Solar System which alters regional insolation on daily (10^{-3} years) and astronomical ($10^4 - 10^6$ years) timescales (see Section 1.2 for a detailed explanation). *Astronomical cycles* are the source of the most extreme climate variations during the Quaternary—the glacial-interglacial cycles. Relatively moderate insolation changes, especially those in high latitude regions, modulate the growth and retreat of polar ice sheets and their changing volume triggers additional climate and carbon cycle feedbacks that magnify the climate response. Paleoclimate records of the early Cenozoic reveal that greenhouse climates were subjected to astronomically forced climate-carbon cycle perturbations as well, even in absence of large dynamic ice sheet. A series of early Cenozoic 'hyperthermal events', characterized by temporary global warming, carbon release, and ocean acidification, are linked to astronomical cycling although the climate-CO_2 feedbacks that amplify the temperature response and trigger carbon release are still poorly understood.

Astronomical cycles on Earth have been relatively sedate but the moderate changes in insolation have had major consequences for the evolution of our climate (and life) through

time. Now, imagine an exoplanet in a foreign planetary system with different gravitational dynamics and therefor astronomical cycles of different magnitude and frequency. The climate variability and rate of change in surface conditions may be more extreme than those on Earth and must be considered when assessing the 'habitability potential' of an exoplanet. As we search for exoplanets that have the potential to harbour life, it is crucial to estimate the incoming energy and determine if that energy supply is sufficient to maintain 'habitable' surface conditions, i.e. sufficiently high to prevent total freezing but sufficiently low to avoid evaporation of all surface water or atmospheric escape. Extreme astronomical cycles continuously change the balance between incoming (stellar) and outgoing energy and could have great consequences for the evolving surface climate and habitability on astronomical timescales. Fortunately, the astronomical dynamics experienced by a planet can to some extent be evaluated by considering the planet-planet interactions in observable planetary systems. One of the bigger challenges is to determine how the spin dynamics of a planet respond to the gravitational interactions and their impact on surface climate variability.

1.2 Introduction to Astronomical Forcing

The idea of an astronomical influence on Earth's climate was put forward about 200 years ago. In 1826, Jens Esmark, a Danish-Norwegian geologist, was the first to reconcile geological evidence for past extensive glaciations across northern Europe with a theory proposing that Earth's orbit used to be more elliptic and was '*subjected to a strong degree of cold in its aphelium*' (Esmark, 1826). A few years later, the connection between changes in climate and Earth's orbital elements was made (Herschel, 1832), followed by

the formulation of the theory of the ice ages (Agassiz, 1840) and further refined by taking into consideration not only the orbital elements but also the rotation of Earth's axis (Adhémar, 1842; Croll, 1864). Perhaps the real breakthrough occurred in 1942 when Mutilin Milankovitch published his computations of past insolation for given latitudes and time-of-year based on previous calculations describing Earth's movement in the Solar System over time (Milankovitch, 1941). This facilitated direct comparison between the incoming solar energy and paleoclimate records that propelled research on the impacts of astronomical forcing (see Hilgen (2010) for a full review) and is the crux of the work presented here. In this section, I provide a basic overview of planetary system dynamics and their relation to astronomical (insolation) forcing.

The annual mean incoming solar energy on any planet is determined by the luminosity of the star(s) in the system and the star-planet distance. However, the orbit of a planet is rarely perfectly circular, meaning that the distance varies across an orbital year with consequences for the total annual mean amount of incoming radiation. The relationship between the incoming energy and orbital characteristics follows:

$$\overline{F}_{annual} = \frac{L_\star}{(16\pi a^2\sqrt{(1-e^2)})} \tag{1.1}$$

where $\overline{F}_{annual}$ is the annual mean insolation flux (in Wm^{-2}), $L_\star$ is the luminosity of the star (in W), a is the planet's semi-major axis (in m^2), and e the eccentricity. Earth's orbit today deviates 1.67% from full circularity with a modern *eccentricity* of 0.0167. Gravitational interactions between planets quasiperiodically perturb the shape of their orbits. In our own Solar System, Jupiter is the most massive and gravitationally influential planet, pushing

and pulling Earth in and out of near-circular orbit in cycles of 100 kyr and 405 kyr across which eccentricity varies between about 0 and 0.067 with consequences for the incoming solar radiation and, ultimately, global surface temperatures. However, eccentricity cycles alone account for only 0.7 Wm^{-2} variation in the annual global mean insolation with an average value of 340 Wm^{-2} on Earth.

The climatic effects of eccentricity are amplified by the orientation (*precession*) and angle (*obliquity*) of Earth's tilt with respect to the orbital plane (Figure 1.1). Earth's axis today is tilted 23.4° relative to the orbit normal with the Northern Hemisphere (NH) oriented away from the Sun when Earth is near its closest approach to the Sun (*perihelion*) at 102° from the spring equinox. Precession and obliquity do not impact the annual mean amount of insolation but dictate the latitudinal and seasonal isolation patterns (Figure 1.2). Summers and winters in the NH are currently mild as opposed to the hot summers and cold winters of the Southern Hemisphere (SH). This seasonality only arises from non-zero obliquity—a steeper obliquity increases the seasonal extremes.

Earth experiences precession and obliquity cycles via quasiperiodic gravitational perturbations between the Earth, Moon, and Sun. Because our planet is not completely rigid and rotates rapidly around its axis, a bulge is formed at the equator. Lunar and solar torques pull the equatorial bulge toward their ecliptic and thereby gradually change the orientation and angle of Earth's axis. It takes about 25 kyr for Earth's axis to make a full 360° precession while the obliquity angle varies between 22° and 24.5° on a cycle of about 41 kyr. The duration of precession and obliquity cycles was slightly shorter in the past and will become longer in the distant future as the Moon gradually moves outward over

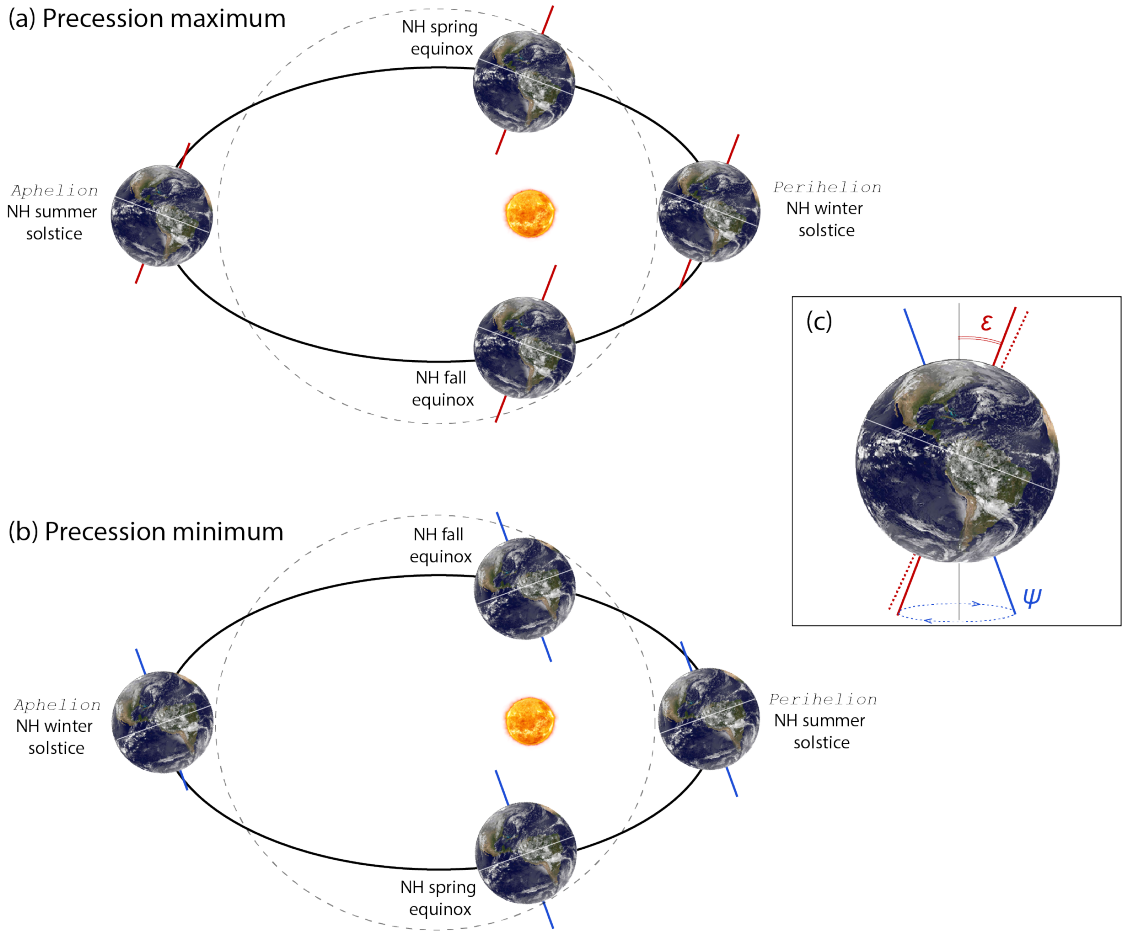

Figure 1.1: Schematic diagram of astronomical dynamics. Earth's circular (dashed grey line) and eccentric (solid black line) clockwise orbit around the Sun. (a) At precession maximum, the Northern Hemisphere (NH) is tilted away from the Sun at perihelion passage, i.e. mild NH winters. The NH is tilted to the Sun during aphelion passage, i.e. mild NH summers. (b) At precession minimum, the NH is tilted to the Sun at perihelion passage, i.e. warm NH summers. The NH is tilted away from the Sun during aphelion passage, i.e. cold NH winters. (c) Obliquity (ϵ) varies between 22° and 24.5° in cycles of ca. 41 kyr. Earth's axis precesses 360° in roughly 25.8 kyr relative to the fixed background stars. When also accounting for orbital (apsidal) precession, a full climatic precession (ψ) cycle is ca. 21 kyr.

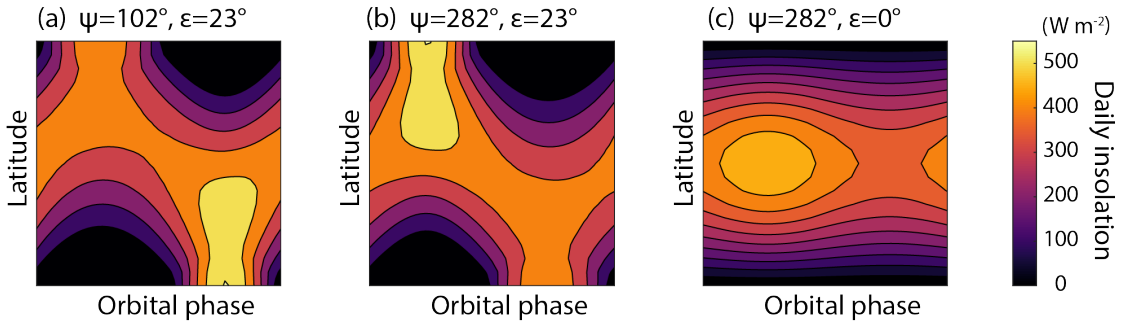

Figure 1.2: Seasonal insolation patterns as a function of precession and obliquity. Eccentricity is 0.06 in all panels. (a) Daily mean insolation for precession (ψ) of 102° and obliquity (ϵ) of 23°, i.e. precession maximum. (b) Daily mean insolation for ψ=282° and ϵ=23°, i.e. precession minimum. (c) Daily mean insolation for ψ=282° and ϵ=0°, i.e. no seasonality.

time due to the exchange of angular momentum between the Earth and Moon via tidal interaction. I refer the reader to Chapter 5 (Section 5.2.3) in this dissertation for a more detailed explanation of the physics behind precession and obliquity motions.

Eccentricity, precession, and obliquity combined directly control the astronomical climate variability on Earth through changes in spatiotemporal insolation forcing, or indirectly via their impact on climate feedback processes that act to either amplify or weaken the astronomical response (see Chapter 3 and 4). However, the frequency and amplitude of these cycles are Earth-specific and strongly depend on the architecture of the planetary system (see Chapter 5). Exoplanets will have their own unique astronomical signature driving long-term surface climate cycles. The intensity of the climate cycles will be regulated by the characteristics of the astronomical cycles and large array of planetary properties.

1.3 Dissertation Outline

In this dissertation, I aim to improve our understanding of the surface climate behaviour in response to internal and external perturbations. The outcomes and findings of the work herein will benefit paleoclimate research and facilitate interpretation of paleoclimate records to reveal climate-carbon dynamics throughout Earth's geologic history—information that ultimately will be crucial to predict the future climatic pathway of our planet. Moreover, now that the era of exoplanet characterization has begun, we should start considering the climate dynamics on planets beyond our Solar System to identify those exoplanets that have the potential to be habitable for prolonged periods of time in search for evidence of life elsewhere in the universe. This work explores the long-term climate evolution in response to astronomical forcing in other planetary systems. I contribute pieces to the puzzle through three main objectives forming the base of my research.

- Constrain the forcings and impacts of past (natural) carbon release events
- Understand astronomical cycles in Earth's climate and carbon cycle
- Consider astronomical forcing on exoplanets and their impact on potential habitability

In Chapter 2, I present a framework that estimates the carbon fluxes associated with past carbon release events that are preserved in the geological record as negative carbon isotope excursions. This framework allows users to assess the negative carbon isotope excursion alongside proxies indicative of environmental change to quantify the possible carbon input and removal fluxes across the perturbation and identify potential distortions of the sedimentary signal. In the following two chapters, the impact of astronomical forcing

on the physical ocean and marine inorganic (Chapter 3) and organic (Chapter 4) carbon cycle, and its expression in key paleoceanographic variables is investigated with a series of transient astronomically forced Earth system model simulations. This study is the fist ever to model the response of the Earth system to changes in the astronomical radiative forcing in a 3D Earth system model on multi-million-year-long timescales needed to capture the impact of the longest astronomical cycles. Chapter 5 covers a deep dive into the physics that drive astronomical cycles with emphasis on the gravitational interactions between objects in planetary systems. With a large ensemble of planetary system simulations and obliquity models, I examine how massive companion planets, such as Jupiter, influence the astronomical cycles and subsequent climate variability on smaller planets in the Habitable Zone, such as Earth. Results are discussed in terms of long-term climatic habitability with implication for future exoplanet research that aims to identify planetary systems that have the greatest potential to maintain habitable conditions over the prolonged periods of time. The dissertation is concluded in Chapter 6 with some final remarks that tie the findings of each chapter into the bigger picture.

1.4 Submitted Material

At the time of writing, Chapter 2 and 3 have been accepted and published in peer reviewed journals with their references below. Chapter 5 is accepted for publication in *The Astrophysical Journal* but not yet published, and Chapter 4 is in preparation at present to be submitted for publication.

Chapter 2 – Vervoort, P., Adloff, M., Greene, S.E. and Kirtland Turner, S., 2019. Negative carbon isotope excursions: an interpretive framework. *Environmental Research Letters*, 14(8), p.085014.

Chapter 3 – Vervoort, P., Kirtland Turner, S., Rochholz, F. and Ridgwell, A., 2021. Earth System Model Analysis of How Astronomical Forcing Is Imprinted Onto the Marine Geological Record: The Role of the Inorganic (Carbonate) Carbon Cycle and Feedbacks. *Paleoceanography and Paleoclimatology*, 36(10), p.e2020PA004090.

Chapter 5 – Vervoort, P., Horner, J., Kane, S.R., Kirtland Turner, S., and Gilmore, J., 2022. System Architecture and Planetary Obliquity: Implications for Long-Term Habitability. *The Astrophysical Journal*, 164(4), p.130.

Chapter 2

Negative Carbon Isotope Excursions: An Interpretative Framework

Abstract - Numerous negative carbon isotope excursions (nCIEs) in the geologic record occurring over 10,000 to 100,000 years are interpreted as episodes of massive carbon release. nCIEs help to illuminate the connection between past carbon cycling and climate variability. Theoretically, the size of a nCIE can be used to determine the mass of carbon released, provided that the carbon source is known or other environmental changes such as temperature or ocean pH can be constrained. A simple isotopic mass balance equation often serves as a first order estimate for the mass of carbon input, but this approach ignores the effects of negative carbon cycle-climate feedbacks. Here, we show, using 432 earth system model simulations, that the mass of carbon release and associated environmental

impacts for a nCIE of a given size and carbon source depend on the onset duration of that nCIE: the longer the nCIE onset duration, the greater the required carbon input in order to counterbalance the input of ^{13}C-enriched carbon through carbonate compensation and weathering feedbacks. On timescales greater than 1,000 years, these feedbacks remove carbon from the atmosphere so that the relative rise in atmospheric CO_2 decreases with the nCIE onset duration. Consequently, the impacts on global temperature, surface ocean pH and saturation state are reduced if the nCIE has a long onset duration. The framework provided here demonstrates how constraints on the total nCIE duration and relative shape — together determining the onset duration — affect the interpretation of sedimentary nCIEs. Finally, we evaluate selected well-studied nCIEs, including the Eocene Thermal Maximum 2 (∼54 Ma), the Paleocene-Eocene Thermal Maximum (∼56 Ma), and the Aptian Oceanic Anoxic Event (∼120 Ma), in the context of our model-based framework and show how modeled environmental changes can be used to narrow down the most likely carbon emissions scenarios.

2.1 Introduction

Transient negative carbon isotope excursions (or 'nCIEs') in the geologic record have garnered increasing attention because of the parallels with the modern climate experiment. As anthropogenic emissions of fossil fuel carbon accumulate in the atmosphere, the carbon isotopic composition of atmospheric carbon dioxide ($\delta^{13}C_{CO2}$) has declined by 1.5‰ (the Suess effect) (Suess, 1955; Mook, 1986; Keeling et al., 1979, 1980). Ultimately, the Suess effect will be recorded as a nCIE in the sedimentological record of the future (Norris

et al., 2013). Numerous nCIEs in the geological record are coeval with evidence for increasing global temperature and/or ocean acidification — a combination of impacts that are the hallmark of atmospheric greenhouse gas loading (Hönisch et al., 2012). Investigating rates and masses of carbon release for past nCIEs in combination with environmental impacts informs us about climate sensitivity under various carbon emission scenarios and background climate states. Comparison of these events with the modern provides essential insight into the long-term response of the Earth system to fossil fuel emissions. An increasing number of nCIEs have emerged from the geological record as high-resolution measurements on marine sediment cores become more abundant, leading to hypotheses that these events may represent threshold or tipping point processes rather than independent, stand-alone events (Lunt et al., 2011; DeConto et al., 2012; Armstrong McKay & Lenton, 2018). Hence, geological nCIEs may also provide an opportunity to investigate the sensitivity and role of carbon cycle feedbacks in amplifying or diminishing the consequences of massive carbon release.

The carbon stored in the exchangeable reservoir, consisting of atmospheric carbon (CO_2), dissolved inorganic (DIC) and organic carbon (DOC) in the oceans, and carbon stored in land biota and soils, has a residence time of $\sim 10^5$ years (Figure 2.1). For nCIEs that are represented globally in both deep and shallow marine and terrestrial settings and occur on timescales shorter than 10^5 years, the presumption is these originate from the release of isotopically light carbon to the exchangeable carbon reservoir (Dickens et al., 1995). Fluxes of carbon required to generate a given nCIE are often calculated by a simple isotopic mass balance approach (Equation 2.1).

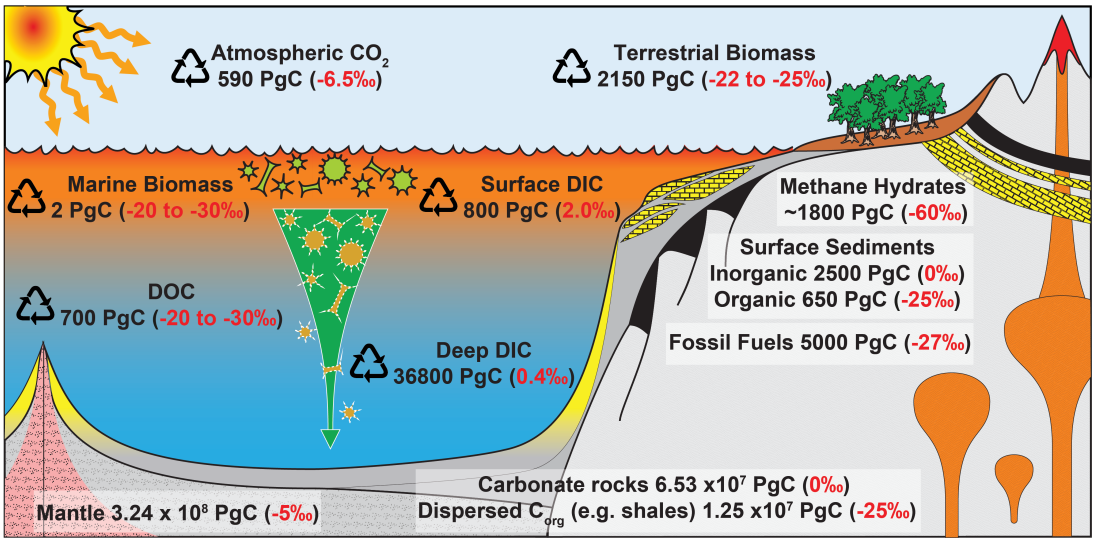

Figure 2.1: Carbon cycle schematic indicating pre-industrial carbon reservoirs (black) and associated isotopic values (red). Atmospheric carbon dioxide (CO_2), marine dissolved inorganic carbon (DIC), marine dissolved organic carbon (DOC), and terrestrial biomass and soil carbon make up the total exchangeable carbon reservoir (triangular arrow symbols). Figure adapted from Andy Ridgwell, personal communication, with reservoir sizes from Sundquist et al. (2005) except for methane hydrates Archer, Buffett, and Brovkin (2009). Isotopic compositions from Jones et al. (2013). cGENIE experiments in this study have slightly different reservoir sizes and isotopic compositions to better match conditions of the early Cenozoic and Mesozoic. The cGENIE exchangeable carbon reservoir in all our experiments includes 1,770 Pg C atmospheric CO_2 with $\delta^{13}C_{CO2}$ of -4.9‰, 30,300 Pg C DIC with $\delta^{13}C_{DIC}$ of 1.7‰, and 7 Pg C of marine DOC with a $\delta^{13}C_{DOC}$ of -27.4‰. Note that the version of cGENIE used here does not include a representation of terrestrial biomass or soil carbon and there is no explicit standing stock of marine biomass.

$$M_a = \frac{M_i \times (\delta_f - \delta_i)}{(\delta_a - \delta_f)} \tag{2.1}$$

The mass of carbon required (M_a) to generate a nCIE of a particular magnitude ($\delta_f - \delta_i$) in the exchangeable carbon reservoir (M_i) with an initial carbon isotopic composition (δ_i) depends on the source of the added carbon and hence its isotopic signature (δ_a). Volcanic activity, for instance, emits CO_2 with a $\delta^{13}C$ that approximates the mantle value of -5 to -8‰(Javoy, Pineau, & Delorme, 1986), while photosynthetic fractionation leaves marine and terrestrial organic matter more depleted in ^{13}C, with $\delta^{13}C$ signatures ranging from -20 to -30‰(Boutton, 1991). Organic carbon reservoirs occurring in the form of coal, oil or gas may reach isotopic values lower than -40‰(Boutton, 1991) while microbial breakdown of organic matter drives the $\delta^{13}C$ of the resulting methane even lower (more negative than -50‰) (Kvenvolden, 1993). A particular-sized nCIE can be generated by the input of either a relatively large mass of carbon with higher $\delta^{13}C$ or a small mass of carbon with lower $\delta^{13}C$. Hence, a well-known issue interpreting nCIEs is that the isotopes alone do not provide sufficient information to estimate the mass of carbon input responsible or the magnitude of change in atmospheric CO_2 associated with a nCIE. A greater mass of carbon added to the exchangeable reservoir should equate to a greater rise in atmospheric CO_2 on 10^3-year timescales, with different implications for radiative forcing and temperature response.

A less often considered difficulty with the isotopic mass balance approach is that it assumes that the total mass of released carbon is instantaneously distributed through the exchangeable reservoir to produce a globally uniform nCIE. This assumption is problematic both for very rapid or very slow release of carbon. If carbon is released more rapidly than

the mixing times between the various pools in the exchangeable reservoir (10^3 years), some of these carbon pools will record an amplified nCIE (Turner & Ridgwell, 2016). For carbon release over longer timescales that approach the residence time of carbon in the exchangeable reservoir, it becomes crucial to account for feedbacks such as carbonate compensation and rock weathering. More recently, modeling approaches have been utilized that explicitly consider the timing of a nCIE derived from sedimentary age models (Cui et al., 2011, 2013; Jones et al., 2013; Gutjahr et al., 2017) in calculating the mass of carbon required to generate a particular nCIE.

However, even constraining the size of a nCIE to use in isotope mass balance calculations or more sophisticated modeling for a single event is not straightforward. Marine carbonates are often used as targets for reconstructing nCIEs because they are presumed to reflect the isotopic composition of the DIC pool, by far the largest pool in the exchangeable surface reservoir (Figure 2.1). However, marine carbonate nCIEs may vary between locations for the same event due to many factors, including spatial variations in bioturbation and dissolution intensity (Sluijs & Dickens, 2012) and whether the carbonate originated from a benthic (seafloor) or planktonic (surface) source. Water depth (for benthic carbonates) may also lead to variations between records. It is possible to identify nCIEs from organic matter as well, though these records must be interpreted with the further caveat that changes in atmospheric CO_2 may lead to changes in the fractionation between DIC and organic matter or changes in organic matter composition that overprint the record of the nCIE as seen by the global exchangeable reservoir (Corsetti et al., 2005).

When considering multiple nCIEs in the geologic record, there is wide variation not only in magnitude, but also in shape and duration, all of which complicate the calculation of required carbon input. This nuance is not captured in a simple isotopic mass balance approach. Importantly, the goal in using isotopic mass balance to infer the magnitude of carbon released is often to constrain past climate sensitivity (or the global temperature increase due to a doubling of atmospheric CO_2) by relating this carbon release to a change in atmospheric CO_2 and combining this with estimates of temperature change. Uncertainty in carbon source and nCIE size will result in the misinterpretation of carbon input required to explain $\delta^{13}C$ excursions (Equation 2.1) but assumed duration and relative timing of an event will also influence 1) the carbon input required, as various reservoir exchanges and feedbacks act on different timescales and 2) the proportional increase in atmospheric CO_2 by determining the fraction of the total emitted carbon that remains in the atmosphere following its release. Hence, uncertainty in age models translates into uncertainty in reconstructed climate sensitivity because for a given mass of carbon release to the exchangeable reservoir, one cannot infer the increase in atmospheric CO_2 without constraining the timing of that carbon input. Instantaneous carbon release will lead to the maximum change in atmospheric CO_2 while slower release of the same mass of carbon will dampen the atmospheric CO_2 rise.

The many nCIEs across the geological record demonstrate that the carbon cycle has been disrupted frequently throughout Earth's history (Saltzman et al., 2012). Perhaps the most well studied nCIE, the Paleocene-Eocene Thermal Maximum (PETM, ∼56 Ma) (Figure 2.2b), is characterized by a rapid onset of several thousand years, negative $\delta^{13}C$

excursion of 3-4‰ and complete isotopic recovery on timescales of 10^5 years (McInerney & Wing, 2011; Röhl et al., 2007; Westerhold, Röhl, Wilkens, et al., 2018; Zachos et al., 2008). Another well-known nCIE is Eocene Thermal Maximum 2 (ETM-2) (Figure 2.2), which is characterized by a nCIE that is half the magnitude of the PETM and more symmetrical in shape, i.e. the onset duration is equal to the duration of the recovery phase (Lourens et al., 2005; Stap et al., 2009). The PETM, ETM-2, and other smaller nCIEs of the early Cenozoic are known collectively as hyperthermals (Thomas & Zachos, 1999). Many of these purported hyperthermals are more similar to the magnitude and shape of ETM-2, i.e. nCIEs of 1-2‰occurring over 40-100 kyr (Kirtland Turner et al., 2014; Sexton et al., 2011; Westerhold, Röhl, Donner, & Zachos, 2018). Though a precise definition of 'hyperthermal' is lacking, these events are typified by simultaneous deep-sea warming and carbonate dissolution in addition to a negative δ^{13}C excursion.

While not always described in the 'hyperthermal' terminology, a number of Mesozoic events share similar characteristics. For instance, the Toarcian Oceanic Anoxic Event (T-OAE, ∼183 Ma) is characterized by a nCIE of ∼6‰between two positive δ^{13}C excursions (Hermoso et al., 2012; H. Jenkyns, 1988; Müller et al., 2017). Similarly, nCIEs have been reconstructed in association with the end-Permian mass extinction (∼252 Ma) (Meyer, Yu, Jost, Kelley, & Payne, 2011), the end-Triassic mass extinction (∼201 Ma) (Pálfy et al., 2001), and preceding multiple Cretaceous OAEs (particularly Aptian OAE-1a (∼120 Ma) (Menegatti et al., 1998) (Figure 2.2a), and OAE-1b (∼111 Ma) (Wilson & Norris, 2001). One complication in comparing these older events to the Cenozoic hyperthermals is that deep sea records are scarce, and nCIEs are often reconstructed from shallow marine set-

tings using carbonate that may have an unclear diagenetic history or using organic matter that may reflect a combination of sources (Corsetti et al., 2005). However, carbon isotope records of these events have been previously evaluated as reflecting changes in the exchangeable carbon reservoir as a result of massive carbon input similar to the Cenozoic hyperthermals.

Given the range of nCIEs observed in the geologic record in terms of size, duration, and shape, as well as varying confidence regarding age control, we herein present an ensemble of modeled nCIEs using the Earth system model 'cGENIE' to reproduce variable nCIEs assuming various carbon sources. We generate 432 experiments (Figure 2.3) and calculate the associated fluxes of carbon and impacts on marine and atmospheric chemistry and temperature for each. Advancing beyond a simple isotope mass balance approach, our modeling utilizes a 3D dynamical ocean model and incorporates carbon cycle feedbacks such as changes in ocean solubility and carbon speciation, carbonate compensation, and temperature-dependent rock weathering. Our framework facilitates assessment of individual nCIEs throughout the geologic record by providing an interpretive template for relating nCIEs of a given size, duration, and shape in the marine DIC reservoir to particular carbon cycle drivers and climatic and environmental consequences.

2.2 Methods

2.2.1 cGENIE Model and Set-Up

In this study, we use the intermediate complexity carbon-Grid ENabled Integrated Earth system model (cGENIE). cGENIE comprises a 3D frictional geostrophic ocean model

and a simple energy-moisture balance atmosphere (Edwards & Marsh, 2005). We include a CO_2–climate feedback: radiative forcing due to CO_2 doubling in cGENIE is $\sim$4 W m^{-2}. We also include temperature-dependent continental weathering (Colbourn, Ridgwell, & Lenton, 2013) with a 1:1 carbonate to silicate weathering ratio and allow transport of alkaline species from the terrestrial into the marine environment. To balance terrestrial input, we couple a sediment model that calculates the sedimentary preservation of inorganic carbon in the form of calcium carbonate ($CaCO_3$) in deep sea sediments (Ridgwell & Hargreaves, 2007). Biogeochemical cycling of elements and isotopes is represented throughout these four model components (Ridgwell et al., 2007). A detailed description and evaluation of the carbon isotope ($\delta^{13}C$) cycle in cGENIE is provided in Ridgwell et al. (2007) and Turner and Ridgwell (2016). Marine (export) productivity is calculated by the local availability of phosphate with modifiers for light limitation and sea ice extent (Ridgwell et al., 2007). Phosphate is modeled as a closed system, with no input or burial fluxes, so its oceanic distribution is controlled by a combination of modeled patterns in export production and physical ocean circulation (which returns nutrients from the deep ocean to the surface). Calcium carbonate ($CaCO_3$) export is calculated using a fixed ratio of calcium carbonate to particulate organic carbon (POC) of 0.2. Both POC and $CaCO_3$ are remineralized in the water column using fixed depth-dependent profiles. Any POC reaching the seafloor is remineralized there (hence we do not account for sedimentary organic carbon burial). Importantly, our model also excludes any representation of land biota or soils, so that the exchangeable carbon reservoir is approximated as atmospheric carbon and marine dissolved inorganic and organic carbon only, which make up about 95% of the pre-industrial exchangeable reservoir (Figure 2.1).

Because our goal is to provide a general interpretative framework for CIEs applicable throughout the geological record, we use a simplified low-resolution (18x18) continental configuration with a single symmetric pole-to-pole continent and 16 ocean depth levels. Still, the model ocean circulation is comparable to that in a higher resolution configuration run for the late Paleocene (Figure A.1, Table A1-A2). Both configurations show a dominant Southern Ocean overturning circulation, though the configuration used here shows overall weaker overturning strength and more symmetrical circulation between hemispheres. Due to differences in the overturning circulation and hence differences in nutrient distribution, the symmetric configuration yields slight increases in fluxes of particulate organic and inorganic carbon and a slight increase in the size of the marine dissolved organic carbon reservoir. However, due to the highly idealized continental configuration and its influence on the modeled circulation pattern, we cannot make explicit comparisons to the behavior of ocean circulation in previous Paleocene cGENIE experiments (Turner & Ridgwell, 2016).

The model is equilibrated to greenhouse climate conditions, with atmospheric CO_2 concentrations of three times preindustrial values (834 ppm), to approximate Mesozoic and Cenozoic greenhouse conditions (Fletcher, Brentnall, Anderson, Berner, & Beerling, 2008). We use the same initial carbon cycle conditions as the published cGENIE Paleocene configuration including: atmospheric $\delta^{13}C$ of -4.9‰, adjusted major ion concentrations (Ca^{2+} 18.2 mmol kg^{-1}, Mg^{2+} 29.9 mmol kg^{-1}), and lower alkalinity (1975 μmol kg^{-1}) along with modern (pre-industrial) inventories for phosphate (2.16 μmol kg^{-1}) and sulfate (15.0 mmol kg^{-1}) (Ridgwell & Schmidt, 2010). The model is run to steady state with carbon input from volcanic outgassing and alkaline run-off from the continent balanced by

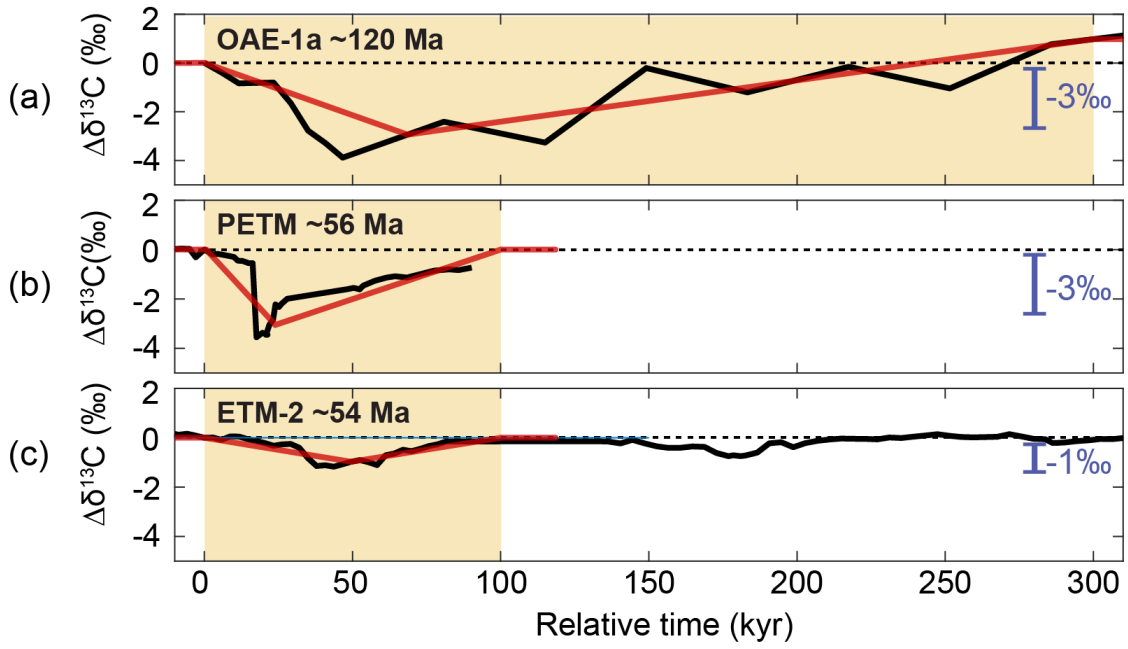

Figure 2.2: Three examples of geologic negative carbon isotope excursions. (a) Bulk δ^{13}C record for the Aptian Ocean Anoxic Event (OAE-1a) from Resolution Guyot (H. C. Jenkyns et al., 1995) with linear interpolation between nCIE onset, peak and end, based on the age model from Malinverno et al. (2010) (black line). (b) Bulk δ^{13}C record for the Paleocene-Eocene Thermal maximum (PETM) from ODP Site 1001 (Bralower et al., 1997) (black line). (c) Bulk record for the Eocene Thermal Maximum 2 (ETM-2) from Site 1258 (Kirtland Turner et al., 2014). The red lines indicate simulated nCIEs from this study that most closely resemble the bulk δ^{13}C records.

carbon removal through burial of $CaCO_3$. The resulting modeled global average sea surface temperature is ∼26°C, sea ice is absent and mean sedimentary wt% $CaCO_3$ is 42%.

2.2.2 Experimental Methodology

Our ensemble tests various combinations of nCIE duration (3), size (4), and carbon source (4) and applies 9 different $\delta^{13}C$ profiles that vary the shape of the nCIE for a total of $3\times4\times4\times9 = 432$ experiments (Figure 2.3). We employ an inverse modeling technique to produce nCIEs, wherein the isotopic signature of the surface ocean dissolved inorganic carbon pool ($\delta^{13}C$ DIC) is forced to follow a prescribed $\delta^{13}C$ profile, while an internal algorithm determines how much atmospheric CO_2 input with a specified isotopic signature is necessary to match this profile (Cui et al., 2011, 2013; Dunkley Jones et al., 2018; Kirtland Turner & Ridgwell, 2013). We choose to force surface DIC $\delta^{13}C$ rather than atmospheric CO_2 $\delta^{13}C$ because the former is a closer approximation to data from marine carbonates. When modeled surface DIC $\delta^{13}C$ values are higher than prescribed, a pulse of isotopically light CO_2 is released into the atmosphere. CO_2 with the same isotopic signature is removed from the atmosphere when modeled surface DIC $\delta^{13}C$ drops below the prescribed value. Hence, CO_2 is artificially removed when carbonate compensation and weathering feedbacks are unable to sufficiently restore surface DIC $\delta^{13}C$ values, but this carbon removal does not represent any particular physical process.

We impose carbon input (and removal) with isotopic signatures of -6‰, -12‰, -22‰, and -60‰, conceptually corresponding to carbon input from volcanism, a mixture of volcanism and organic carbon, organic carbon, and biogenic methane, respectively. The

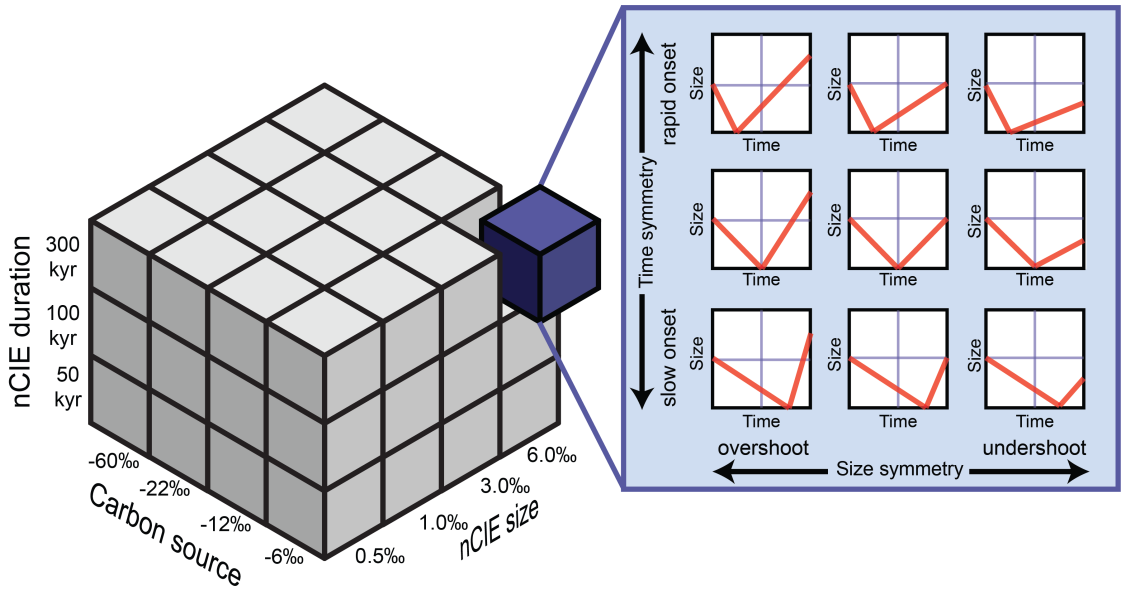

Figure 2.3: Experimental design. Ensemble of $4 \times 3 \times 4 \times 9 = 432$ inversions of surface ocean DIC δ^{13}C varying nCIE size (4), duration (3), carbon isotopic composition of the carbon source (4) and shape (9).

nCIE profiles vary in size (0.5‰, 1.0‰, 3.0‰, and 6.0‰) and duration (50 kyr, 100 kyr, and 300 kyr) to represent the wide range of nCIEs recorded in the geological record. Furthermore, we define nine nCIE shapes (Figure 2.3). We identify three dimensions of symmetry in duration: events can be 1) symmetrical in duration with equal duration onset and recovery phases (δ^{13}C minimum occurs halfway through the event duration) or asymmetrical with either 2) a relatively rapid onset and slow recovery (δ^{13}C minimum occurs at 1/4 of event duration) or 3) relatively slow onset and rapid recovery (δ^{13}C minimum occurs at 3/4 of event duration). We also identify three dimensions of symmetry in size: 1) δ^{13}C values at the onset and recovery are identical, 2) final δ^{13}C values are 50% higher than initial (overshoot) and 3) final δ^{13}C values are 50% lower than initial (undershoot). Hence, the most rapid modeled nCIE onset is 12.5 kyr in experiments with a total duration of 50 kyr. The slowest nCIE onset of 225 kyr occurs in experiments with a total duration of 300 kyr. A

1‰ nCIE with an overshoot will end with DIC δ^{13}C values 0.5‰ higher than initial while a 1‰ nCIE with an undershoot will end with DIC δ^{13}C values 0.5‰ lower than initial.

2.3 Results

Our large ensemble of nCIE experiments allows us to compare both the required carbon input and removal in terms of total mass and fluxes for particular nCIEs and relate the range of these values to uncertainty in carbon source, event duration, and event shape. We calculate 1000-year-binned average values of input and removal fluxes and sum net masses of carbon input/removal over the onset/recovery phases. We also compare the resulting carbon cycle and climate changes in the context of these same nCIE characteristics. In particular, we evaluate modeled changes in atmospheric CO_2, sea surface temperature (SST), surface ocean pH, surface ocean saturation state, weathering rates and wt% $CaCO_3$ at the nCIE peak.

2.3.1 Diagnosed Carbon Forcing

All modeled nCIEs require an input of isotopically light carbon during the onset phase, while carbon needs to be removed during nCIE recovery to restore surface DIC δ^{13}C to higher values. The total mass of carbon necessary to produce a nCIE of specific size depends to a first order on the isotopic signature of the source carbon. Total masses of carbon input diagnosed in our experiments vary by three orders of magnitude (Figure 2.4, A.2). On the high end, to generate the largest size (6‰) nCIE from volcanic carbon with a δ^{13}C of -6‰ requires a carbon input mass that is an order of magnitude larger than

the entire mass of ∼32,000 Pg C in the modeled exchangeable reservoir at the start of the experiment. This contrasts with just a few thousand Pg C necessary to generate the same nCIE with carbon derived from methane with δ^{13}C signature of -60‰ (Figure 2.4, A.2). Significant variability in the required carbon input is also generated by variations in the duration and shape of the nCIE alone. Our results generally show that increasing assumed nCIE duration leads to an increase in the total carbon input on the 10^4-year input timescales modeled here. Increases greater than 50% occur for some combinations of nCIE size and carbon source (Figure 2.4a - left panel and Figure A.2 - moving left to right within each of subplots e-h). Assuming the total duration of the nCIE is also known, varying the duration symmetry still causes variability in the calculated total carbon input. Increasing the relative onset duration from rapid to slow for a nCIE of a given size and total duration generally increases the total carbon input required (Figure 2.4 - compare 2.4b to 2.4c, Figure A.2 - moving from the top to bottom row within each column, i.e. comparing subplots a, e, and i for a given nCIE size, Figure A.3). The effect is more pronounced for longer total durations. Whether a nCIE ends with an undershoot or an overshoot in surface DIC δ^{13}C does not impact the total mass of carbon input required during the onset phase.

Total carbon removal necessary to restore surface DIC δ^{13}C for a nCIE of a given size and shape is similarly controlled to a first order by the imposed isotope composition of the carbon perturbation. In all our experiments, additional carbon removal occurs via the same isotopic composition as carbon input, allowing us to make a straightforward comparison between the relative masses of carbon input and removal, which we illustrate as the net carbon input to the exchangeable reservoir (Figure A.4). nCIEs with a δ^{13}C over-

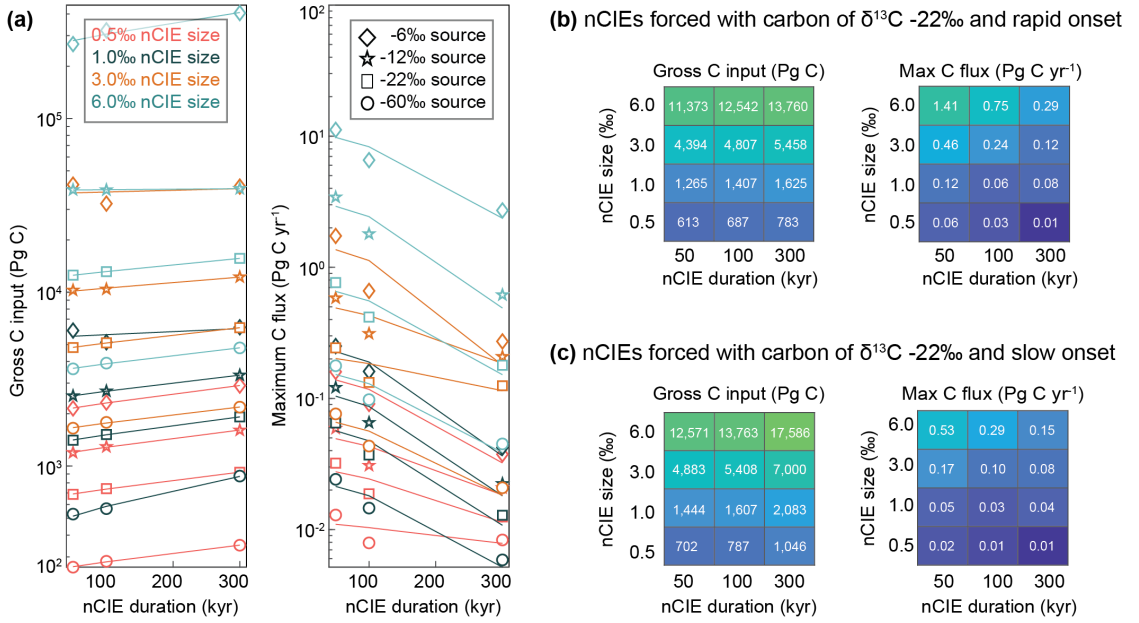

Figure 2.4: Gross carbon input and maximum sustained carbon fluxes for simulated nCIEs. (a) The mass of carbon (left panel) and the maximum sustained flux (right panel) required to produce a prescribed, symmetric nCIE of a given size forced with carbon of predetermined isotope composition against the total duration of the nCIE. (b-c) The mass of carbon (left panel) and the maximum sustained flux (right panel) required as a function of nCIE total duration and nCIE size for an excursion forced with carbon of δ^{13}C -22‰ with a rapid (b) and slow (c) onset (also see supplementary information, Fig. S2 and S4).

shoot (Figure A.4, left columns) are generally created by net removal of carbon over the total nCIE duration (indicated by blue colors) except for those with a long total duration of 300 kyr. nCIEs ending with a δ^{13}C undershoot (Figure A.4, right columns), or nCIEs that are symmetrical in size ('no-shoot', Figure A.4, middle columns) always require a larger mass of carbon input compared to carbon removal (indicated by red colors). In other words, the average carbon isotopic composition of the surface DIC pool is exactly restored, but to achieve this, less carbon is removed than is added. Similarly, nCIEs that are symmetrical in size or with an undershoot leave the exchangeable reservoir significantly larger than at the experiment onset, particularly in the case of the largest nCIEs with the longest duration. In contrast, nCIEs with an overshoot always leave the exchangeable reservoir smaller than at the experiment onset, regardless of nCIE size or duration (Figure A.5).

Rate of carbon input to generate a nCIE of a given size also depends to a first order on the source of carbon input (Figure 2.4, A.5). The maximum sustained rates of carbon input, calculated from 1000-year bins of the yearly average rate, exceed 20 Pg C yr^{-1} and are required to generate the 6‰ nCIE using volcanic carbon with δ^{13}C of -6.0‰. Total event duration is significant for determining rate of carbon input for a given nCIE size and assuming a particular carbon source. Decreasing total duration from 300 kyr to 50 kyr more than doubles the maximum rate of carbon input for all nCIE sizes (Figure A.6 – moving from right to left within each subplot). In other words, compared with the total carbon input, the rate of carbon input is more sensitive to calculated event duration.

Rate is also sensitive to assumptions about duration symmetry. For a nCIE of a given duration, varying the shape from a slow onset to a rapid onset can result in more than

a doubling of the maximum sustained rate of carbon emissions. Hence, the relationship between nCIE duration or shape and maximum carbon flux is the opposite as between nCIE duration or shape and gross carbon input (Figure 2.4a). Maximum carbon flux is highest for shorter, rapid onset events whereas gross carbon input is highest for longer, slower onset events. Overall, our ensemble results in an enormous range of maximum sustained rates in carbon input during nCIE onset phases. The smallest nCIEs require rates of $\sim$0.01 Pg C yr^{-1} assuming depleted carbon sources of either biogenic methane or organic carbon. However, even the smaller nCIEs of 0.5 and 1.0‰ require relatively large sustained rates of carbon input (between 0.03-1.91 Pg C yr^{-1}) if the assumed carbon source is volcanism with a δ^{13}C of -6‰.

None of our simulated nCIEs forced with biogenic methane (δ^{13}C -60‰) or organic carbon (δ^{13}C -22‰) require rates of carbon input reaching the current anthropogenic emission rate of 10 Pg C yr^{-1}. Even a 6‰ nCIE occurring over 50 kyr with a rapid onset over just 12.5 kyr requires a maximum sustained input of only about 1.4 Pg C yr^{-1} assuming an organic carbon (δ^{13}C -22‰) source. In fact, only the experiments with volcanic (δ^{13}C -6‰) carbon as the source ever require input rates in excess of the current anthropogenic value. All nCIEs forced with the mixture of volcanism and organic carbon (δ^{13}C -12‰) have maximum diagnosed emissions less than 6 Pg C yr^{-1}.

2.3.2 Carbon Cycle and Climate Impacts

We focus on carbon cycle and climate changes that could feasibly be estimated using available proxies, including the change in atmospheric CO2 (Figure 2.5, A.7), surface ocean pH (Figure A.8), surface ocean saturation state (Figure A.8) and sea surface temper-

ature (SST) (Figure A.9). Given the dynamic ocean model in cGENIE, ocean circulation in our experiments is not fixed, yet we find minor changes of less than ∼3% in ocean overturning at the nCIE peak for most experiments (less than 1 Sv for all experiments except the 6‰ nCIEs forced with -6‰ volcanic carbon, which still show less than 3 Sv change at the nCIE peak). These subtle changes in ocean circulation also result in small changes in export production, which, in our model, is a function only of phosphate availability with modifiers for light limitation and sea ice extent (although no sea ice occurs in our experiments). These export production changes are small relative to changes in the size of the atmospheric and inorganic ocean carbon reservoirs (less than 1 Pg C yr^{-1} change at the nCIE peak in all but a few 6‰ nCIE experiments that show a maximum change of 3 Pg C yr^{-1} at the nCIE peak). The simulated changes to the carbon cycle are thus driven primarily by the total mass and rate of carbon input and associated feedbacks in the carbonate chemistry — the focus of our discussion henceforth — rather than changes in primary productivity or ocean circulation.

Our experiments result in an extremely large range of rates and total masses of carbon input (Figure 2.4) that diverge from estimates based on the simple mass balance approach (Figure 2.5). The most pronounced difference between the mass balance approach and our nCIE simulations occurs for the nCIE of 6‰ with a 225 kyr-long onset phase forced with δ^{13}C carbon of -6‰. Simple isotope mass balance predicts that ∼147,200 Pg C input is required, while cGENIE requires nearly three times as much carbon input (∼413,800 Pg C). We use the results for environmental variables, particularly temperature, to test whether these results are realistic. For instance, the maximum atmospheric CO_2 reached in any of

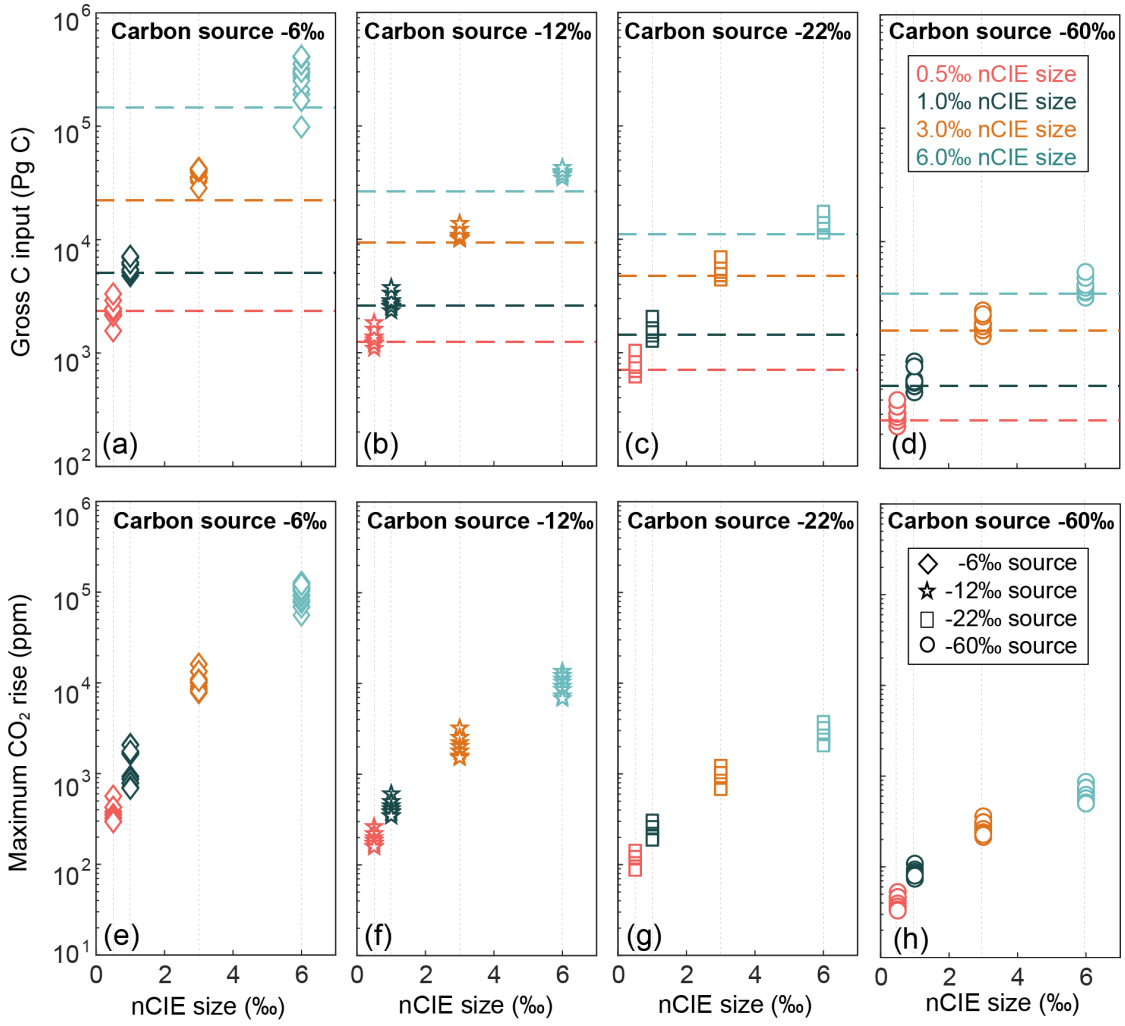

Figure 2.5: Gross carbon input required to produce nCIEs of given size (a-d) and the maximum atmospheric CO_2 rise associated with each (e-h), for nCIEs forced with carbon of volcanic origin ($\delta^{13}C$ -6‰) (a,e), a mixture of organic and volcanic carbon ($\delta^{13}C$ -12‰) (b,f), organic carbon ($\delta^{13}C$ -22‰) (c,g), and biogenic methane ($\delta^{13}C$ -60‰) (d,h). The range of gross carbon input and atmospheric CO_2 rise for a given nCIE size results from different nCIE durations and shapes. The horizontal dashed lines (a-d) indicate the mass of carbon input calculated using a simple mass balance approach (Equation 1).

our experiments is over 120,000 ppm CO_2, which is equivalent to slightly more than seven doublings from the initial concentration of 834 ppm. In cGENIE, the imposed radiative forcing due to CO_2 doubling is $\sim$4 W m^{-2} resulting in a typical surface temperature rise of 3.2°C per CO_2 doubling (Figure A.12).

The largest increases in atmospheric CO_2 occur in our long duration (300 kyr) experiments with a 6‰nCIE driven by a -6‰ (volcanic) source, leading to an increase in average surface air temperature of almost 28°C or an absolute maximum average surface air temperature of $\sim$50°C. SST rises by $\sim$22°C. In contrast, when the most isotopically depleted carbon source is assumed, this yields an increase in atmospheric CO_2 equivalent to approximately one doubling and SST warming of just 2.6°C. The smallest nCIEs of 0.5‰ lead to a minor increase in atmospheric CO_2 of less than 150 ppm if the assumed carbon source is either organic carbon or biogenic methane. The associated increase in SST is just a few tenths of a degree Celsius. For a nCIE of a given size and carbon source, the maximum increase in CO_2 and maximum increase in SST both correspond to the maximum carbon addition rate rather than the total mass of carbon added, such that shorter durations and rapid onsets lead to greater increases in CO_2 and temperature.

The sole exception occurs for 6‰ nCIEs forced by volcanic carbon (-6‰), where larger increases in CO_2 and SST occur for relatively longer duration events with slower onsets. For these nCIEs only, the maximum change in CO_2 and SST corresponds to the largest gross carbon input rather than the highest carbon input rate. The atmosphere in these scenarios becomes a proportionally larger carbon reservoir than the ocean, i.e. the ocean contains 17,121 Pg C at the nCIE peak, while the atmosphere contains nearly double

that mass (27,429 Pg C) as a consequence of reduced CO_2 solubility with extreme warming. This means that ocean uptake is unable to remove excess CO_2 even when that CO_2 is emitted relatively slowly, so it continues to accumulate in the atmosphere. It is important to note that such large masses and rates of carbon input may not be representative of the events that occurred during any time in the Mesozoic or Cenozoic.

With greater atmospheric carbon input, greater quantities of CO_2 dissolve into the surface ocean, lowering surface ocean pH and the saturation state with respect to calcite and aragonite (Ω_{cal} and Ω_{arg}, respectively). The largest change in mean surface ocean pH (a decrease of 1.7) occurs in 6‰ nCIEs forced with volcanic carbon. Aside from the 6‰ nCIEs forced by enormous quantities of volcanic carbon described above, the relative decline in surface ocean pH for each experiment is equivalent to the relative increase in CO2 - in other words, a shorter onset duration and hence more rapid rate of carbon input leads to a larger decline in surface ocean pH for a nCIE of a given size and carbon source. The largest change in saturation state with respect to calcite (a decrease of 5) occurs in 6‰ nCIEs forced with volcanic carbon that have the shortest onset durations of 12.5 to 25 kyr. In the initial model state prior to carbon emissions, the surface ocean is everywhere oversaturated with respect to calcite ($\Omega_{cal} > 1$) and 99.2% of the grid cells are oversaturated with respect to aragonite ($\Omega_{arg} > 1$). While aragonite undersaturation ($\Omega_{arg} < 1$) can occur in parts of the surface ocean with very modest carbon forcing, calcite undersaturation requires input greater than 10,000 Pg C. Both calcite and aragonite undersaturation occurs predominately at the high latitudes where carbon uptake is maximized due to the higher solubility of CO_2.

Carbon forcing greater than 40,000 Pg C over 12.5 kyr or shorter is required to drive $\Omega_{arg} < 1$ at low latitudes.

Onset duration (or the time to the nCIE peak) controls whether or not the response of the mean surface ocean pH and saturation state behave similarly in response to a given carbon input (Figure A.8). As nCIE duration increases, the magnitude of the surface pH decrease is slightly reduced (with the exception of 6‰ nCIEs forced by volcanic carbon (-6‰)), but the magnitude of the surface saturation state decrease is more notably reduced. The same relative effect is seen as a function of temporal symmetry – a rapid onset and slow onset of a nCIE with the same total duration show similar declines in surface ocean pH but the rapid onset nCIE shows a larger decline in saturation state. Hence, the mean surface ocean pH is more sensitive to total C input and surface saturation state is more sensitive to C flux. These results are consistent with the findings of (Hönisch et al., 2012) who demonstrated that ocean pH and saturation state change are progressively decoupled when carbon input occurs over long timescales. Notable decoupling begins for carbon input over 10^4 years or more.

We can also evaluate how each of the above variables evolves with time across each experiment. As an example, we show the response of atmospheric CO_2, surface ocean pH and saturation state with respect to calcite, deep sea carbonate content (wt% $CaCO_3$), weathering flux (in terms of Ca^{2+}) and SST for a modeled nCIE similar to Eocene Thermal Maximum 2 (ETM-2, 53 Ma) (Figure 2.6a). We take a nCIE of 1‰ with a total duration of 100 kyr and a symmetric shape (50 kyr onset duration) as the best approximation and evaluate the modeled response of the above variables across the experiment duration. At-

mospheric CO_2 and SST peak at the same time as gross C input, coincident with minimum $\delta^{13}C$ in surface ocean DIC. Simultaneously, surface ocean pH and saturation state reach their minima while weathering fluxes reach their maxima. Sedimentary wt% $CaCO_3$, however, shows a minimum that precedes the peak in SST and weathering flux and has already begun to rebound before the $\delta^{13}C$ minimum. The later rebound in $CaCO_3$ shows maximum accumulation approximately coeval with maximum surface ocean saturation state. In a similar manner, a comparison is made between the PETM, OAE-1a, and the nCIE simulations performed to establish the framework presented here (Figure A.11).

2.4 Discussion

2.4.1 Diagnosed Carbon Input

Our experiments highlight the significance of considering timing in diagnosing the carbon input required to generate a nCIE. Of particular importance is the time to peak nCIE (onset duration), which is controlled by both nCIE duration and nCIE shape in our experimental framework. Overall, we find that greater carbon input is necessary to generate a nCIE with a longer onset duration, but the rise in atmospheric CO_2 decreases with onset duration. The experiments start from steady state with respect to the exchangeable carbon reservoir (carbon inputs from weathering fluxes and volcanism are balanced by sedimentary carbonate burial), on top of which carbon inputs diagnosed by the inversion scheme are added from an external, specified source. Carbon addition diagnosed by the inversion scheme during the nCIE onset directly increases the size of the exchangeable

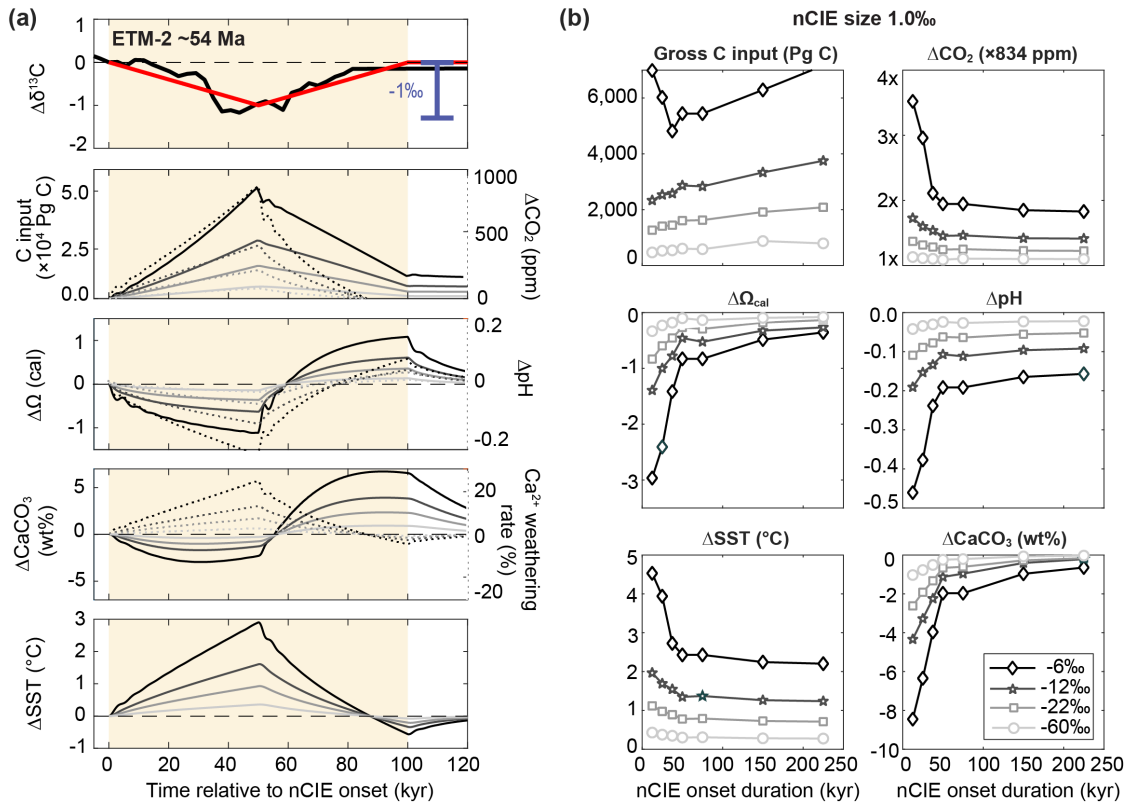

Figure 2.6: Carbon cycle evolution and environmental impacts of a nCIE with a size of 1‰. (a) In the upper panel, bulk δ^{13}C record of the ETM-2 from Site 1258 (Kirtland Turner et al., 2014) (black line) and the simulated nCIE that best matches this record: symmetric in time with a total duration of 100 kyr (red line). Below, the evolution of the gross carbon input (solid), change in atmospheric CO_2 (dashed), change in surface ocean calcite saturation state (Ω_{cal}, solid) and surface ocean pH (dashed), change in global mean sedimentary wt% $CaCO_3$ (solid), percentage of change in rock weathering rate relative to initial conditions (dashed), and the change in sea surface temperature (SST) for 1‰ nCIEs, forced with -6‰, -12‰, -22‰, and -60‰ δ^{13}C carbon. (b) The maximum change in carbon cycle and environmental parameters compared with initial model conditions as a function of onset duration for 1‰ nCIEs.

carbon reservoir. The exchangeable reservoir also grows or shrinks because of the indirect effects of global temperature and ocean chemistry on weathering rates and the preservation of sedimentary $CaCO_3$. These feedbacks operate over characteristic timescales, such that nCIE duration exerts an important control on the total carbon mass in the exchangeable reservoir as well as the relative distribution of carbon among atmospheric CO_2 and the oceanic DIC and DOC pools. At the start of each experiment, the exchangeable reservoir totals just over 31,800 Pg C (atmospheric CO_2 of ~1800 Pg C, marine DIC of ~30,000 Pg C, and marine DOC of ~6.7 Pg C). For a 6‰, 300 kyr nCIE with a relatively rapid onset (75 kyr) driven by -22‰ carbon, the masses of these reservoirs total just over 48,000 Pg C (atmosphere ~7000 Pg C, DIC ~41,000 Pg C, and DOC ~6.9 Pg C) at the nCIE peak, an increase of about 17,000 Pg C over initial conditions. However, the inversion scheme diagnoses a gross C input over this interval of 13,760 Pg C. Thus >3000 Pg C (more than 20% of the total exchangeable carbon reservoir increase) is attributable to excess weathering not balanced by increased $CaCO_3$ burial by the time of the nCIE peak. Further, there has been a relative redistribution of carbon such that the atmosphere is a proportionally larger carbon pool (although DIC still dominates the exchangeable reservoir mass) because as atmospheric CO_2 rises and surface ocean pH declines, the ocean's buffering capacity is reduced.

A mass balance framework utilizes only information about the initial mass of the exchangeable carbon reservoir, the size of the nCIE, and the inferred carbon source. Our more nuanced framework, by incorporating inorganic carbon cycle feedbacks, also utilizes constraints provided by age models on the total and relative duration of a nCIE and provides

a refined first order estimate regarding the range of possible carbon fluxes and cumulative input masses. Figure 2.5 illustrates the difference between the simple isotope mass balance calculations for carbon input and our cGENIE model results for gross carbon addition. While the simple isotope mass balance approach (Equation 1) provides a single value for a particular size nCIE given an assumed carbon source (with specified δ^{13}C), our experiments generate a range of estimates for carbon input, depending on the duration and shape of the nCIE. The discrepancy between our cGENIE diagnosed carbon inputs and a simple mass balance approach is most pronounced for larger nCIEs generated using carbon sources with higher δ^{13}C. For instance, assuming a volcanic carbon source (Figure 2.5a), the isotope mass balance approach provides an estimate of input mass that falls nearly in the middle of the range calculated by cGENIE for a 0.5‰ and 1‰ nCIE, but isotope mass balance gives a value closer to the lower range of diagnosed carbon inputs for nCIEs of 3‰ and 6‰. This increasing discrepancy between isotope mass balance and our results for large input masses is due to the temperature-dependent weathering parameterization (i.e. weathering increases by more and thus gross carbon must increase by relatively more to compensate as total carbon input increases).

Both our approach and the simple isotope mass balance (Equation 1) require information about initial carbon cycle conditions. In the mass balance approach, this is simply the mass of the total exchangeable reservoir. Our approach requires not only this information, but also makes presumptions about the initial buffering capacity of the oceans, which will influence how carbon is exchanged between reservoirs and how much seafloor carbonate dissolves. These carbon cycle assumptions must be considered when comparing our results

against particular geological events, especially those that occurred prior to the advent of widespread pelagic calcification during the Jurassic (∼170 Ma) (Arvidson, Mackenzie, & Berner, 2014).

We do not explicitly test the impact of varying initial carbon cycle conditions on our results; however, we can infer the general impact of particular assumptions. While it is likely that the marine DIC pool (by far the largest of the exchangeable carbon pools) was similar in mass through much of the Cenozoic, it was likely larger during much of the Mesozoic (Ridgwell, 2005). If the mass of the total exchangeable reservoir (atmospheric CO_2 and ocean DIC and DOC) was significantly larger, the required carbon input of a given isotopic signature for a given nCIE would have been larger. Varying initial carbon cycle conditions, including alkalinity or major ion composition, would have a more nuanced influence, altering the relative partitioning of carbon between reservoirs and controlling the strength of feedbacks that are sensitive to this distribution. For example, initial carbon cycle conditions characterized by higher relative partitioning into atmospheric CO_2 (lower surface ocean pH) requires relatively larger masses of CO_2 emitted to achieve the same nCIE in the surface ocean DIC pool because a greater proportion of emissions will remain in atmosphere, i.e. the global mean Revelle factor is higher in a high pCO_2/low pH world. With a greater increase in atmospheric CO_2, the resultant enhanced weathering that releases relatively isotopically heavy alkaline carbon species will dampen the signal of the ^{13}C-depleted emissions and hence require even greater ^{13}C-depleted CO_2 emissions to generate the same nCIE in the surface ocean. Thus, when interpreting an individual geologic event in the context of our hypothetical framework, it is necessary to consider whether initial

mean surface ocean pH is likely to have been lower or higher than what is modeled here (pH is ∼7.7).

2.4.2 Diagnosed Carbon Removal

Restoration of surface DIC $\delta^{13}C$ to pre-excursion values during the recovery phase requires addition of relatively heavy carbon (via carbonate dissolution and weathering) and/or removal of isotopically light carbon. The model calculates fluxes of carbon (and its isotopes) both within the exchangeable reservoir and including sediment and weathering feedbacks, and then compensates for any remaining deviations of the surface ocean DIC $\delta^{13}C$ pool from the target curve through removal of CO_2 with a specified $\delta^{13}C$ from the atmosphere. In other words, carbon simply disappears from the model atmosphere if the simulated carbon cycle feedbacks have failed to restore surface ocean DIC $\delta^{13}C$ sufficiently to match the prescribed curve. This process is conceptually simple, but it has consequences that are most likely not realistic. First, this diagnosed additional atmospheric carbon removal is not simulated as any particular physical mechanism. Second, the fact that the carbon removal flux has a specified isotopic composition (here we use the same value as the carbon input), means that we are not adjusting the isotopic composition of the removed carbon based on the composition of exchangeable reservoir or based on likely fractionations of real removal processes (e.g. organic matter formation). Third, our method does not account for removal of carbon at a different isotopic composition than the input, though in reality these values may be very different (e.g. input of volcanic CO_2 followed by removal via organic carbon burial). An alternative approach for calculating carbon removal, even without explicitly modeling organic carbon burial, would be to remove carbon with an

isotopic composition matching that of the modeled particulate organic carbon pool (Gutjahr et al., 2017), rather than using an assigned value.

Only nCIEs with an undershoot where the final $\delta^{13}C$ is lower than the initial $\delta^{13}C$, and/or a long duration and slow recovery result in diagnosed carbon removal fluxes substantially less than input fluxes, in other words, they show a large positive net carbon input (Figure A.4). This indicates that modeled feedbacks are nearly sufficient to match the surface DIC $\delta^{13}C$ signature in these cases and little additional diagnosed carbon removal is necessary. In modeled nCIEs where the diagnosed mass of carbon removal rivals or even exceeds the diagnosed carbon input, this implies that the carbonate compensation and weathering feedbacks alone were insufficient to drive the recovery of surface DIC $\delta^{13}C$ and additional carbon removal (modeled as CO_2 artificially removed from the atmosphere) was necessary. A deficiency in our experiments is thus the lack of organic carbon burial, which might help explain the recovery of surface ocean DIC $\delta^{13}C$ without requiring an additional removal flux via our inversion methodology for the larger and/or shorter duration nCIEs. Given that a number of nCIEs in the geologic record are followed by black shale deposition and associated positive $\delta^{13}C$ excursions, e.g. the Toarcian and Aptian OAEs, there is clear evidence that organic carbon feedbacks not only played a role in recovery of the exchangeable reservoir from carbon input but often led to 'overshoot' behavior (H. Jenkyns, 2010).

2.4.3 Carbon Cycle and Climate Impacts

The change in atmospheric CO_2 and associated warming generated in each of our experiments allows us to reasonably rule out certain carbon input scenarios for certain nCIEs. In particular, the massive carbon inputs required to generate 6‰ nCIEs using

volcanic carbon of -6‰ raise atmospheric CO_2 to levels that lead to an average ocean temperature greater than 40° C, inconsistent with data for even the Mesozoic greenhouses. The highest reconstructed low latitude surface temperatures during the Cretaceous are reconstructed from the TEX86 archaeal lipid SST proxy, and are a maximum of ∼36° C (Schouten et al., 2013). Further, evidence for SST in excess of 40°C during the PETM from Tanzania in combination with the exclusion of planktic foraminifera has been provided as evidence of a temperature threshold for these organisms (Aze et al., 2014). It seems likely that widespread temperatures this high would have resulted in significant extinction and widespread dead zones. Adding the effects of severe thermal stress on marine organisms (not modeled here) could increase CO_2 even further if the biological carbon pump were to collapse. This suggests that large nCIEs occurring over the timescales modeled here and similar to several Mesozoic nCIEs are unlikely to have been driven by isotopically heavy carbon input (e.g. mantle-derived volcanism) alone. nCIEs of 3‰ forced with -6.0‰ carbon and 6‰ nCIEs forced with -12‰ carbon have maximum CO_2 concentrations 7,500-17,000 ppm and maximum global mean SSTs of 33-36° C, more consistent with proxy temperature records.

Our experiments highlight the importance of nCIE duration and shape for determining carbon input rate, which has significant impacts on atmospheric CO_2, SST and saturation state (Figure A.10). While nCIEs with short onset durations require less total input of carbon than nCIEs with longer onset durations, maximum atmospheric CO_2 concentrations are highest in the shortest nCIEs. Again, this can be attributed to marine carbonate compensation and terrestrial rock weathering, which both act to stabilize

ocean saturation state and modulate atmospheric CO_2 concentrations over 10^4-10^5-year timescales (Archer & Maier-Reimer, 1994; Archer, Kheshgi, & Maier-Reimer, 1997; Archer, 2005; Archer, Eby, et al., 2009; Goodwin & Ridgwell, 2010; Walker, Hays, & Kasting, 1981). In particular, the temperature-dependent weathering feedback in cGENIE operates with an e-folding timescale of ∼240 kyr (Colbourn, Ridgwell, & Lenton, 2015). As carbon input extends over intervals of time commensurate with the e-folding weathering timescale, the required total carbon input increases while the effect of those emissions on atmospheric CO_2 (and hence temperature rise) is limited.

The differential sensitivity of surface ocean saturation state and pH to nCIE onset duration (Figure A.8) that occurs in our experiments has been noted previously (Hönisch et al., 2012) and is a further example of how the timescale of carbon release interacts with the timescales of negative inorganic carbon cycle feedbacks (Hönisch et al., 2012). A consequence of the weathering feedback is that when carbon input is sufficiently slow, the dominant sedimentary response is an increase in $CaCO_3$ accumulation rate. In our experiments, modeled sedimentary $CaCO_3$ concentrations drop initially in response to carbon addition, but after approximately 20-30 kyr (or less, for the shortest onset experiments) global sedimentary wt% $CaCO_3$ starts increasing. In fact, for most of our experiments this carbonate overshoot (Penman et al., 2016) exceeds initial dissolution in terms of the change in global mean wt% $CaCO_3$. It is important to note that we employ a fixed rain ratio (i.e. constant ratio of particulate organic carbon to particulate inorganic carbon throughout our experiments) and fixed remineralization profiles so that carbonate fluxes only change along with changes in calculated export productivity. The duration of carbonate dissolution is

hence related to the weathering timescale and not to the duration of carbon input. As enhanced weathering delivers excess alkalinity to the oceans, carbonate burial will recover and rebound, regardless of whether carbon input to the atmosphere has ceased.

2.4.4 Comparison With Past nCIEs

A primary goal of our ensemble is to provide a framework for interpretation of past geological events. Below, we provide examples in comparing our model experiments to three events: ETM-2, the PETM and OAE-1a.

ETM-2

The Eocene Thermal Maximum 2 (ETM-2, ∼54 Ma) is a relatively short-lived warming event marked by a symmetric nCIE of 1.0 to 1.5‰ and widespread deep sea $CaCO_3$ dissolution (Lourens et al., 2005; Stap et al., 2009) (Figure 2.2c). The nCIE scenario modeled in this study that is most similar to the ETM-2 is the symmetric 1‰ nCIE with a total duration of 100 kyr without under- or overshoot in surface DIC $\delta^{13}C$ (Figure 2.6a). To produce a nCIE of this size with an isotopically heavy carbon input (-6‰), approximately 5200 Pg C is required, resulting in atmospheric CO_2 increase of 900 ppm and SST increase of 2.6°C. An input of isotopically lighter carbon (-12 to -22‰) over 50 kyr produces a 1‰ nCIE with 2700 to 1500 Pg C respectively, and leads to a global mean SST increase of 1.5 to 0.8°C. Previous studies based on proxy data estimate (regional) SST increases during ETM-2 of 3-5°C (Lourens et al., 2005; Sluijs et al., 2009), which fits best to a carbon input of mantle-derived volcanic source. However, the orbital pacing of a sequence of early Eocene hyperthermals, including ETM-2, seems inconsistent with a volcanic origin.

Increases in SST of 1.5 to 0.8°C produced by -12 and -22‰ carbon input are low compared to available SST proxies, but the maximum ETM-2 magnitude of 1.5‰ recorded in bulk carbonate is 0.5‰ larger than the 1‰ nCIE we compare to here and the true nCIE magnitude may have been even larger (Sluijs et al., 2009). An nCIE of 1‰ driven by isotopically light (-60‰) methane requires ∼600 Pg C, produces an increase in atmospheric CO_2 of only 80 ppm and a 0.3°C SST increase. The latter would be nearly undetectable in most noisy proxy data. Furthermore, the widespread deep sea carbonate dissolution associated with ETM-2 does not result from experiments with isotopically lighter carbon sources. Less than 2.5 wt% global average $CaCO_3$ decline results from a 1‰ nCIE driven by either -60‰ or -22‰ carbon inputs. Hence, a larger carbon input (and therefore a carbon input with mean $\delta^{13}C$ signature heavier than -22‰) is most consistent with the extent of environmental changes during ETM-2. An alternative scenario that could explain the large temperature increase and globally widespread carbonate dissolution that is that ETM-2 onset occurred on timescales much shorter than 50 kyr. nCIEs with an onset duration shorter than 50 kyr result in a significant drop in surface ocean calcite saturation state (Ω_{arg}) which promotes the dissolution of $CaCO_3$ (Figure 2.6b and Figure A.8, A.10). Likewise, the SST rise associated with a more rapid nCIE onset is larger compared to a nCIE onset duration over 50 kyr (Figure 2.6b and Figure A.9).

PETM

The Paleocene-Eocene Thermal Maximum (PETM, ∼56 Ma) is the greenhouse gas driven global warming event most often suggested as an analog for the modern (Zeebe & Zachos, 2013). Many more records of the PETM nCIE from a greater variety of settings

are available in comparison to other Mesozoic and Cenozoic hyperthermals (McInerney & Wing, 2011). The nCIE varies in size between different reservoirs, but the average bulk carbonate nCIE is closest in size to the 3‰ nCIEs modeled here (Figure 2.2b). The PETM is well known for its asymmetric shape, with a rapid onset of <10 kyr and a total duration of ∼200 kyr (McInerney & Wing, 2011; Turner, 2018). None of our experiments shows an onset as rapid as the PETM — the most rapid modeled onset for a 100 kyr nCIE is 25 kyr. We compare the PETM to the 100 kyr, rapid onset 3‰ nCIE without under- or overshoot in surface DIC δ^{13}C (Figure A.11b). Estimated total carbon input is between 1600 to more than 40,000 Pg C depending on carbon source. Only the -12‰ carbon source leads to an increase in SST (5°C) consistent with compiled temperature proxy records (Jones et al., 2013), resulting in an increase in atmospheric CO_2 levels by ∼2,500 ppm and declines in surface ocean pH and calcite saturation state (Ω_{cal}) of 0.47 and 2.7, respectively. The total carbon input for this scenario (>10,000 Pg C) is also consistent with recent estimates (Gutjahr et al., 2017)]. However, the onset duration of the PETM is estimated to be shorter than 25 kyr and we can use our framework to explore the environmental consequences of more rapid onset duration as well. When a 3‰ nCIE onset is produced over 12.5 kyr (from the experiment with a modeled total duration of 50 kyr) using a carbon source with δ^{13}C of -22‰, approximately 10,000 Pg carbon input is required. This increases atmospheric CO_2 levels by 3,200 ppm, the global mean SST rises by 5.6‰C, surface pH drops 0.57 units and Ω_{cal} declines by 3.4.

OAE-1a

The Aptian Ocean Anoxic Event (OAE-1a) is one of the two major Cretaceous OAEs with a recorded nCIE preceding wide-spread organic carbon burial (Menegatti et al., 1998; Herrle, Kößler, Friedrich, Erlenkeuser, & Hemleben, 2004; H. Jenkyns, 2010) and might hold important information on carbon reservoir changes involved in the expansion of marine anoxia during this time. Aptian nCIEs are most commonly recorded with sizes ranging from -1 to -3‰. Using a nCIE at the upper limit of that interval from carbonate deposits at the Resolution Guyot (H. C. Jenkyns et al., 1995) and age models based on cyclostratigraphy (Malinverno et al., 2010), the nCIE at the onset of OAE 1a most closely resembles our 300 kyr-long simulations with rapid onset and δ^{13}C values ending in an overshoot (Figure A.11a). nCIEs of this shape and duration can be produced by δ^{13}C -60‰ biogenic methane emissions without drastically perturbing climate and ocean carbonate chemistry, but such a forcing mechanism cannot account for the reconstructed simultaneous rise in SST of 2-5°C (Mutterlose, Bottini, Schouten, & Sinninghe Damsté, 2014; Naafs & Pancost, 2016), the atmospheric CO_2 increase of a few hundred to several thousand ppm (Naafs & Pancost, 2016), or the crisis of marine calcifying nannoplankton (Erba, Bottini, Weissert, & Keller, 2010). A purely volcanic source of carbon results in a pCO_2 rise of 10 to 20 times pre-nCIE values, a stark decrease in surface pH and ocean calcite saturation, and a rise in global mean SST up to 10°C. Those environmental impacts are far more extreme than the proxy-based reconstructions suggest. Based on our framework and the age model provided by (Malinverno et al., 2010), the Aptian nCIE was most likely caused by a combination of organic and mantle carbon sources, resulting in the net emission of

carbon of intermediate isotopic composition. However, recently published high-resolution records from shallow carbonate platforms suggest that the nCIE onset might have lasted significantly longer (Kuhnt, Holbourn, & Moullade, 2011; Lorenzen et al., 2013; Graziano & Raspini, 2018), in which case a forcing from δ^{13}C -6‰ volcanic carbon becomes more plausible for the OAE-1a since longer nCIE onsets result in reduced impacts in climate and ocean chemistry, but a slight increase in the total amount of carbon that needs to be added to the ocean-atmosphere system (Figure A.10).

2.5 Conclusion

Our large ensemble of modeled nCIEs provides a template for interpreting past geologic events in terms of required carbon input and likely environmental consequences. We include the effects of various feedbacks such as changes in ocean solubility, carbon speciation, carbonate compensation and temperature-dependent weathering on the global carbon cycle. The earth system modeling approach allows us to track changes in the partitioning and fractionation of carbon between various carbon pools within the exchangeable reservoir. Our four dimensions of variability in defining modeled nCIEs (including size, carbon source, duration, and shape) adds two new dimensions compared to the conventional isotopic mass balance approach that neglects variability in duration and shape. Our results highlight the significant variability these two factors can generate in both the total carbon input required to generate a nCIE of a particular magnitude with a particular carbon source, but also the maximum rate of carbon input as a result of the interaction with modeled carbon cycle feedbacks. Thus, our experiments can be used to bracket the carbon emissions

scenarios capable of driving any number of past nCIEs. Furthermore, these experiments demonstrate how environmental impacts scale with all four dimensions of variability. Hence, a comparison of available proxy data (e.g. changes in temperature, surface ocean pH, or changes in saturation state inferred from sedimentary carbonate dissolution) to our results can also be used to evaluate the likelihood of various carbon sources for a nCIE of a given magnitude.

Chapter 3

Earth System Model Analysis of how Astronomical Forcing is Imprinted Onto the Marine Geological Record

The Role of the Inorganic Carbon Cycle and Feedbacks

Abstract - Astronomical cycles are strongly expressed in marine geological records, providing important insights into Earth system dynamics and an invaluable means of constructing age models. However, how various astronomical periods are filtered by the Earth system and the mechanisms by which carbon reservoirs and climate components respond, particularly in absence of dynamic ice sheets, is unclear. Using an Earth system model that includes feedbacks between climate, ocean circulation, and inorganic (carbonate) carbon cycling relevant to geological timescales, we systematically explore the impact of astronomically-modulated insolation forcing and its expression in model variables most comparable to key paleoceanographic proxies (temperature, the δ^{13}C of inorganic carbon, and sedimentary carbonate content). Temperature predominately responds to short and long eccentricity and is little influenced by the modeled carbon cycle feedbacks. In contrast, the cycling of nutrients and carbon in the ocean generates significant precession power in atmospheric CO_2, benthic ocean δ^{13}C, and sedimentary wt% $CaCO_3$, while inclusion of marine sedimentary and weathering processes shifts power to the long eccentricity period. Our simulations produce reduced pCO_2 and DIC δ^{13}C at long eccentricity maxima and, contrary to early Cenozoic marine records, $CaCO_3$ preservation in the model is enhanced during eccentricity modulated warmth. Additionally, the magnitude of δ^{13}C variability simulated in our model underestimates marine proxy records. These model-data discrepancies hint at the possibility that the Paleogene silicate weathering feedback was weaker than modeled here and that additional organic carbon cycle feedbacks are necessary to explain the full response of the Earth system to astronomical forcing.

3.1 Introduction

High-resolution paleoclimate records across the Cenozoic Era show that global climate and carbon cycling are closely connected on astronomical timescales on the order of 10^4 to 10^6 years (Mix et al., 1995; Sigman & Boyle, 2000; Zachos et al., 2001; Palike et al., 2006; Wang et al., 2010; Kirtland Turner et al., 2014; Peterson et al., 2014; Westerhold, Röhl, Donner, & Zachos, 2018; Barnet et al., 2019). In particular, during the early, ice-free Cenozoic, benthic foraminiferal oxygen and carbon isotopes (δ^{18}O and δ^{13}C) show a strongly coherent astronomical influence (Cramer et al., 2003; Zachos et al., 2010; Westerhold et al., 2011; Kirtland Turner, 2014; Littler et al., 2014), suggesting tightly coupled carbon cycle-climate dynamics. Multiple records reveal periodic, astronomically paced negative δ^{13}C excursions with a magnitude of 0.3 to 1.0‰ coinciding with deep water warming of 2-4°C as well as reductions in sedimentary calcium carbonate content (Lourens et al., 2005; Zachos et al., 2010; Sexton et al., 2011). Explanations for an astronomical trigger for these events, known as hyperthermals, invoke dynamics of a reduced carbon reservoir such as methane hydrates (Dickens, 2003; Lunt et al., 2011), permafrost (DeConto et al., 2012), wetlands (Kurtz et al., 2003; Zachos et al., 2010), or marine dissolved organic matter (Sexton et al., 2011), potentially in combination with thresholds in the climate system (Lunt et al., 2011).

Variations in global climate and the carbon cycle during the early, ice-free Cenozoic, including 'hyperthermals', are predominately paced by short and long eccentricity cycles (Zachos et al., 2001; Westerhold et al., 2011; Westerhold, Röhl, Donner, & Zachos, 2018; Kirtland Turner, 2014; Littler et al., 2014; Lauretano et al., 2015; Barnet et al., 2019). While eccentricity is the only astronomical parameter that alters Earth's annual

global mean solar energy insolation, the total variability is small ($\sim$0.5 Wm^{-2}) (Laskar et al., 2004). Local seasonal insolation forcing related to precession is much stronger (Berger, 1978), and therefore one hypothesis is that carbon-climate variability is driven by precession forcing but modulated by eccentricity cycles (Maslin & Ridgwell, 2005; Zeebe et al., 2017). Additionally, the large mass of dissolved inorganic carbon in the ocean should act as a lowpass filter on carbon cycle variability, producing muted precession signals relative to eccentricity (Cramer et al., 2003; Palike et al., 2006).

Numerical models are key tools for testing hypotheses about the origin of astronomically forced climate-carbon cycles. Previous studies have utilized atmosphere-ocean global climate models (GCMs) to reveal the mechanisms by which the astronomical configuration exerts a significant control on surface dynamics. For instance, the GENESIS GCM (Thompson & Pollard, 1997) was used to evaluate Eocene (paleo)oceanographic differences between two precession configurations (Sloan & Huber, 2001). That same model (with a slab-ocean) was used to reconstruct the extent of Eocene permafrost under various astronomical configurations, providing evidence for astronomically triggered carbon release at high latitudes (DeConto et al., 2012). Lunt et al. (2011) used the fully-coupled HadCM3L GCM to show differences in ocean circulation under certain astronomical configuration, suggesting that variations in intermediate water mass temperature might drive the periodic destabilization of methane hydrates.

Because GCMs are computationally expensive, simulations usually apply fixed astronomical parameters, as in the studies described above, with the consequence that results cannot be compared directly to spectral analyses of proxy time series data. Exceptions

include simulation of the complete deglacial transition with transient astronomical forcing (Z. Liu et al., 2009), although this time interval is too short to capture complete astronomical cycles. Other studies have employed simpler box models to simulate the transient effects of astronomical forcing on the carbon cycle, typically using artificial forcing functions in the form of Eccentricity-Tilt-Precession (Ma et al., 2011; Laurin et al., 2015), or seasonal insolation curves (Palike et al., 2006; Zeebe et al., 2017). While such models can simulate the transfer of spectral power amongst reservoirs and capture potential spectral shifts, the construction of the forcing functions requires basic presumptions about the mechanisms that drive the climate response.

Earth system Models of Intermediate Complexity (EMICs) bridge the gap between the most complex GCMs and box models that lack a dynamic ocean. Their computational efficiency allows generation of large ensembles of experiments and/or long integration time. EMIC studies of astronomical forcing, including those with the LOVECLIM (Goosse et al., 2010), CLIMBER-2 (Petoukhov et al., 2000; Ganopolski et al., 2001), and UVic (Weaver et al., 2001) models, have focused on the Quaternary (Bounceur et al., 2015; Menviel et al., 2011; Heinemann et al., 2014; Xiao et al., 2013; Konijnendijk et al., 2011; Calov et al., 2005; Brovkin et al., 2002) or the Pliocene (Willeit et al., 2013). While these studies demonstrate the sensitivity of the climate and carbon cycle to insolation forcing, a modeling framework that systematically evaluates the imprint of astronomical forcing in various components of the carbon cycle is missing. Moreover, even these model simulations, with time-varying orbital parameters, have been too short to evaluate the spectral power in model output on astronomical timescales ($>10^5$ years). There remains a need to evaluate how astronomical

forcing translates into the variables ultimately recorded by proxies (such as $\delta^{18}O$, $\delta^{13}C$, and $CaCO_3$ content) on these timescales.

Here we take a first step in this direction, driving the 'cGENIE' EMIC (Ridgwell et al., 2007) with time-varying astronomical forcing over multi-million-year simulations. We develop and present a framework to assess the transient response of the Earth's climate-carbon system to astronomical forcing under ice-free greenhouse conditions, by separately quantifying the impact of insolation forcing on climate variability due to feedbacks in ocean circulation, marine productivity, $CaCO_3$ compensation, and terrestrial weathering. The simulations presented here focus on feedbacks involving the marine inorganic (carbonate) carbon cycle. A follow-up companion paper will separately interrogate the role of temperature-dependent feedbacks in the marine organic matter cycle. Our experimental framework hence provides a systematic model evaluation of the propagation of spectral signals through the Earth system to facilitate comparison to proxy datasets.

3.2 Methods

The cGENIE model combines a dynamic 3D ocean model with a simplified 2D energy-moisture-balance atmosphere model (Edwards & Marsh, 2005). cGENIE includes a detailed representation of ocean biogeochemical cycles (Ridgwell et al., 2007) plus the long-term (inorganic) carbon cycle represented through input and removal of dissolved carbon species via terrestrial rock weathering and calcium carbonate burial in marine sediments (Ridgwell & Hargreaves, 2007; Colbourn et al., 2013). This configuration of cGENIE has previously been employed on timescales up to 1 Myr to assess past climate events (Gutjahr

et al., 2017) as well as the long-term future carbon cycle response to fossil fuel carbon release (Winkelmann et al., 2015; Lord et al., 2016). Our methodological advance is to include spatiotemporal insolation forcing based on astronomical parameters using equations from Berger (1978). Parameters for eccentricity, obliquity, and precession (longitude of perihelion) are updated every 1000 years and the daily mean insolation at each latitude is recalculated accordingly. We select parameters from the La2004 astronomical solution for an early Cenozoic time slice between 57 and 53 Ma (Laskar et al., 2004) and assume a solar constant of 1361.7 Wm^{-2}, consistent with this interval.

3.2.1 Continental Configuration

We employ a pair of deliberately idealized continental configurations (Figure 3.1) in order to distinguish climatic effects related to the carbon cycle from any astronomically-forced effects that relate to the specific distribution of landmasses (Short et al., 1991). This provides a more generalized understanding of the ice-free Earth system response to astronomical forcing than would have been possible if we had chosen a specific continental configuration. However, it should be noted that it is not possible to understand all the ways in which paleogeography impacts atmosphere and ocean circulation and how these patterns may interact with astronomical forcing, using only a pair of end-member configurations.

In the first configuration (SYMM), a single continent spans pole to pole, creating a hemispherically symmetric landmass distribution (Vervoort et al., 2019). In the second, asymmetric configuration (ASYM), a single super-continent covers the northern polar region. While no Cenozoic continental plate arrangement closely reflects either end-member,

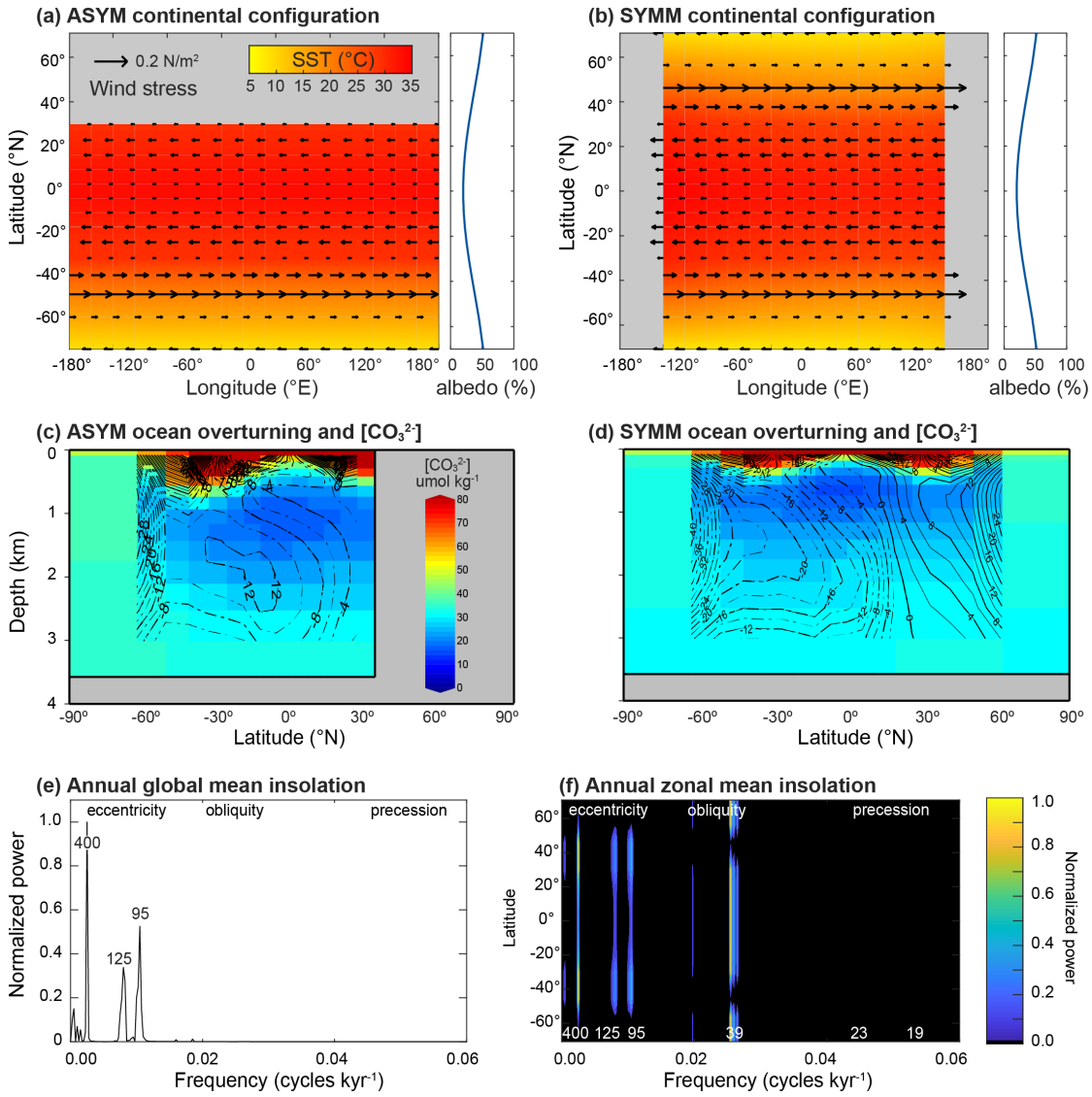

Figure 3.1: cGENIE configuration. (a-b) The continental landmass distribution (grey), prescribed wind stress fields (vectors), albedo profiles, and simulated sea surface temperature (SST, color coded) for ASYM (a) and SYMM (b) simulations. (c-d) The zonal mean ocean overturning strength indicated by contour lines, dashed for a counter-clockwise circulation, solid lines for clockwise movement. Carbonate ion $[CO_3^{2-}]$ concentrations for ASYM (c) and SYMM (d) are color coded. The bottom panels include normalized power spectra for (e) the annual global mean insolation and (f) the annual zonal mean insolation.

we focus primarily on results using the ASYM setup because of the relative bias in the Northern Hemisphere landmass distribution throughout the Cenozoic. Comparable results for all SYMM experiments are included in the Supplementary Information (Appendix B).

Because our model configuration lacks a dynamical atmosphere, a simplified zonally averaged wind-stress profile is generated and applied to the ocean surface with matching wind products used in the atmospheric advection of heat and moisture and in calculating air-sea gas exchange. Similarly, a meridional albedo profile is prescribed independent of the continental configuration but as a function of latitude only with the highest albedo values in the high latitudes where the angle of incoming solar radiation enhances reflectivity. While differences in continental configuration should correspond to differences in albedo, our cGENIE experiments lack a land surface model to provide a more realistic pattern. Both SYMM and ASYM continental configurations consist of 18×18 equal-area grids and 16 ocean depth levels of exponentially increasing thickness with depth. We truncate the vertical grid at 14 levels, giving a maximum depth of ∼3575 meters to approximate modern ocean volume and adopt a flat-bottom bathymetry. We generate and apply a random spatial distribution of ocean sediment depths consistent with the modern hypsometric curve that is used in the pressure-dependent calculation of calcium carbonate preservation. Boundary conditions were generated using the 'muffingen' software suite v0.9.25 (DOI: 10.5281/zenodo.5130677) and are shown in Figure 3.1 and B.1.

3.2.2 cGENIE Spin-Up Stages

The model is equilibrated in a two-step spin-up process for each of the SYMM and ASYM configurations. An initial 20,000-year spin-up equilibrates ocean dynamics and ocean

biogeochemical cycling with atmospheric CO_2 concentrations fixed at 834 ppm (Ridgwell & Schmidt, 2010), emulating an early Cenozoic 'warm climate' and yielding sufficiently high temperatures to prevent both perennial and seasonal sea ice formation at the high latitudes. Values for the astronomical parameters are fixed during spin-up at their average values across the modeled interval (53-57 Ma). The initial values of mean ocean alkalinity (ALK), dissolved inorganic carbon (DIC), nutrient (phosphate) concentrations, and major ion concentrations of Ca^{2+}, Mg^{2+}, and SO_4^{2-} of the model follows previous Paleocene cGENIE configurations (Ridgwell & Schmidt, 2010).

In the second stage spin-up, also with fixed astronomical parameters, the long-term carbon cycle is enabled by allowing loss of solutes from the ocean through marine $CaCO_3$ burial and balancing this with a terrestrial weathering flux. Atmospheric CO_2 is stabilized close to 834 ppm by adjusting the balance between volcanic outgassing and terrestrial silicate weathering (dependent on land temperature as described in Colbourn et al. (2013) and Lord et al. (2016). The final steady-states of ocean carbonate chemistry differ slightly between SYMM and ASYM – a consequence of the differences in continental distribution and hence large-scale pattern of ocean circulation (Figure 3.1c-d, Table B.1).

3.2.3 Experimental Design

Starting from these initial steady states, the effects of astronomical forcing on climate and the carbon cycle are systematically investigated – running cGENIE transiently for four million years to allow the evaluation of astronomical cycles with periods up to 500 kyr. We conduct a set of five simulations for both SYMM and SYM in which the complexity of

Table 3.1: Experimental design. Shows which carbon-climate feedbacks are excluded (-) and included (✓) for Exp.0–4. Experiments are performed under SYMM (hemispherically symmetric continent) and ASYM (Northern Hemisphere supercontinent) configurations.

	Climate-CO_2 feedback	Marine export feedback	$CaCO_3$ compensation	Terrestrial weathering
Exp.0	–	–	–	Tracking
Exp.1	✓	–	–	Tracking
Exp.2	✓	✓	–	Tracking
Exp.3	✓	✓	✓	Fixed
Exp.4	✓	✓	✓	Responsive

Note. Marine surface productivity is present, but unresponsive to astronomical forcing in Exp.0 and 1 while surface productivity varies with astronomical forcing in Exp.2–4. For terrestrial weathering, 'tracking' indicates that weathering fluxes are exactly equal to (variable) $CaCO_3$ burial fluxes, 'fixed' means weathering fluxes are fixed and decoupled from $CaCO_3$ burial, "responsive" indicates weathering rates vary in response to changes in land temperature.

the carbon cycle is sequentially increased (Table 3.1). In the simplest experiment (Exp.0), we disable all carbon cycle feedbacks and fix radiative forcing with respect to an atmospheric CO_2 composition of 828 ppm for ASYM and 834 ppm for SYMM (Table B.1). Variability in global climate is thus only a function of the temporal radiative balance and feedbacks relating to physical processes, such as meridional ocean and atmospheric heat transport, and ocean-atmosphere exchange of heat and moisture. Cycles produced in atmospheric CO_2 have no influence on the modeled temperature variability.

In the subsequent experiment (Exp.1), we allow variations in atmospheric CO_2 to modulate surface temperature. The magnitude and spatial distribution of export production of both organic carbon (POC) and $CaCO_3$ is fixed, and weathering fluxes are forced to exactly track $CaCO_3$ burial such that the ocean ALK and calcium ion inventories become invarient. Global climate now additionally responds to carbon cycle feedbacks related to the controls of ocean circulation and solubility on ocean CO_2 uptake. Resultant changes in ocean carbonate chemistry will impact the preservation of $CaCO_3$ (but does not cause

any change in ocean ALK and calcium ion inventories) plus the distribution of DIC δ^{13}C. With fixed export, preservation of $CaCO_3$ in surface sediments varies as a function of temperature, salinity, and $[CO_3^{2-}]$ of overlying seawater. δ^{13}C of DIC is controlled by multiple fractionation processes. First, isotopic partitioning occurs during re-equilibration between CO_2, HCO^{3-}, and CO_3^{2-} (Zeebe & Wolf-Gladrow, 2001; Ridgwell et al., 2007). A second temperature-dependent isotopic fractionation occurs during the air-sea gas exchange (Zhang et al., 1995; Ridgwell et al., 2007). We also model the fractionation associated with organic matter formation as a function of aqueous CO_2 concentration (Rau et al., 1996; Ridgwell et al., 2007) as well as temperature-dependent isotopic fractionation between $[HCO_3^-]$ and $CaCO_3$ (Mook, 1986). See Turner and Ridgwell (2016) for a detailed description of the representation of δ^{13}C in cGENIE including evaluation of simulated spatial patterns.

In Exp.2, POC (with $CaCO_3$ in a fixed ratio of 0.2 mol:mol) export is now allowed to vary in space and time as a function of light and nutrient (phosphate) availability following Ridgwell et al. (2007). Exported POC is remineralized through the water column according to a fixed exponential decay depth profile (Ridgwell et al., 2007). Again, all carbon, ALK, and calcium removed from the system through $CaCO_3$ burial is automatically replenished with an equal flux from terrestrial weathering. This configuration provides ocean-atmosphere carbon cycle feedbacks but no geological carbon feedbacks.

We add the first geological carbon feedback in Exp.3 by decoupling terrestrial weathering (providing the alkaline building blocks for $CaCO_3$ production) from marine $CaCO_3$ burial. Weathering rates are fixed at the values obtained from the end of the open system spin-up, while $CaCO_3$ preservation varies based on $CaCO_3$ export productivity and

the saturation state of overlying water. The ocean ALK (and Ca^{2+}) inventory can now vary and impact pCO_2 via 'carbonate compensation'.

Finally, Exp.4 completes the representation of the long-term (inorganic) carbon cycle by including a terrestrial weathering feedback (see Lord et al. (2016) for an analysis of the modes of response and characteristic timescales of the complete system). Carbonate weathering varies linearly with mean global air temperature over land whereas silicate weathering responds exponentially (Colbourn et al., 2013).

To elucidate the role of each set of carbon cycle feedbacks in the Earth system response to astronomical forcing, we investigate the difference between each set of experiments, e.g. output of Exp.3 is subtracted from output of Exp.4 to isolate the impact of the astronomically forced weathering feedback on the Earth system. Hence while Figure 3.3d-f presents the response in pCO_2, benthic DIC $\delta^{13}C$, and wt% $CaCO_3$ that results from the astronomically forced changes in ocean circulation and the solubility feedback (Exp.1), subsequent figures (3.4d-f through 3.6d-f) are shown in the form of anomaly plots for the difference from the previous experiment. Likewise, we plot the change in the power spectra (ΔFFT) with respect to the previous experiment to demonstrate the relative weakening (negative power) or amplification (positive power) of astronomical cycles when adding feedbacks.

3.2.4 Timeseries Analysis

Spectral analysis was performed on model output variables with a simple Fast Fourier Transform (FFT) to extract the dominant cycles (shorter than 500 kyr) and their average ranges. The average range is equal to twice the average amplitude across the

4 million year interval for each spectral peak determined by the FFT. Because model output is (white) noise-free in the absence of internal interannual variability in cGENIE, further analysis to determine the statistical significance of the astronomical peaks is not required. The phasing between the imposed short and long eccentricity forcing and cycles in model variables of interest are determined using a multi-taper coherence method (Table B.2 and B.3). Because model output is saved at 1000-year intervals over the 4 Myr long experiments, we are unable to diagnose any lags with a duration less than 1000 yr.

3.3 Results and Discussion

In the following sections we describe the main results of Exp.0-4, separately assessing the role of specific carbon cycle feedbacks in the Earth system response to astronomical forcing in proxy relevant model outputs, including ocean temperature, atmospheric pCO_2, DIC $\delta^{13}C$, and sedimentary wt% $CaCO_3$. We focus on mean annual output and evaluate signals in terms of the total variability generated, distribution of spectra power, the average range of individual cycles across the four million year interval, and phasing with respect to astronomical forcing and between model output. Results of the asymmetric (ASYM) world are presented in the main figures, while comparison with the equivalent SYMM simulations is provided in the final paragraph of each subsection. Corresponding graphical SYMM analyses are provided as Figures B.2-B.8. See Table B.2 and B.3 for a summary of cycle ranges and phasing calculated for each experiment. Comparison between ASYM and SYMM results allows us to evaluate how latitudinal heterogeneity in the landmass distribution impacts the global response to astronomical forcing. Figure 3.1 shows the power

spectra of mean annual insolation as a global mean (Figure 3.1e) and with latitude (Figure 3.1f). Annual global mean insolation power spectra is dominated by eccentricity, while for most latitudes, obliquity dominates mean annual power spectra. Precession only appears significantly in seasonal insolation power spectra.

3.3.1 Global Climate Response

In Exp.0 (Figure 3.2), annual global mean air temperature responds to annual global mean insolation forcing but with no CO_2 feedback on climate. In the ASYM configuration, the maximum variability in atmospheric temperature in response to astronomical forcing is 1.7°C. Spectral power in the global mean annual air temperature is dominated by the 400 kyr (long eccentricity) and 125 and 95 kyr (short eccentricity) periods (Figure 3.2c). The distribution of spectral power in global mean annual air temperature is similar to the distribution of spectral power in mean annual temperature at individual latitudes (Figure 3.2f). Seasonal averaging removes power in Earth's mean annual temperature response at higher frequencies, and local mean annual temperature does not respond linearly to the local mean annual insolation (contrast Figure 3.1f with Figure 3.2f). Mean annual insolation at most latitudes is dominated by obliquity power (Figure 3.1f), and obliquity power also appears in global mean annual air temperatures. In ASYM simulations, small precession cycles in the global mean annual air temperature result from the different heat capacity of each hemisphere and are consistent with the dominance of precession power in mean annual air temperature over the modeled Northern Hemisphere (NH) landmass (also recognized by Short et al. (1991)) (Figure 3.2f). The NH – where the continent is located – has a smaller heat capacity than the Southern Hemisphere (SH) and thus the increase in

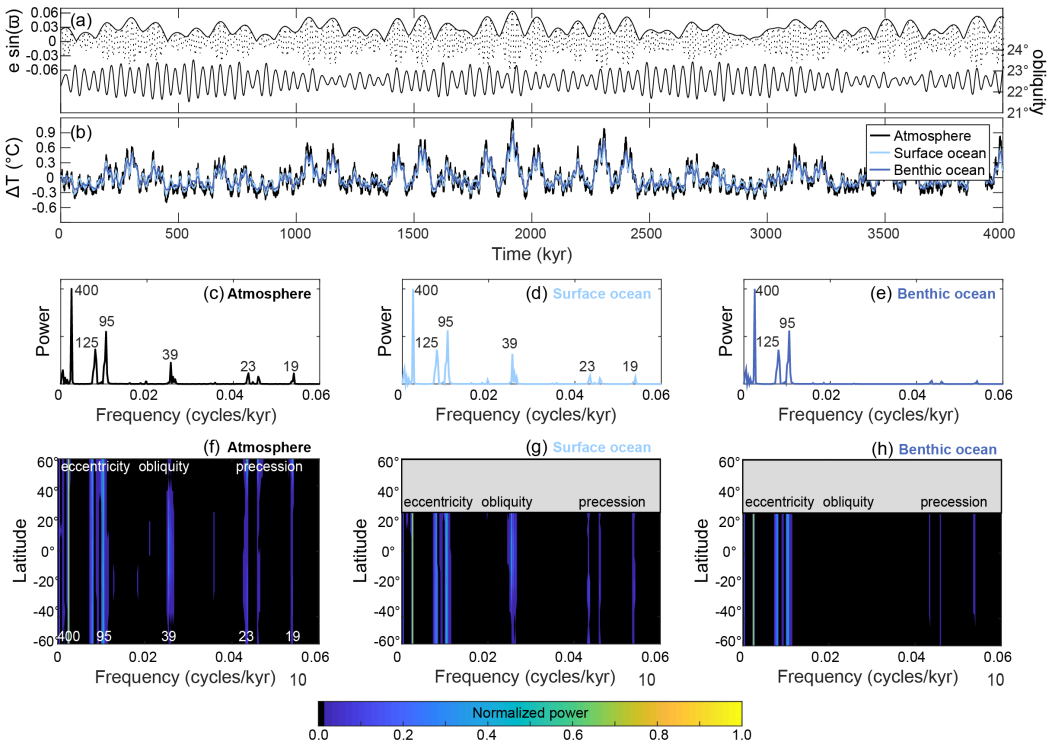

Figure 3.2: Astronomical climate evolution in ASYM of Exp.0. (a) The eccentricity, obliquity, and the precession index (e sin(ω)) used to calculate the daily mean insolation across four million years of cGENIE simulation. (b) The simulated change in the global annual mean temperature in the atmosphere (black), surface (light blue), and benthic ocean (dark blue) with their respective normalized power spectra in panels (c-e) calculated using the Fast Fourier Transform. Each value near a spectral peak indicates the associated period of the cycle in kyr. The power spectra of temperature in the (f) atmosphere, (g) surface, and (h) deep ocean are shown for each latitude.

the global annual mean temperature is greater when the NH is tilted toward the Sun at perihelion, compared to when the SH is tilted toward the Sun at perihelion.

Changes in the surface air temperature are instantaneously (with a lag less than the 1 kyr interval of model data saving) transferred to the surface ocean. Although the maximum variability in global mean annual sea surface temperature (SST) is slightly smaller than global mean annual surface air temperature (1.3°C versus 1.7°C), the distribution of spectral power is nearly identical (Figure 3.2c-d). Astronomically forced temperature

changes in the benthic ocean are slightly reduced compared to the surface ocean, with a maximum variability of 1.1°C and spectral power is dominated by eccentricity (Figure 3.2e) with respective average ranges of 0.25°C and 0.30°C for the short and long eccentricity cycles. The major difference between the SST and benthic ocean temperature power spectra is a loss of power at obliquity and precession frequencies. On a global mean, benthic ocean temperature lags eccentricity forcing by ∼1 kyr, consistent with the timescale of ocean overturning.

Astronomically forced climate evolution in SYMM is comparable to ASYM in Exp.0 with the exception that the maximum varability in temperature is slightly reduced and precession cycles are absent (Figure B.2). We attribute the loss of precession power to the similar heat capacity of both hemispheres in SYMM.

3.3.2 Ocean Solubility Pump

Astronomical forcing induces spatiotemporal variations in ocean temperature (Figure 3.2), and alters the strength of ocean overturning circulation. By enabling a CO_2-climate feedback in Exp.1 (Figure 3.3), changes in atmospheric pCO_2 resulting from the influence of solubility and ocean circulation on ocean carbon uptake can now modulate the direct temperature response to astronomical forcing (cf. Exp.0).

The power spectrum of modeled global ocean overturning is dominated by precession (Figure 3.3c). Ocean overturning is a seasonal process driven by maximum deep-water formation close after the coldest months at latitudes where seasonal insolation is dominated by precession power. Precession periodically facilitates relatively more intense overturn-

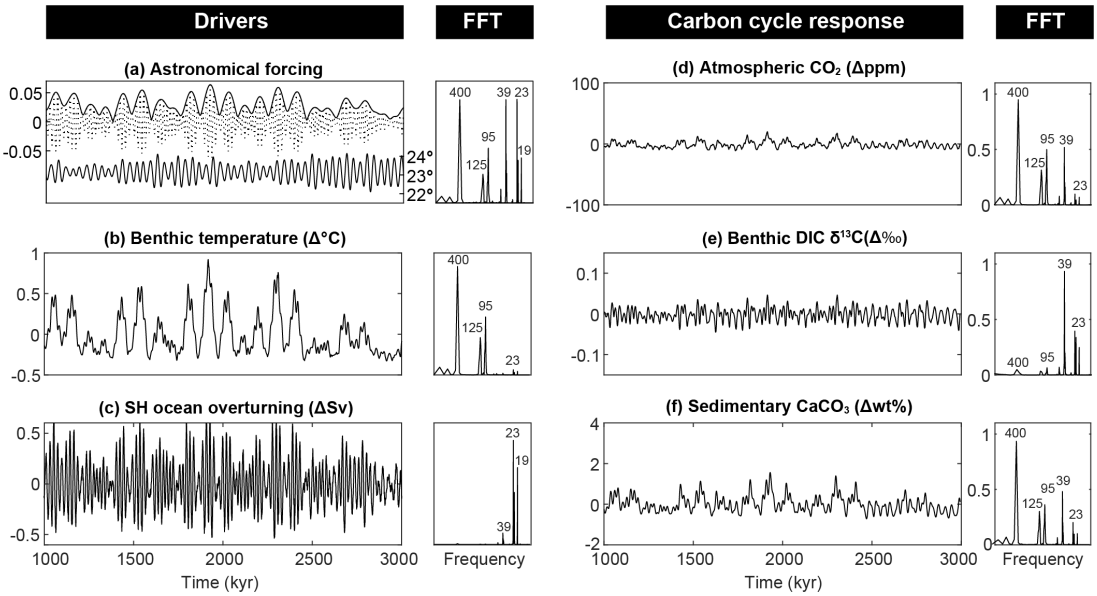

Figure 3.3: Exp.1, ocean circulation and CO_2 solubility feedbacks in ASYM. (a) Astronomical forcing parameters (eccentricity, obliquity (in degrees), and precession index (e $\sin(\omega)$)) and their Fast Fourier Transform (FFT) normalized to the highest individual power. (b) Change in benthic ocean temperature. (c) Change in the maximum Southern Hemisphere ocean overturning strength, defined by the maximum overturning strength reached in the SH across all ocean depth levels. (d) Change in atmospheric CO_2. (e) Change in benthic δ^{13}C of DIC. (f) Change in wt% $CaCO_3$. All variables are annual global mean values and are accompanied by their respective FFTs, normalized to the peak with maximum power.

ing when the SH winter occurs at aphelion compared to perihelion. Enhanced deep-water formation and increased ventilation of the ocean interior physically transports respired carbon back to the surface ocean, and thereby slightly increases atmospheric $p\mathrm{CO}_2$. However, the relatively small changes in the strength of ocean overturning (maximum variability of $\sim$1 Sv, corresponding to a change in the maximum ocean ventilation age of $\sim$100 years) are insufficient to drive major redistributions of carbon between the ocean and atmosphere. The average range of precession cycles in $p\mathrm{CO}_2$ is $<$3 ppm (Figure 3.3d). The $p\mathrm{CO}_2$ power spectra is instead dominated by long eccentricity with a significant contribution of power at short eccentricity and obliquity. The total variability is $\sim$32 ppm with average ranges of obliquity and short eccentricity cycles in $p\mathrm{CO}_2$ of $\sim$5 ppm and $\sim$6 ppm for long eccentricity cycles, resulting from feedbacks due to ocean solubility and carbon uptake. More CO_2 is released from the surface ocean into the atmosphere at eccentricity maxima when global annual mean temperatures are highest (Figure 3.3d). However, CO_2 uptake is not spatially or seasonally uniform and is most significant at cold months in the high latitudes, resulting in obliquity cycles with a range comparable to eccentricity cycles.

The global mean benthic DIC $\delta^{13}\mathrm{C}$ power spectrum shows maximum variability of 0.09‰. Obliquity and precession dominate the power spectrum with very little power at eccentricity (Figure 3.3e). The lack of eccentricity power in $\delta^{13}\mathrm{C}$ timeseries demonstrates that the local and seasonal changes in temperature are particularly significant controls on the modeled fractionation processes. Precession power is consistent with the impact of ocean overturning on the physical transport of low-$\delta^{13}\mathrm{C}$ remineralized carbon from the deep to the surface ocean, generating cylces with an average range of $\sim$0.02‰ that are

anti-phased between the surface and deep ocean (Figure 3.3e). Obliquity power arises primarily due to changes in fractionation associated with export production and generates cycles with a comparable average range of ∼0.02‰ also anti-phased with surface ocean DIC δ^{13}C cycles. Reduced fractionation in the surface ocean leads to isotopically lighter surface DIC while relatively heavier carbon respires at depth which increases the benthic DIC δ^{13}C. Although the magnitude and spatial patterns of export are fixed, fractionation in the formation of organic matter depends on the concentration of aqueous CO_2 and fractionation in the formation of calcite is temperature-dependent, both of which drive changes in δ^{13}C in response to obliquity-paced changes in temperature and air-sea gas exchange.

The power spectrum for global mean marine sedimentary wt% $CaCO_3$ closely resembles that of pCO_2, but with slightly amplified obliquity and precession power (Figure 3.3d,f). Strong eccentricity power in wt% $CaCO_3$ is consistent with the dominance of eccentricity on deep ocean temperature (Figure 3.3b). Higher temperature at eccentricity maxima increases ω_{cal} and lowers $CaCO_3$ solubility, promoting $CaCO_3$ preservation. Precession and obliquity cycles are consistent with the influence of ocean circulation and solubility-driven changes in CO_2 uptake on ocean chemistry. Changes in benthic ocean $[CO_3^{2-}]$, which also drive changes in Ω_{cal}, are dominated by precession and obliquity (Figure B.9a).

The relative loss of high frequency power in wt% $CaCO_3$ compared to benthic ocean $[CO_3^{2-}]$ is also a function of calculating wt% $CaCO_3$ from the sedimentary mixed layer, i.e. the upper ca. 5 cm of the sediment column in which mixing homogenizes the solid composition (Ridgwell & Hargreaves, 2007). This mixing acts as a low-pass filter, amplifying eccentricity-driven cycles in wt% $CaCO_3$ arising from temperature-dependency relative

to the precession and obliquity cycles from $[CO_3^{2-}]$-dependency. Averaging sedimentary content over the upper 5 cm also induces a lag between 100 and 400 kyr eccentricity forcing and the global wt% $CaCO_3$ of 8 (29°) and 9 kyr (7°), respectively.

Including solubility-related carbon feedbacks in the SYMM Exp.1 simulation results in similar power spectra compared to ASYM, despite the relative symmetry of ocean overturning (Figure 3.1c-d). Ocean overturning in SYMM is also primarily paced by precession (Figure B.3c), creating distinct ∼20 kyr cycles in benthic DIC $\delta^{13}C$ (Figure B.3e). However, precession power is absent in global mean wt% $CaCO_3$ (Figure B.3f). Astronomically forced changes in ocean chemistry largely cancel out on precession timescales because the NH and SH overturning operate with roughly comparable strengths and in consequence, benthic ocean $[CO_3^{2-}]$ is dominated by eccentricity and absent of precession power (Figure B.9b). The lag between 100 and 400 kyr eccentricity forcing and global $CaCO_3$ wt% in SYMM is 7 kyr.

3.3.3 Marine Surface Productivity

Exp.2 elucidates how feedbacks involving marine productivity modifies the Earth system response to astronomical forcing. Global mean POC export production in ASYM (Figure 3.4b) is dominated by precession, illustrating the influence of changes in ocean circulation on surface nutrient supply and consistent with the seasonality of production. POC export also shows eccentricity modulation because elevated global ocean temperatures at eccentricity maxima result in stronger ocean overturning (Figure 3.3c), and elevated

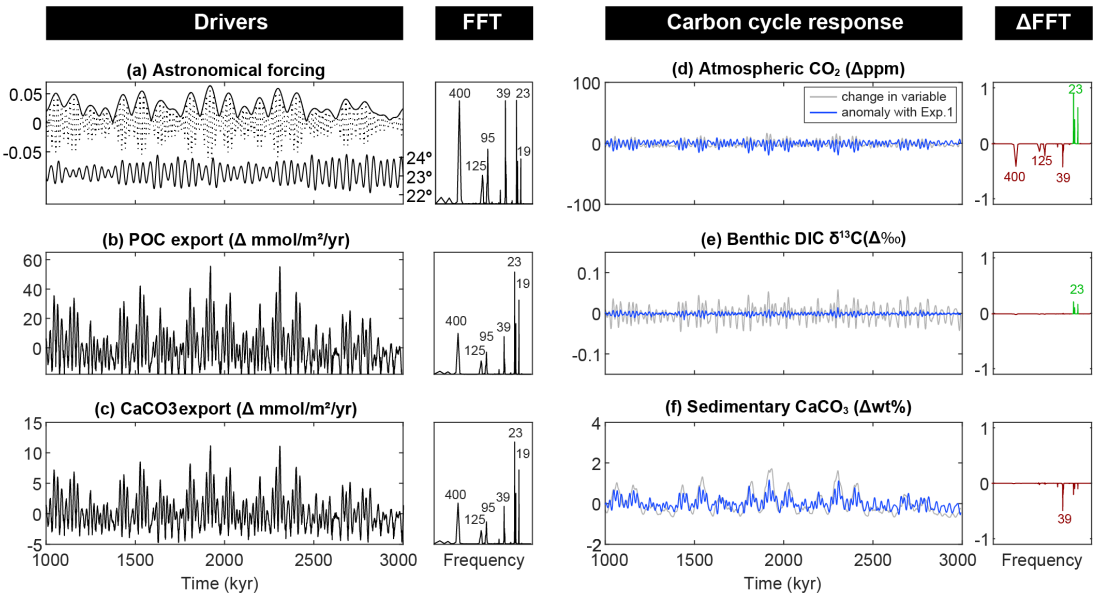

Figure 3.4: Exp.2, marine surface productivity feedback in ASYM. (a) Astronomical forcing parameters (as per Figure 3.3a). (b) Change in the export of particulate organic carbon (POC). (c) Change in the export of $CaCO_3$. (d) Change in atmospheric CO_2. (e) Change in benthic $\delta^{13}C$ of DIC. (f) Change in wt% $CaCO_3$. All variables are annual global mean values and are accompanied by their respective FFTs, normalized to the peak with maximum power. In blue, the values are plotted as anomalies with the previous experiment and depict the change driven by the marine productivity feedback only. Likewise, the FFTs are plotted as anomalies. A positive (green) value on the y-axis indicates an increase in relative power and a negative (red) value indicates a decrease in relative power compared to the previous experiment.

surface nutrient availability. $CaCO_3$ export shows the same power spectrum as POC export because of the use of a fixed rain ratio (Figure 3.4c).

Relative to Exp.1, precession cycles in pCO_2 become more pronounced at the expense of eccentricity cycles (Figure 3.4d) which reduces the total pCO_2 variability to $\sim$26 ppm. Increased precessional power is a direct consequence of the impact that production and export of organic matter and carbonate has on surface DIC and ALK. The net impact is a decrease in mean annual surface ocean [CO_2(aq)] of 0.7% (or 0.173 μmol kg^{-1}) corresponding to maximum surface productivity. This translates roughly to a 0.7% reduction in pCO_2, equating to precession cycles with an average range of $\sim$6 ppm, double the magnitude from Exp.1.

Changes in the magnitude and spatial pattern of export production do not notably change the power spectrum of benthic DIC δ^{13}C compared to Exp.1 except for a slight increase in precession power (Figure 3.4e). The similarity in the carbon isotope response of Exp.1 and Exp.2 is because Exp.1 already incorporated the astronomically-driven changes in isotope fractionation associated with export production as described in Section 3.2.3. Sedimentary wt% $CaCO_3$ shows a slight loss of higher frequency power along with an increase in the maximum variability (Figure 3.4f). This shift in the power spectrum contrasts with the response of atmospheric pCO_2 and benthic δ^{13}C to the addition of varying export production. As $CaCO_3$ export increases in response to seasonal precession and obliquity forcing, surface and deep ocean [CO_3^{2-}] decreases, lowing ω_{cal} and promoting $CaCO_3$ dissolution. Hence, even though $CaCO_3$ export and rain to the seafloor increases, the lower [CO_3^{2-}] prevents further $CaCO_3$ preservation. On eccentricity timescales, $CaCO_3$ export

and benthic [CO_3^{2-}] vary in-phase and amplify short and long eccentricity power. The relative phasing between eccentricity forcing and $CaCO_3$ is unaffected by the responsive export productivity.

Global mean export production in SYMM Exp.2 (Figure B.4c) varies less than ASYM Exp.2 (Figure 3.4c). In ASYM, the impact of precession is amplified because most of the export productivity occurs in the SH. Hemispheric productivity in SYMM is roughly balanced, which cancels out precession-induced changes and leaves eccentricity to dominate power spectra of atmospheric pCO_2. Variations in annual global mean pCO_2, benthic DIC $\delta^{13}C$, and $CaCO_3$ burial are muted as a result of this hemispheric cancellation and there is little change with respect to Exp.1 (Figure B.4d-f).

3.3.4 Carbonate Compensation

We evaluate the impact of the carbonate compensation feedback in modifying the response to astronomical forcing in Exp.3 by now allowing burial of $CaCO_3$ to modify the global ocean ALK inventory while no longer forcing weathering fluxes to always track burial, and contrast these results with Exp.2. The total variability in atmospheric pCO_2 increases to 64 ppm in Exp.3 and is relatively elevated during eccentricity maxima compared to Exp.2. The burial-weathering imbalance reduces the ocean carbon uptake capacity and this feedback impacts atmospheric pCO_2 more than enhanced productivity. Thus, pCO_2 shows enhanced eccentricity power and reduced power at high frequencies relative to Exp.2 (Figure 3.5d). Eccentricity cycles are significantly increased compared to Exp.2, with an average cycle range of almost 20 ppm for long eccentricity.

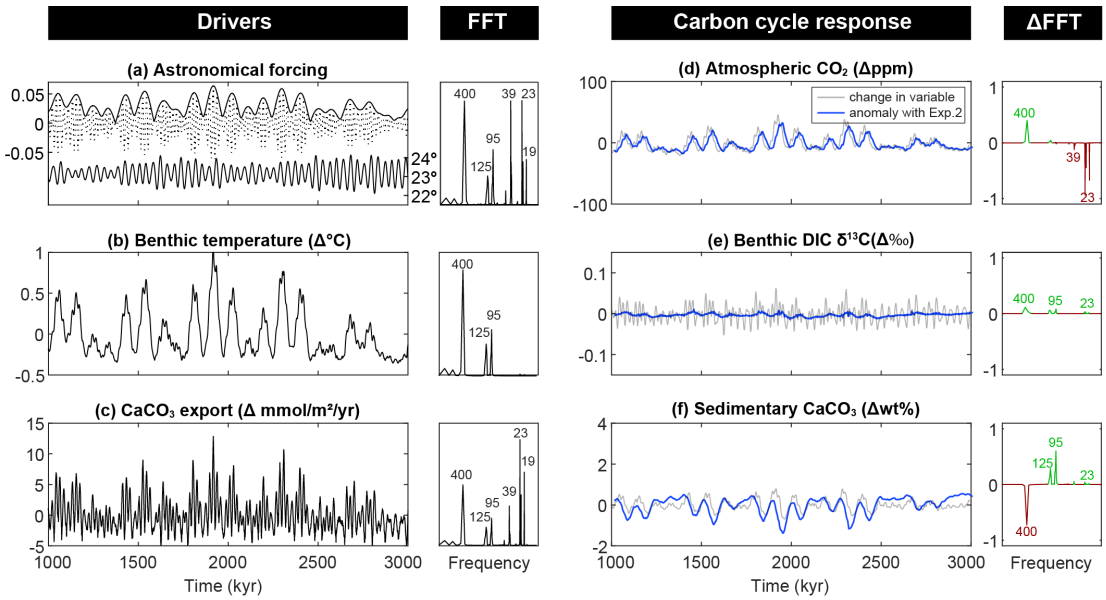

Figure 3.5: Exp.3, deep marine $CaCO_3$ feedback in ASYM. (a) Astronomical forcing parameters (as per Figure 3.3a). (b) Change in benthic ocean temperature. (c) Change in the export of $CaCO_3$. (d) Change in atmospheric CO_2. (e) Change in benthic $\delta^{13}C$ of DIC. (f) Change in wt% $CaCO_3$. All variables are annual global mean values and are accompanied by their respective FFTs, normalized to the peak with maximum power. In blue, the values are plotted as anomalies with the previous experiment and depict the change driven by the marine $CaCO_3$ feedback only. Likewise, the FFTs are plotted as anomalies. A positive (green) value on the y-axis indicates an increase in relative power and a negative (red) value indicates a decrease in relative power compared to the previous experiment.

Consistent with $p\mathrm{CO}_2$, power in benthic $\delta^{13}\mathrm{C}$ becomes slightly amplified at eccentricity frequencies in Exp.3 relative to Exp.2. The average range of long eccentricity cycles increases from 0.006‰ to 0.011‰. Yet, obliquity and precession still remain the dominant cycles and control the total variability in DIC $\delta^{13}\mathrm{C}$ of 0.11‰. Compared to Exp.0-2, increased CaCO_3 burial now removes ALK that is not resupplied by weathering (which is fixed), leading to lower deep ocean ω_{cal} that counteracts increased burial. This results in reduced 100 and 400 kyr wt% CaCO_3 cycles in Exp.3 compared to Exp.2. The wt% reduction in 400 kyr cycles is much larger (from 0.7 to 0.2 wt%) than that of 100 kyr cycles (from 0.5 to 0.4 wt%) because the CaCO_3-weathering imbalance is sustained over a much longer period that exceeds the residence time of carbon in the ocean, shifting the dominant spectral power from the 400 kyr to the 100 kyr eccentricity cycles (Figure 3.5f). The wt% CaCO_3 is now leading short eccentricity forcing by 5 kyr.

The change in the CaCO_3 preservation cycles in SYMM (Figure B.5) are similar to ASYM because the impact of the ocean ALK imbalance on CaCO_3 at eccentricity maxima is similar. In SYMM too, this feedback amplifies 100 and 400 kyr cycles in $p\mathrm{CO}_2$ with the 400 kyr cycle producing the greatest increase in the average range. The long eccentricity remains the dominant $p\mathrm{CO}_2$ cycle with a value normalized to 1 and therefore does not show up as an increase in the ΔFFT plot, contrary to ASYM in which dominant power shifted from precession to long eccentricity. The long eccentricity cycle in $\delta^{13}\mathrm{C}$ increases in average range from 0.002‰ to 0.003‰ and is considered negligible.

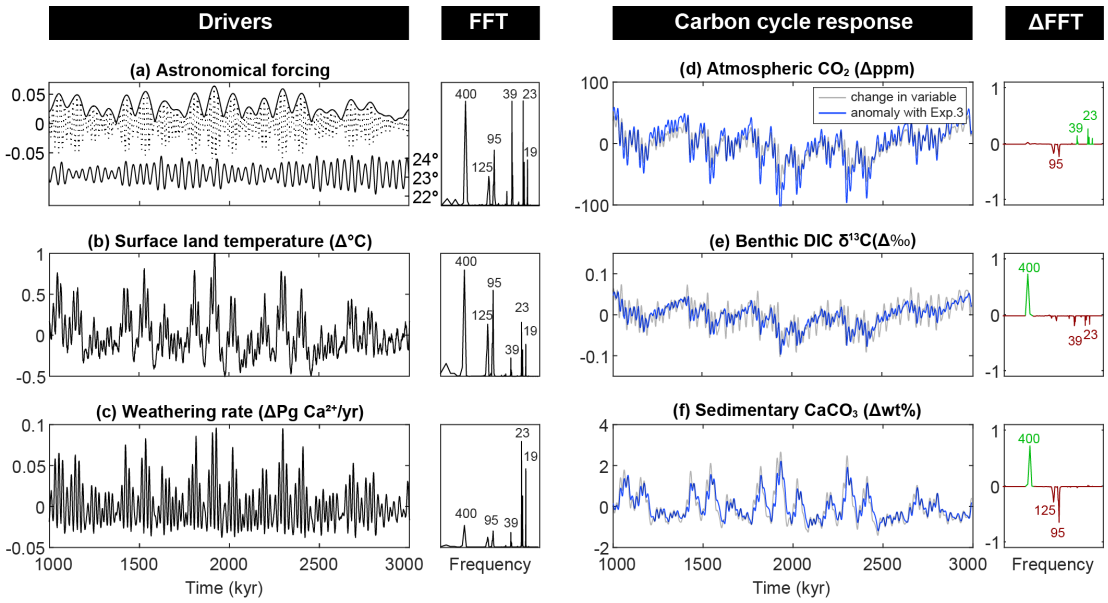

Figure 3.6: Exp.4, terrestrial rock weathering feedback in ASYM. (a) Astronomical forcing parameters (as per Figure 3.3a). (b) Change in surface land temperature. (c) Change in the rate of terrestrial weathering. (d) Change in atmospheric CO_2. (e) Change in benthic $\delta^{13}C$ of DIC. (f) Change in wt% $CaCO_3$. All variables are annual global mean values and are accompanied by their respective FFTs, normalized to the peak with maximum power. In blue, the values are plotted as anomalies with the previous experiment and depict the change driven by the terrestrial weathering feedback only. Likewise, the FFTs are plotted as anomalies. A positive (green) value on the y-axis indicates an increase in relative power and a negative (red) value indicates a decrease in relative power compared to the previous experiment.

3.3.5 Terrestrial Weathering Feedback

In our final experiment (Exp.4), we employ a temperature-dependent weathering parameterization (Colbourn et al., 2013) as opposed to keeping weathering rates invariant (Exp.3) or always balancing burial with weathering (Exp.0-2). As air temperatures over land rise, terrestrial silicate and carbonate weathering accelerate and thereby increase the transport of dissolved carbon and ALK to the surface ocean, allowing for greater carbon uptake and enhanced sedimentary $CaCO_3$ preservation. The power spectrum of annual global mean surface land temperature is dominated by 100 and 400 kyr eccentricity (Figure 3.6b). The relatively amplified precession power in land temperature compared to atmospheric temperature is a consequence of the asymmetric landmass distribution in ASYM. Land temperatures, and therefore global weathering rates, are elevated when the NH is tilted maximally toward the Sun. Weathering rates consequently are dominated by precession cycles (Figure 3.6c).

Precession power in the weathering rate generates precession cycles in atmospheric pCO_2 with an average range of 17 ppm, significantly larger compared to Exp.3. The average range of 400 kyr CO_2 cycles increases in comparison to Exp.3 to a value of 26 ppm. This relative increase in 400 kyr power is not apparent in the ΔFFT plot (Figure 3.6d) because the power spectra are normalized, meaning that the dominant cycle (long eccentricity) maintains a value of 1 for Exp.3. The dominance of long eccentricity on atmospheric CO_2 is a result of the long ocean-atmosphere carbon residence time due to relatively slow weathering rates. The slow response time of the ocean's carbon reservoir acts as a low-pass filter (Cramer et al., 2003; Palike et al., 2006; Laurin et al., 2015), further demonstrated by

large phase differences of 112° and 125° between $p\mathrm{CO}_2$ and the short and long eccentricity forcing, respectively, that did not exist before. The total variability modeled in $p\mathrm{CO}_2$ increases to 132 ppm.

Maximum variability of 0.19‰ in benthic DIC δ^{13}CC arises from the imbalance between weathering δ^{13}C and the δ^{13}C of buried CaCO_3 (Figure 3.6e). Benthic DIC δ^{13}C declines in response to elevated weathering and carbonate burial at long eccentricity maxima because relatively heavy carbon ($\delta^{13}\mathrm{C}_{CaCO3} = \delta^{13}\mathrm{C}_{DIC} + 1.9‰$) is removed from the ocean through the burial of CaCO_3. Burial of carbonate thus dominates the response of benthic DIC δ^{13}C despite the input of high δ^{13}C via weathering at eccentricity maxima. A high δ^{13}C value for weathered carbonate is required in our model framework to balance volcanic carbon input because we do not simulate organic carbon burial. Inclusion of organic carbon burial would allow us to use a δ^{13}C of weathered CaCO_3 more comparable to the δ^{13}C of marine CaCO_3. However, because the response of benthic DIC δ^{13}C is negative at long eccentricity maxima, a lower value for the δ^{13}C of weathered carbon would mean that weathering less effectively counteracts the impact on benthic DIC δ^{13}C of increasing CaCO_3 burial and would drive an even greater decline in DIC δ^{13}C. Sedimentary wt% CaCO_3 also shows a relative increase in power at the long eccentricity frequency and greater phase lag with eccentricity forcing, consistent with the slow weathering feedback. The wt% CaCO_3 lags the short eccentricity forcing by 10 kyr.

The primary difference in SYMM simulations is the lack of precession power in the weathering rate and consequently in $p\mathrm{CO}_2$, benthic DIC δ^{13}C, and global mean wt% CaCO_3. With landmasses distributed evenly, both the NH and SH have an equal amount

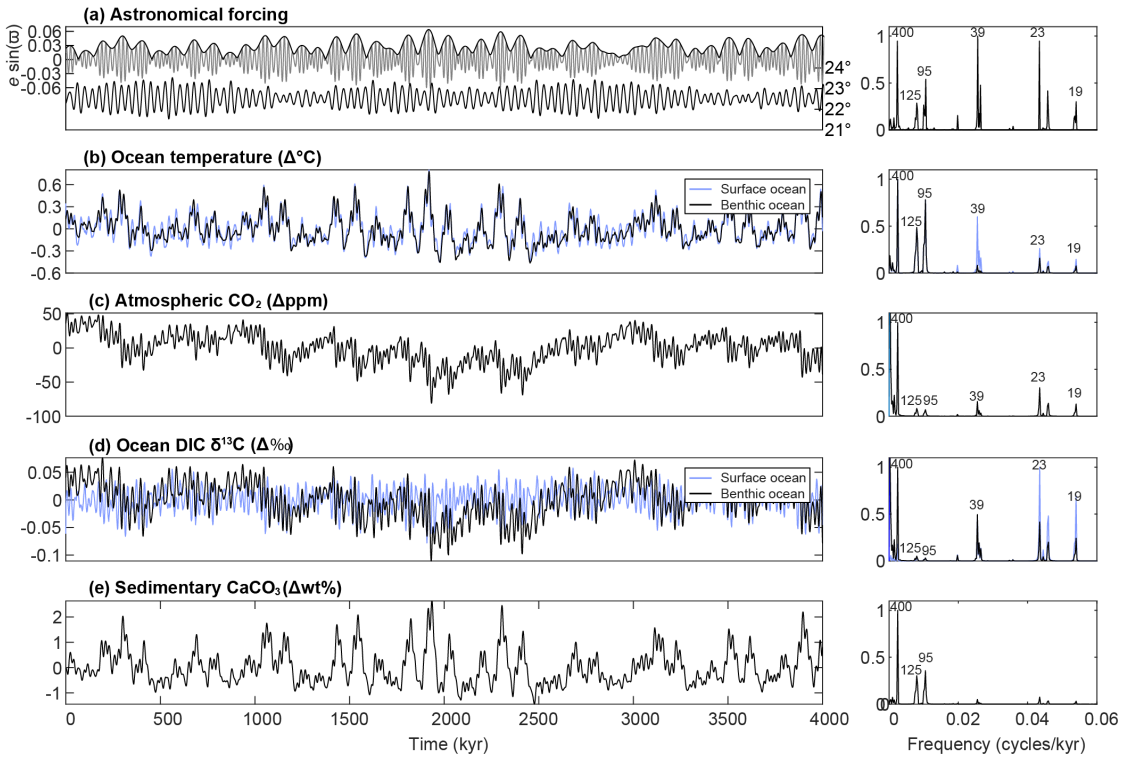

Figure 3.7: Cumulative astronomical impact of ASYM simulations. (a) Astronomical forcing parameters (as per Figure 3.3a). (b) Annual global mean temperature change in the benthic (black) and surface (blue) ocean. (c) Annual global mean pCO_2 change. (d) Annual global mean $\delta^{13}C$ change in the deep (black) and surface (blue) ocean DIC reservoir. (e) Global mean sedimentary $CaCO_3$ change. All variables are accompanied by their respective FFTs, normalized to the peak with maximum power. The combined impact of all four climate-carbon feedbacks on atmospheric, ocean, and sedimentary reservoirs.

of terrestrial area available for weathering, which minimizes the temporary imbalance on precessional timescales. Power spectra still show the relative shift towards long eccentricity forcing driven by the low pass filtering effect of the ocean carbon reservoir, consistent with ASYM (Figure B.6).

3.3.6 Astronomical Response to (Inorganic) Carbon Cycle Feedbacks

In addition to allowing us to elucidate the role of individual feedbacks, our experimental framework provides the net (Earth system) astronomical forcing response of ocean circulation, CO_2 solubility, ocean productivity, $CaCO_3$ dissolution and terrestrial weathering feedbacks combined (Figure 3.7 for ASYM and Figure B.7 for SYMM). Under the modeled ice-free greenhouse climate state, ocean circulation, CO_2 solubility, and $CaCO_3$-dissolution feedbacks are positive with respect to the astronomically-driven temperature change and generate an increase in the average range in atmospheric CO_2 of $\sim$6 ppm (circulation and solubility) and $\sim$14 ppm (19 minus 3.5 ppm) ($CaCO_3$ dissolution) at the long eccentricity period in ASYM. On the other hand, marine productivity reduces the average long eccentricity range in pCO_2 by $\sim$3 ppm (6.2 minus 3.5 ppm) and terrestrial weathering increases the range, but flips the phase, equating to a change of $\sim$45 ppm (19 plus 26 ppm) in the long eccentricity cycle in ASYM (Table B.2). Hence, marine productivity and terrestrial weathering act as negative feedbacks. The net ΔpCO_2 as simulated in Exp.4 is dominated by the terrestrial weathering feedback and slightly negative on eccentricity timescales, resulting in a reduced average range in global mean benthic temperature of 0.25°C at long eccentricity periods compared to a 0.30°C average range in Exp.0 that excludes all carbon-climate feedbacks. For SYMM, ocean circulation and solubility, and $CaCO_3$ dissolution increase the 400 kyr average range in pCO_2 by 4.5 ppm and 13 ppm, respectively, whereas marine productivity decreases the range by 0.5 ppm and terrestrial weathering flips the phasing between eccentricity and pCO_2, equating to a change of 41 ppm (17 plus 24 ppm).

Our framework considers two groups of feedbacks — (1) astronomically forced changes in CO_2 solubility, ocean circulation, and marine surface productivity, which redistribute carbon between the ocean and atmosphere, and (2) astronomical forcing of carbonate compensation and silicate weathering feedbacks, which remove and add carbon to the atmosphere-ocean system. The feedbacks related to carbon redistribution act on timescales comparable to or smaller than those of global ocean overturning and therefore respond rapidly to astronomical forcing. Redistribution of carbon contributes to high frequency cyclicity produced in atmospheric pCO_2, global mean DIC $\delta^{13}C$, and global mean $CaCO_3$ preservation. However, the well-ventilated ocean simulated here as a result of the simplified continental configurations likely results in a lower estimate of ocean circulation variability in response to astronomical forcing. For example, a more poorly ventilated ocean basin would store more carbon in the deep ocean reservoir and could release relatively more CO_2 to the atmosphere in response to small changes in ocean overturning strength, as shown with a theoretical framework along with a 3D ocean biogeochemistry model (Kwon et al., 2011) and more specifically for the Last Glacial Maximum using the cGENIE model (Ödalen et al., 2018).

By removing and adding carbon to the atmosphere-ocean system, carbonate compensation and silicate weathering feedbacks drive the most distinct responses in the carbon cycle, both in terms of the total variability in response to astronomical forcing and shifts in spectral power. Generally, long-term carbon feedbacks enhance power at low frequencies at the expense of high frequencies by acting as a low-pass filter at timescales comparable to the residence time of carbon in the ocean-atmosphere. This occurs in both ASYM and SYMM

simulations and is therefore independent of the continental configuration. The spectral signals in ASYM and SYMM of modeled pCO_2, benthic DIC $\delta^{13}C$, and wt% $CaCO_3$ are thus similar in the sense that the long eccentricity cycle dominates. However, a notable difference is the absence of precession cycles in SYMM (Figure B.7) and their presence in ASYM (Figure 3.7) due to the hemispherically asymmetric impact of ocean circulation, solubility, and marine productivity on the redistribution of carbon between the surface and deep ocean in ASYM. High frequency cycles are particularly execarbated in DIC $\delta^{13}C$ of ASYM where marine productivity is greatest in the SH and local, seasonal changes in temperature and $[CO_2\ (aq)]$ affect the carbon isotope fractionation of POC and $CaCO_3$.

While these simulations provide a systematic analysis of mechanisms through which astronomical forcing impacts the climate-carbon system, our experiments do not include a comprehensive representation of all relevant mechanisms. Our focus in this current paper is on the inorganic (carbonate) carbon cycle and feedbacks. We do not include a terrestrial biosphere (land plants and soils) or other reduced carbon reservoir (e.g. permafrost, methane hydrates). We also deliberately use the most simplistic parameterization of export productivity, so it is likely that we underestimate its sensitivity to astronomical forcing. Export productivity in these experiments is dependent only on the nutrient (phosphate) concentration, with a modifier for light availability. Temperature dependence in parameterizations of export production of particulate organic matter and carbonate (Monteiro et al., 2012), and water column remineralization (John et al., 2014; Crichton et al., 2021) likely modify the carbon cycle response to astronomical forcing. (See Crichton et al. (2021) for an analysis of the role of temperature in remineralization.)

Moreover, we have applied a reflective boundary for organic matter and phosphate at the sediment-water interface, neglecting organic matter burial and assume an invariant nutrient inventory. Organic matter preservation and burial processes, in addition to reflecting changes in overlying export production, are temperature and oxygen dependent (Hülse, Arndt, Wilson, Munhoven, & Ridgwell, 2017), implying several different pathways by which astronomical forcing may additionally impact atmospheric pCO_2 and DIC $\delta^{13}C$. Furthermore, inclusion of an open system for phosphate may result in distinct astronomical fingerprints as the phosphate residence time is similar in duration to high frequency astronomical cycles (Van Cappellen & Ingall, 1996).

In comparison to benthic high-resolution paleoclimate records throughout the Cenozoic (Palike et al., 2006; Holbourn et al., 2013; Littler et al., 2014; Beddow et al., 2016; Westerhold, Röhl, Donner, & Zachos, 2018; Tian et al., 2018; Barnet et al., 2019), our simulations show minor variability in $\delta^{13}C$ on astronomical timescales (the maximum variability in simulated $\delta^{13}C$ cycles is less than 0.2‰ in ASYM). This model-data discrepancy is especially pronounced as we are evaluating modeled water column $\delta^{13}C$ and not considering the impact of bioturbation on the range of preserved cycles. The muted simulated $\delta^{13}C$ cycles very likely reflect missing feedbacks in the organic carbon cycle. (Feedbacks in the marine organic carbon cycle will be addressed systematically in a follow-on paper.)

Finally, an important caveat to our results is that, while cGENIE includes a dynamic ocean model, the 2D energy-moisture balance atmosphere does not reflect the potential impacts of astronomical forcing on atmospheric dynamics, for instance including changing patterns of winds or cloud cover. It is unclear exactly how inclusion of these dynamics

in response to astronomical forcing would modify the changes in the global MAT simulated here. However, the maximum variability in MAT without carbon feedbacks in Exp.0 (1.7°C) corresponds well with the difference in MAT between and eccentricity maxima and minima for the Eocene with 2× (∼1.5°C) and 4× (∼2°C) preindustrial CO_2 concentrations simulated with the HadCM3L GCM (Lunt et al., 2011).

3.3.7 Implications for the Interpretation of Marine Proxy Records

While simulated cycles in benthic temperature, $\delta^{13}C$, and wt% $CaCO_3$ show modest ranges in comparison to proxy records of temperature (e.g. $\delta^{18}O$), carbon isotopes ($\delta^{13}C$), and $CaCO_3$ from early Cenozoic ice-free climates, we can also compare model and data in terms of the relative distribution of power and phasing in key climate and carbon cycle metrics in response to astronomical forcing. Early Cenozoic deep-sea proxy records generally show pronounced 100 and 400 kyr eccentricity cycles (Zachos et al., 2010; Sexton et al., 2011; Westerhold et al., 2011; Littler et al., 2014; Lauretano et al., 2015; Barnet et al., 2019). Our results demonstrate that mean annual temperature spectra are dominated by eccentricity, despite the small impact of eccentricity on the insolation forcing. Strong 400 and 100 kyr power is also consistent with our modeled wt% $CaCO_3$ records, but 100 kyr power is notably lacking from modeled $\delta^{13}C$.

Importantly, modeled wt% $CaCO_3$ is the only model metric we report that is influenced by the low-pass filter effect of sedimentary mixing. Thus, $CaCO_3$ preservation is also dominated by 100 and 400 kyr cycles, despite the significance of precession in carbonate export and deep ocean chemistry. The spectral difference between carbonate export, deep ocean $[CO_3^{2-}]$ and wt% $CaCO_3$ is hence also likely to shift power in proxy records of

temperature and $\delta^{13}C$ towards longer periods. However, this process cannot create power at the shorter 100 kyr period that is currently absent from modeled water column $\delta^{13}C$. Other processes, not included here, must be invoked to produce the 100 kyr $\delta^{13}C$ eccentricity cycles in proxy records.

Early Cenozoic benthic foraminiferal records that contain evidence for astronomically paced 'hyperthermals' (∼60 to 48 Ma) also record characteristic phase relationships between temperature, $\delta^{13}C$, and $CaCO_3$. Eccentricity-paced temperature maxima lead $\delta^{13}C$ minima by 5-20 kyr and $CaCO_3$ minima often lead $\delta^{13}C$ minima by ∼2-40 kyr (Kirtland Turner, 2014; Littler et al., 2014; Westerhold, Röhl, Donner, & Zachos, 2018). However, our model simulations including all four feedbacks (Exp.4) show significant differences in the phase relationship between temperature, global mean wt% $CaCO_3$, and the $\delta^{13}C$ (Figure 8). Most strikingly, global mean wt% $CaCO_3$ is higher during eccentricity temperature maxima – a consequence in the model of elevated export production, warmer deep ocean temperatures, and elevated deep ocean $[CO_3^{2-}]$ caused by both stronger ocean overturning and enhanced terrestrial weathering. A few possibilities could explain this model-data discrepancy. First, the terrestrial weathering feedback might have been weaker than modeled here during the early Cenozoic (Kump & Arthur, 1997; Caves et al., 2016; van der Ploeg et al., 2018). Second, changes in shallow shelf carbonate burial might have compensated for deep sea burial. Changes in shelf burial might have corresponded to sea level fluctuations even in an ice-free world (Li et al., 2018; D. Liu et al., 2021). Third, additional carbon cycle feedbacks (not modeled) involving the organic carbon cycle might have dominated the phase relationship between temperature and carbonate preservation.

The hypothesis for a weaker weathering feedback has been postulated across climatic warming events including the Middle Eocene Climate Optimum (van der Ploeg et al., 2018) as well as the end-Permian (Kump, 2018). A gradual strengthening of the weathering feedback over the past 50 Myr has also been proposed to explain the long-term decline in pCO_2 across the Cenozoic and to explain why the early Cenozoic was more sensitive to sudden carbon cycle perturbations (e.g. hyperthermals) than the mid and late Cenozoic (Caves et al., 2016). If silicate weathering rates are limited by factors like the thickness of soils (Kump, 2018), rock weatherability (Caves et al., 2016; van der Ploeg et al., 2018), or rate of rock uplift (Kump & Arthur, 1997) that prevent a strong positive response to increasing temperature, then the silicate weathering feedback would not have operated as modeled here in response to eccentricity-induced warming. Indeed, in Exp.3 with fixed terrestrial weathering, sedimentary carbonate content is relatively reduced during eccentricity-driven temperature maxima (compared to Exp.1, 2 and 4) when the weathering flux of carbonate ions to the ocean is insufficient to sustain $CaCO_3$ burial.

The second possibility is that the residual flux of the products of weathering to the open ocean were modulated by changes in shelf burial. An astronomical forcing that induces a greater shallow marine deposition response as compared to the total global weathering response, will result in the net supply to the open ocean becoming anti-phased. This could occur at least partly in response to changes in sea level (Li et al., 2018; D. Liu et al., 2021) and greater shelf area due to the thermal expansion of seawater (Opdyke & Wilkinson, 1988; Lyle et al., 2008), or directly from temperature controls on coral growth. However,

the neritic system is complex and we lack a model representation of shallow water carbonate burial able to account for sea-level and accommodation space controls on neritic deposition.

Finally, the reduced carbon cycle may also play a key role in early Cenozoic carbon-climate variability, with, for instance, massive release of ^{13}C-depleted carbon into the ocean-atmosphere proposed to explain hyperthermal warming (Dickens, 2003; Zachos et al., 2010; Lunt et al., 2011; DeConto et al., 2012; Komar, Zeebe, & Dickens, 2013; Zeebe et al., 2017). Given that our model framework currently neglects the dynamics of both terrestrial and marine reduced carbon reservoirs, we instead estimate the consequences of reduced carbon release in association with eccentricity maxima using previous cGENIE simulations without astronomical forcing. Vervoort et al. (2019) simulated 0.5‰ negative δ^{13}C excursions with a duration of 100 kyr (comparable in size and duration to early Cenozoic δ^{13}C cycles) via input of 600-1,500 Pg carbon with a δ^{13}C signature of -22‰. The required carbon input masses resulted from the prescribed carbon input durations between 25 to 75 kyr (or a maximum rate of 0.02 Pg yr^{-1}). This forcing yields an increase in global temperature of 0.5 to 1°C. Yet, these 'slow' perturbations to the carbon cycle do not generate notable changes in modeled wt% $CaCO_3$ since the temperature-dependent weathering feedback increases transport of alkaline carbon species to the ocean at comparable rates (Vervoort et al., 2019). Carbon fluxes must exceed 0.2 Pg yr^{-1} to offset enhanced weathering fluxes and drive dissolution coincident with warming.

Moreover, model-data discrepancy exists between the small 5-20 kyr lag between δ^{18}O and δ^{13}C in early Cenozoic proxy records, compared to the large lag of ∼100 kyr simulated in cGENIE between benthic temperature and benthic DIC δ^{13}C on eccentricity

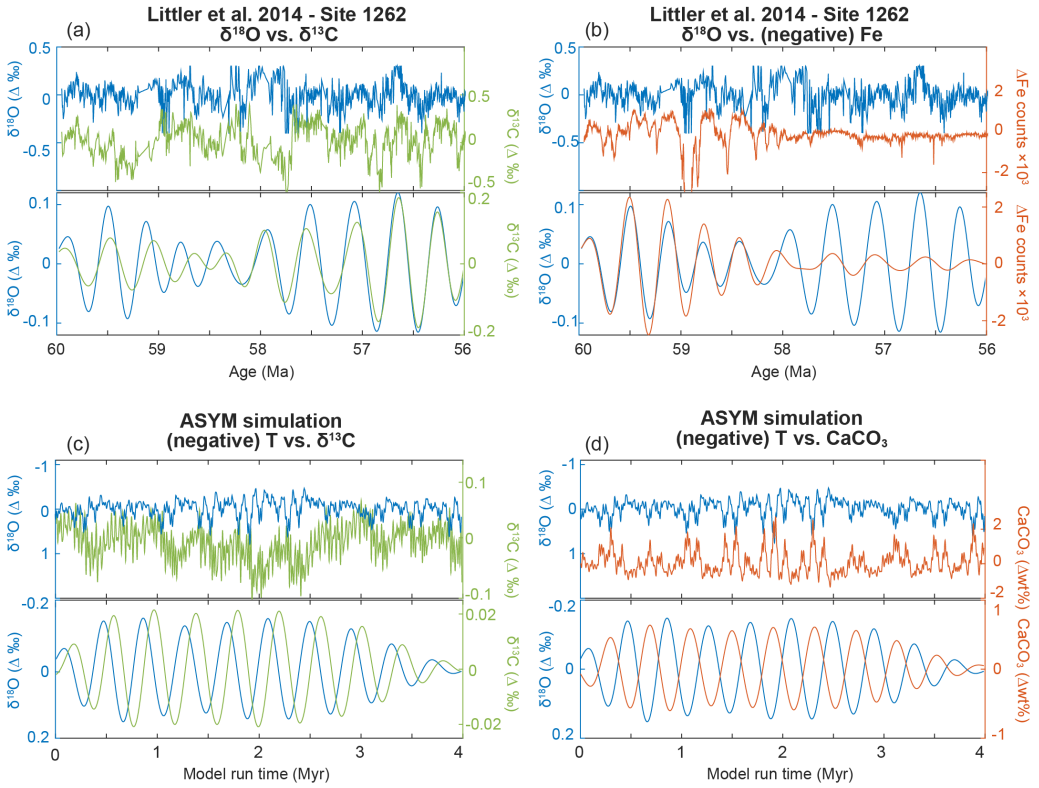

Figure 3.8: Phase analysis of paleoclimate proxies and comparable model output. (a-b) Benthic paleoenvironmental records from ODP Site 1262 of temperature (δ^{18}O, in blue), stable carbon isotopes (δ^{13}C, in green), and Fe counts (in orange). Below, the associated bandpass filtered signal of the long eccentricity cycle (320-480 kyr). (c-d) Simulated (negative) annual global mean deep ocean temperature (in blue), δ^{13}C of DIC (in green), and sedimentary carbonate weight percentage (in orange) of ASYM simulations Exp.4. Below, the associated bandpass filtered signal of the long eccentricity cycle.

timescales (Figure 3.8a vs 3.8d, Table B.2 and B.3). Large modeled lags between temperature and $\delta^{13}C$ are produced only in experiments including $CaCO_3$ compensation and/or weathering feedbacks and occur because the small isotopic difference between inorganic carbon reservoirs requires long-sustained imbalances to produce a noticeable effect in the isotopic signature of the deep ocean DIC reservoir. Rapid input of low $\delta^{13}C$ carbon would leave a notable imprint on the DIC reservoir much more rapidly due to the larger isotopic difference. Hence, geologically rapid release of low $\delta^{13}C$ carbon at eccentricity paced intervals therefore fits best with the phase relationships observed between $\delta^{18}O$, $\delta^{13}C$, and $CaCO_3$ across astronomical timescales in early Cenozoic marine paleoclimate records and strongly points to the exclusion of dynamic reduced carbon reservoirs as the primary reason for model-data mismatch.

3.4 Conclusion

We have simulated the transient impact of astronomical forcing on the climate and (inorganic) carbon cycle using a dynamic 3D carbon-enabled Earth system model under ice-free conditions. Global annual mean temperature is dominated by eccentricity power with cycles of 1.3 to 1.7°C, depending on the continental distribution. While eccentricity also dominates power spectra of early Cenozoic benthic foraminiferal $\delta^{18}O$ records, observed variations correspond to cycles of 2-3°C in deep ocean temperature, suggesting that additional feedbacks, not modeled here, roughly doubled the temperature response to insolation forcing. We focused in this paper on feedbacks involving CO_2 solubility, marine productivity, $CaCO_3$ sedimentation, and terrestrial weathering. While these do not significantly

amplify modeled temperature variability, they do cause distinct shifts in modeled carbon cycle proxies. The CO_2 solubility feedback, ocean circulation, and marine primary production redistribute carbon between the atmosphere, surface and deep ocean, producing high frequency (precession and obliquity) spectral signals in the benthic DIC $\delta^{13}C$ reservoir. Long-sustained imbalances between $CaCO_3$ sedimentation and terrestrial weathering dampen high frequency variability in $\delta^{13}C$ and shift power spectra toward long eccentricity. Global mean wt% $CaCO_3$ increases during eccentricity-driven warm intervals when enhanced weathering elevates ocean ALK. The opposite relationship between temperature and wt% $CaCO_3$ in early Cenozoic records implies that the strength of the terrestrial weathering feedback was reduced, a shift in shallow shelf versus deep carbonate burial, and/or carbon cycle dynamics were controlled by additional (organic) carbon feedbacks. Geologically rapid, short-lived fluxes of reduced carbon into the atmosphere-ocean reservoir at eccentricity maxima are likely necessary to reconcile model-data discrepancies.

Chapter 4

Earth System Model Analysis of how Astronomical Forcing is Imprinted Onto the Marine Geological Record

The Role of the Organic Carbon Cycle and Feedbacks

Abstract - The impact of astronomical forcing on surface climate-carbon cycle dynamics in ice-free greenhouse climate states is revealed by the prominent eccentricity-paced oxygen (δ^{18}O) and carbon (δ^{13}C) isotopes excursions throughout the early Cenozoic. Intervals of elevated global temperatures during eccentricity maxima, have been linked to the periodic release of isotopically light carbon based on the in-phase δ^{18}O-δ^{13}C relationship but the individual feedbacks that may have contributed to the carbon cycle perturbations during warm intervals have not yet been tested mechanistically. In this follow-up study to Vervoort et al. (2021), we simulate the response of the marine organic carbon (C_{org}) and phospohorus (P) cycle to astronomical forcing with a series of transient multi-million-year-long Earth system model simulations and investigate the resulting astronomical evolution of $p\mathrm{CO}_2$, δ^{13}C of DIC, and wt% CaCO_3. Results suggest that higher bicarbonate and nutrient fluxes to the ocean at eccentricity maxima result in enhanced export production and burial rates of CaCO_3 and C_{org}, thereby decreasing $p\mathrm{CO}_2$ while increasing ocean δ^{13}C and CaCO_3 preservation, as opposed to the lower δ^{13}C and wt% CaCO_3 during intervals of warmth recorded in the early Cenozoic. The low-pass filtering effect of the marine carbon and P reservoirs shift spectral power from the 100 kyr to 405 kyr eccentricity cycle and removes all power at the short eccentricity band. Additional feedbacks, likely related to terrestrial carbon cycling, are required to explain the relative phasing, amplitude, and spectral signal of early Cenozoic proxy records.

4.1 Introduction

Globally distributed temperature (δ^{18}O) and carbon cycle (δ^{13}C, wt% $CaCO_3$) proxy records of the early Cenozoic show quasicyclic variations with frequencies linked to eccentricity, precession, and obliquity cycles with respective periods of 100-400 kyr, 20 kyr, and 40 kyr (Barnet et al., 2019; Lauretano et al., 2015; Littler et al., 2014; Westerhold et al., 2011; Westerhold, Röhl, Donner, & Zachos, 2018; Zachos et al., 2010). Yet, the pathways by which astronomical forcing impacts Earth's climate and (bio)geochemical cycles are poorly understood, particularly in absence of large dynamic ice sheets. A reoccurring feature in all early Cenozoic proxy records is the coincidence of elevated global temperatures with negative excursions in δ^{13}C and reduced $CaCO_3$ preservation on eccentricity timescales — the most extreme of such excursions are coined 'hyperthermal events' (Lourens et al., 2005; Zachos et al., 2010; Kirtland Turner et al., 2014). The release of isotopically light carbon to the ocean-atmosphere system is generally invoked to explain the climate-carbon relationship but the carbon source remains a point of speculation (Dickens, 2003; Zachos et al., 2010; Lunt et al., 2011; Sexton et al., 2011; DeConto et al., 2012; Zeebe et al., 2017).

Before attempting to identify the source and quantify the magnitude of the carbon perturbations that produced the astronomically paced features in the proxy data, it is crucial that we comprehend how astronomical forcing impacts the fundamental major physical and (bio)geochemical feedback processes relevant for climate and carbon cycling in absence of exceptional threshold perturbations. In a previous companion study, we simulated the behavior of the physical ocean and inorganic carbonate cycle to astronomical forcing over four million years with a transiently forced Earth system model (Vervoort et al., 2021).

The processes driven by astronomical forcing in that study include ocean circulation, CO_2 solubility, nutrient dependent marine export production, $CaCO_3$ compensation, and terrestrial weathering feedbacks. Results can be summarized by two model-data discrepancies. First, eccentricity forcing drives an in-phase relationship between global temperature and wt% $CaCO_3$ in the model as opposed to an anti-phase relation in early Cenozoic deep marine sediments (Lourens et al., 2005). Second, while the simulated benthic δ^{13}C of DIC declines during periods of global warmth, its variability is small (less than 0.2‰) and 100 kyr δ^{13}C cycles are weak compared to those in early Cenozoic records (Littler et al., 2014; Westerhold, Röhl, Wilkens, et al., 2018). These finding support the idea that additional marine and/or terrestrial organic carbon (C_{org}) cycle processes, with a greater isotopic fractionation effect than the inorganic carbon cycle feedbacks, are needed to reproduce the full variability in climate-carbon cycling as recorded in early Cenozoic proxy data.

Components of the marine C_{org} cycle impacted by astronomical forcing include the surface export production controlled by nutrient availability (Maier-Reimer, 1993; Ridgwell et al., 2007) and ambient sea surface temperatures (Monteiro et al., 2012), water column remineralization rates closely coupled to the seawater temperature-depth profile (John et al., 2014; Boscolo-Galazzo et al., 2018), and marine C_{org} burial controlled by the amount of organic matter supply to the seafloor (Lyle, 1988; Dunne et al., 2007) and ocean oxygenation (Arndt et al., 2013; Hülse et al., 2018). We have shown that nutrient controlled export production increases during eccentricity maxima through enhanced ocean ventilation that allows nutrients to be recycled more readily to the surface ocean under the assumption that the total nutrient inventory remains unchanged (Vervoort et al., 2021). CO_2 is drawn

from the atmosphere into the ocean and thereby poses a negative feedback on eccentricity timescales. However, the global marine nutrient inventory varies as the balance between nutrient input and removal fluxes changes on geologic timescales (Paytan & McLaughlin, 2007). For oceanic phosphorus, a limiting nutrient for primary productivity (Smith, 1984; Wallmann, 2003), the influx is controlled by climate-dependent river runoff whereas the outflux equals the burial of phosphorus in sediments to some extent controlled by the phosphorus regeneration rates as a function of ambient oxygen concentrations (Van Cappellen & Ingall, 1994; Wallmann, 2003). Its residence time is estimated to be on the order of 10^4 to 10^5 years (Froelich et al., 1982; Ruttenberg & Berner, 1993), comparable to the timescale of astronomical forcing with consequences for their mutual interaction. Moreover, the simplified nutrient-dependent-only scheme ignores temperature effects on marine export production or water column remineralization rates, meaning increased export inevitably leads to more C_{org} transport to the seafloor. This is not necessarily true as pelagic and benthic fluxes can become decoupled when accounting for greater metabolic rates of respiring bacteria at higher temperatures (Rivkin & Legendre, 2001), a process that can convert a negative into a positive feedback (John et al., 2014; Griffith et al., 2021).

Changes in the supply of C_{org} to the seafloor, whether through changes in the export productivity or water column remineralization rates, lead to variable global C_{org} burial rates that further impact the atmosphere-ocean carbonate chemistry on astronomical timescales. Because of the vast atmospheric and oceanic carbon reservoirs, a long-sustained imbalance between carbon release (e.g., through volcanic outgassing or kerogen weathering) and sequestration (e.g., though silicate weathering or C_{org} burial) is required to notably

change the carbon cycle dynamics (Palike et al., 2006). This so-called low-pass filtering effect removes power at high frequencies while relatively increasing power at the lower frequencies in the power spectra of environmental proxies (Boulila et al., 2012; Kocken et al., 2019; Paillard & Donnadieu, 2014; Sproson, 2020).

The follow-up study to Vervoort et al. (2021) presented here provides a comprehensive evaluation of the climatic and environmental impacts of individual components of the global marine C_{org} cycle in response to astronomical forcing in ice-free greenhouse climates. We use transiently forced four-million-year-long Earth system simulations in which marine export production, phosphorus input and output fluxes, and marine C_{org} burial vary with astronomical forcing and report results in terms of the modeled global mean $p\mathrm{CO}_2$, $\delta^{13}\mathrm{C}$ of DIC, and wt% CaCO_3 for direct comparability with benthic paleoclimate proxies.

4.2 Methods

4.2.1 cGENIE Model and Configuration

The cGENIE Earth system model of intermediate complexity combines a dynamic 3D ocean model with a simplified 2D energy-moisture-balance model atmosphere (Edwards & Marsh, 2005) and a detailed representation of ocean biogeochemical cycles (Ridgwell et al., 2007). The geologic carbon cycle is represented through input of dissolved carbon species via volcanic outgassing and carbonate, silicate, and kerogen weathering, and removal via the accumulation of calcium carbonate and organic carbon in marine sediments (Colbourn et al., 2013; Ridgwell & Hargreaves, 2007). Boundary conditions of Vervoort et al. (2021) are applied for comparability with the previous study that describes the influ-

ence of astronomical forcing on inorganic carbon cycle feedbacks. The model is equilibrated to atmospheric CO_2 concentration of ∼834 ppm to prevent the formation of sea ice under greenhouse conditions, the solar constant of 1361.7 Wm^{-2} is consistent with the early Eocene greenhouse period, and initial biogeochemical state of the model follows previous Paleocene configurations (Ridgwell & Schmidt, 2010).

We use a highly idealized continental configuration to separate the astronomical impacts related to the carbon cycle from those related to the specific distribution of landmasses. The SYMM configuration contains one continent spanning from the polar north to south, is hemispherically symmetric, and includes a 175-meter-deep shallow shelf along the west coast. The shallow shelf area is 28.3×10^6 km^2, comparable to the modern continental shelf area. The model is equilibrated to the above boundary conditions in two stages. First, a 'closed system' (in)organic carbon cycle is imposed to bring the ocean dynamics and biogeochemistry to steady state. The removal or burial of marine inorganic carbon in the form of calcium carbonate ($CaCO_3$) is controlled by the saturation state of seawater and is compensated by an equal amount of inorganic carbon input via silicate and carbonate weathering. In addition, the burial of marine C_{org} is included as a non-linear function of the particulate organic carbon (POC) rain flux to the sediments following an empirically derived equation (Dunne et al., 2007). A 3.0× scaling factor is applied to obtain global burial rates that are within the range of estimates for modern marine sediment C_{org} burial rates of about 0.1-0.2 Pg C yr^{-1} (Burdige, 2007). Phosphorus (P) is buried alongside C_{org} based on an empirical relationship between the C_{org}:P ratio of remineralized fluxes and ambient

ocean oxygen concentration (Wallmann, 2003). The removal of C_{org} and P is balanced by an equal amount input via volcanic outgassing and weathering.

In the second stage of the spin-up process, the $CaCO_3$, C_{org}, and P burial fluxes are diagnosed, and the weathering fluxes are manually set to equal the burial fluxes while also maintaining isotopic mass balance in an 'open system'. The weathering fluxes of carbonate and silicate rocks are temperature dependent (Colbourn et al., 2013) and regulate the (alkaline) carbon and PO_4 input via runoff. The kerogen weathering flux and volcanic outgassing that balance the burial of C_{org} are invariant and do not provide any feedback response to astronomical forcing. The astronomical parameters in both spin-up stages remain invariant and are set to fixed values.

4.2.2 Experimental Design

To simulate the transient response of Earth's climate and carbon cycle dynamics to astronomical forcing the amount and distribution of incoming solar radiation is calculated from a timeseries of astronomical parameters consistent with a those between 57-53 Ma (Laskar et al., 2004) using equations from Berger (1978) as per Vervoort et al. (2021). The daily mean insolation at each latitude is calculated as a function of the time of year (seasonality) and the orbital configuration that changes in steps of 1000 year. The complexity of the model in terms of the number of feedbacks that are included is systematically increased with each experiment (Figure 4.1). A total of four million years of astronomical forcing is simulated in order to capture several 405 kyr-long eccentricity cycles.

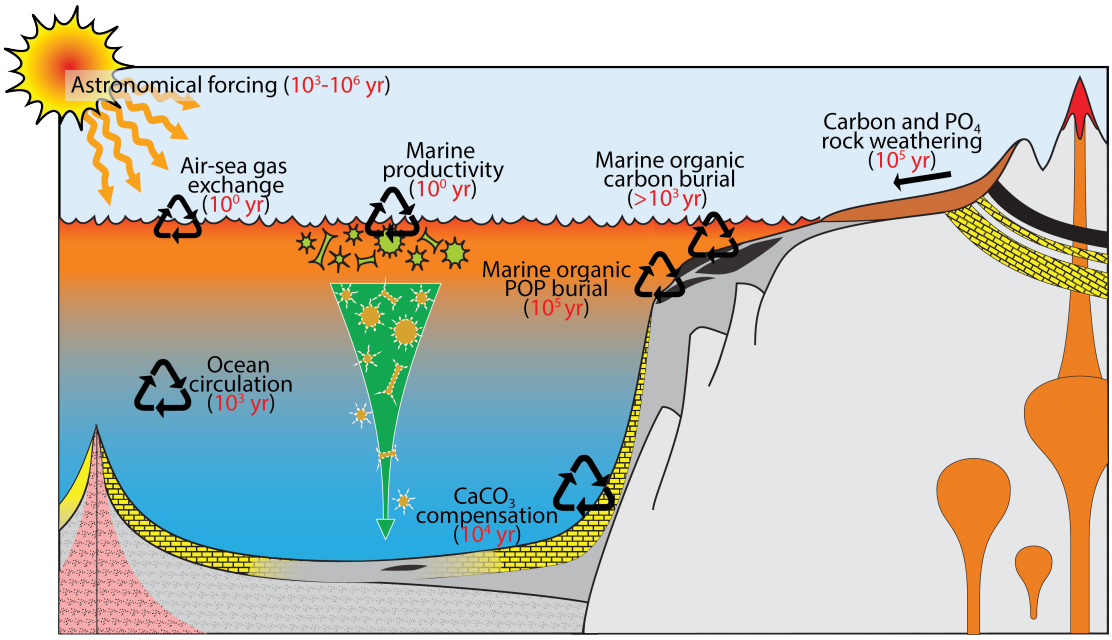

Figure 4.1: cGENIE carbon cycle feedbacks and their response time compared to the timescale of astronomical forcing. In Exp.4, astronomical forcing impacts the CO_2 solubility, ocean circulation, marine productivity, $CaCO_3$ compensation, and carbon weathering feedback. The response of marine C_{org} burial to astronomical forcing is added in Exp.5. In Exp.6, astronomical forcing additionally impacts PO_4 weathering rates and P burial fluxes with consequences for the total PO_4 inventory and marine productivity.

In the base experiment (Exp.4), ocean circulation, CO_2 solubility, surface export production, marine $CaCO_3$ sedimentation, and terrestrial weathering all respond to astronomical forcing (Exp.4 in Vervoort et al. (2021)), either directly through its influence on surface temperature, or indirectly through resulting changes in ocean circulation, nutrient availability, or carbonate chemistry. Each feedback process produces a unique response in the global carbon cycle and surface climate and thereby alters the spectral signals recorded in the atmospheric CO_2, $\delta^{13}C$ of dissolved inorganic carbon (DIC), and wt% $CaCO_3$. The burial of C_{org} and P, and weathering of kerogen and PO_4 are prescribed in Exp.4 presented here and do not vary with astronomical forcing. A brief overview of the combined astronomical imprint of these processes is provided in Section 4.3.1.

In Exp.5, we evaluate how astronomically forced marine C_{org} burial impacts carbon cycling. The mass of C_{org} removed from the ocean-atmosphere is calculated from the POC rain flux to the sediments. The local C_{org} burial varies non-linearly with the local POC rain based on an empirically derived equation (Dunne et al., 2007):

$$F_{POCburial} = SCL \times F_{POCrain} \times \frac{0.013 + 0.53F_{POCrain}^2}{(7.0 + F_{POCrain)^2}} \tag{4.1}$$

where $F_{POCburial}$ is the C_{org} burial rate, SCL is the scaling factor, and $F_{POCrain}$ is the POC rain flux to the sediments. The removal of isotopically light C_{org} is balanced by carbon input via volcanic outgassing ($\delta^{13}C_{CO2}$ = -6‰) and a fixed kerogen weathering flux ($\delta^{13}C_{ker} \approx$ -27‰). The fraction of C_{org} that is not preserved is returned to the ocean in remineralized form. The burial of carbon is decoupled from that of phosphorus in Exp.5, i.e., the P burial

flux remains fixed and does not change as a function of C_{org} burial (closed P cycle), but the removal of carbon is set to vary with astronomical forcing (open C cycle).

In Exp.6, the P cycle is opened up and P remineralization fluxes (and subsequent burial) are calculated as a fraction of the C_{org} remineralization fluxes depending on the ambient ocean oxygen concentrations following Wallmann (2010). Weathered input of PO_4 via runoff varies with temperature dependent silicate weathering. Changes in the marine nutrient inventory affect the surface export production, POC rain, and ultimately the C_{org} burial fluxes on astronomical timescales.

4.3 Results and Discussion

Below, we describe the response of (in)organic carbon cycle feedbacks to astronomical forcing and their impacts on proxy relevant model outputs including annual mean temperatures, atmospheric CO_2 concentrations, benthic $\delta^{13}C$ of DIC, and wt% $CaCO_3$. Global annual mean values are reported in terms of total variability (max-min) and distribution of spectral power across the four-million-year-long simulated interval in addition to the phasing between astronomical forcing and proxy relevant model output.

4.3.1 Inorganic Carbon Cycling

Ocean circulation, CO_2 solubility, nutrient dependent marine surface export production, carbonate compensation, and terrestrial weathering are all impacted directly or indirectly by astronomical forcing. These processes redistribute carbon among the atmosphere, surface, and deep ocean while only the geological processes of carbonate compen-

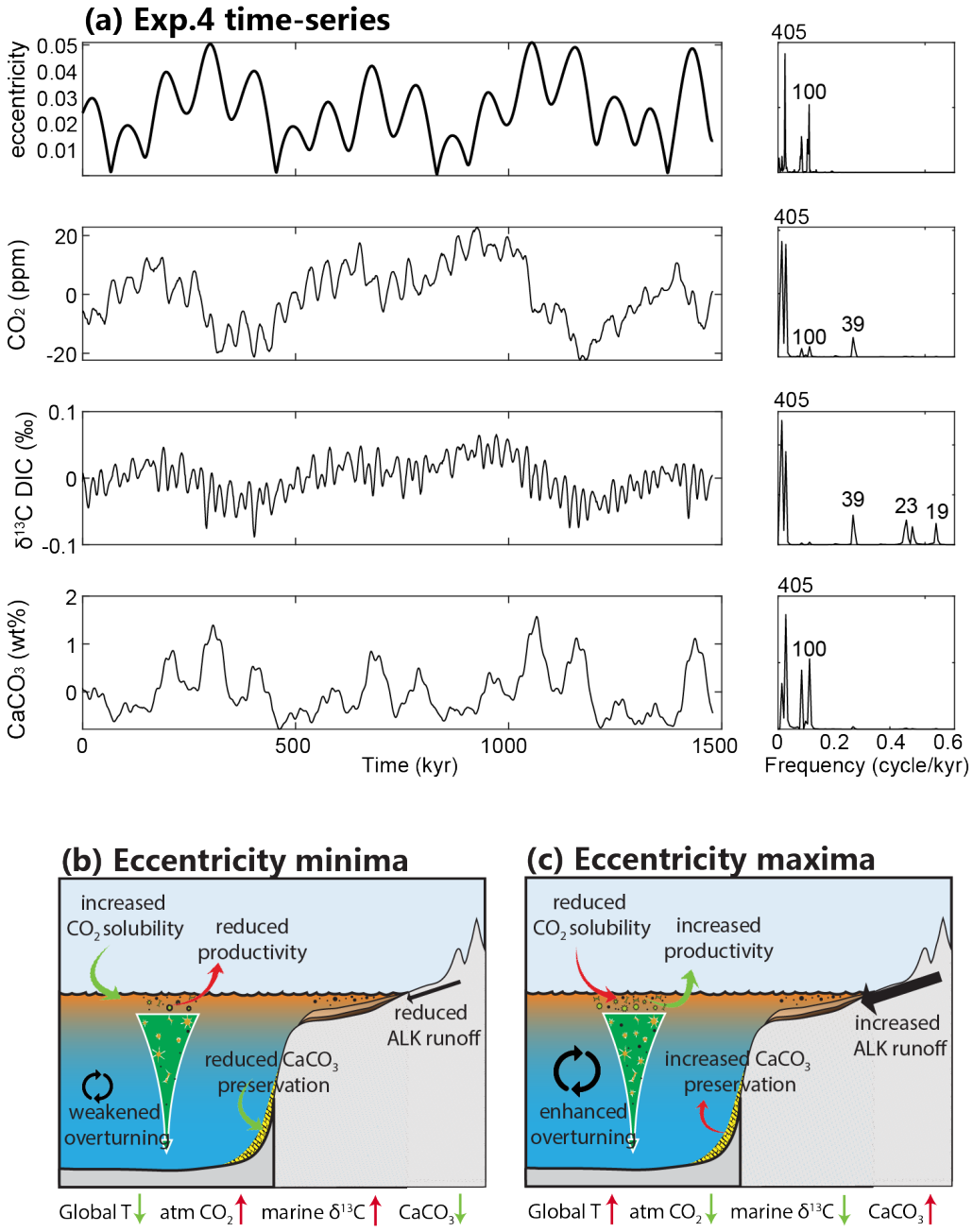

Figure 4.2: Astronomical evolution of key paleoceanographic proxies in Exp.4 including inorganic carbon cycle feedbacks. (a) Time-series and associated Fast Fourier Transforms (FFTs) of eccentricity forcing, and the resulting pCO_2, $\delta^{13}C$, and wt% $CaCO_3$. FFT peaks indicate peak astronomical periods in kyr. Feedback response during eccentricity (b) minima and (c) maxima.

sation and weathering add or remove carbon from the ocean-atmosphere system entirely. Each feedback produces unique astronomical imprints on proxy relevant variables as described in detail in Vervoort et al. (2021). Changes in ocean circulation, CO_2 solubility, and marine productivity are largely driven by local, seasonal temperature changes dominated by precession and obliquity forcing that result in 19, 23 kyr (precession), and 39 kyr (obliquity) cycles in the global atmospheric pCO_2, benthic DIC $\delta^{13}C$, and wt% $CaCO_3$. However, global and seasonal averaging in the SYMM hemispherically symmetric world, mutes these high-frequency signals. Temperature dependent terrestrial weathering combined with carbonate compensation inflicts the greatest changes to the carbon cycle on a global scale (Figure 4.2). During eccentricity maxima, the global temperature rises by $\sim$1°C (Vervoort et al., 2021) which results in higher rates of terrestrial (carbon) weathering. The higher input of alkalinity in the form of bicarbonate to the ocean and increased ocean temperatures promote the uptake of atmospheric CO_2 and preservation of $CaCO_3$. In this processes, isotopically heavier carbon is removed from the ocean, leaving the ocean DIC reservoir slightly isotopically depleted during eccentricity maxima.

An astronomically forced imbalance between carbon input and removal produces predominantly 405-kyr-long eccentricity cycles in pCO_2 and DIC $\delta^{13}C$. Even though terrestrial weathering varies mainly with precession forcing (surface land temperatures vary seasonally and locally), the low-pass filtering effect of the large carbon reservoir removes high frequency cycles and amplifies low frequency (405 kyr) cycles. The combined effect of these carbon cycle feedbacks in Exp.4 results in a maximum variability in pCO_2 of 46 ppm,

maximum variability in DIC $\delta^{13}C$ of 0.15‰, and 2.4 wt% variability in $CaCO_3$ in the SYMM configuration (Figure 4.2).

4.3.2 Marine Organic Carbon Burial

When the burial rates of C_{org} vary with astronomical forcing, as opposed to fixed C_{org} burial in Exp.4, the burial rates fluctuate between 0.100-0.111 Pg C yr^{-1}, mainly in response to obliquity and precession forcing insolation changes. C_{org} burial rates co-vary with the seasonally-driven marine export that is controlled by the nutrient supply to the surface ocean via enhanced ocean overturning. As previously addressed in Vervoort et al. (2021), the annual global mean export (and thus burial) variability on astronomical timescales is minimal because enhanced export on one hemisphere during favorable astronomical conditions is canceled out by simultaneous reduced export on the opposite hemisphere. Eccentricity has only a small influence on the C_{org} burial rates globally. During eccentricity maxima, the ocean overturning is slightly more efficient at recycling nutrients to the surface but the resulting changes in the three paleoceanographic proxies due to variable C_{org} burial rates alone are negligable (blue lines in Figure 4.3).

The combined effect of the inorganic carbon cycle feedbacks and C_{org} in Exp.5 results in a maximum variability in pCO_2 of 47 ppm, maximum variability in DIC $\delta^{13}C$ of 0.16‰, and 2.5 wt% variability in $CaCO_3$ in the SYMM configuration, comparable to those in Exp.4 (Figure 4.3).

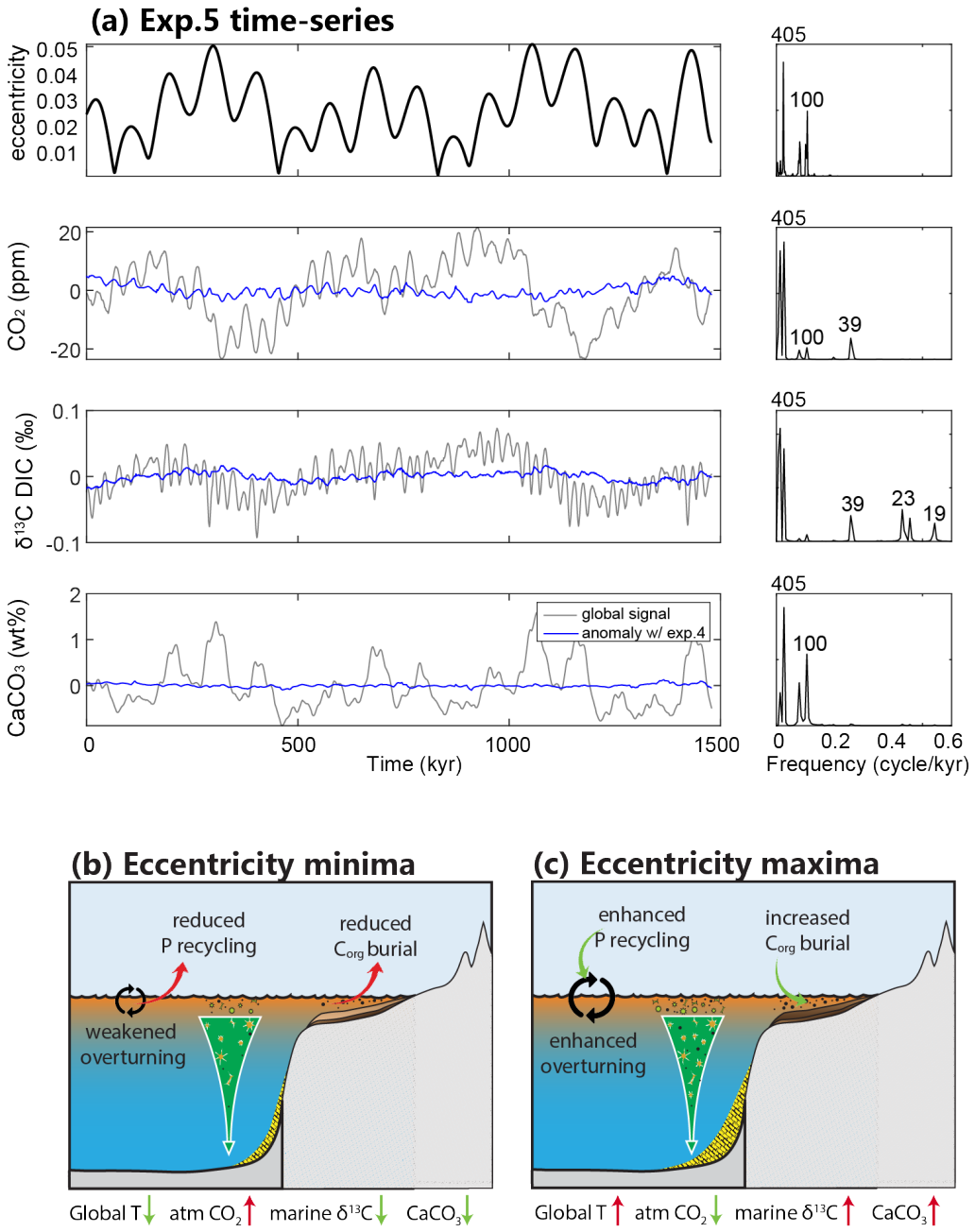

Figure 4.3: Astronomical evolution of key paleoceanographic proxies in Exp.5 including inorganic carbon cycle feedbacks. (a) Time-series and associated FFTs of eccentricity forcing, and the resulting pCO_2, $\delta^{13}C$, and wt% $CaCO_3$. FFT peaks indicate peak astronomical periods in kyr. In blue, the difference between Exp.5 and Exp.4, illustrating the isolated impact of the C_{org} burial feedback on the paleoceanographic proxies. Feedback response during eccentricity (b) minima and (c) maxima.

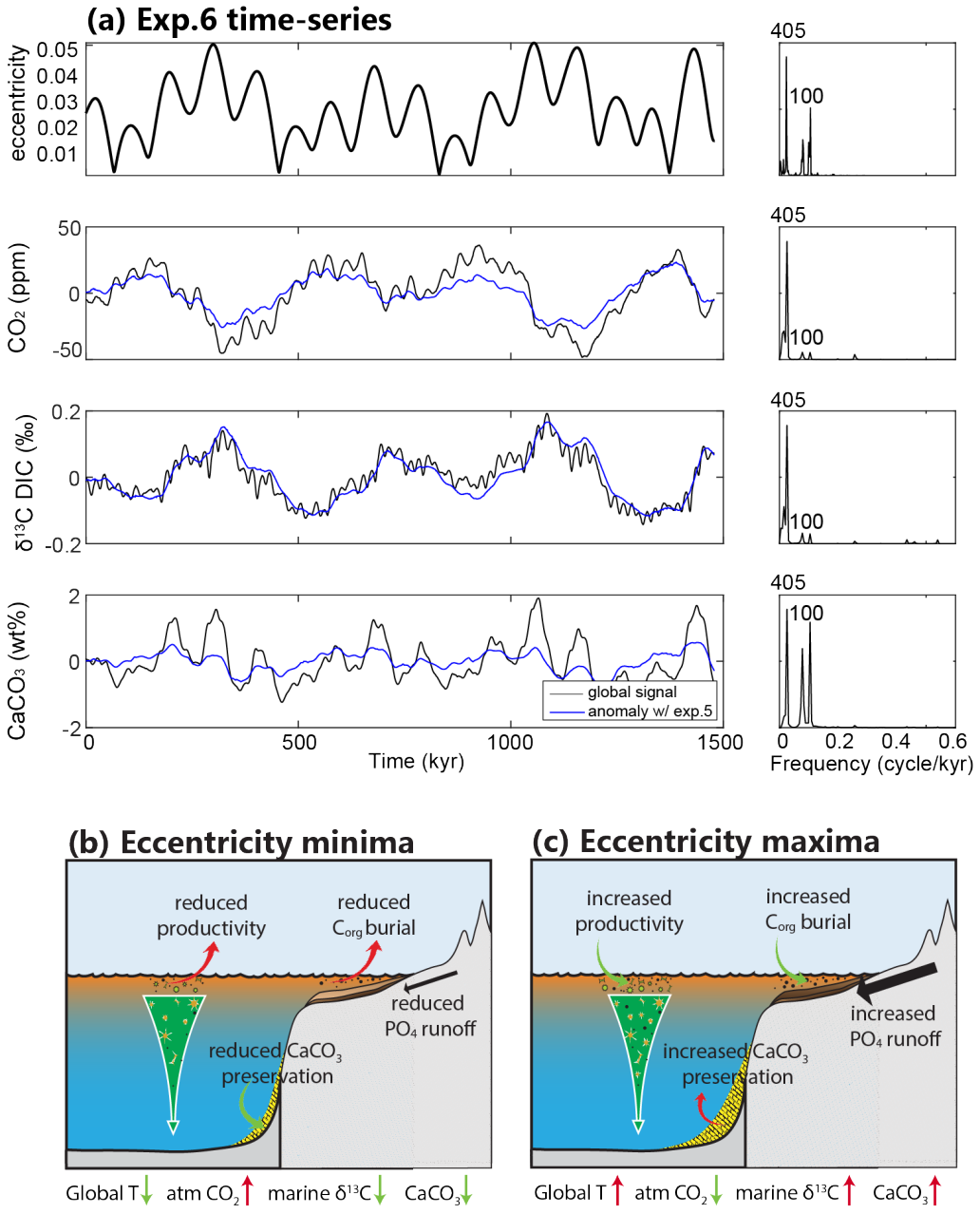

Figure 4.4: Astronomical evolution of key paleoceanographic proxies in Exp.6 including inorganic carbon cycle feedbacks. (a) Time-series and associated FFTs of eccentricity forcing, and the resulting pCO_2, $\delta^{13}C$, and wt% $CaCO_3$. FFT peaks indicate peak astronomical periods in kyr. In blue, the difference between Exp.6 and Exp.5, illustrating the isolated impact of the phosphorus cycle feedback on the paleoceanographic proxies. Feedback response during eccentricity (b) minima and (c) maxima.

4.3.3 Phosphorus Cycling

In Exp.6, the total ocean PO_4 inventory varies with astronomical forcing as the changing weathering fluxes carry PO_4 to the ocean via river runoff in a fixed ratio with temperature dependent silicate weathering, and P is removed from the ocean alongside the variable C_{org} burial as a function of ambient oxygen concentrations. During eccentricity maxima, global temperatures rise and terrestrial input of carbon and PO_4 is enhanced, mainly via eccentricity forcing and a much smaller contribution of obliquity-driven changes in global temperature (Figure 4.4). Because of the vast oceanic PO_4 inventory (2.95×10^{15} mol in our cGENIE set-up) and the relatively small weathering input fluxes (1.15×10^{11} mol yr^{-1}), several consecutive thousands of years of enhanced input are required to noticeably change the total PO_4 inventory. As a result, changes in the PO_4 inventory lag PO_4 weathering fluxes by ~12 kyr. Marine primary producers benefit from the rise in nutrient availability during eccentricity maxima and the enhanced export of POC (and $CaCO_3$) ultimately generates greater POC and P burial fluxes. A temporal imbalance between the input and output fluxes is inevitable due to the long PO_4 residence time of ~25 kyr in our cGENIE set-up. The imbalance regulates the size of the PO_4 inventory, resulting in high-amplitude 100 and 405 kyr eccentricity cycles in marine PO_4 concentrations.

Consequently, global burial rates of C_{org} vary between 0.090 and 0.139 Pg C yr^{-1} on eccentricity timescales. An excess of about 7,000 Pg C of isotopically light C_{org} is buried during eccentricity maxima which lowers atmospheric CO_2 concentrations and increases the $\delta^{13}C$ of DIC. The low-pass filtering effect of the marine carbon reservoir shifts spectral power from the shortest eccentricity cycles to the long 405 kyr eccentricity cycles, almost

completely removing any spectral power in the 100 kyr eccentricity band. In addition, $CaCO_3$ preservation becomes slightly enhanced at eccentricity maxima under the influence of an open P cycle as the $CaCO_3$ rain to the sediments increases. The combined effect of the inorganic carbon cycle feedbacks, variable C_{org} burial, open P cycle in Exp.6 results in a maximum variability in pCO_2 of 89 ppm, maximum variability in DIC $\delta^{13}C$ of 0.35‰, and 3.6 wt% variability in $CaCO_3$, roughly double the variability simulated in Exp.4 and Exp.5 (Figure 4.3).

4.3.4 Geographic Controls

The hemispherically symmetric SYMM world is highly idealized and designed to remove any effects that geography may have on the astronomical response of the Earth system (Short et al., 1991; Roychowdhury & DeConto, 2019). As a result, the impact of precession and obliquity cycles is minimized by hemispheric cancellation and seasonal averaging. To illustrate, enhanced seasonal C_{org} burial in the Northern Hemisphere is canceled out by a roughly equal amount of reduced burial in the Southern Hemisphere when the distribution of ocean shelves and basins is latitudinally mirrored, thereby muting the seasonal impacts of precession and obliquity. Naturally, the continental distribution throughout Earth's history has never been perfectly symmetric across latitudes. To study the impact of this simplification on our results, we design a completely asymmetric continental configuration (ASYM_SH) with a landmass only in the Southern Hemisphere and 175-meter-deep shallow shelves along the west and east coast of the continent. The total landmass and shelf area are equal to that of the SYMM world.

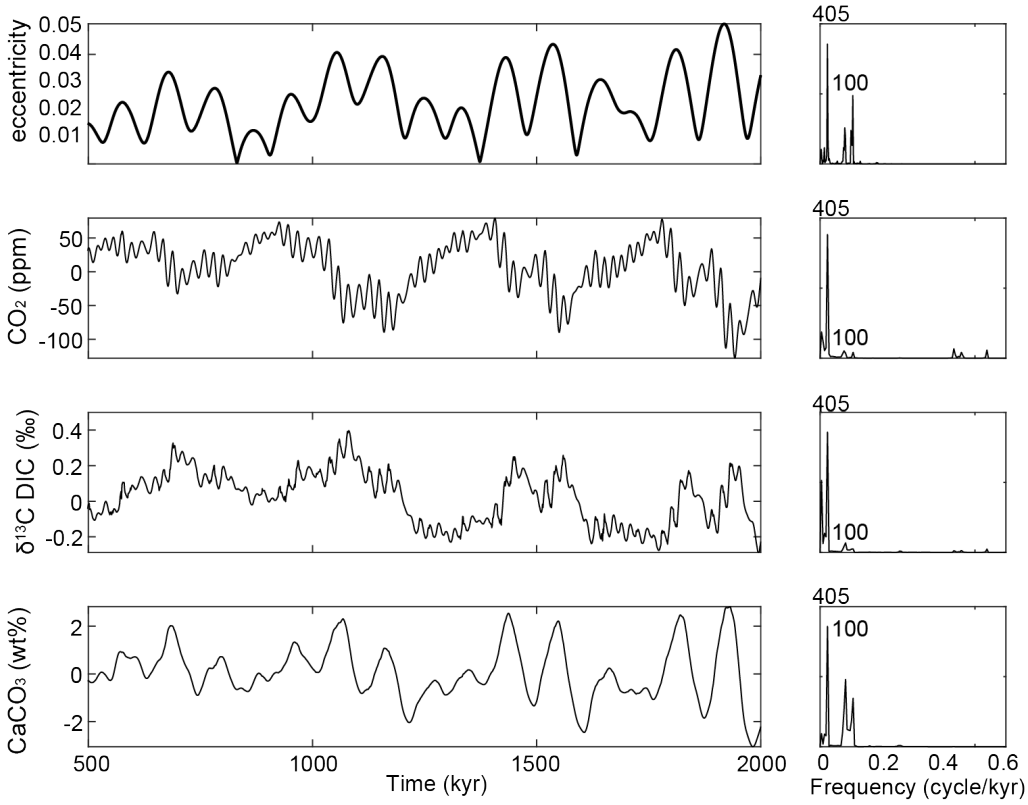

Figure 4.5: Astronomical evolution of key paleoceanographic proxies in Exp.6 including inorganic carbon cycle feedbacks in a hemispherically asymmetric world (ASYM_SH) and associated FFTs of eccentricity forcing, and the resulting $p\mathrm{CO}_2$, $\delta^{13}C$, and wt% CaCO_3. FFT peaks indicate peak astronomical periods in kyr. During the first 500 kyr of the simulation, the model is equilibrating to new conditions. Hence, this interval has been removed from the analyis.

The responses of pCO_2, benthic $\delta^{13}C$ of DIC, and wt% $CaCO_3$ to astronomical forcing in the ASYM_SH experiment with the same set of feedbacks as the previously described Exp.6, including inorganic carbon cycle processes, variable C_{org} burial, and an open P cycle, are comparable to those in SYMM (Figure 4.5). During eccentricity maxima, terrestrial weathering of carbon and P is enhanced which leads to reduced atmospheric CO_2 concentrations, global rise in $\delta^{13}C$ of DIC, and increased $CaCO_3$ preservation as global POC and $CaCO_3$ export and marine burial rates are elevated. The global C_{org} burial rates vary between 0.146 and 0.194 Pg C yr^{-1}. The 405 kyr cycle is the dominant frequency in all three proxies with a small contribution of short eccentricity in wt% $CaCO_3$. Similar to SYMM, precession and obliquity cycles are absent or only weakly present due to the low-pass filtering effect of the vast ocean carbon and PO_4 reservoir. An important difference between SYMM and ASYM_SH is that the burial of C_{org} in ASYM_SH has a strong precession component that is missing in SYMM due to hemispheric cancelation, although precession power does not carry over into the CO_2 and $\delta^{13}C$ of DIC in ASYM_SH.

Interhemispheric differences in the distribution of landmass and shelves roughly double the amplitude of the astronomical variability recorded in the key environmental variables. The maximum variability in pCO_2 is 228 ppm, maximum variability in DIC $\delta^{13}C$ is 0.60‰, and about 5.9 wt% variability is simulated in $CaCO_3$ (Figure 4.5). The amplitude of benthic $\delta^{13}C$ cycles approach those of early Cenozoic hyperthermals but the phasing with respect to the global temperature on eccentricity timescales is opposite.

4.3.5 Climate-Carbon Feedbacks of the Early Cenozoic

Benthic paleoclimate records of the early Cenozoic reveal a strong in-phase relationship between $\delta^{18}O$, $\delta^{13}C$, and $CaCO_3$ preservation on 100 kyr timescales linked to eccentricity forcing (Littler et al., 2014; Westerhold et al., 2011; Westerhold, Röhl, Donner, & Zachos, 2018) (Figure 4.6ac). Elevated global temperatures (low $\delta^{18}O$) coincide with the release of isotopically light carbon (low $\delta^{13}C$) and dissolution of deep marine $CaCO_3$ (low coarse fractions or high iron (Fe) counts). While our results have improved our understanding of Earth system response to astronomical forcing, the marine C_{org} burial dynamics and global phosphorus cycling simulated here, on top of the inorganic feedbacks (Vervoort et al., 2021), do not bring us closer to reconstructing the phase relation in proxy records of the Paleocene and Eocene. Instead, the cumulative response of the key oceanographic processes to astronomical forcing generates elevated $\delta^{13}C$ of DIC and enhanced preservation of $CaCO_3$ during warm intervals at eccentricity maxima (Figure 4.6bd).

In addition, astronomically forced variations in the input and removal fluxes of carbon from the atmosphere-ocean reservoir simulated in this study by terrestrial weathering and marine sediment accumulation are too small to reproduce the notable 100 kyr cycles in the early Cenozoic benthic $\delta^{13}C$ records. The carbon residence time (total carbon inventory divided by the input flux) regulates the strength of this low-pass filtering effect (Palike et al., 2006). A greater change in the carbon fluxes than those simulated here would reduce the residence time and weaken the spectral shift to lower frequency cycles.

Our study supports the idea that additional carbon cycle feedbacks need to be invoked to explain the low $\delta^{13}C$ and reduced $CaCO_3$ during the warmer intervals of eccen-

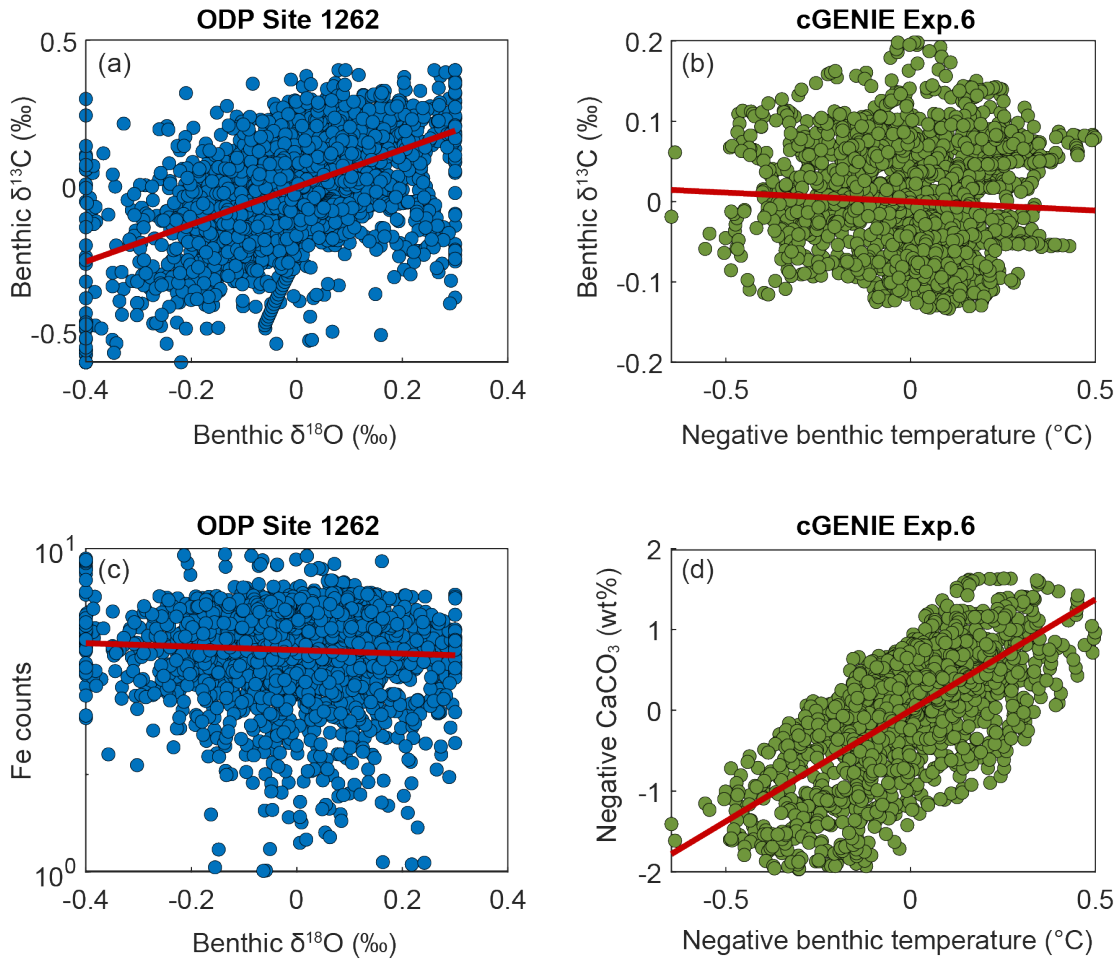

Figure 4.6: Comparison between early Cenozoic paleoceanographic proxy records of ODP Site 1262 (Littler et al., 2014) and cGENIE model output in Exp.6. (a) ODP Site 1262, benthic $\delta^{18}O$ (negative temperature) versus benthic $\delta^{13}C$. (b) cGENIE model, benthic negative temperature versus benthic $\delta^{13}C$. (c) ODP Site 1262, benthic $\delta^{18}O$ (negative temperature) versus iron (Fe) counts (negative $CaCO_3$). (d) cGENIE model, benthic negative temperature versus negative benthic $CaCO_3$. Linear trend lines indicated by the red line.

tricity maxima. For instance, Griffith et al. (2021) show that while surface export increases during Eocene hyperthermals, the burial of marine C_{org} is reduced in open ocean settings as metabolic rates of bacteria that break down C_{org} increase with temperature. This feedback reduces open ocean burial of C_{org}, slightly lowers $\delta^{13}C$, and increases $p\mathrm{CO}_2$, providing a positive feedback mechanism but it is unlikely that such temperature dependent remineralization processes largely affect C_{org} burial rates in the neritic zone where the overwhelming majority of marine organic matter burial occurs. In the cGENIE simulations presented here, about 86% of C_{org} burial accumulates on the shelves and only 14% in deep ocean sediments. C_{org} accumulation rates in neritic environments vary more strongly in response to astronomically forced changes in redox conditions and/or nutrient availability that controls surface export production (Kuypers et al., 2004). The enhanced supply of nutrients via weathering during periods of warmth will lead to increased export production, expanded oxygen minimum zones, and elevated marine organic matter accumulation (Poulton et al., 2015; Ruvalcaba Baroni et al., 2020), similar to what we find in Exp.6.

In-phase δ^{18}O-δ^{13}C relationships similar to those in the early Cenozoic have been identified across the Oligocene and Miocene (Palike et al., 2006; Holbourn, Kuhnt, Schulz, Flores, & Andersen, 2007). It has been proposed that during this time interval, the burial ratio of CaCO_3 to C_{org} increases at eccentricity maxima as a result of enhanced nutrient input to the shelves, thereby promoting preservation of shallow marine CaCO_3 at the expense of C_{org}, and lowering ocean $\delta^{13}C$ (Holbourn et al., 2007; Ma et al., 2011). While reefal CaCO_3 deposits are not simulated in our study, the ratio of CaCO_3 to C_{org} burial does increase during eccentricity maxima but the mean global burial rates of CaCO_3 as well

as C_{org} are elevated overall. However, the enhanced removal of relatively isotopically heavy $CaCO_3$ is roughly balanced by the enhanced input of weathered $CaCO_3$ of similar isotopic signature so it does not majorly impact the global δ^{13}C (Figure 4.2). Only the enhanced removal of isotopically light marine C_{org} during eccentricity maxima affects the global δ^{13}C, driving a positive δ^{13}C excursion during warm intervals (Figure 4.4).

Other feedbacks that have been proposed to contribute to the Paleocene-Eocene climate-carbon cycling include methane hydrate dynamics (Dickens, 2003; Lunt et al., 2011) and terrestrial feedbacks such as temperature dependent terrestrial soil respiration (Kirtland Turner, 2014; Honegger et al., 2020), wet-dry cycles and their influence on carbon stored in wetlands (Zachos et al., 2010; Zeebe et al., 2017), and high-latitude permafrost growth-thaw cycles (DeConto et al., 2012), though the occurrence of extensive methane hydrate and permafrost formation may be unlikely during the warm greenhouse climate state of the early Cenozoic (Buffett & Archer, 2004; Sluijs et al., 2009; Eberle et al., 2010). Additional Earth system model experiments that simulate the response of the methane cycle and terrestrial carbon storage to astronomical forcing are required to determine whether these feedbacks are able to reduce the $\delta^{13}C$ of DIC and $CaCO_3$ preservation during warm intervals driven by eccentricity forcing. The potential carbon release from these feedbacks needs to be sufficiently high to counteract (and exceed) the impact of weathering on wt% $CaCO_3$ to initiate carbonate dissolution during periods of global warming. Likewise, the carbon release needs to be sufficiently high to overrule the impact of marine C_{org} burial on $\delta^{13}C$. In Exp.6, the excess C_{org} burial across 50 kyr of eccentricity maxima is about 7,000 Pg C. This implies that the carbon input from other sources needs to: (1) be greater

than 7,000 Pg C, (2) have a much lighter isotopic signature than marine C_{org}, and/or (3) be released more rapidly than marine C_{org} is buried across intervals of maximum eccentricity.

4.4 Conclusion

We have simulated the transient impact of astronomical forcing on climate and the marine organic carbon and phosphorus cycle using a dynamic 3D carbon-enabled Earth system model configured under greenhouse (ice-free) conditions. Particularly eccentricity cycles control the annual global mean surface temperatures with direct consequences for the terrestrial weathering rates of bicarbonate and nutrients—the primary controls on (in)organic carbon and P cycle dynamics. During eccentricity maxima, global temperatures are elevated by about 1°C and terrestrial weathering rates of alkaline carbon species and P increase. The enhanced supply of bicarbonate and nutrients via runoff in tandem with the elevated global temperatures promote the export production and burial rates of $CaCO_3$ and C_{org}, thereby removing isotopically light carbon from the ocean-atmosphere system. The 100 kyr and 405 kyr eccentricity cycles are prominently present in the astronomically forced marine burial rates, yet, 100 kyr frequencies are removed from the resulting variations in pCO_2 and $\delta^{13}C$ of DIC by the low-pass filtering effects of the ocean carbon and P reservoir. The 405 kyr eccentricity maxima coincide with reduced pCO_2, and higher oceanic $\delta^{13}C$ and wt% $CaCO_3$ in our simulations including C_{org} burial and P feedbacks. These results are inconsistent with the in-phase relationships of δ^{18}O-δ^{13}C-$CaCO_3$ recorded in for instance early Cenozoic paleoceanographic records, suggesting that additional feedbacks other than those tested here, likely related to the terrestrial carbon cycle, are needed

to fully explain the dominant climate-carbon cycle dynamics on astronomical timescales during ice-free greenhouse climate states.

Chapter 5

System Architecture and Planetary Obliquity: Implications for Long-Term Habitability

Abstract - In the search for life beyond our Solar system, attention should be focused on those planets that have the potential to maintain habitable conditions over the prolonged periods of time needed for the emergence and expansion of life as we know it. The observable planetary architecture is one of the determinants for long-term habitability as it controls the orbital evolution and ultimately the stellar fluxes received by the planet. With an ensemble of n-body simulations and obliquity models of hypothetical planetary systems, we demonstrate that the amplitude and period of eccentricity, obliquity, and precession cycles of an Earth-like planet are sensitive to the orbital characteristics of a giant companion planet. A series of transient, ocean-coupled climate simulations show how these

characteristics of astronomical cycles are decisive for the evolving surface conditions and long-term fractional habitability relative to the modern Earth. The habitability of Earth-like planets increases with the eccentricity of a Jupiter-like companion, provided that the mean obliquity is sufficiently low to maintain temperate temperatures over large parts of its surface throughout the orbital year. A giant companion closer in results in shorter eccentricity cycles of an Earth-like planet but longer, high-amplitude, obliquity cycles. The period and amplitude of obliquity cycles can be estimated to first order from the orbital pathways calculated by the n-body simulations. In the majority of simulations, obliquity amplitude relates directly to the orbital inclination whereas the period of obliquity cycles is a function of nodal precession and the proximity of a giant companion.

5.1 Introduction

A wide range of factors determine whether or not an exoplanet may be considered habitable (Horner & Jones, 2010; Cockell et al., 2016), although observational constraints often limit us to applying the 'Habitable Zone' (HZ) concept to evaluate planetary habitability. The HZ describes the region around a star in which an Earth-sized planet can theoretically host liquid surface water based on assumptions about the atmospheric properties and the incident stellar flux. One of the great advantages of the HZ concept is that the luminosity of a host star and the semi-major axis of an exoplanet, that both control the stellar flux, can typically be well constrained by observation (Marcy et al., 2005), allowing the HZ status of a given planet to be quickly and easily assessed.

However, it is crucial to take the temporal evolution of those variables into consideration when assessing a planet's long-term habitability potential (Menou & Tabachnik, 2003; Spiegel et al., 2010; Meadows & Barnes, 2018; Truitt et al., 2020). In terms of planet habitability, attention should be focused on those planets that are likely to maintain temperate conditions over the prolonged periods of time relevant for the emergence and expansion of life as we know it. This requires a detailed investigation of the dynamic evolution of the planetary system. For instance, the luminosity of stars slowly increase during their time on the "main sequence" phase, e.g. the Sun's luminosity increased by at least 30% over the last four billion years (Feulner, 2012). The HZ slowly moves outward on billion-year timescales as the stellar luminosity evolves (Rushby et al., 2013; Truitt et al., 2020).

The star-planet distance varies on much shorter timescales, particularly for planets on eccentric orbits. Eccentric planets experience great changes in the stellar flux as the planet moves along its orbit around the star (Spiegel et al., 2010; Dressing et al., 2010; Linsenmeier et al., 2015) and, in the most extreme cases, planets could leave and re-enter the traditional HZ through the course of an orbital year (Kane & Gelino, 2012; Williams & Pollard, 2002; Bolmont et al., 2016). Whilst temporarily leaving the HZ does not necessarily make a planet inhospitable (Dressing et al., 2010), the stellar flux variability that results from such eccentric orbits will have consequences for the prevalent surface climate conditions that should be evaluated and quantified.

The distribution of the incoming stellar flux is a function of 1) the rotation rate, i.e. daytime vs nighttime duration, 2) the tilt (obliquity) of a planet's rotational axis relative to the star, and 3) the orientation (precession) of the axial tilt during a given time

of year (Milankovitch, 1941; Berger, 1978; Dobrovolskis, 2013; Linsenmeier et al., 2015). Hemispheric differences in the incident stellar flux arise from precession. On eccentric planets, the hemisphere pointing to the star during perihelion receives greater stellar flux in summer than the other. Obliquity regulates the seasonal intensity as the axial tilt controls the stellar flux at a given latitude throughout the orbital year. The influence of obliquity can dominate over the influence of eccentricity depending on the degree of tilt and orbital ellipticity (Kane & Torres, 2017). Ultimately, eccentricity in tandem with obliquity and precession control the incoming stellar flux and regulate the spatiotemporal surface conditions. Several studies have demonstrated the impact of obliquity on surface climate (Spiegel et al., 2009; Ferreira et al., 2014; Linsenmeier et al., 2015; Kilic et al., 2017; Colose et al., 2019) and found that multiple stable climate states (ice-free, partially ice-covered, fully ice-covered) can exists under a range of obliquity values, assuming Earth-like atmospheric composition and rotation rates (Kilic et al., 2017). Yet, obliquity and precession are often ignored when assessing planetary habitability potential because these astronomical parameters are unattainable with the current observational technology (Gaidos & Williams, 2004).

An additional complication comes from the fact that planets are rarely solitary. Gravitational interactions between planets drive cyclic variations in orbital eccentricity and inclination on timescales of thousands to millions of years that, in turn, perturb the axial obliquity and precession (Kinoshita, 1977; Laskar, Joutel, & Boudin, 1993; Atobe et al., 2004). The extremity and duration of these quasi-periodic orbital and rotational cycles control the surface conditions and can significantly influence the potential habitability of a

planet in the long-term (Spiegel et al., 2010; Armstrong et al., 2014; Way & Georgakarakos, 2017; Deitrick, Barnes, Bitz, et al., 2018). For Earth, variations in its orbital eccentricity, mainly induced by Jupiter's gravitational influence, are relatively small ($\sim$5%) (Laskar, Joutel, & Boudin, 1993). Nonetheless, those modest variations in combination with obliquity and precession dynamics, have regulated the growth and retreat of polar ice caps across the Quaternary glacial-interglacial cycles. Large parts of the Earth's surface fortunately remained ice-free (i.e. habitable) even during the most extreme glacial cycles of the recent geologic past. Astronomical cycles on other HZ exoplanets may, however, be more extreme and cause those planets to experience variations in stellar flux of different magnitude and frequency that could repeatedly increase or decrease its habitability (Spiegel et al., 2010; Armstrong et al., 2014).

Despite the observational challenges that limit full characterization of HZ exoplanets and the planetary architecture of their host systems, the use of n-body simulations in combination with obliquity and climate models can help to identify the HZ planets with the greatest long-term habitability potential. N-body simulations are now regularly used to evaluate the dynamical stability of planetary systems, refine orbital parameters, and reconstruct the orbital evolution of newly discovered exoplanets on timescales of millions of years (Marshall et al., 2010, 2020; Horner et al., 2011, 2019; Matsumura et al., 2013; Tóth & Nagy, 2014; Agnew et al., 2019; Kane et al., 2021). An obvious extension of such modelling is to apply the orbital results to obliquity models to calculate a range of possible obliquity solutions based on assumptions about the planetary characteristics (Shan & Li, 2018; Quarles et al., 2020, 2022). Finally, the eccentricity, obliquity, and precession param-

eters can be applied to climate models to simulate the long-term climate cycles of the given planet. This sequential methodology has been applied to both hypothetical (Armstrong et al., 2014) and observed (Shields et al., 2016; Quarles et al., 2020, 2022) planetary systems.

The simplest simulations of exoplanet climates feature steady state scenarios that generate surface climate conditions under a fixed astronomical configuration, providing first order estimates of how surface climate conditions might change with astronomical forcing (Williams & Pollard, 2003; Spiegel et al., 2009; Dressing et al., 2010; Dobrovolskis, 2013; Ferreira et al., 2014; Linsenmeier et al., 2015; Wang et al., 2016; Kilic et al., 2017; Kang, 2019). However, climate systems do not transition instantaneously from one stable state into another, but instead experience some form of climate inertia and require time to adjust to new conditions. Slowly responding ice sheets, vast ocean basins with a large heat capacity, or slow (bio)geochemical processes can make climate systems resistant to rapid changes in the radiative energy balance. Transient climate simulations that include processes contributing to climate inertia are therefore necessary to study the long-term astronomical climate evolution that results from the dynamical evolution of a planetary system (Spiegel et al., 2010; Armstrong et al., 2014; Way & Georgakarakos, 2017; Deitrick, Barnes, Quinn, et al., 2018; Georgakarakos et al., 2018).

In this study, we use a n-body ensemble of hypothetical planetary systems (Horner et al., 2020) and apply obliquity calculations to investigate the extent to which planetary architecture influences the long-term dynamical evolution of an Earth-like planet in the HZ. Transient ocean-coupled climate models, with the three astronomical parameters varying simultaneously, are applied to a subset of these across the million-year timescale relevant for

the evolutionary development of life, to evaluate their impact on the long-term habitability potential.

The methods are outlined in Section 5.2. Our results are presented in Section 5.3, following which, we discuss the implications for the long-term climate evolution and habitability in Section 5.4. Two parameters important for the reconstruction of obliquity cycles, but uncertain for most HZ planets in other exoplanet systems, are the dynamical ellipticity and tidal torques. Their impact on spin dynamics are addressed in Section 5.5 before summarizing our main findings in Section 5.6.

5.2 Methods

To illustrate to what extent planetary architecture and orbital dynamics influence the long-term habitability potential of planets in the Habitable Zone, we use an ensemble of pre-existing hypothetical planetary systems very similar to our own Solar system (Horner et al., 2020). The planetary architecture is modified to create hypothetical systems via systematic changes to the initial orbital characteristics of the Jupiter-mass planet. The resulting orbital evolution of the Earth-like planet is recorded and used as input to the obliquity model to calculate its obliquity and precession cycles. Finally, transient climate simulations are carried out to estimate the impact of the eccentricity, obliquity, and precession on the surface climate. The results are reported in terms of areal sea ice extent and fractional habitability (as per Spiegel et al. (2009)), allowing us to assess the impact of planetary architecture on the long-term habitability potential. For direct comparability between the habitability potential of our planet in its current state and that of an Earth-like

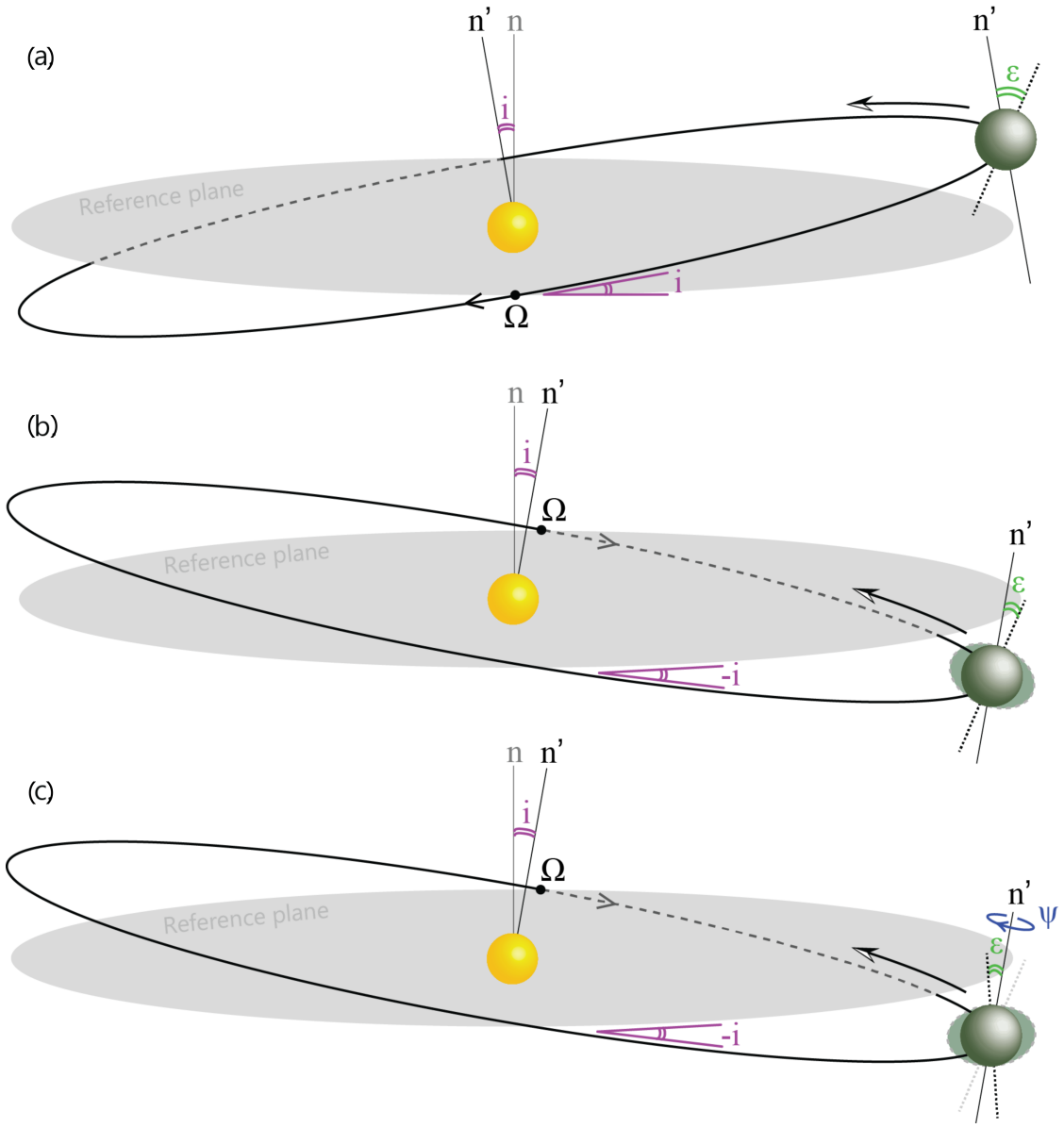

Figure 5.1: Schematic depiction of the impact of nodal precession Ω on the obliquity ϵ of a planet. (a) The orbit is tilted i° relative to the reference plane with orbital normal n. The Northern Hemisphere of the planet is tilted away during a given time of year with an angle ϵ between the rotational axis and the orbit normal n'. (b) The nodal precession has rotated the orbital plane 180° and the orbit is tilted -i° relative to the reference plane. If the rotational axis would remain fixed relative to the fixed background stars, the new obliquity is $\epsilon - 2i$. (c) However, solar and lunar torques pull the equatorial bulge toward the solar and lunar planes, driving precession of the rotational axis while affecting the obliquity

planet in a planetary system with a different architecture, we adopt Earth-like parameter values in the obliquity and climate models.

5.2.1 Dynamical *n*-Body Simulations

A detailed description of the n-body framework is provided in (Horner et al., 2020). In summary, an extensive suite of n-body simulations was carried out using the Hybrid integrator within the *Mercury* software (Chambers, 1999). The software was modified to take account of first-order post-Newtonian corrections (Gilmore & Ross, 2008) to ensure that the orbital evolution of the planet Mercury, and its resulting perturbations on the other planets, is accurately described. The ensemble consists of 159,201 individual hypothetical ('alternative Solar system') simulations in which the initial orbits of Mercury, Venus, Earth, Mars, Saturn, Uranus, and Neptune were consistent with the modern Solar system configuration and Jupiter's initial orbit was altered. Our hypothetical systems are not tied to any prior planet formation modelling. Rather than presenting the final results of a planet formation process, they are instead used as theoretical test cases to illustrate how different planetary architectures would impact the orbital variability of an Earth-like planet - using the modern Earth as a convenient and well-studied example.

In the ensemble of 399×399 simulations, the initial Jupiter semi-major axis (a_J) ranges from 3.2 to 7.2 au, within the 3-10 au range of peak-frequency proposed for gas giants (Bryan et al., 2016). The initial eccentricity of Jupiter (e_J) ranges from 0.0 to 0.4, consistent with the observed range of eccentricities in multi-planet systems (Weiss et al., 2013; Motalebi et al., 2015; Van Eylen & Albrecht, 2015). It is likely that Jupiter-like planets at orbital radii less than 3.5 au would limit the formation of terrestrial planets

beyond 1 au, whilst a Jupiter as the inner most giant at greater than 10 au orbital radii would allow formation of additional planets beyond Mars' current semi-major axis and would thus likely result planetary architectures very different than our own Solar system (Nagasawa et al., 2007). Stable simulations were integrated over 10 Myr. Approximately 74% of the simulations were deemed unstable and terminated prematurely when any of the planets collided with the Sun, with each other, or reached a heliocentric distance of 40 au.

5.2.2 Obliquity Model

We use the spin dynamics model described in (Laskar, Joutel, & Boudin, 1993), based on the equations of the rigid-Earth theory (Kinoshita, 1977), to calculate the obliquity and climatic precession cycles of an Earth-like planet and their evolution over time (see Appendix and equations therein). The model is calibrated specifically to Earth for which the spin dynamics are, to the first order, controlled by orbital dynamics and tidal interaction with the Moon and the Sun (Ward, 1982; Laskar, Joutel, & Boudin, 1993; Laskar, Joutel, & Robutel, 1993; Williams, 1993; Neron de Surgy & Laskar, 1997; Waltham, 2015). Other planet dependent parameters, including Earth's angular momentum ($\nu = 2\pi\ 24\mathrm{h}^{-1}$) and dynamical ellipticity ($E_D = 0.00328$) are taken to be equal to the canonical values for the modern day Earth. An initial obliquity of $\epsilon_0 = 23.4^\circ$ is chosen to maintain consistency across all experiments, but we note that the solution of any obliquity model will be sensitive to the chosen initial conditions as shown in detail for a moonless Earth by (Lissauer et al., 2012). A sensitivity analysis is conducted to verify our results (see Appendix C).

The obliquity model is integrated for 10 Myr of which the last million years are simulated with the climate model. The relatively short integration time provides a lower

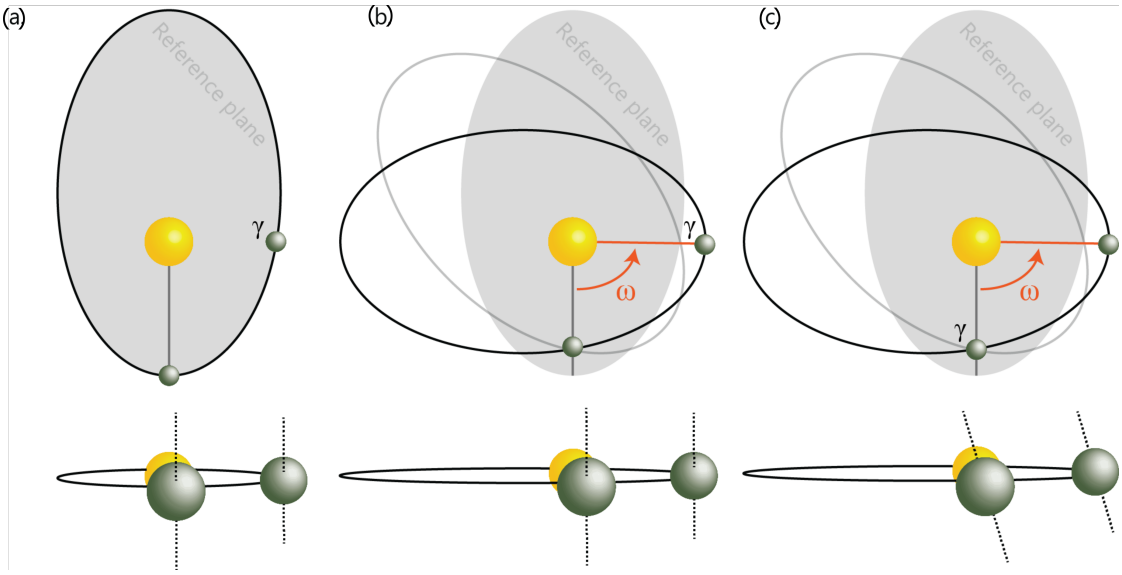

Figure 5.2: Schematic depiction of the impact of apsidal and axial precession on the planet's climatic precession. Upper panels show top-views. Bottom panels show side-views. (a) A planet on a plane of reference with the Southern Hemisphere tilted to the Star during perihelion and the position of the vernal equinox indicated with ϒ. (b) The orbit has rotated relative to the fixed background stars, a movement known as apsidal precession ω. If the rotational axis would remain fixed relative to the background stars, the vernal equinox now occurs during perihelion. (c) However, the planetary axis rotates over time so the location of the vernal equinox moves relative to the reference direction. The apsidal precession direction is opposite from the axial precession thus climatic precession cycles experienced by the planet are more rapid than the axial precession cycles.

estimate for the total range of obliquity variations. The total range of variation on 100 Myr-timescales likely differs by a few degrees (Lissauer et al., 2012). Planetary system chaos may induce a shift in the mean obliquity on Gyr timescales that we are unable to capture, however, when observing a planet and assessing its long-term habitability potential in search for life, the most recent past and future (±500 Myr) obliquity variations are most relevant.

A caveat of this obliquity model is that it does not account for any changes in the angular momentum of the Earth-Sun and Earth-Moon system. Angular momentum scales directly with eccentricity, and any major deviations in the orbital eccentricities of

the Earth and Moon may therefore impact the results. However, the model has previously been used to reconstruct the Earth's obliquity and precession cycles for the past 10 million years and beyond within reasonable error (Laskar, Joutel, & Boudin, 1993), and is expected to produce accurate results in >82% of simulations in which the angular momentum of the Earth-like planets is similar to that of the modern Earth (Figure 5.3b, blue-white shading). Hypothetical systems with more extreme eccentricity variations should be interpreted with caution as the deviation in angular momentum relative to its circular counterpart grows (Figure 5.3b, red shading) (Barnes & Quinn, 2004; Kane & Raymond, 2014).

A near circular orbit of the Moon is assumed in all simulations to allow for direct comparability with our Earth. Whilst studies have suggested potential higher lunar eccentricities during the early evolution of the Earth-Moon system (Touma & Wisdom, 1998), tidal dissipation has circularized the lunar orbit over time (Zahnle et al., 2015). Periodically elevated eccentricities of Earth may inject eccentricity into the lunar orbits that the model does not account for.

5.2.3 Obliquity-Precession Dynamics

Gravitational interactions between Earth and the other planets in the Solar system cause quasi-periodic variability in Earth's eccentricity e, orbital inclination i, the longitude of the ascending node Ω (the angle between a reference direction and the ascending node, measured in a reference plane), and the argument of perihelion ω (the angle between the ascending node and perihelion, measured in the orbital plane). Such orbital cycles directly translate into systematic perturbations of the climatic precession $e \sin \varpi$ and obliquity ϵ

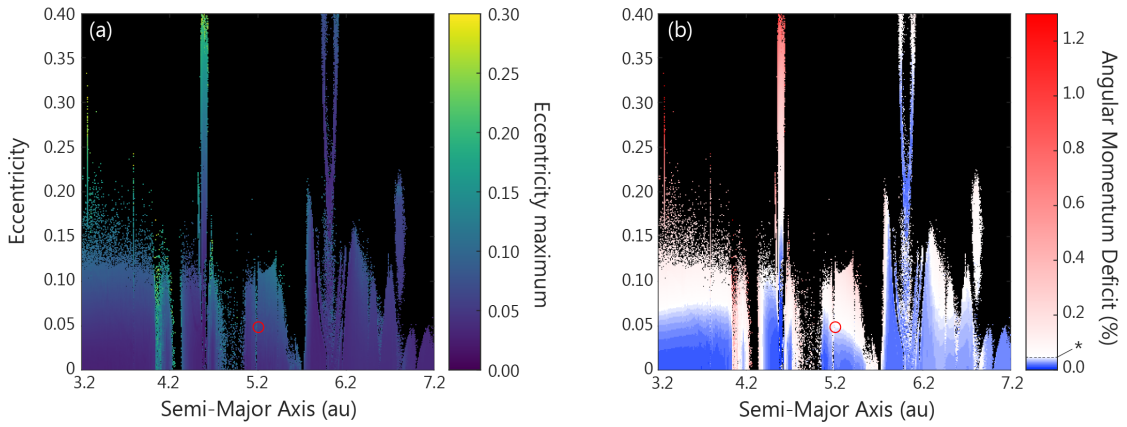

Figure 5.3: Maximum eccentricity and mean angular momentum deficit. (a) The maximum eccentricity of an Earth-like planet under different planetary architectures, i.e. with a Jupiter-like planet having different initial semi-major axes and eccentricity. (b) The percentage of deviation in angular momentum (AMD) relative to that of a circular orbit, calculated as the mean deviation across the 10 Myr integration time. Blue colors indicate AMDs less than the modern Earth, below 0.0477%. The red circle is the current position of Jupiter in our Solar system.

experienced by the Earth. To emphasize: inclination is defined throughout the text as the angle between the orbital plane and a reference plane whereas obliquity refers to the angle between the planetary orbit normal and the rotational axis (Figure 5.1).

Nodal precession describes the change in the orientation of the orbit normal relative to a reference plane. In other words, the tilt of the orbit relative to the fixed background stars changes over the course of a nodal precession cycle. A positive change reflects a clockwise motion when looking down at the system from above its north pole, as currently experienced by Earth. Planets in other systems can rotate anti-clockwise (negative change). To illustrate the effect of nodal precession on the planetary obliquity, assume for simplicity that the axial orientation remains fixed relative to the background stars. At t_0, Earth's obliquity is ϵ_0 (Figure 5.1a). After half a nodal precession cycle the orbital inclination has

rotated by 180°, and the axial obliquity would reduce by twice the orbital inclination angle ($\epsilon_0 - 2i$) (Figure 5.1b).

However, the Earth is markedly oblate as a result of its relatively fast rotation. The orientation of the planet's spin axis rotates when solar and lunar torques essentially pull the equatorial bulge toward the ecliptic. These forces have been proposed to stabilize the long term obliquity oscillations of our planet (Ward, 1982; Laskar, Joutel, & Robutel, 1993; Williams, 1993), although more recent work suggests that obliquity variations would still remain relatively sedate in absence of a large moon (Lissauer et al., 2012; Li & Batygin, 2014). Because the planet's rotational axis as well as the orbit normal both precess in a clockwise direction (top-down view), the location of the equinoxes rotate. The equinoxes are defined by the two locations in a planetary orbit where the Sun is positioned directly above the equator (Figure 5.1c). The nodal and axial precession of a planet combine to drive the axial obliquity cycles relative to the orbital plane. The full equations are shown in Appendix C. To first order, the period of obliquity cycles can be approximated by:

$$\frac{1}{P_\psi} - \frac{1}{P_\Omega} = \frac{1}{P_\epsilon} \tag{5.1}$$

where P_ψ and P_Ω are the periods of axial and nodal precession, respectively. P_ϵ is the resulting period of the axial obliquity cycle. For the modern Earth (in yr),

$$\frac{1}{25,700} - \frac{1}{68,000} \approx \frac{1}{41,000}$$

Apsidal precession describes the rotation of the orbital plane of a planet relative to the fixed background stars and, together with axial precession, determines the period of the climatic precession cycles (Figure 5.2). The climatic precession ϖ is the change in the angle between the moving vernal equinox and perihelion, modulated by the orbital eccentricity following $e \sin \varpi$. When the orientation of the orbital plane is fixed, the vernal equinox rotates (clockwise) with an angular velocity equal to the axial precession (Figure 5.2b). However, the orbital plane also rotates over time, in the opposite direction for modern Earth, and thus the vernal equinox occurs slightly earlier (Figure 5.2c). The full equations are shown in Appendix C. To first order, the period of climatic precession cycles can be approximated by:

$$\frac{1}{P_\psi} - \frac{1}{P_\omega} = \frac{1}{P_\varpi} \tag{5.2}$$

where P_ω and is the period of apsidal precession, and P_ϖ is the resulting period of the climatic precession cycle. For the modern Earth (in yr),

$$\frac{1}{25,700} - \frac{1}{-303,000} \approx \frac{1}{23,000}$$

5.2.4 Atmosphere-Ocean-Sea Ice Model

The simultaneous impact of the alternate eccentricity, obliquity, and climatic precession cycles on the surface temperature and sea ice extent are simulated with the GENIE Earth system model comprised of a coupled 2D Energy Moisture Balance Model (EMBM), 3D frictional geostrophic ocean model (Edwards & Marsh, 2005; Marsh et al., 2011), and

a thermodynamic sea ice model (Weaver et al., 2001). The model, coupled to models of atmospheric chemistry and marine biogeochemistry, has previously been used to successfully simulate recent glacial and interglacial conditions (Marsh et al., 2006; Ma & Tian, 2014; Kemppinen et al., 2019), to reconstruct a wide variety of other paleoclimate states throughout Earth's geologic history (Donnadieu et al., 2006; Meyer et al., 2008; Panchuk et al., 2008; Crichton et al., 2020), for comparison between steady state and transient runs (Lunt et al., 2006), and to simulate changing surface conditions over a multi-million-year timescale in response to astronomical forcing (Vervoort et al., 2021).

Heat exchange between the ocean, sea ice, atmosphere, and the continents is balanced by incoming short wave radiation, sensible and latent heat fluxes, and outgoing long wave radiation calculated from the atmospheric relative humidity and greenhouse gas concentrations (Edwards & Marsh, 2005). We use a seasonally resolved set-up with 96 time steps per year and apply the modern solar constant of 1368 Wm^{-2}. The distribution of the incoming radiation is calculated directly from the astronomical parameters (Berger, 1978), which are specified in 1000 year intervals. The incoming short wave radiation is also a function of the prescribed surface albedo and temperature-dependent sea ice albedo. Atmospheric heat diffusivity is given by an exponential function that includes latitude as an input variable (Edwards & Marsh, 2005). Sea ice growth rates are calculated from the ice thickness, areal fraction, heat fluxes from the overlying atmosphere and underlying ocean, the density for water and ice, and the latent heat of fusion of ice (Weaver et al., 2001).

For the purpose of this study, and to facilitate direct comparison with the present-day Earth, we adopt a planetary rotation rate of 2π $24\mathrm{h}^{-1}$ and use a continental distribution

similar to the Earth's modern configuration on a 36 by 36 equal-area grid (10° longitude and uniform in sine of latitude). Geostrophic ocean dynamics are simulated spatially and across eight vertical ocean depth levels with a maximum depth of 5000 meters. Atmospheric CO_2 concentrations are prescribed to 278 ppm to recreate preindustrial greenhouse gas forcing. When implementing modern (fixed) astronomical input parameters, the simulated global mean air temperature is about 13°C, and the sea ice area is approximately $10{\times}10^6$ km^2, consistent with the preindustrial surface of the Earth (Peng & Meier, 2018).

5.3 Results

The dynamical results of the hypothetical n-body systems are published in (Horner et al., 2020). To summarize, the ensemble shows that an eccentric Jupiter-mass planet in close proximity to an inner Earth-like planet results in more rapid eccentricity and inclination cycles of the Earth-like planet. Likewise, a Jupiter-mass planet that is located at greater heliocentric distance, or on a more circular orbit, drives low frequency orbital cycles of the Earth-like planet. The orbital parameters of this ensemble serve to generate the time series of climatic precession and obliquity used in this work. Multitaper method spectral analysis is applied using *Astrochron* (Meyers, 2014) to the output of the obliquity model to extract the period of the main spin cycles. For each of the stable simulations, the spectral peak with the highest significant power is identified and their frequencies converted to the respective period. The results are summarized in Figures 5.4 and 5.5.

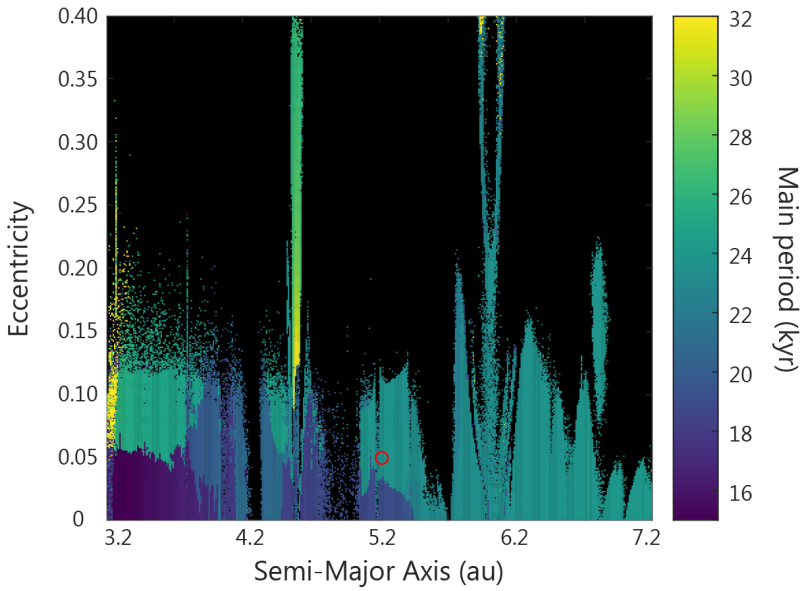

Figure 5.4: The period of the main climatic precession cycle of an Earth-like planet under different planetary architectures, i.e. with a Jupiter-like planet having different initial semi-major axes and eccentricity. Climatic precession is defined here as $e \sin \varpi$. The red circle indicates the current position of Jupiter in our Solar system.

5.3.1 Precession Cycles

The period of climatic precession cycles is sensitive to the architecture of a planetary system (Figure 5.4). In our ensemble of simulations, abrupt changes in the main period of precession cycles are attributed to a switch between the planet(s) with the strongest influence on the apsidal precession of the Earth-like planet.

Jupiter exerts a dominant control on the apsidal movement of Earth's orbit in our own Solar system, with a frequency g_5 of 4.3" yr^{-1}, or period $P_{\omega 5}$ of 303 kyr, resulting in climatic precession cycles with a period of 23 kyr (Equation 2). If the Jupiter-mass planet is instead located at a smaller heliocentric distance, its apsidal precession cycles accelerate, and the frequency g_5 decreases. Whilst the apsidal precession of an Earth-like planet inherits some of this signal by precessing at a lower frequency, the impact on the

climatic precession period is small, following Equation 5.2. When a Jupiter-mass planet is located between 3.2 and 5.3 au and has an eccentricity lower than approximately 0.05, the apsidal precession of Earth-like and Mars-like planets display resonant behaviour. The apsidal precession of the Earth-like planet varies rapidly with a frequency g_3 86.4" yr^{-1} (or period of 15 kyr) while the apsidal precession of a Mars-like planet is about twice as rapid, varying with a frequency g_4 178.7" yr^{-1} (or period of 7.3 kyr). The switch in the dominant resonant interaction is evident from the stark color transition that distinguishes dominant 24 kyr cycles driven by the Jupiter-mass planet from cycles with a period less than 17 kyr driven by the interaction between the Earth-like and Mars-like planets (Figure 5.4).

The climatic precession period exceeds 30 kyr when the Jupiter-mass planet is located near 3.2 au with an eccentricity greater than 0.05, or when the Jupiter-mass planet is located near 4.6 au with an eccentricity close to 0.15 (yellow areas in Figure 5.4). Longer precession cycles near 3.2 au result from the interaction between the apsidal precession of the Earth-like, Mars-like and Jupiter-like planets with g_5 1.82" yr^{-1}. When $a_J \approx 4.6$ au, the apsidal precession of the Earth-like, Venus-like, Jupiter-like, and Saturn-like planets are intimately connected, varying with frequency g_5 7.52" yr^{-1}.

5.3.2 Obliquity Cycles

The obliquity period is related to the nodal precession frequency. With a Jupiter-mass planet closer to the star, the nodal precession cycles of the inner Earth-like planet shorten, resulting in obliquity cycles of lower frequency because the nodal and axial precession both rotate in a clockwise direction (Equation 5.2, Figure 5.5, Figure C.2). The main

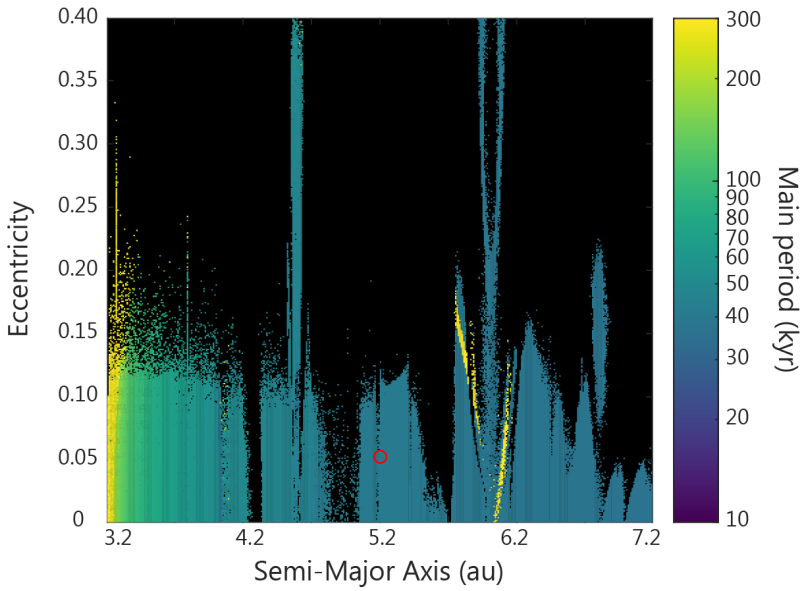

Figure 5.5: The period of the main obliquity cycle of an Earth-like planet plotted on a logarithmic scale, under different planetary architectures, i.e. with a Jupiter-like planet having different initial semi-major axes and eccentricity. The red circle indicates the current position of Jupiter in our Solar system.

axial obliquity cycles reach a period greater than 300 kyr when the Jupiter-mass planet is located near 3.2 au. Here, the nodal precession of the Earth-like and Mars-like planets display resonant behaviour with frequency s_3 of 43.03" yr^{-1} and frequency s_4 about twice as high. If the giant planet is positioned close to 6.1 au, the dominant obliquity cycles have a relatively low frequency. The orbital architecture of the planetary system here results in low amplitude 40 kyr obliquity cycles superimposed on chaotic, high amplitude cycles with a period greater than 1 Myr as a result of secular resonance between the Venus-like and Earth-like planet.

The frequency of obliquity (and climatic precession) cycles have a critical influence on the surface climate evolution via time dependent climatic processes (Spiegel et al., 2010; Armstrong et al., 2004; Deitrick, Barnes, Quinn, et al., 2018). However, the amplitude of the

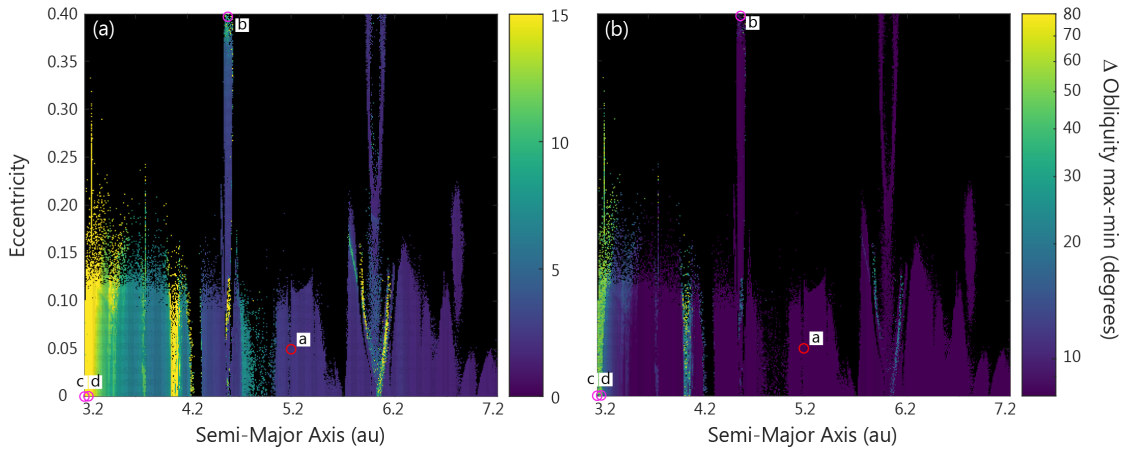

Figure 5.6: The maximum variation in the obliquity (in degrees) of an Earth-like planet, under different planetary architectures, i.e. presence of a Jupiter-like planet with different initial semi-major axes and eccentricity. Both panels display the same data on (a) linear and (b) logarithmic scales to distinguish between high and low amplitude variations. The red circle tagged 'a' indicates the current position of Jupiter in our Solar system. Pink circles tagged 'b', 'c', 'd' indicate simulations used for the reconstruction of surface climate conditions.

cycles are equally important from a climatological perspective. The amplitude determines the variation in the amount of stellar energy received at any given latitude, both on seasonal and astronomical timescales. In the majority of our simulations, the obliquity does not vary by more than 5° (Figure 5.6), consistent with the range of the simulated orbital inclinations (Horner et al., 2020). More extreme obliquity oscillations occur at $e_J = 4.1$ au, 4.5 au, and 4.7 au, where the high amplitude obliquity oscillations are the direct result of high amplitude oscillations in the orbital inclination. For instance, a 15° range in the orbital inclination translates to a $2 \times 15° \approx 30°$ range in the obliquity (Figure 5.1).

Some exceptionally high obliquity variations unrelated to orbital inclination are simulated when the Jupiter-mass planet is located at small semi-major axes (Figure 5.6 and 5.7a) and the period of a nodal precession cycle P_Ω is shorter than that of the axial

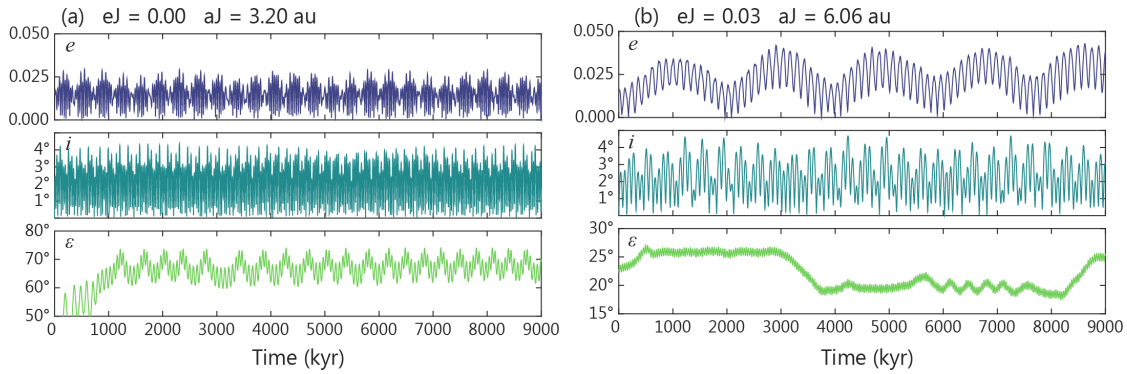

Figure 5.7: Eccentricity e, inclination i, and obliquity ϵ cycles over nine million years for two example Earth-like planets. (a) High obliquity Earth-like planet that varies with an amplitude greater than the amplitude of orbital inclination. (b) Chaotic behaviour in the obliquity cycles of an Earth-like planet. Note the different y-axis scale for the bottom panels.

precession cycle P_ψ (Equation 5.2). The frequency of the nodal precession of the Earth-like planet is high enough to excite the axial obliquity to angles greater than those associated with the orbital inclination (Horner et al., 2020). The resonant behaviour between the Venus-like and Earth-like planets excites the obliquity to values much greater than those of the orbital inclination in the region near 6.1 au (Figure 5.6). The obliquity evolution displays chaotic behaviour in these regions over the simulated timescales (Figure 5.7b).

5.3.3 Surface Climate Simulations

We select four examples to evaluate the impact of planetary architecture and orbital dynamics on the long-term climate conditions and habitability potential of an Earth-like planet. The four example cases, indicated in Figure 5.6, represent Earth-like planets that experience a wide range of orbital frequencies and amplitudes. Their calculated temporally-evolving eccentricity, precession, and obliquity parameters are applied to the

Earth system model to calculate the total amount and spatial distribution of incoming stellar radiation. The model is integrated for 1 Myr (Figure 5.8). Two variables of interest for the purpose of discussing the impact of planetary architectures on the long-term climate evolution and habitability are the surface temperature and the areal extent of (sea) ice. Seasonally resolved 3D model output is generated every 2500 years by averaging the surface temperature and sea ice extent across three-month intervals to evaluate the changing surface conditions over astronomical timescales and the seasonal contrast under different astronomical configurations. The method described by Spiegel et al. (2009) is adopted to calculate the annual global mean fractional habitability for each saved time interval in all four simulations. A grid cell is deemed habitable and assigned a value of 1 if the overlying air temperature lies between 0-100°C. Grid cells covered in sea ice and/or with an overlying air temperature below 0°C or above 100°C, are assigned a value of 0 and are considered inhospitable. The annual global mean fractional habitability is spatially averaged and the seasonal range in fractional habitability is shown in grey (Figure 5.8e).

First, we simulate the evolution of Earth's surface conditions in our own Solar system (Figure 5.8a). The annual mean sea ice extent is about 11×10^6 km^2 with minima during the Northern Hemisphere (NH) summer months of 4.5×10^6 km^2 and maxima during NH winters of 15×10^6 km^2 – consistent with observational satellite data (Peng & Meier, 2018). The extent of perennial (year-round) sea ice is largely controlled by the NH summer insolation driven by eccentricity-modulated precession forcing. Seasonal (winter) sea ice extends to an area about four times as large, and is less sensitive to precession and eccentricity. The amount of irradiation that reaches polar latitudes during winter is

minimal and partially controlled by the obliquity angle. Across the 1 Myr simulation, the annual mean fractional habitability varies only minimally. Approximately 75% of land area is considered habitable whereas the fractional habitability of the surface ocean is about 90% (Figure 5.8e), resulting in a weighted global mean fractional habitability of 85%. This value is identical to that of the fractional habitability inferred from the 2004 NCEP/NCAR temperature reconstructions (Spiegel et al., 2009).

The second example demonstrates the climatic effect of relatively short period and high amplitude eccentricity and precession cycles using a simulation with a Jupiter-mass planet located at 4.65 au and an eccentricity of 0.40. The two main eccentricity cycles experienced by the Earth-like planet have periods of 50 and 100 kyr varying over a total range of 0.2. Precession cycles have a 25 kyr period (Figure 5.4). The extent of seasonal sea ice is directly controlled by eccentricity forcing. A more eccentric orbit results in elevated global mean temperatures and reduced polar sea ice, particularly during the NH summer months. The extent of perennial sea ice varies more rapidly with precession forcing modulated by the eccentricity (Figure 5.8b). The low obliquity angle minimizes seasonal contrast and allows for a relatively greater maximum extent of perennial sea ice (13×10^6 km^2) when the NH is tilted toward the star during aphelion, regardless of the orbital eccentricity of the Earth-like planet at the time. Despite the greater annual mean extent of sea ice in this simulation compared to that of the modern Earth, the fractional habitability of the surface ocean is greater (Figure 5.8e). For the Earth-like planets in this study, the fractional habitability is determined mainly by the lower 0°C limit rather than the upper 100°C limit. Even at high eccentricity, the thermal inertia of the ocean maintains

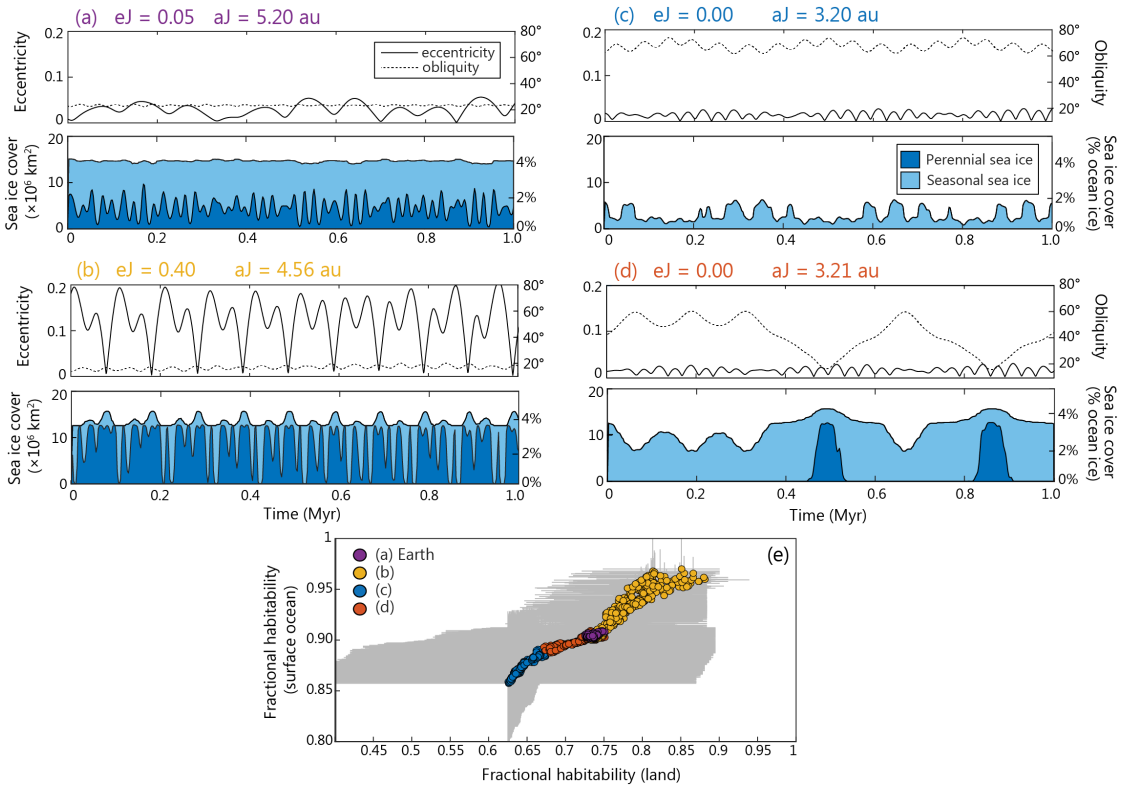

Figure 5.8: Sea ice extent and fractional habitability on an Earth-like planet for four exemplar dynamically stable planetary systems. (a) Current Earth with Jupiter eccentricity e_J=0.05 and Jupiter semi-major axis a_J=5.20 au. (b) Highly eccentric Jupiter-mass planet e_J=0.40 and a_J=4.56 au. (c) Close-in Jupiter-mass planet with circular orbit e_J=0.00 and a_J=3.20 au. (d) Close-in Jupiter-mass planet with circular orbit e_J=0.00 and a_J=3.21 au. Eccentricity (solid) and obliquity (dashed) over time in the upper panels. The areal extent of perennial (year-round) and seasonal sea ice (in 10^6 km^2 and % ocean area covered in ice) in the lower panels. (e) The annual mean fractional habitability over land versus ocean for each 2,500-year time interval of the four Earth-like planets. The grey area indicates the seasonal range in fractional habitability over land and ocean.

temperatures well below 100°C. However, large parts of the sea ice-free Southern Ocean that experience subzero temperatures on the modern Earth reach temperatures above 0°C when the eccentricity is higher and obliquity lower. This raises the fractional habitability. The fractional habitability over land is also higher compared to the modern Earth simulation because the annual global mean stellar energy received at the top of the atmosphere increases with eccentricity, resulting in higher overall temperatures and a reduced extent of regions with temperatures below 0°C. This scenario has the smallest seasonal range in fractional habitability due to the low obliquity (Figure 5.8e).

The smallest areal extent of sea ice is simulated in the third scenario, where a Jupiter-mass planet is positioned at 3.20 au. The mean obliquity angle across the 1 Myr simulation is approximately 70° (Figure 5.8c). All sea ice melts during summer but winter temperatures drop below freezing, facilitating the production of seasonal sea ice with a maximum area of 7×10^6 km^2 when the obliquity angle is smallest. The fractional habitability over land and ocean is much reduced compared to Earth today (Figure 5.8e) because the extreme obliquity drives winter temperatures below 0°C across a wide range of latitudes. The minimum fractional habitability over land and ocean is 37% and 80%, respectively.

High amplitude variations in the obliquity angle occur when a Jupiter-mass planet is located at 3.21 au (Figure 5.8d). The ∼60° obliquity angle prevents the formation and preservation of sea ice throughout the summer months so sea ice is only present during winter in the first 400 kyr. When the obliquity falls below ∼30°, the polar summer insolation becomes sufficiently low to preserve perennial sea ice. In this scenario, the eccentricity variations in the orbit of the Earth-like planet are too small to exert a notable effect on

the surface conditions. The mean fractional habitability is slightly lower than that of our Earth due to the periodically high obliquity and extreme seasonality that cause an increase in the area experiencing sub-freezing temperatures during winter (Figure 5.8e).

A recurring feature in all simulations is that the fractional habitability over the surface ocean is typically greater than over land. The large heat capacity of the ocean helps to maintain relatively warm temperatures throughout the winter and mutes seasonal variability. In addition to the transient simulations, two steady state runs were carried out for each of the four examples, with fixed astronomical parameters corresponding to certain time intervals. Steady state simulations were run for a total of 20 kyr to ensure equilibrium surface conditions. By comparing the steady state to transient conditions at corresponding time intervals, we quantify the degree to which time dependent climate processes respond to varying astronomical forcing. In all examples, the differences between the transient snapshots and steady state simulations are small (Figure 5.9). The annual global mean air temperature does not differ by more than 0.08°C while the areal sea ice extent in steady state simulations does not deviate more than 1.2% from that simulated in transient runs.

However, differences between the transient versus steady state conditions should be considered a minimum. The only processes providing climatic inertia in our climate model set-up are sea ice growth and deep ocean circulation that also control the model equilibrium timescale. Inclusion of additional slowly responding components of the Earth system, such as land-based ice or much larger ocean volume, could drive greater differences between transient and steady state experiments. Our results are consistent with the comparison

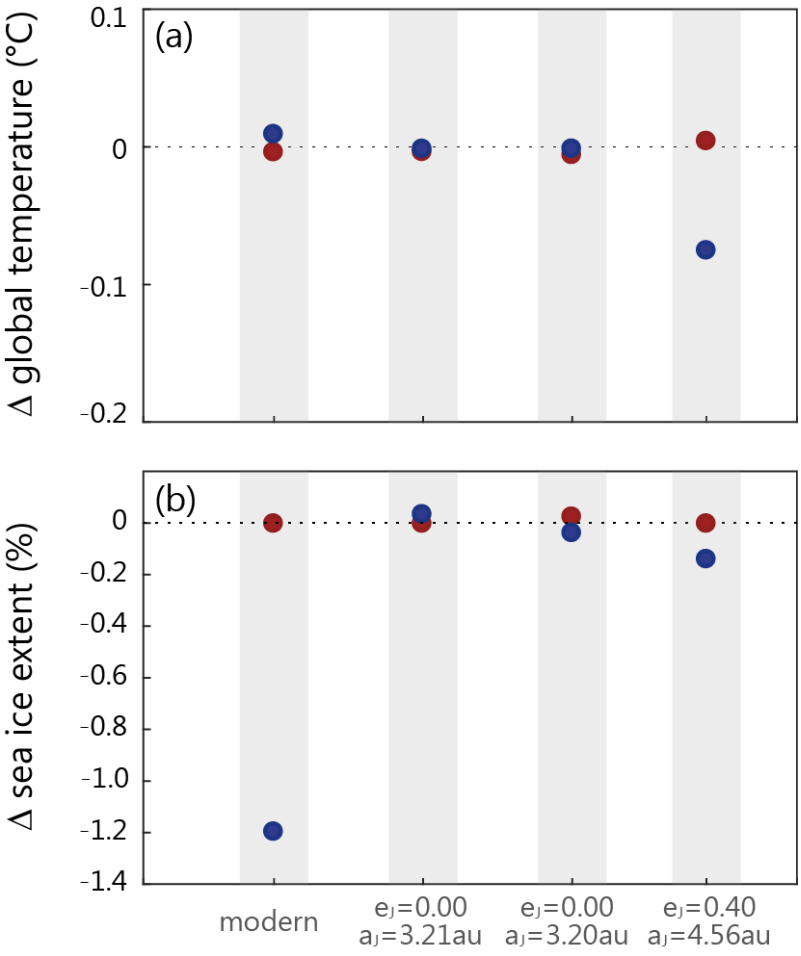

Figure 5.9: The difference in (a) the annual global mean air temperature (in °C) and (b) the annual mean sea ice extent (in %) between eight steady state runs and transient snapshots corresponding to the four examples in Figure 5.8

made in Lunt et al. (2006), who found good agreement between equilibrium and transient simulations in the ocean-atmosphere system.

5.4 Implications for Long-Term Habitability Potential

Geological archives on Earth contain ample evidence that small variations in astronomical forcing contribute to global climate variations, most famously the extensive glacial-interglacial cycles of the Quaternary period linked to the gravitational dynamics between Jupiter and the inner terrestrial planets (Milankovitch, 1941; Hays et al., 1976; Imbrie et al., 1992). This leads us to wonder about the impact of astronomical cycles on surface climate variability and habitability in planetary systems with different architectures. Our n-body, obliquity, and million-year-long climate simulations suggest that extreme eccentricity cycles, such as those in systems with a highly eccentric giant companion planet, increase the fractional habitability (Figure 5.8e) while also preventing global freezing of planets at the outer edge of the HZ (Spiegel et al., 2010; Dressing et al., 2010). In contrast, extreme obliquity variations such as those in systems with a giant planet closer inward (Figure 5.8cd) can also expand the outer edge of the HZ (Armstrong et al., 2014) but simultaneously reduce the fractional habitability (Figure 5.8e) as a greater surface area experiences extremely cold or hot temperatures when the planet is (temporarily) highly tilted relative to the orbital plane. Hence, to assess the long-term habitability of a planet, eccentricity variations should ideally be considered in tandem with potential obliquity (and precession) cycles.

In none of the examples does the fractional habitability drop to zero, implying that the surface remains at least partially habitable during the four 1 Myr simulated intervals.

It should, however, be noted that the variability simulated here is likely an underestimation for the following reasons. First, our model lacks continental ice sheets and snow coverage, and only simulates thermodynamically formed sea ice. To account for the missing albedo effect of land-based ice and snow, we imposed a fixed albedo over the polar latitudes, thereby omitting any snow and ice-albedo feedbacks over land that might alter the climate response to astronomical forcing. It is not necessarily obvious that land-based ice and sea ice respond similarly to astronomical forcing. Continental snow and ice caps have a higher albedo (Perovich et al., 1986; Key et al., 2001), thereby making them more resilient against melting and able to grow more rapidly. In addition, the wavelengths at which these surfaces reflect (Joshi & Haberle, 2012; Shields et al., 2013) and their dynamical controls (Pollard, 1978; Weaver et al., 2001) are different from sea ice. Continental ice/snow volume is driven mainly by atmospheric conditions and internal feedbacks but sea ice volume is additionally driven by the thermodynamics of the underlying ocean. What this implies for the rate at which ice sheets respond to isolation forcing remains uncertain (Bamber et al., 2007).

Secondly, a greater climate sensitivity to astronomical forcing can result from additional (positive) feedbacks related to physical, chemical, and biological processes. For example, during glacial-interglacial intervals, the cycling and storage of carbon in the ocean and atmosphere changed in response to astronomical forcing. During cold glacials, more carbon is stored in the ocean and less carbon resides in the atmosphere, which subsequently lowers the CO_2 radiative forcing and thereby cools global climate further (Sigman & Boyle, 2000; Kohfeld & Ridgwell, 2009). Such positive feedback loops amplify the astronomical climate variability though negative feedbacks also exist. The net impact is uncertain on

exoplanets that likely experience physical, chemical, and potentially biological processes of different magnitudes and timescales.

Finally, the simplified physics in the atmosphere model likely reduces the simulated astronomical climate variability, particularly when considering the impact of astronomical cycles that deviate notably from the modern Earth in both amplitude and frequency. For instance, the obliquity angle has great control over the meridional heat transport (Spiegel et al., 2009; Ferreira et al., 2014; Linsenmeier et al., 2015; Kilic et al., 2017). Whilst our model accounts for diffusive atmospheric and oceanic heat transport, the wind patterns (affecting sensible heat and moisture transport) are fixed and unresponsive to astronomical forcing. When obliquity reaches a critical threshold of 54°, the polar regions receive more insolation than the equatorial regions on an annual mean basis and thus heat is net transported from the high to low latitudes which would cause a dramatic reorganization of atmospheric dynamics (Williams & Pollard, 2003; Ferreira et al., 2014; Linsenmeier et al., 2015). Likewise, we do not account for changes in the cloud coverage and cloud feedbacks. Both could behave very differently on planets spinning at highly oblique angles (Kang, 2019).

Whilst considering the above caveats, the surface climate remains habitable in all four examples, with temperate conditions and a large ice-free area across the 1 Myr simulation time. In the context of habitability and the ability of any life forms to survive at the surface, we must also consider the interannual variability. The most extreme three-month average seasonal contrast (∼80°C) occurs above land under the highest obliquity angles, compared to a maximum seasonal contrast of ∼38°C in the simulation most comparable to the modern Earth. Studies of the impact of climate change on ectotherms have shown that

species living at the highest latitudes on Earth are generally more resilient to temperature fluctuations as they evolved to have a broader thermal tolerance to survive seasonal temperature fluctuations (Addo-Bediako et al., 2000; Deutsch et al., 2008). A high seasonal temperature contrast is thus not necessarily deleterious for life as we know it. However, organisms that evolved under moderate seasonal temperature fluctuation (such as those living in tropical regions on Earth) have a much narrower thermal tolerance range and are much more susceptible to change (Deutsch et al., 2008). This may pose a problem in the fourth example scenario (Figure 5.8d) when the obliquity angle fluctuates dramatically and thereby surface conditions experience cycles of sedate-to-extreme seasonal contrast. In terms of habitability, it is important to assess the seasonal surface variability, but also the variability on astronomical timescales.

The response time of the surface conditions (climate inertia) to climate perturbations comes into play when the radiative balance is rapidly perturbed, as would happen when the distribution of incidence stellar flux is continuously altered through high frequency astronomical cycles (Armstrong et al., 2014; Georgakarakos et al., 2018). The surface system may not be able to re-equilibrate fully under the influence of rapid oscillations and may subsequently experience a weakened response to astronomical forcing. An example is the suppressed positive ice-albedo feedback during rapid obliquity cycles (Armstrong et al., 2014). The transient non-steady state simulations presented here take into account the more rapid ocean-sea ice feedbacks, but the period of even the shortest simulated astronomical cycles is long enough for sea ice to equilibrate to the new radiative conditions (Figure 5.9). More rapid oscillations than those simulated here are required to suppress the (sea)

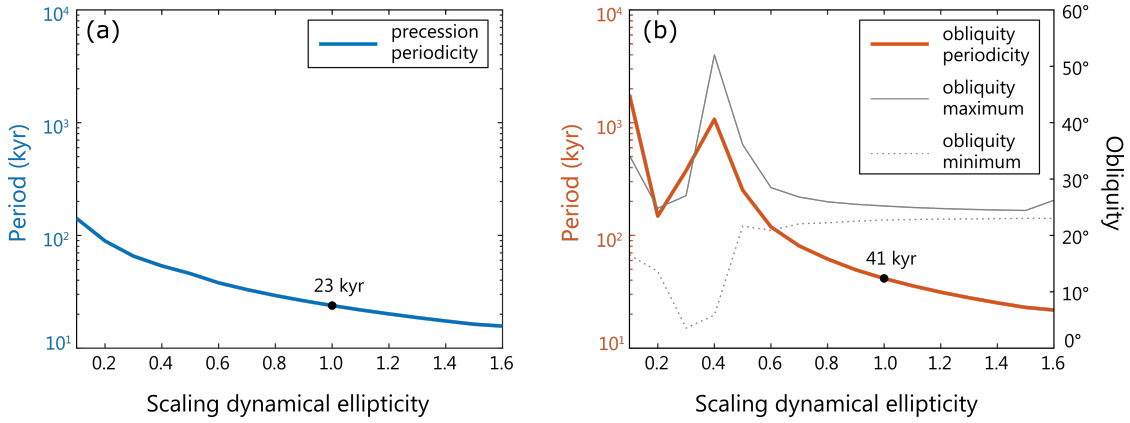

Figure 5.10: Duration of climatic precession (left panel) and obliquity (right panel) cycles as a function of the dynamical ellipticity scaling factor, following Laskar, Joutel, and Boudin (1993), for simulation where Jupiter is located at it's current position with an eccentricity of 0.05. A scaling factor of 1.0 equates to a dynamical ellipticity of 0.00328 equal to the value for the modern Earth.

ice-albedo feedback, although we note that the presence of dynamic continental ice sheets (not modeled here) may change the ice-albedo response time.

5.5 Application to HZ Planets

For the majority of the dynamical simulations presented here, the amplitude and frequency of obliquity cycles can be estimated directly from the orbital elements i, Ω, and ω, in combination with the parameter that describes the axial precession, ψ. The time evolution of the orbital elements of exoplanets in known systems can thus be modelled with n-body simulations and provide a first order estimate for the frequency and amplitude at which the obliquity varies (Atobe et al., 2004; Armstrong et al., 2014; Shan & Li, 2018), as has recently been done for Kepler-62f (Shields et al., 2016; Quarles et al., 2020). Such simulations also reveal whether the spin motions of a terrestrial planet may be subjected

to intense perturbations due to resonant behavior, and are therefore a useful tool for exoplanet research toward reconstructing possible climate states of terrestrial exoplanets in the Habitable Zone.

The major unknowns required to reconstruct the spin dynamics of planets beyond the Solar system are related to the precession rate of the rotational axis (Equation 5.3 and C.3). This motion depends on the dynamical ellipticity (proportional to the planetary rotation rate for rapidly rotating planets), tidal torques, and the initial obliquity of the planet. These parameters are currently unobtainable for exoplanets or can only be roughly estimated at best. Below, we evaluate how tidal torques and dynamical ellipticity influence the simulation of precession and obliquity cycles using the following equation:

$$\frac{d\psi}{dt} = \frac{3}{2}\left(\frac{M_m n_m^2}{\nu} + \frac{M_s n_s^2}{\nu}\right) E_D \cos\epsilon \tag{5.3}$$

where M_m is the ratio between the mass of the Moon and the summed mass of the Moon and Earth, and n_m is the mean motion of the Moon (2π/27.3 days). M_s is the ratio between the mass of the Sun and the summed mass of the Sun and Earth (≈ 1). The mean motion of the Earth is n_m (2π/365.25 days). Finally, ν is Earth's angular momentum, E_D is the dynamical ellipticity, and ϵ is the axial obliquity.

5.5.1 Tidal Torques

The Earth may be a rare case in that our planet is accompanied by a relatively large moon. The benefits of having a moon in terms of planetary habitability and the origin of life have been discussed in various studies (Laskar, Joutel, & Robutel, 1993; Lathe, 2004;

Lissauer et al., 2012). Because many terrestrial exoplanets may not have a massive satellite (Elser et al., 2011), we evaluate how the frequency of axial precession and obliquity cycles are affected in the absence of lunar torques. Following Equation 5.3, Earth's axial precession rotates at 6.744×10^{-7} rad per day, when accounting for tidal contributions from both the Moon and Sun. The axial precession rate decreases to 2.124×10^{-7} rad per day when tidal torques from the Moon are eliminated from the equation, resulting in an axial precession cycle with a approximately 81 kyr period. The resulting obliquity cycles would have a period of 424 kyr (Equation 5.1), and climatic precession would oscillate with a period of 64 kyr (Equation 5.2). Even though various studies have shown that the amplitude of the obliquity cycles would increase in absence of a Moon (Laskar, Joutel, & Robutel, 1993; Lissauer et al., 2012; Li & Batygin, 2014), the period of those cycles would become significantly longer, making the rate of change experienced by the surface relatively more sedate.

Other objects in the Solar system, including Jupiter, are either too distant or have a mass too small to induce significant tidal effects on Earth. However, tidal torques scale with distance and it is worth investigating whether a giant planet would exert a notable torque τ_{Jup} on the equatorial bulge of an Earth-like planet if it was positioned in closer proximity. We use the following relationship:

$$\tau \propto \frac{m}{a^3} \tag{5.4}$$

where m is the mass of the object exerting the torque in solar masses ($M_\odot$) and a is the average distance between the object and Earth in astronomical units (au). The torque of the Moon $\tau_{moon} \propto 2.2$ is about twice as strong as the tidal torque from the Sun $\tau_{sun} \propto 1$. With

Jupiter located at its current semi-major axis of 5.2 au, $\tau_{Jup} \propto 0.00018$, the torque is negligible compared to the solar and lunar torques. Jupiter at 3.2 au results in $\tau_{Jup} \propto 0.00030$ and thus remains a negligible force on the planet's equatorial bulge in comparison.

5.5.2 Dynamical Ellipticity

The dynamical ellipticity E_D is a measure of the oblateness of a planet partly caused by centrifugal forces associated with the planetary rotation, and to a lesser extent by the geography, topography (Ward et al., 1979), presence and location of massive ice caps (Dehant et al., 1990; Rubincam, 1990; Ito et al., 1995), core-mantle dynamics (Neron de Surgy & Laskar, 1997; Forte & Mitrovica, 1997; Correia, 2006), and atmospheric thickness (Barnes et al., 1983; Volland, 1996). The torques on a more oblate planet with a larger equatorial bulge are stronger compared to the torques on a more spherical planet, resulting in a more rapid precession of the rotational axis (Figure 5.10). Using a parameterization for E_D in the obliquity model used here (Laskar, Joutel, & Boudin, 1993), we simulate how this impacts the frequency of climatic precession and obliquity cycles.

Increasing the E_D scaling factor to 1.6 shortens the obliquity period to about 20 kyr whilst a more rigid Earth with a dynamical ellipticity scaling factor of 0.6 lengthens obliquity cycles to 119 kyr. For comparison, the dynamical ellipticity of Mars is estimated at $E_D = 0.0054$ (1.6×Earth) (Bouquillon & Souchay, 1999) and that of Venus is likely much smaller, $E_D = 0.000013$ due to its slow rotation rate (Yoder, 1995; Correia et al., 2003). Considering how sensitive the frequency of astronomical cycles are to the dynamical ellipticity, it will be essential to determine the rotation rates of HZ exoplanets before being

able to discuss the long-term habitability and stability of the surface conditions on geological and astronomical timescales.

5.6 Conclusion

Surface conditions and fractional habitability of (exo)planets in the HZ vary over time as a function of the architecture of their planetary system and orbital dynamics. The frequency and amplitude of eccentricity and orbital inclination cycles of an Earth-like planet are sensitive to the relatively minor variations in the orbital characteristics of companion planets (Horner et al., 2020). These in turn drive the magnitude and frequency of axial obliquity and precession cycles with implications for surface climate conditions and long-term habitability. This study is the first to apply n-body and obliquity model output to a 3D ocean-coupled climate model where the eccentricity, obliquity, and precession vary transiently on the million-year timescales relevant for the evolutionary development of life.

Even the more extreme orbital cycles presented here result in (partially) habitable surface conditions. The large heat capacity of the vast ocean basin maintains temperate ocean temperatures although the fractional habitability over land varies strongly seasonally and annually on astronomical timescales. A planet is less likely to be suitable for life when the fractional habitability drops, permanently or temporarily, to near zero values, which may happen for exoplanets closer to the edge of the HZ and/or with low thermal inertia in the climate system while experiencing extreme astronomical cycles.

Our results support previous work that demonstrates how eccentricity and obliquity cycling can act to inhibit large-scale freezing with a sufficiently large heat reservoir, and

thereby expand the outer edge of the HZ. At the same time, high mean obliquity or extreme obliquity cycles that arise when a giant planet is close-in, can act to reduce the habitable surface area. In contrast, the habitable surface area increases under extreme eccentricity cycles that arise under the influence of an eccentric giant planet. An eccentric giant companion may therefore be favorable for the habitability of a smaller terrestrial planet, provided its distance is large enough from the smaller planet to prevent high-amplitude obliquity cycles.

Transient ocean-climate simulations differ from conventional steady state models because slower climate processes, such as the growth of sea ice and heat storage in the vast ocean basin, prevent the system from reaching full equilibrium with respect to changing orbital parameters. However, even the most rapid astronomical changes investigated here (50 kyr eccentricity cycles) are sufficiently slow for sea ice and ocean heat storage to approach an equilibrium state. A planet with smaller heat capacity or more rapid changes to the radiative balance may not be buffered against rapid climate variability.

A similar sequential methodology of using n-body simulations, obliquity models, combined with transient ocean-coupled climate simulations can be applied to assess the long-term habitability potential of HZ exoplanets in planetary systems provided that the planetary masses and orbital architecture are relatively well constrained. A series of n-body simulations produces possible dynamical evolution pathways of the orbital elements (i, Ω, ω) that give insight into the dynamical stability of the system and allow a first-order estimate of the potential amplitude and frequency of obliquity cycles using educated assumptions about the rate of axial precession.

The era of exoplanet exploration and characterization has only just begun. Many of the parameters required to reliably simulate orbital and spin dynamics of HZ exoplanets such as the planetary rotation rate, initial obliquity, axial precession rate, or dynamical ellipticity are currently unobtainable. However, it is expected that significant advances will be made in observational facilities and analysis techniques in the coming years. This, combined with our growing understanding of the evolution of protoplanetary disks and planet formation, will undoubtedly provide us with a plethora of new tools to improve exoplanet characterization, and provide the critical data needed to more reliably assess the potential habitability of newly discovered exoplanets to help focus the future search for evidence of life beyond the Earth to the most promising targets.

Chapter 6

General Conclusions

I have used numerical approaches to investigate the role of changing greenhouse gas concentrations and astronomical forcing on the surface climate, carbon cycling, and the environmental consequences of associated feedback processes, on Earth and beyond, with a particular focus on the impacts on geological ($> 10^3$ yr) timescales.

My first goal was to create a modeling framework that facilitates the interpretation of geological records that preserve past carbon release events as negative carbon isotope excursions (nCIEs) in order to better understand how Earth responds to carbon perturbations. The presented framework allows users to (1) estimate the amount and rate of carbon release during a past event, (2) narrow down the most likely source(s) of the released carbon and its isotopic signature, (3) evaluate the relation between the carbon perturbation and environmental change, (4) identify the presence of potential sedimentary distortions, (5) track the partitioning of carbon between the atmosphere, ocean, and sediments across the event, and (6) estimate the carbon removal fluxes during recovery. The work also high-

lights the importance of considering the event duration when estimating past carbon fluxes and their environmental impact. As a result of the negative weathering feedback, a geologically brief interval (< 10 kyr) of carbon release requires less total carbon input to produce a nCIE of the same size as that of a carbon release event of longer duration, although the environmental consequences are more severe for the shorter nCIE. This feedback effect is often overlooked in reconstructions of past carbon release, yet, should not be ignored when drawing a comparison with the anthropogenic carbon release 'event'.

The early Cenozoic is riddled with nCIEs that are accompanied by evidence for global warming and deep marine carbonate dissolution (ocean acidification). The 'hyperthermals' have been linked to astronomical forcing but the processes and feedbacks responsible for episodic carbon release have not been tested beyond speculation. The research presented here demonstrates that eccentricity forcing has a strong influence on the global temperature as relatively small spatiotemporal insolation changes control the global heat distribution, leading to elevated temperatures during eccentricity maxima, consistent with the eccentricity-paced hyperthermals. However, it has proven much more challenging to reproduce the nCIE and carbonate dissolution synchronous with episodes of global warming. The feedbacks that contribute most to the marine carbon isotope signal and carbonate preservation are organic matter burial and terrestrial weathering, respectively. In fact, enhanced marine organic matter burial and increased terrestrial weathering of nutrients and alkaline carbon species during periods of warmth result in an increase (not decrease) in marine carbon isotope values and enhanced preservation (not dissolution) of marine carbonates. These results support the idea that additional feedbacks not (yet) included in our

model, such as terrestrial carbon cycling and/or methane dynamics, likely played a critical role in the episodic carbon release on astronomical timescales during the early Cenozoic greenhouse. An important implication of the work is that the carbon release needed to be sufficiently high to not only produce the nCIE and carbonate dissolution but also to counteract the effects of the weathering and organic matter burial feedbacks. Identifying the source(s) of the natural carbon release during global warming episodes is directly relevant for future climate projections considering that similar climate-amplifying processes could potentially be triggered by anthropogenic warming.

While we do not quite yet fully comprehend the intricacies of astronomical climate forcing on Earth, it is crucial to think about how astronomical forcing may contribute to climate variability on exoplanets. The field of astrobiology is moving to identify planets in the Habitable Zone with the greatest potential for life to have emerged and sustained over prolonged periods of time. Consequently, planets experiencing extreme seasonal-scale or astronomical-scale variations may be less suitable targets for future astrobiology space missions. With the help of planetary system simulators and observable architecture of known system, it becomes relatively straightforward to estimate the orbital evolution of planets, but the difficulty lies in estimating their obliquity and precession dynamics—two parameters that control seasonality. The work presented here dissects the relation between the planetary architecture and the frequency and amplitude of obliquity and precession cycles using a large ensemble of dynamical simulations and assesses their impact on the evolving surface climate. In terms of planetary architecture, the presence of a giant companion planet may be favorable for Habitable Zone exoplanets with a sufficiently large heat capacity as the

eccentricity cycles induced by its gravitational influence act to maintain temperate surface temperatures. The distance between the giant and Habitable Zone planet influences obliquity cycles and should therefore be large enough to prevent high-mean or high-amplitude obliquity variations that cause seasonal extremes across large parts of the planet's surface. It is important to note, however, that no two planetary systems are identical in their formation history and architecture. The results presented here are thus not meant to be taken at face value but instead, illustrate that dynamical simulations combined with transient climate models are a useful tool to assess the long-term habitability potential of exoplanets.

The research presented in this dissertation has brought us a few steps closer to understanding how changes in the radiative balance impact planetary surface conditions on geological timescales. Yet, many uncertainties and unanswered questions still remain that require further investigation, particularly those related to astronomical forcing on Earth and beyond. While we now have a much better comprehension of the feedback response to astronomical forcing, model-data comparison shows that other feedbacks, not included in the studies here, have played a critical role in the climate variability throughout Earth's past. Future research should focus on identifying those missing feedbacks through a combination of more extensive Earth system modeling and generating additional multi-million-year-long paleoclimate records with a resolution high enough to identify astronomical cycle. I would also like to draw attention to the many uncertainties in assessing the potential habitability of planet. It will prove to be crucial to examine the atmospheric composition and pressure, ocean volume, and rock composition, among others, to determine the potential habitability. First and foremost to assess whether the planet is suitable for life as we know it, but an

often overlooked implication is that those variables play a key role in the sensitivity of the climate system and its resilience to perturbations in the radiative balance. Future research toward how such planetary characteristic influence climate resilience and feedback strength, particularly under the influence of varying degrees of astronomical forcing would offer a more detailed picture on long-term climate variability and habitability potential.

References

Addo-Bediako, A., Chown, S. L., & Gaston, K. J. (2000). Thermal tolerance, climatic variability and latitude. *Proceedings of the Royal Society of London. Series B: Biological Sciences*, *267*(1445), 739–745.

Adhémar, J. (1842). Revolutions de la mer: Déluges périodiques, carilian-goeury et v. dalmont. *Paris.–1842*.

Agassiz, L. (1840). *Etudes sur les glaciers*. Aux frais de l'auteur. En commission chez Jent et Gassmann, libraires, à ....

Agnew, M. T., Maddison, S. T., Horner, J., & Kane, S. R. (2019, June). Predicting multiple planet stability and habitable zone companions in the TESS era. *Monthly Notices of the RAS*, *485*(4), 4703-4725. doi: 10.1093/mnras/stz345

Archer, D. (2005). Fate of fossil fuel co2 in geologic time. *Journal of geophysical research: Oceans*, *110*(C9).

Archer, D., Buffett, B., & Brovkin, V. (2009). Ocean methane hydrates as a slow tipping point in the global carbon cycle. *Proceedings of the National Academy of Sciences*, *106*(49), 20596–20601.

Archer, D., Eby, M., Brovkin, V., Ridgwell, A., Cao, L., Mikolajewicz, U., ... others (2009). Atmospheric lifetime of fossil fuel carbon dioxide. *Annual review of earth and planetary sciences*, *37*.

Archer, D., Kheshgi, H., & Maier-Reimer, E. (1997). Multiple timescales for neutralization of fossil fuel co2. *Geophysical Research Letters*, *24*(4), 405–408.

Archer, D., & Maier-Reimer, E. (1994). Effect of deep-sea sedimentary calcite preservation on atmospheric co2 concentration. *Nature*, *367*(6460), 260–263.

Armstrong, J. C., Barnes, R., Domagal-Goldman, S., Breiner, J., Quinn, T. R., & Meadows, V. S. (2014, April). Effects of Extreme Obliquity Variations on the Habitability of Exoplanets. *Astrobiology*, *14*(4), 277-291. doi: 10.1089/ast.2013.1129

Armstrong, J. C., Leovy, C. B., & Quinn, T. (2004, October). A 1 Gyr climate model for Mars: new orbital statistics and the importance of seasonally resolved polar processes. *Icarus*, *171*(2), 255-271. doi: 10.1016/j.icarus.2004.05.007

Armstrong McKay, D. I., & Lenton, T. M. (2018). Reduced carbon cycle resilience across the palaeocene–eocene thermal maximum. *Climate of the Past*, *14*(10), 1515–1527.

Arndt, S., Jørgensen, B. B., LaRowe, D. E., Middelburg, J., Pancost, R., & Regnier, P. (2013). Quantifying the degradation of organic matter in marine sediments: A review and synthesis. *Earth-science reviews*, *123*, 53–86.

Arvidson, R. S., Mackenzie, F. T., & Berner, R. A. (2014). The sensitivity of the phanerozoic inorganic carbon system to the onset of pelagic sedimentation. *Aquatic geochemistry*, *20*(2), 343–362.

Atobe, K., Ida, S., & Ito, T. (2004, April). Obliquity variations of terrestrial planets in habitable zones. *Icarus*, *168*(2), 223-236. doi: 10.1016/j.icarus.2003.11.017

Aze, T., Pearson, P. N., Dickson, A. J., Badger, M. P., Bown, P., Pancost, R. D., ... others (2014). Extreme warming of tropical waters during the paleocene–eocene thermal maximum. *Geology*, *42*(9), 739–742.

Bamber, J. L., Alley, R. B., & Joughin, I. (2007, May). Rapid response of modern day ice sheets to external forcing. *Earth and Planetary Science Letters*, *257*(1-2), 1-13. doi: 10.1016/j.epsl.2007.03.005

Barnes, R., Hide, R., White, A., & Wilson, C. (1983, May). Atmospheric Angular Momentum Fluctuations, Length-of-Day Changes and Polar Motion. *Proceedings of the Royal Society of London Series A*, *387*(1792), 31-73. doi: 10.1098/rspa.1983.0050

Barnes, R., & Quinn, T. (2004, August). The (In)stability of Planetary Systems. *Astrophysical Journal*, *611*(1), 494-516. doi: 10.1086/421321

Barnet, J. S., Littler, K., Westerhold, T., Kroon, D., Leng, M. J., Bailey, I., ... Zachos, J. C. (2019). A high-fidelity benthic stable isotope record of late cretaceous–early eocene climate change and carbon-cycling. *Paleoceanography and Paleoclimatology*, *34*(4), 672–691.

Beddow, H. M., Liebrand, D., Sluijs, A., Wade, B. S., & Lourens, L. J. (2016). Global change across the oligocene-miocene transition: High-resolution stable isotope records from iodp site u1334 (equatorial pacific ocean). *Paleoceanography*, *31*(1), 81–97.

Berger, A. (1978). Long-term variations of daily insolation and quaternary climatic changes. *Journal of Atmospheric Sciences*, *35*(12), 2362–2367.

Bolmont, E., Libert, A.-S., Leconte, J., & Selsis, F. (2016, June). Habitability of planets on eccentric orbits: Limits of the mean flux approximation. *Astronomy and Astrophysics*, *591*, A106. doi: 10.1051/0004-6361/201628073

Boscolo-Galazzo, F., Crichton, K. A., Barker, S., & Pearson, P. N. (2018). Temperature dependency of metabolic rates in the upper ocean: A positive feedback to global climate change? *Global and Planetary Change*, *170*, 201–212.

Boulila, S., Galbrun, B., Laskar, J., & Pälike, H. (2012). A˜ 9 myr cycle in cenozoic δ13c record and long-term orbital eccentricity modulation: Is there a link? *Earth and Planetary Science Letters*, *317*, 273–281.

Bounceur, N., Crucifix, M., & Wilkinson, R. (2015). Global sensitivity analysis of the climate–vegetation system to astronomical forcing: an emulator-based approach. *Earth System Dynamics*, *6*(1), 205–224.

Bouquillon, S., & Souchay, J. (1999, May). Precise modeling of the precession-nutation of Mars. *Astronomy and Astrophysics*, *345*, 282-297.

Boutton, T. W. (1991). Stable carbon isotope ratios of natural materials: 2. atmospheric, terrestrial, marine, and freshwater environments. In *Carbon isotope techniques.*

Bralower, T. J., Thomas, D. J., Zachos, J., Hirschmann, M., Rohl, U., Sigurdsson, H., ... Whitney, D. (1997). High-resolution records of the late paleocene thermal maximum and circum-caribbean volcanism: Is there a causal link? *Geology*, *25*(11), 963–966.

Brovkin, V., Bendtsen, J., Claussen, M., Ganopolski, A., Kubatzki, C., Petoukhov, V., & Andreev, A. (2002). Carbon cycle, vegetation, and climate dynamics in the holocene: Experiments with the climber-2 model. *Global Biogeochemical Cycles*, *16*(4), 86–1.

Bryan, M. L., Knutson, H. A., Howard, A. W., Ngo, H., Batygin, K., Crepp, J. R., ... others (2016). Statistics of long period gas giant planets in known planetary systems. *The Astrophysical Journal*, *821*(2), 89.

Buffett, B., & Archer, D. (2004). Global inventory of methane clathrate: sensitivity to changes in the deep ocean. *Earth and Planetary Science Letters*, *227*(3-4), 185–199.

Burdige, D. J. (2007). Preservation of organic matter in marine sediments: controls, mechanisms, and an imbalance in sediment organic carbon budgets? *Chemical reviews*, *107*(2), 467–485.

Calov, R., Ganopolski, A., Petoukhov, V., Claussen, M., Brovkin, V., & Kubatzki, C. (2005). Transient simulation of the last glacial inception. part ii: sensitivity and feedback analysis. *Climate Dynamics*, *24*(6), 563–576.

Caves, J. K., Jost, A. B., Lau, K. V., & Maher, K. (2016). Cenozoic carbon cycle imbalances and a variable weathering feedback. *Earth and Planetary Science Letters*, *450*, 152–163.

Chambers, J. E. (1999, April). A hybrid symplectic integrator that permits close encounters between massive bodies. *Monthly Notices of the RAS*, *304*(4), 793-799. doi: 10.1046/j.1365-8711.1999.02379.x

Cockell, C. S., Bush, T., Bryce, C., Direito, S., Fox-Powell, M., Harrison, J. P., ... Zorzano, M. P. (2016, January). Habitability: A Review. *Astrobiology*, *16*(1), 89-117. doi: 10.1089/ast.2015.1295

Colbourn, G., Ridgwell, A., & Lenton, T. (2013). The rock geochemical model (rokgem) v0. 9. *Geoscientific Model Development*, *6*(5), 1543–1573.

Colbourn, G., Ridgwell, A., & Lenton, T. (2015). The time scale of the silicate weathering negative feedback on atmospheric co2. *Global Biogeochemical Cycles*, *29*(5), 583–596.

Colose, C. M., Del Genio, A. D., & Way, M. J. (2019, October). Enhanced Habitability on High Obliquity Bodies near the Outer Edge of the Habitable Zone of Sun-like Stars. *Astrophysical Journal*, *884*(2), 138. doi: 10.3847/1538-4357/ab4131

Correia, A. C. M. (2006, December). The core mantle friction effect on the secular spin evolution of terrestrial planets. *Earth and Planetary Science Letters*, *252*(3-4), 398-412. doi: 10.1016/j.epsl.2006.10.007

Correia, A. C. M., Laskar, J., & de Surgy, O. N. (2003, May). Long-term evolution of the spin of Venus. I. theory. *Icarus*, *163*(1), 1-23. doi: 10.1016/S0019-1035(03)00042-3

Corsetti, F. A., Baud, A., Marenco, P. J., & Richoz, S. (2005). Summary of early triassic carbon isotope records. *Comptes rendus palevol*, *4*(6-7), 473–486.

Cramer, B. S., Wright, J. D., Kent, D. V., & Aubry, M.-P. (2003). Orbital climate forcing of δ13c excursions in the late paleocene–early eocene (chrons c24n–c25n). *Paleoceanography*, *18*(4).

Crichton, K. A., Ridgwell, A., Lunt, D. J., Farnsworth, A., & Pearson, P. N. (2020). Data-constrained assessment of ocean circulation changes since the middle miocene in an earth system model. *Climate of the Past Discussions*, 1–36.

Crichton, K. A., Wilson, J. D., Ridgwell, A., & Pearson, P. N. (2021). Calibration of temperature-dependent ocean microbial processes in the cgenie. muffin (v0. 9.13) earth system model. *Geoscientific Model Development*, *14*(1), 125–149.

Croll, J. (1864). Xiii. on the physical cause of the change of climate during geological epochs. *The London, Edinburgh, and Dublin Philosophical Magazine and Journal of Science*, *28*(187), 121–137.

Cui, Y., Kump, L. R., & Ridgwell, A. (2013). Initial assessment of the carbon emission rate and climatic consequences during the end-permian mass extinction. *Palaeogeography, Palaeoclimatology, Palaeoecology*, *389*, 128–136.

Cui, Y., Kump, L. R., Ridgwell, A. J., Charles, A. J., Junium, C. K., Diefendorf, A. F., ... Harding, I. C. (2011). Slow release of fossil carbon during the palaeocene–eocene thermal maximum. *Nature Geoscience*, *4*(7), 481–485.

DeConto, R. M., Galeotti, S., Pagani, M., Tracy, D., Schaefer, K., Zhang, T., ... Beerling, D. J. (2012). Past extreme warming events linked to massive carbon release from thawing permafrost. *Nature*, *484*(7392), 87–91.

Dehant, V., Loutre, M.-F., & Berger, A. (1990, May). Potential impact of the northern hemisphere quaternary ice sheets on the frequencies of the astroclimatic orbital parameters. *Journal of Geophysics Research*, *95*(D6), 7573-7578. doi: 10.1029/JD095iD06p07573

Deitrick, R., Barnes, R., Bitz, C., Fleming, D., Charnay, B., Meadows, V., ... Quinn, T. (2018, June). Exo-Milankovitch Cycles. II. Climates of G-dwarf Planets in Dynamically Hot Systems. *Astronomical Journal*, *155*(6), 266. doi: 10.3847/1538-3881/aac214

Deitrick, R., Barnes, R., Quinn, T., Armstrong, J., Charnay, B., & Wilhelm, C. (2018, February). Exo-Milankovitch Cycles. I. Orbits and Rotation States. *Astronomical Journal*, *155*(2), 60. doi: 10.3847/1538-3881/aaa301

Deutsch, C. A., Tewksbury, J. J., Huey, R. B., Sheldon, K. S., Ghalambor, C. K., Haak, D. C., & Martin, P. R. (2008, May). From the Cover: Impacts of climate warming on terrestrial ectotherms across latitude. *Proceedings of the National Academy of Science*, *105*(18), 6668-6672. doi: 10.1073/pnas.0709472105

Dickens, G. R. (2003). *A methane trigger for rapid warming?* American Association for the Advancement of Science.

Dickens, G. R., O'Neil, J. R., Rea, D. K., & Owen, R. M. (1995). Dissociation of oceanic methane hydrate as a cause of the carbon isotope excursion at the end of the paleocene. *Paleoceanography*, *10*(6), 965–971.

Dobrovolskis, A. R. (2013, September). Insolation on exoplanets with eccentricity and obliquity. *Icarus*, *226*(1), 760-776. doi: 10.1016/j.icarus.2013.06.026

Donnadieu, Y., Pierrehumbert, R., Jacob, R., & Fluteau, F. (2006, August). Modelling the primary control of paleogeography on Cretaceous climate. *Earth and Planetary Science Letters*, *248*(1-2), 426-437. doi: 10.1016/j.epsl.2006.06.007

Dressing, C. D., Spiegel, D. S., Scharf, C. A., Menou, K., & Raymond, S. N. (2010, October). Habitable Climates: The Influence of Eccentricity. *The Astrophysical Journal*, *721*(2), 1295-1307. doi: 10.1088/0004-637X/721/2/1295

Dunkley Jones, T., Manners, H. R., Hoggett, M., Kirtland Turner, S., Westerhold, T., Leng, M. J., ... others (2018). Dynamics of sediment flux to a bathyal continental margin section through the paleocene–eocene thermal maximum. *Climate of the Past*, *14*(7), 1035–1049.

Dunne, J. P., Sarmiento, J. L., & Gnanadesikan, A. (2007). A synthesis of global particle export from the surface ocean and cycling through the ocean interior and on the seafloor. *Global Biogeochemical Cycles*, *21*(4).

Eberle, J. J., Fricke, H. C., Humphrey, J. D., Hackett, L., Newbrey, M. G., & Hutchison, J. H. (2010). Seasonal variability in arctic temperatures during early eocene time. *Earth and Planetary Science Letters*, *296*(3-4), 481–486.

Edwards, N. R., & Marsh, R. (2005). Uncertainties due to transport-parameter sensitivity in an efficient 3-d ocean-climate model. *Climate dynamics*, *24*(4), 415–433.

Elser, S., Stadel, J., Moore, B., & Morishima, R. (2011, November). How common are Earth-Moon planetary systems? In A. Sozzetti, M. G. Lattanzi, & A. P. Boss (Eds.), *The astrophysics of planetary systems: Formation, structure, and dynamical evolution* (Vol. 276, p. 414-415). doi: 10.1017/S1743921311020588

Erba, E., Bottini, C., Weissert, H. J., & Keller, C. E. (2010). Calcareous nannoplankton response to surface-water acidification around oceanic anoxic event 1a. *Science*, *329*(5990), 428–432.

Esmark, J. (1826). Remarks tending to explain the geological history of the earth. *Edinburgh New Philosophical Journal*, *2*, 107–121.

Ferreira, D., Marshall, J., O'Gorman, P. A., & Seager, S. (2014, November). Climate at high-obliquity. *Icarus*, *243*, 236-248. doi: 10.1016/j.icarus.2014.09.015

Feulner, G. (2012, May). The faint young Sun problem. *Reviews of Geophysics*, *50*(2), RG2006. doi: 10.1029/2011RG000375

Fletcher, B. J., Brentnall, S. J., Anderson, C. W., Berner, R. A., & Beerling, D. J. (2008). Atmospheric carbon dioxide linked with mesozoic and early cenozoic climate change. *Nature Geoscience*, *1*(1), 43–48.

Forte, A. M., & Mitrovica, J. X. (1997, December). A resonance in the Earth's obliquity and precession over the past 20 Myr driven by mantle convection. *Nature*, *390*(6661), 676-680. doi: 10.1038/37769

Froelich, P., Bender, M., Luedtke, N., Heath, G., & DeVries, T. (1982). The marine phosphorus cycle. *Am. J. Sci*, *282*(4), 474–511.

Gaidos, E., & Williams, D. M. (2004, November). Seasonality on terrestrial extrasolar planets: inferring obliquity and surface conditions from infrared light curves. *New Astronomy*, *10*(1), 67-77. doi: 10.1016/j.newast.2004.04.009

Ganopolski, A., Petoukhov, V., Rahmstorf, S., Brovkin, V., Claussen, M., Eliseev, A., & Kubatzki, C. (2001). Climber-2: a climate system model of intermediate complexity. part ii: model sensitivity. *Climate Dynamics*, *17*(10), 735–751.

Georgakarakos, N., Eggl, S., & Dobbs-Dixon, I. (2018, April). Giant Planets: Good Neighbors for Habitable Worlds? *Astrophysical Journal*, *856*(2), 155. doi: 10.3847/1538-4357/aaaf72

Gilmore, J. B., & Ross, A. (2008, December). Effective field theory calculation of second post-Newtonian binary dynamics. *Physical Review D*, *78*(12), 124021. doi: 10.1103/PhysRevD.78.124021

Goodwin, P., & Ridgwell, A. (2010). Ocean-atmosphere partitioning of anthropogenic carbon dioxide on multimillennial timescales. *Global Biogeochemical Cycles*, *24*(2).

Goosse, H., Brovkin, V., Fichefet, T., Haarsma, R., Huybrechts, P., Jongma, J., ... others (2010). Description of the earth system model of intermediate complexity loveclim version 1.2. *Geoscientific Model Development*, *3*(2), 603–633.

Graziano, R., & Raspini, A. (2018). High-resolution chronostratigraphy of palaeoecologic and isotopic changes in shallow-marine carbonates: deciphering the completeness of the aptian record in the apennine carbonate platform (southern italy). *Cretaceous Research*, *86*, 97–128.

Griffith, E. M., Thomas, E., Lewis, A. R., Penman, D. E., Westerhold, T., & Winguth, A. M. (2021). Bentho-pelagic decoupling: The marine biological carbon pump during eocene hyperthermals. *Paleoceanography and Paleoclimatology*, *36*(3), e2020PA004053.

Gutjahr, M., Ridgwell, A., Sexton, P. F., Anagnostou, E., Pearson, P. N., Pälike, H., ... Foster, G. L. (2017). Very large release of mostly volcanic carbon during the palaeocene–eocene thermal maximum. *Nature*, *548*(7669), 573–577.

Hawkins, E., Ortega, P., Suckling, E., Schurer, A., Hegerl, G., Jones, P., ... others (2017). Estimating changes in global temperature since the preindustrial period. *Bulletin of the American Meteorological Society*, *98*(9), 1841–1856.

Hays, J. D., Imbrie, J., & Shackleton, N. J. (1976, December). Variations in the Earth's Orbit: Pacemaker of the Ice Ages. *Science*, *194*(4270), 1121-1132. doi: 10.1126/science.194.4270.1121

Heinemann, M., Timmermann, A., Elison Timm, O., Saito, F., & Abe-Ouchi, A. (2014). Deglacial ice sheet meltdown: Orbital pacemaking and co 2 effects. *Climate of the Past*, *10*(4), 1567–1579.

Hermoso, M., Minoletti, F., Rickaby, R. E., Hesselbo, S. P., Baudin, F., & Jenkyns, H. C. (2012). Dynamics of a stepped carbon-isotope excursion: Ultra high-resolution study of early toarcian environmental change. *Earth and Planetary Science Letters*, *319*, 45–54.

Herrle, J. O., Kößler, P., Friedrich, O., Erlenkeuser, H., & Hemleben, C. (2004). High-resolution carbon isotope records of the aptian to lower albian from se france and the mazagan plateau (dsdp site 545): a stratigraphic tool for paleoceanographic and paleobiologic reconstruction. *Earth and Planetary Science Letters*, *218*(1-2), 149–161.

Herschel, J. F. W. (1832). Xvii.—on the astronomical causes which may influence geological phænomena. *Transactions of the Geological Society of London*, *2*(2), 293–300.

Hilgen, F. J. (2010). Astronomical dating in the 19th century. *Earth-Science Reviews*, *98*(1-2), 65–80.

Holbourn, A., Kuhnt, W., Clemens, S., Prell, W., & Andersen, N. (2013). Middle to late miocene stepwise climate cooling: Evidence from a high-resolution deep water isotope curve spanning 8 million years. *Paleoceanography*, *28*(4), 688–699.

Holbourn, A., Kuhnt, W., Schulz, M., Flores, J.-A., & Andersen, N. (2007). Orbitally-paced climate evolution during the middle miocene "monterey" carbon-isotope excursion. *Earth and Planetary Science Letters*, *261*(3-4), 534–550.

Honegger, L., Adatte, T., Spangenberg, J. E., Rugenstein, J. K. C., Poyatos-Moré, M., Puigdefàbregas, C., ... others (2020). Alluvial record of an early eocene hyperthermal within the castissent formation, the pyrenees, spain. *Climate of the Past*, *16*(1), 227–243.

Hönisch, B., Ridgwell, A., Schmidt, D. N., Thomas, E., Gibbs, S. J., Sluijs, A., ... others (2012). The geological record of ocean acidification. *science*, *335*(6072), 1058–1063.

Horner, J., & Jones, B. W. (2010, October). Determining habitability: which exoEarths should we search for life? *International Journal of Astrobiology*, *9*(4), 273-291. doi: 10.1017/S1473550410000261

Horner, J., Marshall, J. P., Wittenmyer, R. A., & Tinney, C. G. (2011, September). A dynamical analysis of the proposed HU Aquarii planetary system. *Monthly Notices of the RAS*, *416*(1), L11-L15. doi: 10.1111/j.1745-3933.2011.01087.x

Horner, J., Vervoort, P., Kane, S. R., Ceja, A. Y., Waltham, D., Gilmore, J., & Kirtland Turner, S. (2020, January). Quantifying the Influence of Jupiter on the Earth's Orbital Cycles. *Astronomical Journal*, *159*(1), 10. doi: 10.3847/1538-3881/ab5365

Horner, J., Wittenmyer, R. A., Wright, D. J., Hinse, T. C., Marshall, J. P., Kane, S. R., ... Johns, D. (2019, September). The HD 181433 Planetary System: Dynamics and a New Orbital Solution. *Astronomical Journal*, *158*(3), 100. doi: 10.3847/1538-3881/ab2e78

Hülse, D., Arndt, S., Daines, S., Regnier, P., & Ridgwell, A. (2018). Omen-sed 1.0: a novel, numerically efficient organic matter sediment diagenesis module for coupling to earth system models. *Geoscientific Model Development*, *11*(7), 2649–2689.

Hülse, D., Arndt, S., Wilson, J. D., Munhoven, G., & Ridgwell, A. (2017). Understanding the causes and consequences of past marine carbon cycling variability through models. *Earth-Science Reviews*, *171*, 349–382.

Imbrie, J., Boyle, E. A., Clemens, S. C., Duffy, A., Howard, W. R., Kukla, G., ... Toggweiler, J. R. (1992, December). On the structure and origin of major glaciation cycles, 1, Linear responses to Milankovitch forcing. *Paleoceanography*, *7*(6), 701-738. doi: 10.1029/92PA02253

Ito, T., Masuda, K., Hamano, Y., & Matsui, T. (1995, January). Climate friction: A possible cause for secular drift of Earth's obliquity. *Journal of Geophysics Research*, *100*(B8), 15147-15162. doi: 10.1029/95JB01061

Javoy, M., Pineau, F., & Delorme, H. (1986). Carbon and nitrogen isotopes in the mantle. *Chemical geology*, *57*(1-2), 41–62.

Jenkyns, H. (1988). The early toarcian (jurassic) anoxic event-stratigraphic, sedimentary, and geochemical evidence. *American Journal of Science*, *288*(2).

Jenkyns, H. (2010). Geochemistry of oceanic anoxic events. *Geochemistry, Geophysics, Geosystems*, *11*(3).

Jenkyns, H. C., et al. (1995). Carbon-isotope stratigraphy and paleoceanographic significance of the lower cretaceous shallow-water carbonates of resolution guyot, mid-pacific mountains. In *Proceedings of the ocean drilling program, scientific results* (Vol. 143, pp. 99–104).

John, E. H., Wilson, J. D., Pearson, P. N., & Ridgwell, A. (2014). Temperature-dependent remineralization and carbon cycling in the warm eocene oceans. *Palaeogeography, Palaeoclimatology, Palaeoecology*, *413*, 158–166.

Jones, T. D., Lunt, D. J., Schmidt, D. N., Ridgwell, A., Sluijs, A., Valdes, P. J., & Maslin, M. (2013). Climate model and proxy data constraints on ocean warming across the paleocene–eocene thermal maximum. *Earth-Science Reviews*, *125*, 123–145.

Joshi, M. M., & Haberle, R. M. (2012, January). Suppression of the Water Ice and Snow Albedo Feedback on Planets Orbiting Red Dwarf Stars and the Subsequent Widening of the Habitable Zone. *Astrobiology*, *12*(1), 3-8. doi: 10.1089/ast.2011.0668

Kane, S. R., & Gelino, D. M. (2012, April). The Habitable Zone Gallery. *Publications of the ASP*, *124*(914), 323. doi: 10.1086/665271

Kane, S. R., Li, Z., Wolf, E. T., Ostberg, C., & Hill, M. L. (2021, January). Eccentricity Driven Climate Effects in the Kepler-1649 System. *Astronomical Journal*, *161*(1), 31. doi: 10.3847/1538-3881/abcbfd

Kane, S. R., & Raymond, S. N. (2014, April). Orbital Dynamics of Multi-planet Systems with Eccentricity Diversity. *Astrophysical Journal*, *784*(2), 104. doi: 10.1088/0004-637X/784/2/104

Kane, S. R., & Torres, S. M. (2017, November). Obliquity and Eccentricity Constraints for Terrestrial Exoplanets. *Astronomical Journal*, *154*(5), 204. doi: 10.3847/1538-3881/aa8fce

Kang, W. (2019, May). Mechanisms Leading to a Warmer Climate on High-obliquity Planets. *Astrophysical Journal, Letters*, *876*(1), L1. doi: 10.3847/2041-8213/ab18a8

Keeling, C. D., Bacastow, R. B., & Tans, P. P. (1980). Predicted shift in the 13c/12c ratio of atmospheric carbon dioxide. *Geophysical Research Letters*, *7*(7), 505–508.

Keeling, C. D., Mook, W. G., & Tans, P. P. (1979). Recent trends in the 13c/12c ratio of atmospheric carbon dioxide. *Nature*, *277*(5692), 121–123.

Kemppinen, K. M. S., Holden, P. B., Edwards, N. R., Ridgwell, A., & Friend, A. D. (2019, June). Coupled climate-carbon cycle simulation of the Last Glacial Maximum atmospheric CO_2 decrease using a large ensemble of modern plausible parameter sets. *Climate of the Past*, *15*(3), 1039-1062. doi: 10.5194/cp-15-1039-2019

Key, J. R., Wang, X., Stoeve, J. C., & Fowler, C. (2001, January). Estimating the cloudy-sky albedo of sea ice and snow from space. *Journal of Geophysics Research*(D12), 12,489-12,497. doi: 10.1029/2001JD900069

Kilic, C., Raible, C. C., & Stocker, T. F. (2017, August). Multiple Climate States of Habitable Exoplanets: The Role of Obliquity and Irradiance. *Astrophysical Journal*, *844*(2), 147. doi: 10.3847/1538-4357/aa7a03

Kinoshita, H. (1977, April). Theory of the Rotation of the Rigid Earth. *Celestial Mechanics*, *15*(3), 277-326. doi: 10.1007/BF01228425

Kirtland Turner, S. (2014). Pliocene switch in orbital-scale carbon cycle/climate dynamics. *Paleoceanography*, *29*(12), 1256–1266.

Kirtland Turner, S., & Ridgwell, A. (2013). Recovering the true size of an eocene hyperthermal from the marine sedimentary record. *Paleoceanography*, *28*(4), 700–712.

Kirtland Turner, S., Sexton, P. F., Charles, C. D., & Norris, R. D. (2014). Persistence of carbon release events through the peak of early eocene global warmth. *Nature Geoscience*, *7*(10), 748–751.

Kocken, I. J., Cramwinckel, M. J., Zeebe, R. E., Middelburg, J. J., & Sluijs, A. (2019). The 405 kyr and 2.4 myr eccentricity components in cenozoic carbon isotope records. *Climate of the Past*, *15*(1), 91–104.

Kohfeld, K. E., & Ridgwell, A. (2009, January). Glacial-interglacial variability in atmospheric CO_2. *Washington DC American Geophysical Union Geophysical Monograph Series*, *187*, 251-286. doi: 10.1029/2008GM000845

Komar, N., Zeebe, R., & Dickens, G. (2013). Understanding long-term carbon cycle trends: The late paleocene through the early eocene. *Paleoceanography*, *28*(4), 650–662.

Konijnendijk, T., Weber, S., Tuenter, E., & Van Weele, M. (2011). Methane variations on orbital timescales: a transient modeling experiment. *Climate of the Past*, *7*(2), 635–648.

Kuhnt, W., Holbourn, A., & Moullade, M. (2011). Transient global cooling at the onset of early aptian oceanic anoxic event (oae) 1a. *Geology*, *39*(4), 323–326.

Kump, L. R. (2018). Prolonged late permian–early triassic hyperthermal: failure of climate regulation? *Philosophical Transactions of the Royal Society A: Mathematical, Physical and Engineering Sciences*, *376*(2130), 20170078.

Kump, L. R., & Arthur, M. A. (1997). Global chemical erosion during the cenozoic: Weatherability balances the budgets. In *Tectonic uplift and climate change* (pp. 399–426). Springer.

Kurtz, A., Kump, L., Arthur, M., Zachos, J., & Paytan, A. (2003). Early cenozoic decoupling of the global carbon and sulfur cycles. *Paleoceanography*, *18*(4).

Kuypers, M. M., Lourens, L. J., Rijpstra, W. I. C., Pancost, R. D., Nijenhuis, I. A., & Damsté, J. S. S. (2004). Orbital forcing of organic carbon burial in the proto-north atlantic during oceanic anoxic event 2. *Earth and Planetary Science Letters*, *228*(3-4), 465–482.

Kvenvolden, K. A. (1993). Gas hydrates—geological perspective and global change. *Reviews of geophysics*, *31*(2), 173–187.

Kwon, E. Y., Sarmiento, J. L., Toggweiler, J., & DeVries, T. (2011). The control of atmospheric pco2 by ocean ventilation change: The effect of the oceanic storage of biogenic carbon. *Global Biogeochemical Cycles*, *25*(3).

Laskar, J., Joutel, F., & Boudin, F. (1993, March). Orbital, precessional, and insolation quantities for the earth from -20 Myr to +10 Myr. *Astronomy and Astrophysics*, *270*, 522-533.

Laskar, J., Joutel, F., & Robutel, P. (1993, February). Stabilization of the Earth's obliquity by the Moon. *Nature*, *361*(6413), 615-617. doi: 10.1038/361615a0

Laskar, J., Robutel, P., Joutel, F., Gastineau, M., Correia, A., & Levrard, B. (2004). A long-term numerical solution for the insolation quantities of the earth. *Astronomy and Astrophysics*, *428*(1), 261–285.

Lathe, R. (2004, March). Fast tidal cycling and the origin of life. *Icarus*, *168*(1), 18-22. doi: 10.1016/j.icarus.2003.10.018

Lauretano, V., Littler, K., Polling, M., Zachos, J. C., & Lourens, L. J. (2015). Frequency, magnitude and character of hyperthermal events at the onset of the early eocene climatic optimum. *Climate of the Past*, *11*(10), 1313–1324.

Laurin, J., Meyers, S. R., Uličnỳ, D., Jarvis, I., & Sageman, B. B. (2015). Axial obliquity control on the greenhouse carbon budget through middle-to high-latitude reservoirs. *Paleoceanography*, *30*(2), 133–149.

Li, G., & Batygin, K. (2014, July). On the Spin-axis Dynamics of a Moonless Earth. *Astrophysical Journal*, *790*(1), 69. doi: 10.1088/0004-637X/790/1/69

Li, M., Hinnov, L. A., Huang, C., & Ogg, J. G. (2018). Sedimentary noise and sea levels linked to land–ocean water exchange and obliquity forcing. *Nature communications*, *9*(1), 1–12.

Linsenmeier, M., Pascale, S., & Lucarini, V. (2015, January). Climate of Earth-like planets with high obliquity and eccentric orbits: Implications for habitability conditions. *Planetary Space Science*, *105*, 43-59. doi: 10.1016/j.pss.2014.11.003

Lissauer, J. J., Barnes, J. W., & Chambers, J. E. (2012, May). Long-Term Obliquity Variations of a Moonless Earth. In *Aas/division of dynamical astronomy meeting #43* (p. 5.07).

Littler, K., Röhl, U., Westerhold, T., & Zachos, J. C. (2014). A high-resolution benthic stable-isotope record for the south atlantic: Implications for orbital-scale changes in late paleocene–early eocene climate and carbon cycling. *Earth and Planetary Science Letters*, *401*, 18–30.

Liu, D., Huang, C., Kemp, D. B., Li, M., Ogg, J. G., Yu, M., & Foster, W. J. (2021). Paleoclimate and sea level response to orbital forcing in the middle triassic of the eastern tethys. *Global and Planetary Change*, *199*, 103454.

Liu, Z., Otto-Bliesner, B., He, F., Brady, E., Tomas, R., Clark, P., ... others (2009). Transient simulation of last deglaciation with a new mechanism for bølling-allerød warming. *science*, *325*(5938), 310–314.

Lord, N. S., Ridgwell, A., Thorne, M. C., & Lunt, D. J. (2016). An impulse response function for the "long tail" of excess atmospheric co2 in an earth system model. *Global Biogeochemical Cycles*, *30*(1), 2–17.

Lorenzen, J., Kuhnt, W., Holbourn, A., Flögel, S., Moullade, M., & Tronchetti, G. (2013). A new sediment core from the bedoulian (lower aptian) stratotype at roquefort-la bédoule, se france. *Cretaceous Research*, *39*, 6–16.

Lourens, L. J., Sluijs, A., Kroon, D., Zachos, J. C., Thomas, E., Röhl, U., ... Raffi, I. (2005). Astronomical pacing of late palaeocene to early eocene global warming events. *Nature*, *435*(7045), 1083–1087.

Lunt, D. J., Ridgwell, A., Sluijs, A., Zachos, J., Hunter, S., & Haywood, A. (2011). A model for orbital pacing of methane hydrate destabilization during the palaeogene. *Nature Geoscience*, *4*(11), 775–778.

Lunt, D. J., Williamson, M. S., Valdes, P. J., Lenton, T. M., & Marsh, R. (2006, November). Comparing transient, accelerated, and equilibrium simulations of the last 30 000 years with the GENIE-1 model. *Climate of the Past*, *2*(2), 221-235.

Lyle, M. (1988). Climatically forced organic carbon burial in equatorial atlantic and pacific oceans. *Nature*, *335*(6190), 529–532.

Lyle, M., Barron, J., Bralower, T. J., Huber, M., Olivarez Lyle, A., Ravelo, A. C., ... Wilson, P. A. (2008). Pacific ocean and cenozoic evolution of climate. *Reviews of Geophysics*, *46*(2).

Ma, W., & Tian, J. (2014, October). Modeling the contribution of dissolved organic carbon to carbon sequestration during the last glacial maximum. *Geo-Marine Letters*, *34*(5), 471-482. doi: 10.1007/s00367-014-0378-y

Ma, W., Tian, J., Li, Q., & Wang, P. (2011). Simulation of long eccentricity (400-kyr) cycle in ocean carbon reservoir during miocene climate optimum: Weathering and nutrient response to orbital change. *Geophysical Research Letters*, *38*(10).

Maier-Reimer, E. (1993). Geochemical cycles in an ocean general circulation model. preindustrial tracer distributions. *Global Biogeochemical Cycles*, *7*(3), 645–677.

Malinverno, A., Erba, E., & Herbert, T. (2010). Orbital tuning as an inverse problem: Chronology of the early aptian oceanic anoxic event 1a (selli level) in the cismon apticore. *Paleoceanography*, *25*(2).

Marcy, G., Butler, R. P., Fischer, D., Vogt, S., Wright, J. T., Tinney, C. G., & Jones, H. R. A. (2005, January). Observed Properties of Exoplanets: Masses, Orbits, and Metallicities. *Progress of Theoretical Physics Supplement*, *158*, 24-42. doi: 10.1143/PTPS.158.24

Marsh, R., Müller, S. A., Yool, A., & Edwards, N. R. (2011, November). Incorporation of the C-GOLDSTEIN efficient climate model into the GENIE framework: "eb_go_gs" configurations of GENIE. *Geoscientific Model Development*, *4*(4), 957-992. doi: 10.5194/gmd-4-957-2011

Marsh, R., Smith, M. P. L. M., Rohling, E. J., Lunt, D. J., Lenton, T. M., Williamson, M. S., & Yool, A. (2006, September). Modelling ocean circulation, climate and oxygen isotopes in the ocean over the last 120 000 years. *Climate of the Past Discussions*, *2*(5), 657-709.

Marshall, J., Horner, J., & Carter, A. (2010, October). Dynamical simulations of the HR8799 planetary system. *International Journal of Astrobiology*, *9*(4), 259-264. doi: 10.1017/S1473550410000297

Marshall, J., Horner, J., Wittenmyer, R., Clark, J., & Mengel, M. (2020, May). Stability analysis of three exoplanet systems. *Monthly Notices of the RAS*, *494*(2), 2280-2288. doi: 10.1093/mnras/staa847

Maslin, M. A., & Ridgwell, A. J. (2005). Mid-pleistocene revolution and the 'eccentricity myth'. *Geological Society, London, Special Publications*, *247*(1), 19–34.

Matsumura, S., Ida, S., & Nagasawa, M. (2013, April). Effects of Dynamical Evolution of Giant Planets on Survival of Terrestrial Planets. *Astrophysical Journal*, *767*(2), 129. doi: 10.1088/0004-637X/767/2/129

McInerney, F. A., & Wing, S. L. (2011). The paleocene-eocene thermal maximum: A perturbation of carbon cycle, climate, and biosphere with implications for the future. *Annual Review of Earth and Planetary Sciences*, *39*, 489–516.

Meadows, V. S., & Barnes, R. K. (2018). Factors Affecting Exoplanet Habitability. In H. J. Deeg & J. A. Belmonte (Eds.), *Handbook of exoplanets* (p. 57). doi: 10.1007/978-3-319-55333-7_57

Menegatti, A. P., Weissert, H., Brown, R. S., Tyson, R. V., Farrimond, P., Strasser, A., & Caron, M. (1998). High-resolution δ13c stratigraphy through the early aptian "livello selli" of the alpine tethys. *Paleoceanography*, *13*(5), 530–545.

Menou, K., & Tabachnik, S. (2003, January). Dynamical Habitability of Known Extrasolar Planetary Systems. *The Astrophysical Journal*, *583*(1), 473-488. doi: 10.1086/345359

Menviel, L., Timmermann, A., Timm, O. E., & Mouchet, A. (2011). Deconstructing the last glacial termination: the role of millennial and orbital-scale forcings. *Quaternary Science Reviews*, *30*(9-10), 1155–1172.

Meyer, K., Yu, M., Jost, A., Kelley, B., & Payne, J. (2011). δ13c evidence that high primary productivity delayed recovery from end-permian mass extinction. *Earth and Planetary Science Letters*, *302*(3-4), 378–384.

Meyer, K. M., Kump, L. R., & Ridgwell, A. (2008, September). Biogeochemical controls on photic-zone euxinia during the end-Permian mass extinction. *Geology*, *36*(9), 747-750. doi: 10.1130/G24618A.1

Meyers, S. (2014). *Astrochron: An r package for astrochronology.*

Milankovitch, M. (1941). Canon of insolation and the iceage problem. *Koniglich Serbische Akademice Beograd Special Publication*, *132*.

Mix, A. C., Pisias, N. G., Rugh, W., Wilson, J., Morey, A., & Hagelberg, T. (1995). Benthic foraminifer stable isotope record from site 849 (0-5 ma): Local and global climate changes.

Monteiro, F. M., Pancost, R. D., Ridgwell, A., & Donnadieu, Y. (2012). Nutrients as the dominant control on the spread of anoxia and euxinia across the cenomanian-turonian oceanic anoxic event (oae2): Model-data comparison. *Paleoceanography*, *27*(4).

Mook, W. (1986). 13c in atmospheric co2. *Netherlands Journal of Sea Research*, *20*(2-3), 211–223.

Motalebi, F., Udry, S., Gillon, M., Lovis, C., Ségransan, D., Buchhave, L. A., ... Watson, C. A. (2015, December). The HARPS-N Rocky Planet Search. I. HD 219134 b: A transiting rocky planet in a multi-planet system at 6.5 pc from the Sun. *Astronomy and Astrophysics*, *584*, A72. doi: 10.1051/0004-6361/201526822

Müller, T., Price, G. D., Bajnai, D., Nyerges, A., Kesjár, D., Raucsik, B., ... others (2017). New multiproxy record of the jenkyns event (also known as the toarcian oceanic anoxic event) from the mecsek mountains (hungary): Differences, duration and drivers. *Sedimentology*, *64*(1), 66–86.

Mutterlose, J., Bottini, C., Schouten, S., & Sinninghe Damsté, J. S. (2014). High sea-surface temperatures during the early aptian oceanic anoxic event 1a in the boreal realm. *Geology*, *42*(5), 439–442.

Naafs, B., & Pancost, R. (2016). Sea-surface temperature evolution across aptian oceanic anoxic event 1a. *Geology*, *44*(11), 959–962.

Nagasawa, M., Thommes, E. W., Kenyon, S. J., Bromley, B. C., & Lin, D. N. C. (2007, January). The Diverse Origins of Terrestrial-Planet Systems. In B. Reipurth, D. Jewitt, & K. Keil (Eds.), *Protostars and planets v* (p. 639).

Neron de Surgy, O., & Laskar, J. (1997, February). On the long term evolution of the spin of the Earth. *Astronomy and Astrophysics*, *318*, 975-989.

Norris, R., Turner, S. K., Hull, P., & Ridgwell, A. (2013). Marine ecosystem responses to cenozoic global change. *Science*, *341*(6145), 492–498.

Ödalen, M., Nycander, J., Oliver, K. I., Brodeau, L., & Ridgwell, A. (2018). The influence of the ocean circulation state on ocean carbon storage and co 2 drawdown potential in an earth system model. *Biogeosciences*, *15*(5), 1367–1393.

Opdyke, B. N., & Wilkinson, B. H. (1988). Surface area control of shallow cratonic to deep marine carbonate accumulation. *Paleoceanography*, *3*(6), 685–703.

Paillard, D., & Donnadieu, Y. (2014). A 100 myr history of the carbon cycle based on the 400 kyr cycle in marine δ13c benthic records. *Paleoceanography*, *29*(12), 1249–1255.

Pálfy, J., Demény, A., Haas, J., Hetényi, M., Orchard, M. J., & Veto, I. (2001). Carbon isotope anomaly and other geochemical changes at the triassic-jurassic boundary from a marine section in hungary. *Geology*, *29*(11), 1047–1050.

Palike, H., Norris, R. D., Herrle, J. O., Wilson, P. A., Coxall, H. K., Lear, C. H., ... Wade, B. S. (2006). The heartbeat of the oligocene climate system. *science*, *314*(5807), 1894–1898.

Panchuk, K., Ridgwell, A., & Kump, L. (2008). Sedimentary response to paleocene-eocene thermal maximum carbon release: A model-data comparison. *Geology*, *36*(4), 315–318.

Paytan, A., & McLaughlin, K. (2007). The oceanic phosphorus cycle. *Chemical reviews*, *107*(2), 563–576.

Peng, G., & Meier, W. N. (2018, July). Temporal and regional variability of Arctic sea-ice coverage from satellite data. *Annals of Glaciology*, *59*, 191-200. doi: 10.1017/aog.2017.32

Penman, D. E., Turner, S. K., Sexton, P. F., Norris, R. D., Dickson, A. J., Boulila, S., ... others (2016). An abyssal carbonate compensation depth overshoot in the aftermath of the palaeocene–eocene thermal maximum. *Nature Geoscience*, *9*(8), 575–580.

Perovich, D. K., Maykut, G. A., & Grenfell, T. C. (1986, August). Optical Properties Of Ice And Snow In The Polar Oceans. I: Observations. In *Society of photo-optical instrumentation engineers (spie) conference series* (Vol. 637, p. 232-241). doi: 10.1117/12.964238

Peterson, C. D., Lisiecki, L. E., & Stern, J. V. (2014). Deglacial whole-ocean δ13c change estimated from 480 benthic foraminiferal records. *Paleoceanography*, *29*(6), 549–563.

Petoukhov, V., Ganopolski, A., Brovkin, V., Claussen, M., Eliseev, A., Kubatzki, C., & Rahmstorf, S. (2000). Climber-2: a climate system model of intermediate complexity. part i: model description and performance for present climate. *Climate dynamics*, *16*(1), 1–17.

Pollard, D. (1978, March). An investigation of the astronomical theory of the ice ages using a simple climate-ice sheet model. *Nature*, *272*(5650), 233-235. doi: 10.1038/272233a0

Poulton, S. W., Henkel, S., März, C., Urquhart, H., Flögel, S., Kasten, S., ... Wagner, T. (2015). A continental-weathering control on orbitally driven redox-nutrient cycling during cretaceous oceanic anoxic event 2. *Geology*, *43*(11), 963–966.

Quarles, B., Barnes, J. W., Lissauer, J. J., & Chambers, J. (2020, January). Obliquity Evolution of the Potentially Habitable Exoplanet Kepler-62f. *Astrobiology*, *20*(1), 73-90. doi: 10.1089/ast.2018.1932

Quarles, B., Li, G., & Lissauer, J. J. (2022, January). Milankovitch cycles for a circumstellar Earth-analogue within α Centauri-like binaries. *Monthly Notices of the RAS*, *509*(2), 2736-2757. doi: 10.1093/mnras/stab3179

Rau, G. H., Riebesell, U., & Wolf-Gladrow, D. (1996). A model of photosynthetic 13c fractionation by marine phytoplankton based on diffusive molecular co2 uptake. *Marine Ecology Progress Series*, *133*, 275–285.

Ridgwell, A. (2005). A mid mesozoic revolution in the regulation of ocean chemistry. *Marine Geology*, *217*(3-4), 339–357.

Ridgwell, A., & Hargreaves, J. (2007). Regulation of atmospheric co2 by deep-sea sediments in an earth system model. *Global Biogeochemical Cycles*, *21*(2).

Ridgwell, A., Hargreaves, J., Edwards, N. R., Annan, J., Lenton, T. M., Marsh, R., ... Watson, A. (2007). Marine geochemical data assimilation in an efficient earth system model of global biogeochemical cycling. *Biogeosciences*, *4*(1), 87–104.

Ridgwell, A., & Schmidt, D. N. (2010). Past constraints on the vulnerability of marine calcifiers to massive carbon dioxide release. *Nature Geoscience*, *3*(3), 196–200.

Rivkin, R. B., & Legendre, L. (2001). Biogenic carbon cycling in the upper ocean: effects of microbial respiration. *Science*, *291*(5512), 2398–2400.

Röhl, U., Westerhold, T., Bralower, T. J., & Zachos, J. C. (2007). On the duration of the paleocene-eocene thermal maximum (petm). *Geochemistry, Geophysics, Geosystems*, *8*(12).

Roychowdhury, R., & DeConto, R. (2019). Interhemispheric effect of global geography on earth's climate response to orbital forcing. *Climate of the Past*, *15*(1), 377–388.

Rubincam, D. P. (1990, May). Mars - Change in axial tilt due to climate? *Science*, *248*, 720. doi: 10.1126/science.248.4956.720

Rushby, A. J., Claire, M. W., Osborn, H., & Watson, A. J. (2013, September). Habitable Zone Lifetimes of Exoplanets around Main Sequence Stars. *Astrobiology*, *13*(9), 833-849. doi: 10.1089/ast.2012.0938

Ruttenberg, K. C., & Berner, R. A. (1993). Authigenic apatite formation and burial in sediments from non-upwelling, continental margin environments. *Geochimica et cosmochimica acta*, *57*(5), 991–1007.

Ruvalcaba Baroni, I., Palastanga, V., & Slomp, C. P. (2020). Enhanced organic carbon burial in sediments of oxygen minimum zones upon ocean deoxygenation. *Frontiers in Marine Science*, *6*, 839.

Saltzman, M., Thomas, E., & Gradstein, F. (2012). Carbon isotope stratigraphy. *The geologic time scale*, *1*, 207–232.

Schouten, S., Hopmans, E. C., Rosell-Melé, A., Pearson, A., Adam, P., Bauersachs, T., ... others (2013). An interlaboratory study of tex86 and bit analysis of sediments, extracts, and standard mixtures. *Geochemistry, Geophysics, Geosystems*, *14*(12), 5263–5285.

Sexton, P. F., Norris, R. D., Wilson, P. A., Pälike, H., Westerhold, T., Röhl, U., ... Gibbs, S. (2011). Eocene global warming events driven by ventilation of oceanic dissolved organic carbon. *Nature*, *471*(7338), 349–352.

Shan, Y., & Li, G. (2018, June). Obliquity Variations of Habitable Zone Planets Kepler-62f and Kepler-186f. *Astronomical Journal*, *155*(6), 237. doi: 10.3847/1538-3881/aabfd1

Shields, A. L., Barnes, R., Agol, E., Charnay, B., Bitz, C., & Meadows, V. S. (2016, June). The Effect of Orbital Configuration on the Possible Climates and Habitability of Kepler-62f. *Astrobiology*, *16*(6), 443-464. doi: 10.1089/ast.2015.1353

Shields, A. L., Meadows, V. S., Bitz, C. M., Pierrehumbert, R. T., Joshi, M. M., & Robinson, T. D. (2013, August). The Effect of Host Star Spectral Energy Distribution and Ice-Albedo Feedback on the Climate of Extrasolar Planets. *Astrobiology*, *13*(8), 715-739. doi: 10.1089/ast.2012.0961

Short, D. A., Mengel, J. G., Crowley, T. J., Hyde, W. T., & North, G. R. (1991). Filtering of milankovitch cycles by earth's geography. *Quaternary Research*, *35*(2), 157–173.

Sigman, D. M., & Boyle, E. A. (2000, October). Glacial/interglacial variations in atmospheric carbon dioxide. *Nature*, *407*(6806), 859-869. doi: 10.1038/35038000

Sloan, L. C., & Huber, M. (2001). Eocene oceanic responses to orbital forcing on precessional time scales. *Paleoceanography*, *16*(1), 101–111.

Sluijs, A., & Dickens, G. R. (2012). Assessing offsets between the δ13c of sedimentary components and the global exogenic carbon pool across early paleogene carbon cycle perturbations. *Global Biogeochemical Cycles*, *26*(4).

Sluijs, A., Schouten, S., Donders, T. H., Schoon, P. L., Röhl, U., Reichart, G.-J., ... Brinkhuis, H. (2009). Warm and wet conditions in the arctic region during eocene thermal maximum 2. *Nature Geoscience*, *2*(11), 777–780.

Smith, S. V. (1984). Phosphorus versus nitrogen limitation in the marine environment 1. *Limnology and oceanography*, *29*(6), 1149–1160.

Spiegel, D. S., Menou, K., & Scharf, C. A. (2009, January). Habitable Climates: The Influence of Obliquity. *Astrophysical Journal*, *691*(1), 596-610. doi: 10.1088/0004-637X/691/1/596

Spiegel, D. S., Raymond, S. N., Dressing, C. D., Scharf, C. A., & Mitchell, J. L. (2010, October). Generalized Milankovitch Cycles and Long-Term Climatic Habitability. *The Astrophysical Journal*, *721*(2), 1308-1318. doi: 10.1088/0004-637X/721/2/1308

Sproson, A. D. (2020). Pacing of the latest ordovician and silurian carbon cycle by a˜ 4.5 myr orbital cycle. *Palaeogeography, Palaeoclimatology, Palaeoecology*, *540*, 109543.

Stap, L., Sluijs, A., Thomas, E., & Lourens, L. (2009). Patterns and magnitude of deep sea carbonate dissolution during eocene thermal maximum 2 and h2, walvis ridge, southeastern atlantic ocean. *Paleoceanography*, *24*(1).

Suess, H. E. (1955). Radiocarbon concentration in modern wood. *Science*, *122*(3166), 415–417.

Sundquist, E., Visser, K., & Schlesinger, W. (2005). The geologic history of the carbon cycle. *Biogeochemistry*, *8*, 425–472.

Thomas, E., & Zachos, J. (1999). Isotopic, paleontologic, and other evidence for multiple transient thermal maxima in the paleocene and eocene. *Eos Trans. AGU*, *80*(46).

Thompson, S. L., & Pollard, D. (1997). Greenland and antarctic mass balances for present and doubled atmospheric co2 from the genesis version-2 global climate model. *Journal of Climate*, *10*(5), 871–900.

Tian, J., Ma, X., Zhou, J., Jiang, X., Lyle, M., Shackford, J., & Wilkens, R. (2018). Paleoceanography of the east equatorial pacific over the past 16 myr and pacific–atlantic comparison: High resolution benthic foraminiferal δ18o and δ13c records at iodp site u1337. *Earth and Planetary Science Letters*, *499*, 185–196.

Tóth, Z., & Nagy, I. (2014, July). Dynamical stability of the Gliese 581 exoplanetary system. *Monthly Notices of the RAS*, *442*(1), 454-461. doi: 10.1093/mnras/stu849

Touma, J., & Wisdom, J. (1998, April). Resonances in the Early Evolution of the Earth-Moon System. *Astronomical Journal*, *115*(4), 1653-1663. doi: 10.1086/300312

Truitt, A. R., Young, P. A., Walker, S. I., & Spacek, A. (2020, February). A Flexible Bayesian Framework for Assessing Habitability with Joint Observational and Model Constraints. *Astronomical Journal*, *159*(2), 55. doi: 10.3847/1538-3881/ab4e93

Turner, S. K. (2018). Constraints on the onset duration of the paleocene–eocene thermal maximum. *Philosophical Transactions of the Royal Society A: Mathematical, Physical and Engineering Sciences*, *376*(2130), 20170082.

Turner, S. K., & Ridgwell, A. (2016). Development of a novel empirical framework for interpreting geological carbon isotope excursions, with implications for the rate of carbon injection across the petm. *Earth and Planetary Science Letters*, *435*, 1–13.

Van Eylen, V., & Albrecht, S. (2015, August). Eccentricity from Transit Photometry: Small Planets in Kepler Multi-planet Systems Have Low Eccentricities. *Astrophysical Journal*, *808*(2), 126. doi: 10.1088/0004-637X/808/2/126

Van Cappellen, P., & Ingall, E. D. (1994). Benthic phosphorus regeneration, net primary production, and ocean anoxia: a model of the coupled marine biogeochemical cycles of carbon and phosphorus. *Paleoceanography*, *9*(5), 677–692.

Van Cappellen, P., & Ingall, E. D. (1996). Redox stabilization of the atmosphere and oceans by phosphorus-limited marine productivity. *Science*, *271*(5248), 493–496.

van der Ploeg, R., Selby, D., Cramwinckel, M. J., Li, Y., Bohaty, S. M., Middelburg, J. J., & Sluijs, A. (2018). Middle eocene greenhouse warming facilitated by diminished weathering feedback. *Nature communications*, *9*(1), 1–10.

Vervoort, P., Adloff, M., Greene, S. E., & Turner, S. K. (2019). Negative carbon isotope excursions: an interpretive framework. *Environmental Research Letters*, *14*(8), 085014.

Vervoort, P., Kirtland Turner, S., Rochholz, F., & Ridgwell, A. (2021). Earth system model analysis of how astronomical forcing is imprinted onto the marine geological record: The role of the inorganic (carbonate) carbon cycle and feedbacks. *Paleoceanography and Paleoclimatology*, *36*(10), e2020PA004090.

Volland, H. (1996, January). Atmosphere and Earth's rotation. *Surveys in Geophysics*, *17*(1), 101-144. doi: 10.1007/BF01904476

Walker, J. C., Hays, P., & Kasting, J. F. (1981). A negative feedback mechanism for the long-term stabilization of earth's surface temperature. *Journal of Geophysical Research: Oceans*, *86*(C10), 9776–9782.

Wallmann, K. (2003). Feedbacks between oceanic redox states and marine productivity: A model perspective focused on benthic phosphorus cycling. *Global biogeochemical cycles*, *17*(3).

Wallmann, K. (2010). Phosphorus imbalance in the global ocean? *Global Biogeochemical Cycles*, *24*(4).

Waltham, D. (2015, August). Milankovitch Period Uncertainties and Their Impact On Cyclostratigraphy. *Journal of Sedimentary Research*, *85*(8), 990-998. doi: 10.2110/jsr.2015.66

Wang, P., Tian, J., & Lourens, L. J. (2010). Obscuring of long eccentricity cyclicity in pleistocene oceanic carbon isotope records. *Earth and Planetary Science Letters*, *290*(3-4), 319–330.

Wang, Y., Liu, Y., Tian, F., Yang, J., Ding, F., Zhou, L., & Hu, Y. (2016, May). Effects of Obliquity on the Habitability of Exoplanets around M Dwarfs. *Astrophysical Journal, Letters*, *823*(1), L20. doi: 10.3847/2041-8205/823/1/L20

Ward, W. R. (1982, June). Comments on the long-term stability of the Earth's obliquity. *Icarus*, *50*(2-3), 444-448. doi: 10.1016/0019-1035(82)90134-8

Ward, W. R., Burns, J. A., & Toon, O. B. (1979, January). Past obliquity oscillations of Mars: the role of the Tharsis uplift. *Journal of Geophysics Research*, *84*, 243-259. doi: 10.1029/JB084iB01p00243

Way, M. J., & Georgakarakos, N. (2017, January). Effects of Variable Eccentricity on the Climate of an Earth-like World. *Astrophysical Journal, Letters*, *835*(1), L1. doi: 10.3847/2041-8213/835/1/L1

Weaver, A. J., Eby, M., Wiebe, E. C., Bitz, C. M., Duffy, P. B., Ewen, T. L., ... others (2001). The uvic earth system climate model: Model description, climatology, and applications to past, present and future climates. *Atmosphere-Ocean*, *39*(4), 361–428.

Weiss, L. M., Marcy, G. W., Rowe, J. F., Howard, A. W., Isaacson, H., Fortney, J. J., ... Seager, S. (2013, May). The Mass of KOI-94d and a Relation for Planet Radius, Mass, and Incident Flux. *Astrophysical Journal*, *768*(1), 14. doi: 10.1088/0004-637X/768/1/14

Westerhold, T., Röhl, U., Donner, B., McCarren, H. K., & Zachos, J. C. (2011). A complete high-resolution paleocene benthic stable isotope record for the central pacific (odp site 1209). *Paleoceanography*, *26*(2).

Westerhold, T., Röhl, U., Donner, B., & Zachos, J. (2018). Global extent of early eocene hyperthermal events: A new pacific benthic foraminiferal isotope record from shatsky rise (odp site 1209). *Paleoceanography and Paleoclimatology*, *33*(6), 626–642.

Westerhold, T., Röhl, U., Wilkens, R., Gingerich, P., Clyde, W., Wing, S., ... Kraus, M. (2018). Synchronizing early eocene deep-sea and continental records–cyclostratigraphic age models for the bighorn basin coring project drill cores. *Climate of the Past*, *14*(3), 303–319.

Willeit, M., Ganopolski, A., & Feulner, G. (2013). On the effect of orbital forcing on mid-pliocene climate, vegetation and ice sheets. *Climate of the Past*, *9*(4), 1749–1759.

Williams, D. M., & Pollard, D. (2002, January). Earth-like worlds on eccentric orbits: excursions beyond the habitable zone. *International Journal of Astrobiology*, *1*(1), 61-69. doi: 10.1017/S1473550402001064

Williams, D. M., & Pollard, D. (2003, January). Extraordinary climates of Earth-like planets: three-dimensional climate simulations at extreme obliquity. *International Journal of Astrobiology*, *2*(1), 1-19. doi: 10.1017/S1473550403001356

Williams, G. (1993, March). History of the earth's obliquity. *Earth Science Reviews*, *34*(1), 1-45. doi: 10.1016/0012-8252(93)90004-Q

Wilson, P. A., & Norris, R. D. (2001). Warm tropical ocean surface and global anoxia during the mid-cretaceous period. *Nature*, *412*(6845), 425–429.

Winkelmann, R., Levermann, A., Ridgwell, A., & Caldeira, K. (2015). Combustion of available fossil fuel resources sufficient to eliminate the antarctic ice sheet. *Science advances*, *1*(8), e1500589.

Xiao, D., Zhao, P., Wang, Y., & Zhou, X. (2013). Modeling the climatic implications and indicative senses of the guliya δ18o-temperature proxy record to the ocean–atmosphere system during the past 130 ka. *Climate of the Past*, *9*(2), 735–747.

Yoder, C. F. (1995, October). Venus' free obliquity. *Icarus*, *117*(2), 250-286. doi: 10.1006/icar.1995.1156

Zachos, J. C., Dickens, G. R., & Zeebe, R. E. (2008). An early cenozoic perspective on greenhouse warming and carbon-cycle dynamics. *nature*, *451*(7176), 279–283.

Zachos, J. C., McCarren, H., Murphy, B., Röhl, U., & Westerhold, T. (2010). Tempo and scale of late paleocene and early eocene carbon isotope cycles: Implications for the origin of hyperthermals. *Earth and Planetary Science Letters*, *299*(1-2), 242–249.

Zachos, J. C., Pagani, M., Sloan, L., Thomas, E., & Billups, K. (2001). Trends, rhythms, and aberrations in global climate 65 ma to present. *science*, *292*(5517), 686–693.

Zahnle, K. J., Lupu, R., Dobrovolskis, A., & Sleep, N. H. (2015, October). The tethered Moon. *Earth and Planetary Science Letters*, *427*, 74-82. doi: 10.1016/j.epsl.2015.06.058

Zeebe, R. E., Westerhold, T., Littler, K., & Zachos, J. C. (2017). Orbital forcing of the paleocene and eocene carbon cycle. *Paleoceanography*, *32*(5), 440–465.

Zeebe, R. E., & Wolf-Gladrow, D. (2001). *Co2 in seawater: equilibrium, kinetics, isotopes* (No. 65). Gulf Professional Publishing.

Zeebe, R. E., & Zachos, J. C. (2013). Long-term legacy of massive carbon input to the earth system: Anthropocene versus eocene. *Philosophical Transactions of the Royal Society A: Mathematical, Physical and Engineering Sciences*, *371*(2001), 20120006.

Zhang, J., Quay, P., & Wilbur, D. (1995). Carbon isotope fractionation during gas-water exchange and dissolution of co2. *Geochimica et Cosmochimica Acta*, *59*(1), 107–114.

Appendix A

Supplementary Information:

Chapter 2

Table A.1: Carbon reservoirs and pumps during cGENIE initial steady-state conditions. Dissolved inorganic carbon (DIC), dissolved organic carbon (DOC), particulate organic carbon (POC), calcium carbonate ($CaCO_3$).

	Symmetric (this study)	Panchuk et al. (2008)
DIC pool	∼30,000 Pg C	∼30,000 Pg C
DOC pool	∼6.7 Pg C	∼5.8 Pg C
POC export	6.96 PgC yr^{-1}	5.95 PgC yr^{-1}
$CaCO_3$ export	1.39 PgC yr^{-1}	1.19 PgC yr^{-1}

Table A.2: Surface water properties during cGENIE initial steady state conditions. Sea surface tempertaure (SST), sea surface salinity (SSS).

	Symmetric (this study)	Panchuk et al. (2008)
Global mean SST	25.75°C	27.02°C
Global mean SSS	34.09 psu	33.76 psu
Global mean pH	7.72	7.74

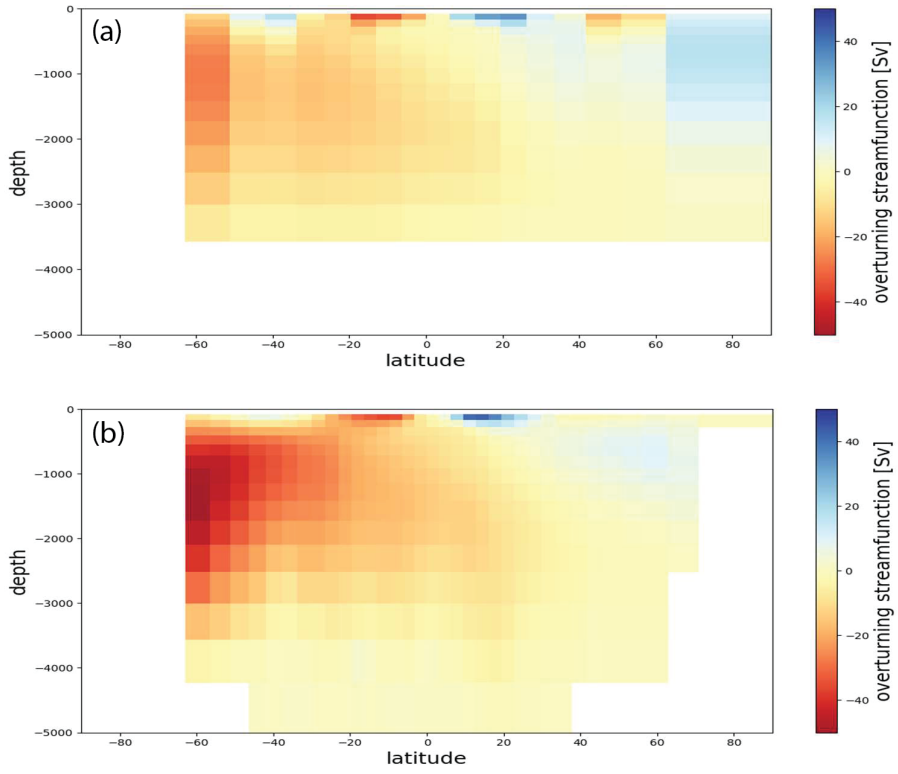

Figure A.1: Zonally averaged overturning circulation strengths in (a) the symmetric pole-to-pole continental configuration used in this study, compared to (b) the late Paleocene as per Panchuk et al. (2008).

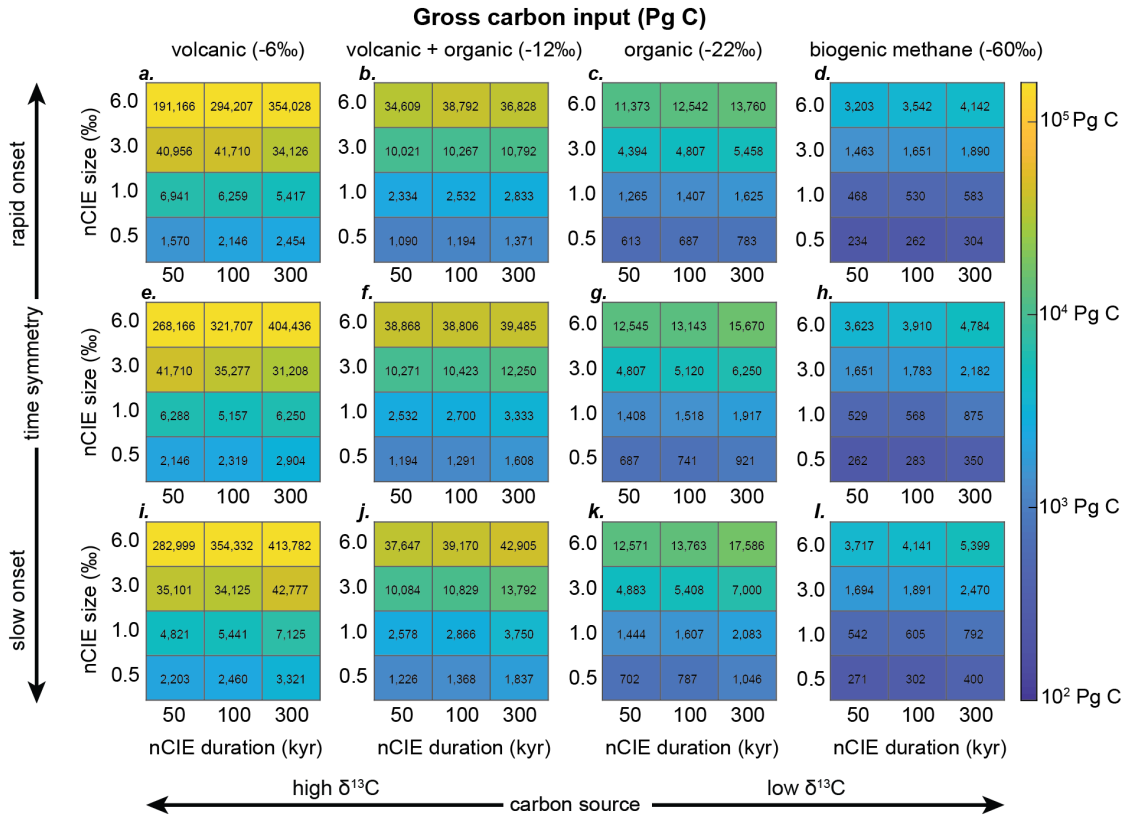

Figure A.2: Gross C input over the nCIE onset for nCIEs that vary in duration, nCIE size, duration symmetry, and carbon source. Subplots a-d are scenarios in which nCIEs have a rapid onset, slow recovery (25% vs 75% of total duration). Subplots e-h are scenarios in which nCIEs have a symmetric shape with equal onset and recovery duration (50% vs 50%). Subplots i-l are scenarios in which nCIEs have a slow onset, rapid recovery (75% vs 25% of total duration). Variations in size symmetry are excluded because the ending δ^{13}C value does not influence gross C input over the experiment onset. The subplot columns from left to right are nCIEs forced with carbon of δ^{13}C -6.0‰, -12‰, -22‰and -60‰, respectively. Within each subplot the gross carbon input required to generate nCIEs with various total durations and sizes is shown and color coded.

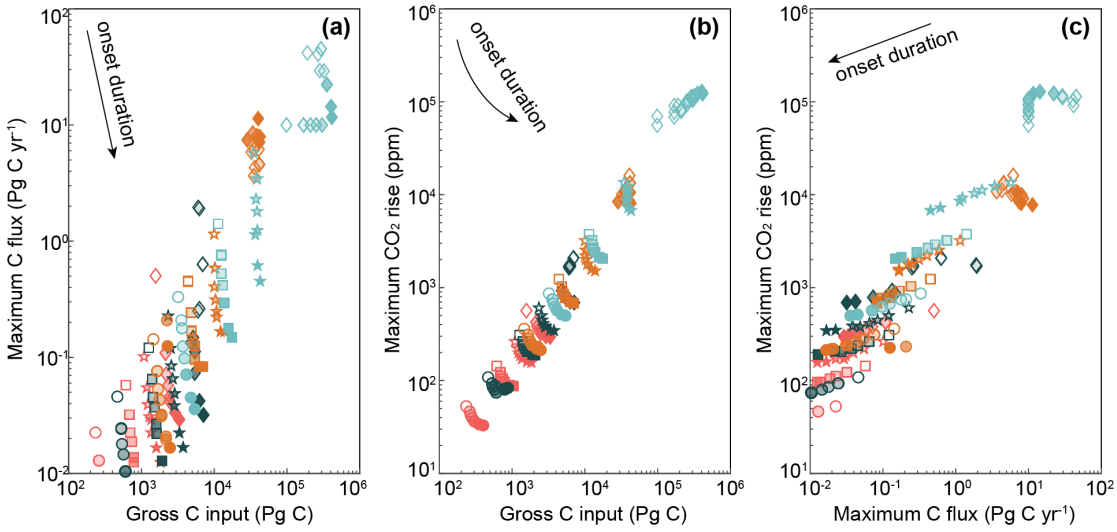

Figure A.3: Cross-plots between the maximum sustained carbon flux, gross carbon input, and atmospheric CO_2. a) The mass of carbon input versus the maximum sustained flux of carbon, b) The mass of carbon input versus the maximum rise in atmospheric CO_2, and c) the maximum sustained flux of carbon versus the maximum rise in atmospheric CO_2 for all simulated nCIEs. For each set of simulations of certain nCIE size and carbon source, the direction of increasing onset duration is indicated with an arrow.

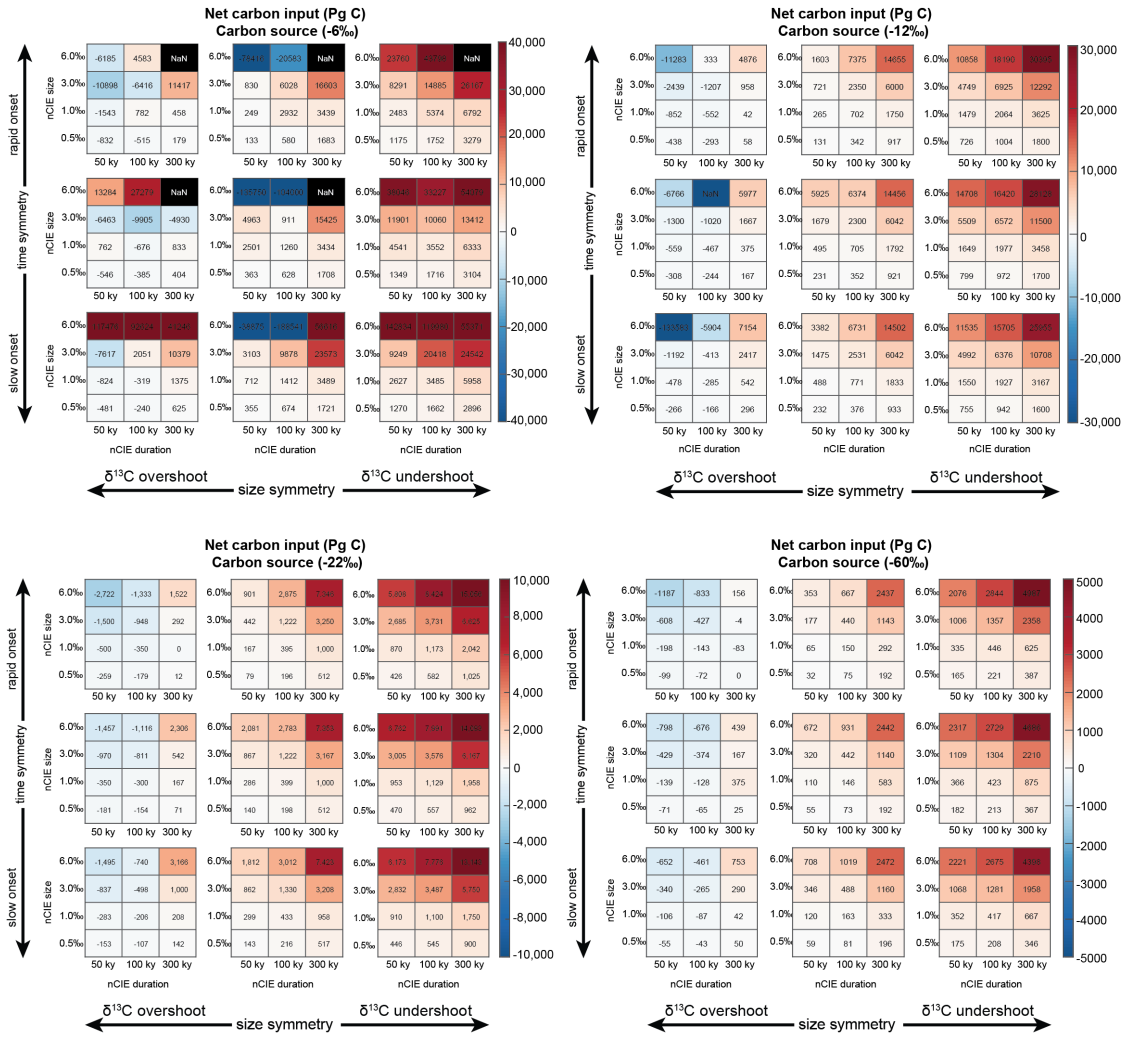

Figure A.4: Net carbon input (carbon input minus removal) throughout the total nCIE duration required to match the prescribed nCIE profile. nCIEs are forced with carbon with a carbon isotopic signature of -6‰ (top left), -12‰ (top right), -22‰ (bottom left), and -60‰ (bottom right). Subplot rows from top to bottom are scenarios in which nCIEs have a rapid onset and slow recovery (25% vs 75% of total duration), a symmetric shape with equal onset and recovery duration (50% vs 50%) or have a slow onset and rapid recovery (75% vs 25% of total duration). The subplot columns from left to right are nCIEs with an overshoot, 'no shoot' and undershoot, respectively. Within each subplot the net carbon input required to generate nCIEs with various total durations and sizes is shown and color coded.

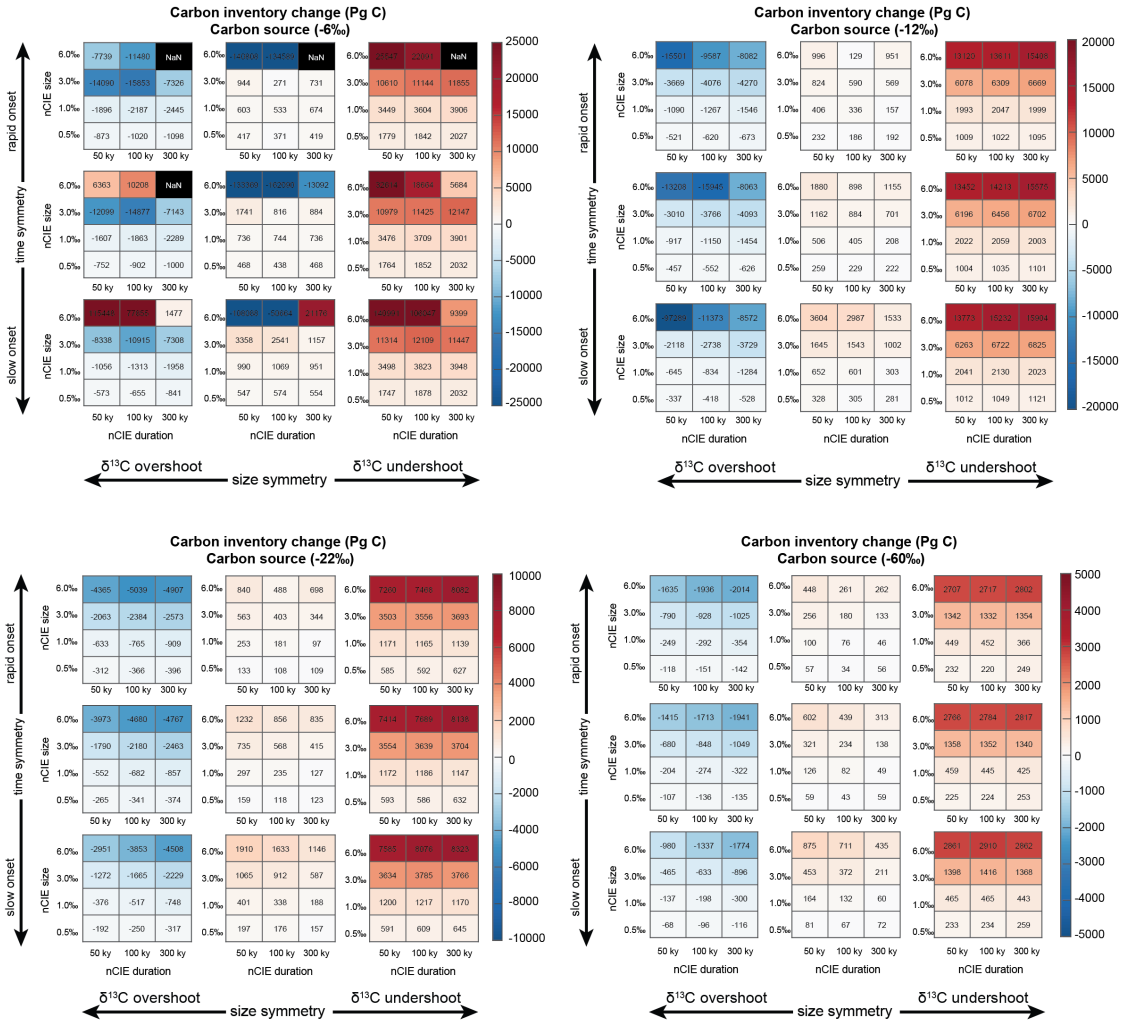

Figure A.5: Change in mass of carbon in the exchangeable reservoir from nCIE onset to end to match the prescribed CIE profile. nCIEs are forced with carbon with a carbon isotopic signature of -6‰ (top left), -12‰ (top right), -22‰ (bottom left), and -60‰ (bottom right). Subplot rows from top to bottom are scenarios in which nCIEs have a rapid onset and slow recovery (25% vs 75% of total duration), a symmetric shape with equal onset and recovery duration (50% vs 50%) or have a slow onset and rapid recovery (75% vs 25% of total duration). The subplot columns from left to right are nCIEs with an overshoot, 'no shoot' and undershoot, respectively. Within each subplot the carbon inventory of the exchangeable reservoir at the end of a nCIE relative to the initial conditions is shown and color coded.

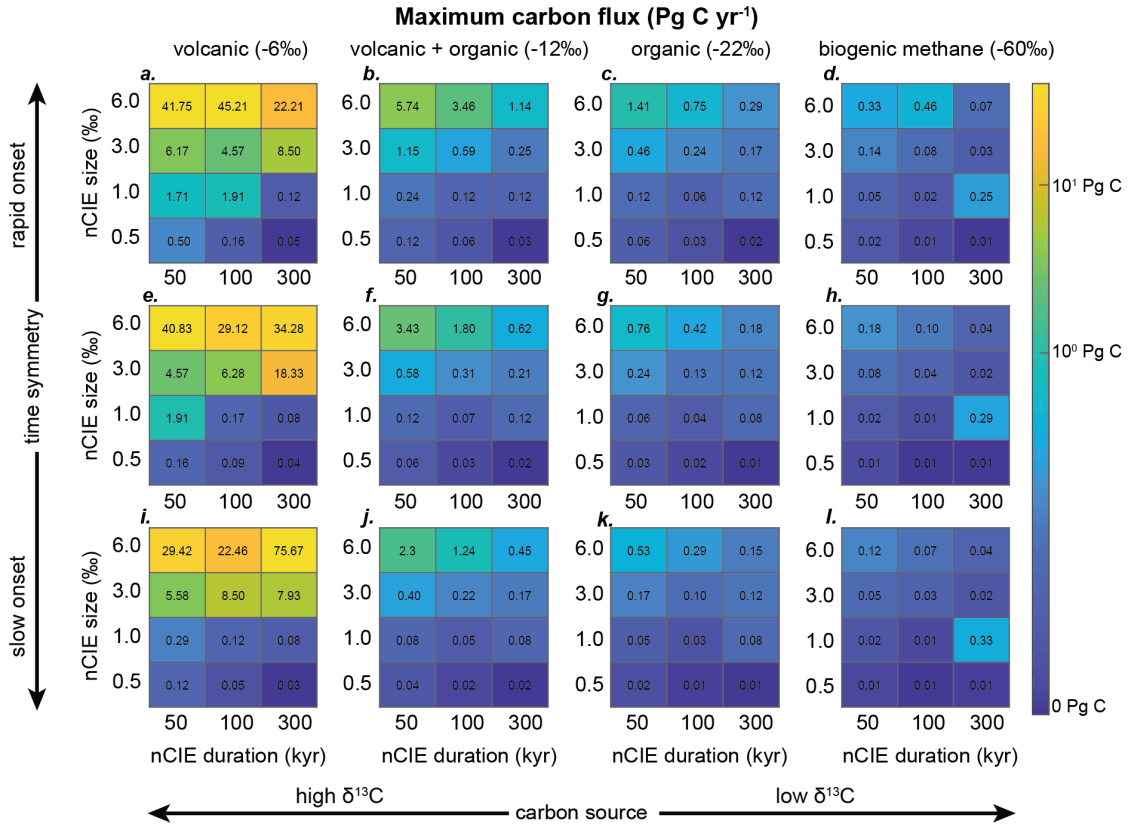

Figure A.6: Maximum carbon input rates during nCIE onset phase required to match the prescribed nCIE profile. Subplots a-d are scenarios in which nCIEs have a rapid onset, slow recovery (25% vs 75% of total duration). Subplots e-h are scenarios in which nCIEs have a symmetric shape with equal onset and recovery duration (50% vs 50%). Subplots i-l are scenarios in which nCIEs have a slow onset, rapid recovery (75% vs 25% of total duration). Variations in size symmetry are excluded because the ending δ^{13}C value does not influence gross C input and associated fluxes over the experiment onset. The subplot columns from left to right are nCIEs forced with carbon of -6.0‰, -12‰, -22‰, and -60‰, respectively. Within each subplot the maximum carbon input fluxes required to generate nCIEs with various total durations and sizes is shown.

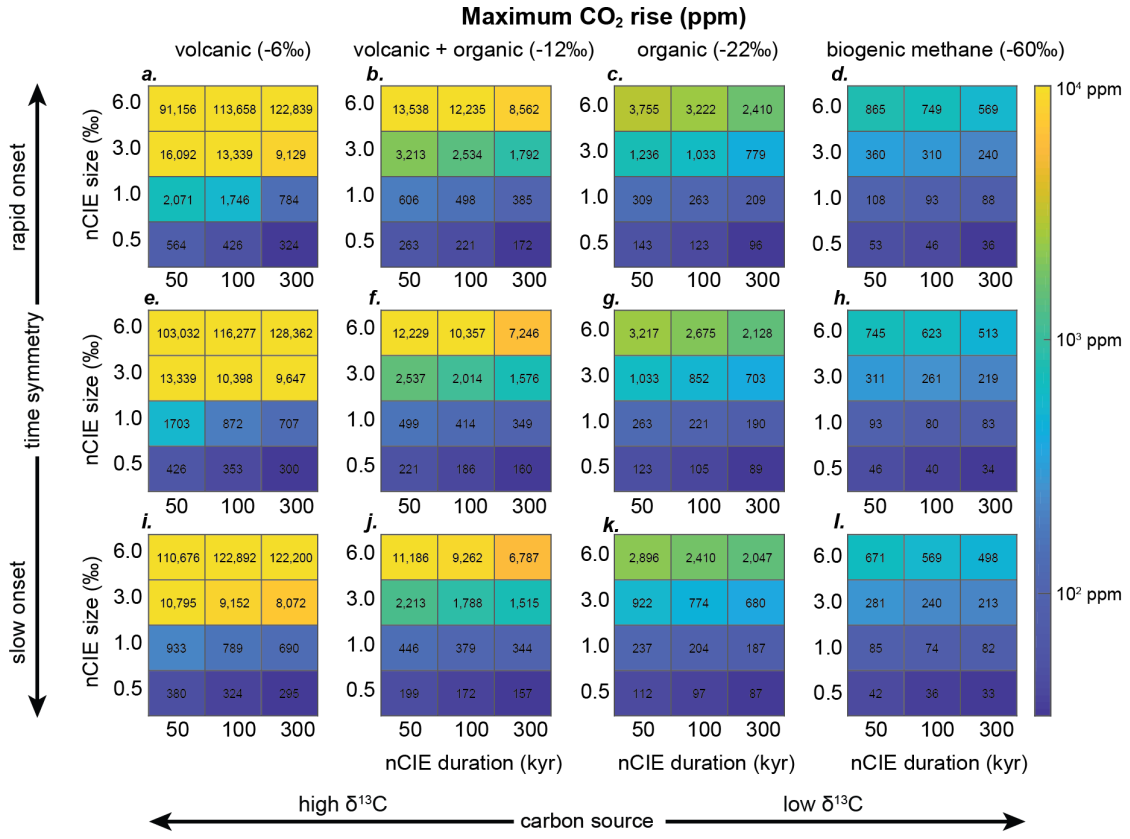

Figure A.7: Maximum increases in atmospheric carbon dioxide (CO_2) concentrations during the nCIE peak. Subplots a-d are scenarios in which nCIEs have a rapid onset, slow recovery (25% vs 75% of total duration). Subplots e-h are scenarios in which nCIEs have a symmetric shape with equal onset and recovery duration (50% vs 50%). Subplots i-l are scenarios in which nCIEs have a slow onset, rapid recovery (75% vs 25% of total duration). Variations in size symmetry are excluded because the final $\delta^{13}C$ value at the end of the recovery phase does not influence C input over the nCIE onset or and associated CO_2 (atm) concentrations. The subplot columns from left to right are nCIEs forced with carbon of -6.0‰, -12‰, -22‰and -60‰, respectively. Within each subplot the maximum increase in CO_2 (atm) associated with the nCIEs of various total durations and sizes is shown.

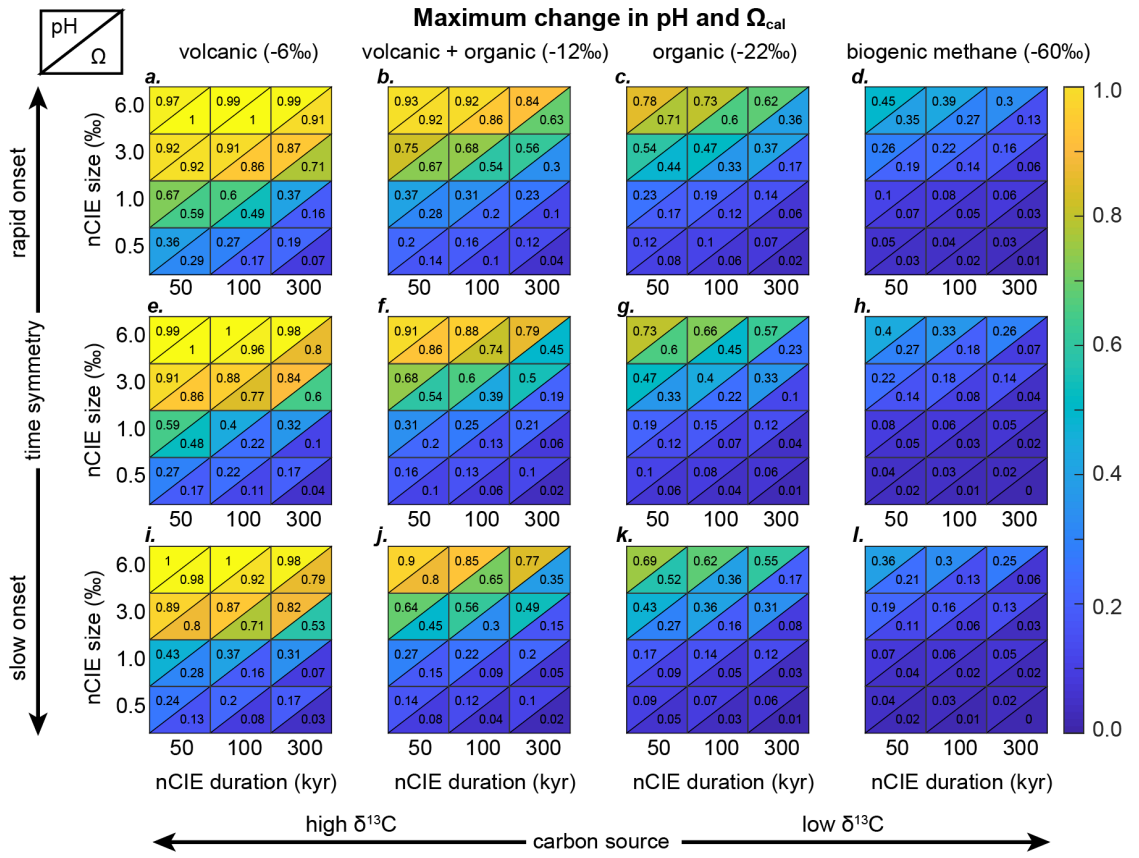

Figure A.8: Maximum change in pH and calcite saturation state (Ω_{cal}) reached during the nCIE peak. Subplots a-d are scenarios in which nCIEs have a rapid onset, slow recovery (25% vs 75% of total duration). Subplots e-h are scenarios in which nCIEs have a symmetric shape with equal onset and recovery duration (50% vs 50%). Subplots i-l are scenarios in which nCIEs have a slow onset, rapid recovery (75% vs 25% of total duration). Variations in size symmetry are excluded because the final $\delta^{13}C$ value at the end of the recovery phase does not influence carbonate chemistry at the nCIE peak. The subplot columns from left to right are nCIEs forced with carbon of -6.0‰, -12‰, -22‰, and -60‰, respectively. Within each subplot the relative changes in pH and Ω_{cal} are shown as a proportion of the maximum changes across all experiments (max. ΔpH = 1.7 and max. $\Delta\Omega_{cal}$ = 5.0), associated with the nCIEs of various total durations and sizes. pH changes are adjusted to a linear scale in order to compare pH and Ω_{cal}. The top left triangle shows maximum pH change while the bottom right triangle shows maximum change in Ω_{cal} for each experiment. Yellow colors indicate maximum change, blue colors indicate little or no change.

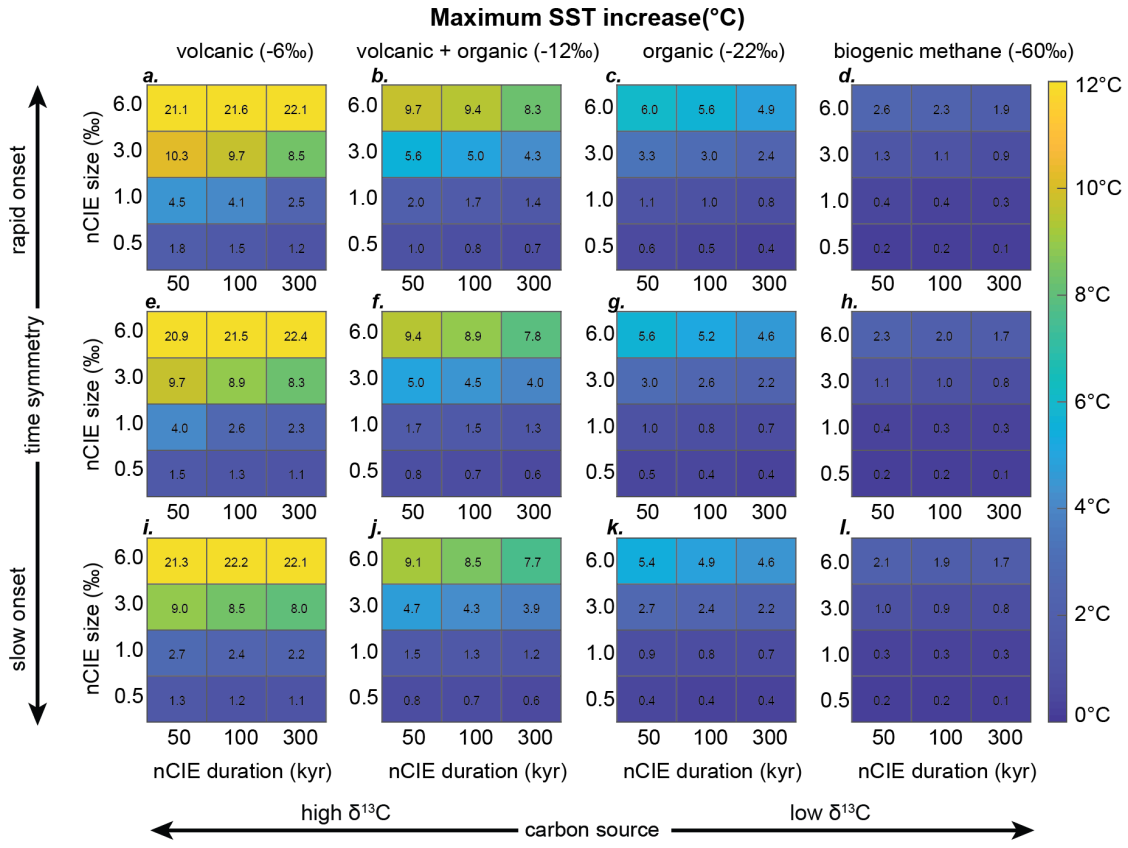

Figure A.9: Maximum global mean sea surface temperature (SST) increase during the nCIE peak. Subplots a-d are scenarios in which nCIEs have a rapid onset, slow recovery (25% vs 75% of total duration). Subplots e-h are scenarios in which nCIEs have a symmetric shape with equal onset and recovery duration (50% vs 50%). Subplots i-l are scenarios in which nCIEs have a slow onset, rapid recovery (75% vs 25% of total duration). Variations in size symmetry are excluded because the final δ^{13}C value at the end of the recovery phase does not influence gross C input and associated temperature rise. The subplot columns from left to right are nCIEs forced with carbon of -6.0‰, -12‰, -22‰, and -60‰, respectively. Within each subplot the maximum increase in global mean SST associated with nCIEs of various total durations and sizes is shown.

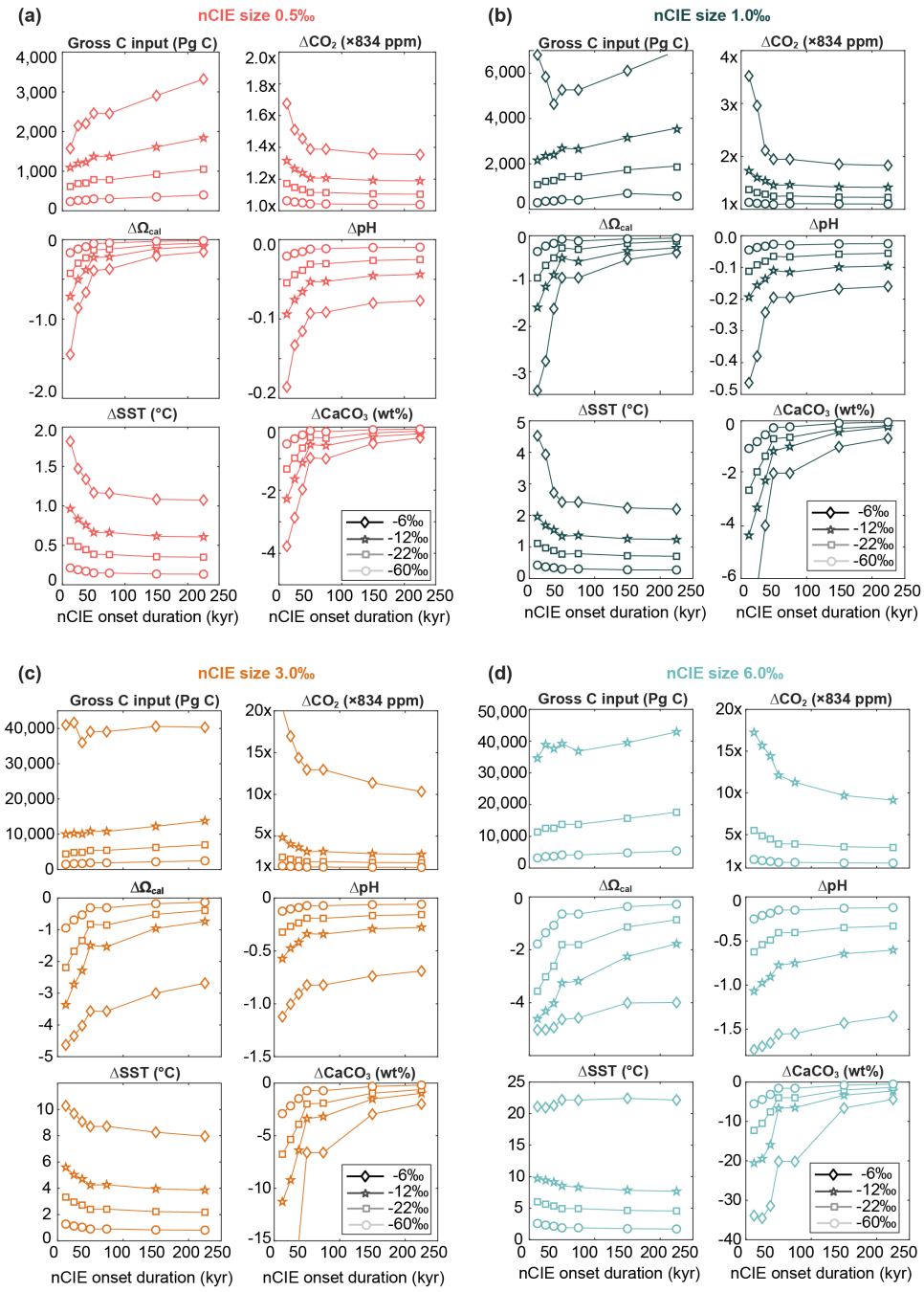

Figure A.10: nCIE onset duration versus six carbon cycle and environmental variables at the nCIE peak. Subplots for each nCIE size are gross carbon input, change in atmospheric CO_2, change in surface ocean saturation state (Ω_{cal}), change in surface ocean pH, change in sea surface temperature (SST), and the change in marine sedimentary wt% $CaCO_3$ for nCIEs with a size of (a) 0.5‰, (b) 1.0‰, (c) 3.0‰, and (d) 6.0‰.

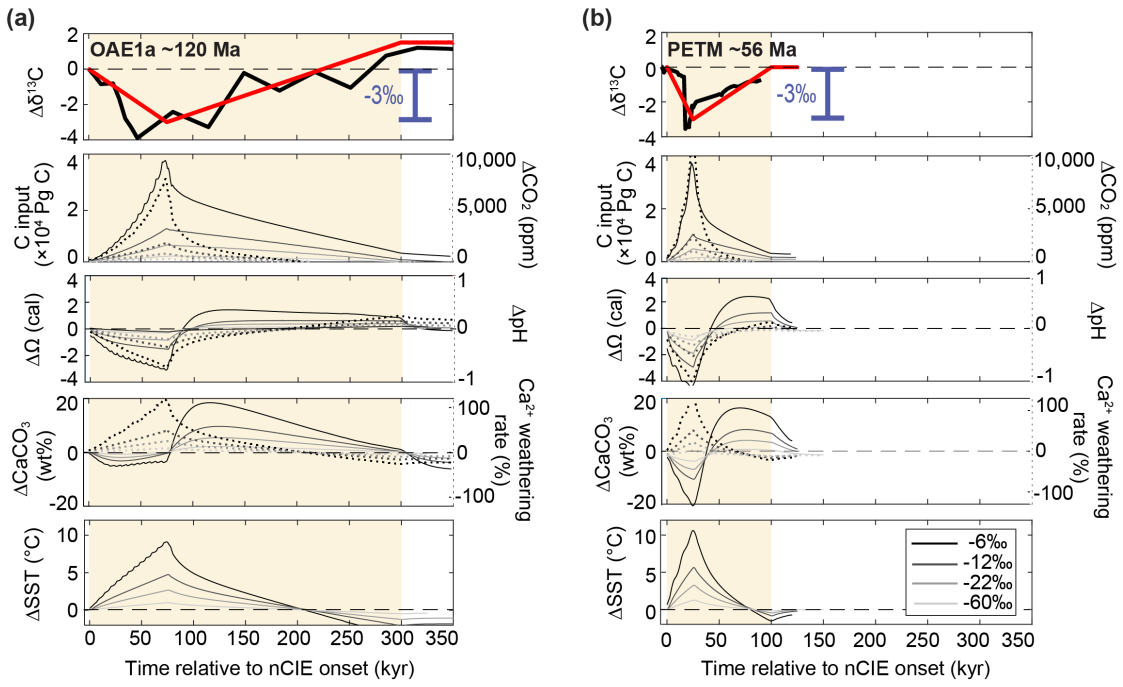

Figure A.11: Carbon cycle evolution and environmental impacts of nCIEs with a size of 3‰ and durations of (a) 300 kyr and (b) 100 kyr. In the left upper panel, (a) bulk δ^{13}C record of the OAE-1a from Resolution Guyot (H. C. Jenkyns et al., 1995) with linear interpolation between nCIE onset, peak and end, based on the age model from Malinverno et al. (2010) (black line) and the simulated nCIE that best matches this record: symmetric in time with a total duration of 300 kyr (red line). In the right upper panel, (b) bulk δ^{13}C record of the PETM from Site 1001A (Bralower et al., 1997) (black line) and the simulated nCIE that best matches this record: a 100 kyr-long nCIE with rapid onset (red line). Below, the evolution of the gross carbon input (solid), change in atmospheric CO_2 (dashed), change in surface ocean calcite saturation state (Ω_{cal}, solid) and surface ocean pH (dashed), change in global mean sedimentary wt% $CaCO_3$ (solid), percentage of change in rock weathering rate relative to initial conditions (dashed), and the change in sea surface temperature (SST) for 3‰ nCIEs, forced with δ^{13}C -6‰, -12‰, -22‰, and -60‰ carbon.

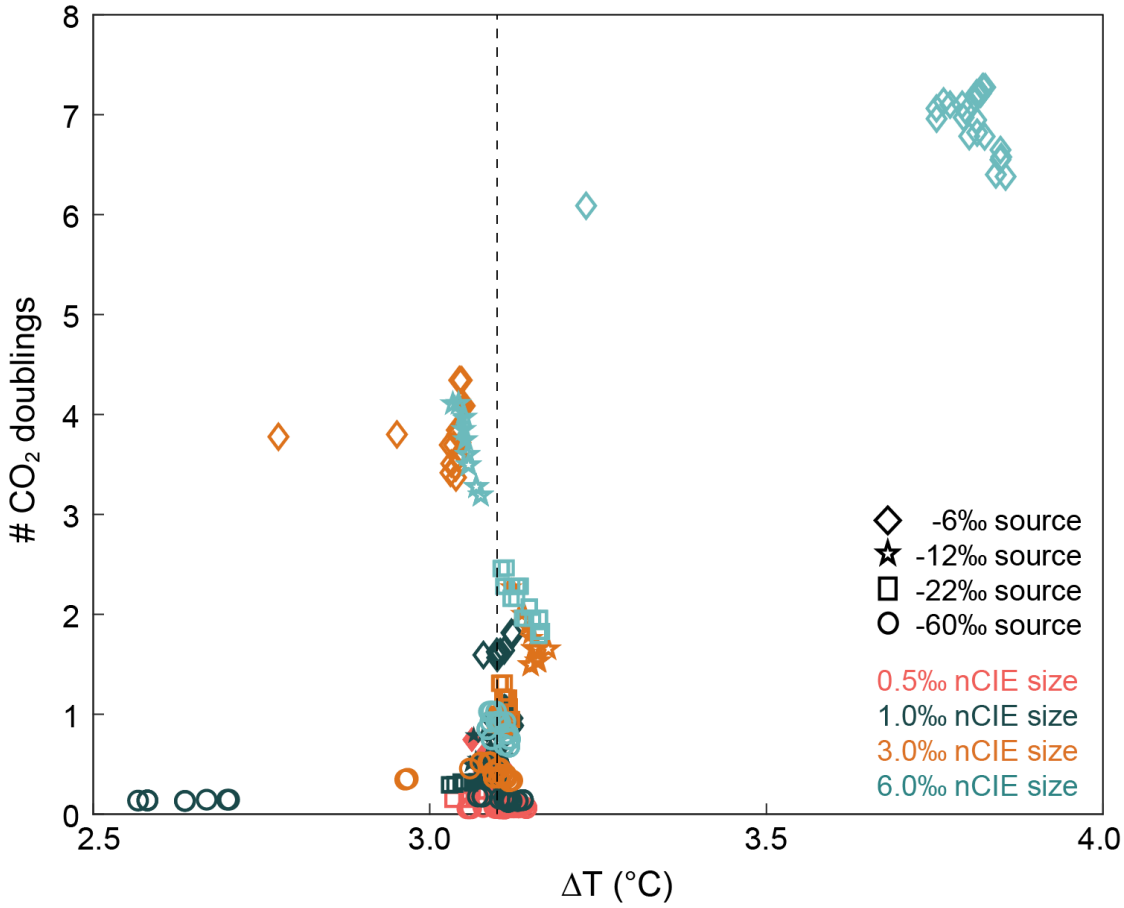

Figure A.12: Climate sensitivity of cGENIE experiments in this study. Maximum temperature is compared to the maximum atmospheric CO_2 increase in terms of the number of doublings from an initial concentration of 834 ppm.

Appendix B

Supplementary Information:

Chapter 3

Table B.1: Input parameters for carbonate (Ca) weathering, silicate (Si) weathering, volcanic outgassing, and the reference temperature for weathering for the initial spin-up state of SYMM and ASYM simulations. Below, the steady state model output values for atmospheric carbon dioxide (pCO_2) concentrations, global annual mean atmospheric temperature, surface and deep ocean temperature, total amount of ocean alkalinity (ALK) and dissolved inorganic carbon (DIC), and global mean calcium carbonate ($CaCO_3$) in marine sediment.

Parameters	**SYMM**	**ASYM**
Ca weathering flux	7.00 Tmol C yr^{-1}	7.00 Tmol C yr^{-1}
Si weathering flux	6.93 Tmol C yr^{-1}	5.60 Tmol C yr^{-1}
Volcanic outgassing	7.00 Tmol C yr^{-1}	7.00 Tmol C yr^{-1}
Reference temperature	23.79°C	29.45°C
Results		
Atmospheric CO_2	834 ppm	828 ppm
Atmospheric temperature	22.6°C	23.1°C
Surface/deep ocean temperature	24.5°C/6.6°C	27.2°C/7.8°C
Ocean ALK	1629 μmol kg^{-1}	1517 μmol kg^{-1}
Ocean DIC	1661 μmol kg^{-1}	1557 μmol kg^{-1}
Sedimentary $CaCO_3$	51 wt%	47 wt%

Table B.2: For ASYM, the average ranges (amplitude×2) of individual astronomical cycles in the global annual mean benthic temperature (ben T), atmospheric CO_2, benthic DIC $\delta^{13}C$, and wt% $CaCO_3$ across the modeled 4 Myr. Average ranges are calculated from the FFT amplitude spectrum. Below, the relative phasing (in degrees) between the imposed short and long eccentricity forcing and the proxies. Positive values indicate eccentricity forcing leads. Negative values indicate the proxy leads eccentricity.

	ASYM				
Average range (amplitude×2)	**Exp.0**	**Exp.1**	**Exp.2**	**Exp.3**	**Exp.4**
ben T, precession	0.07°C	0.05°C	0.06°C	0.06°C	0.11°C
ben T, obliquity	–	0.08°	–	–	0.08°C
ben T, short ecc	0.25°C	0.28°C	0.26°C	0.30°C	0.25°
ben T, long ecc	0.30°C	0.33°C	0.31°C	0.39°C	0.25°C
CO2, precession	2.2 ppm	2.4 ppm	5.5 ppm	3.9 ppm	17 ppm
CO2, obliquity	4.8 ppm	5.2 ppm	1.9 ppm	–	11 ppm
CO2, short ecc	4.8 ppm	5.2 ppm	2.9 ppm	12 ppm	9 ppm
CO2, long ecc	5.6 ppm	6.2 ppm	3.5 ppm	19 ppm	26 ppm
$d^{13}C$, precession	0.016 ‰	0.016 ‰	0.021 ‰	0.021 ‰	0.028 ‰
$d^{13}C$, obliquity	0.024 ‰	0.024 ‰	0.025 ‰	0.022 ‰	0.028 ‰
$d^{13}C$, short ecc	0.005 ‰	0.005 ‰	0.005 ‰	0.009 ‰	0.009 ‰
$d^{13}C$, long ecc	0.005 ‰	0.006 ‰	0.006 ‰	0.011 ‰	0.036 ‰
CaCO3, precession	0.3 wt%	0.3 wt%	0.1 wt%	0.1 wt%	0.4 wt%
CaCO3, obliquity	0.4 wt%	0.4 wt%	0.1 wt%	0.1 wt%	0.3 wt%
CaCO3, short ecc	0.3 wt%	0.3 w%	0.5 wt%	0.4 wt%	0.7 wt%
CaCO3, long ecc	0.4 wt%	0.5 wt%	0.7 wt%	0.2 wt%	1.1 wt%
Relative phasing (multi-taper coherence)					
	Exp.0	**Exp.1**	**Exp.2**	**Exp.3**	**Exp.4**
short ecc - ben T	4°	5°	4°	11°	-9°
short ecc - CO2	6°	7°	6°	36°	-112°
short ecc - $d^{13}C$	29°	29°	29°	33°	-82°
short ecc - CaCO3	29°	29°	31°	-18°	37°
long ecc - ben T	1°	1°	1°	4°	-30°
long ecc - CO2	2°	2°	1°	10°	-125°
long ecc - $d^{13}C$	7°	8°	7°	-22°	-117°
long ecc - CaCO3	6°	7°	8°	-50°	-9°

Table B.3: For SYMM, the average ranges (amplitude×2) of individual astronomical cycles in the global annual mean benthic temperature (ben T), atmospheric CO_2, benthic DIC $\delta^{13}C$, and wt% $CaCO_3$ across the modeled 4 Myr. Average ranges are calculated from the FFT amplitude spectrum. Below, the relative phasing (in degrees) between the imposed short and long eccentricity forcing and the proxies. Positive values indicate eccentricity forcing leads. Negative values indicate the proxy leads eccentricity.

	SYMM				
Average range (amplitude×2)	**Exp.0**	**Exp.1**	**Exp.2**	**Exp.3**	**Exp.4**
ben T, precession	–	–	–	–	–
ben T, obliquity	0.06°C	0.06°	0.05°C	0.06°C	0.07°
ben T, short ecc	0.22°C	0.24°C	0.23°C	0.27°C	0.22°C
ben T, long ecc	0.26°C	0.28°C	0.28°C	0.34°C	0.23°C
CO2, precession	2.6 ppm	2.8 ppm	1.4 ppm	2.7 ppm	3.1 ppm
CO2, obliquity	–	–	2.4 ppm	2.4 ppm	5.9 ppm
CO2, short ecc	3.6 ppm	3.8 ppm	3.4 ppm	12 ppm	7.2 ppm
CO2, long ecc	4.2 ppm	4.5 ppm	4.0 ppm	17 ppm	24 ppm
$d^{13}C$, precession	0.012 ‰	0.012 ‰	0.013 ‰	0.013 ‰	0.013 ‰
$d^{13}C$, obliquity	0.003 ‰	–	0.005 ‰	0.005 ‰	0.005 ‰
$d^{13}C$, short ecc	0.003 ‰	0.003 ‰	0.003 ‰	0.003 ‰	0.008 ‰
$d^{13}C$, long ecc	0.002 ‰	0.002 ‰	0.002 ‰	0.003 ‰	0.032 ‰
CaCO3, precession	–	–	0.2 wt%	0.2 wt%	0.2 wt%
CaCO3, obliquity	0.1 wt%	0.1 wt%	–	0.1 wt%	0.2 wt%
CaCO3, short ecc	0.2 wt%	0.6 wt%	0.6 wt%	0.4 wt%	0.8 wt%
CaCO3, long ecc	0.3 wt%	0.8 wt%	0.9 wt%	0.2 wt%	1.1 wt%
Relative phasing (multi-taper coherence)					
	Exp.0	**Exp.1**	**Exp.2**	**Exp.3**	**Exp.4**
short ecc - ben T	4°	4°	4°	10°	-8°
short ecc - CO2	10°	11°	9°	29°	-96°
short ecc - $d^{13}C$	132°	132°	136°	108°	-126°
short ecc - CaCO3	25°	26°	26°	-17°	31°
long ecc - ben T	1°	1°	1°	3°	-30°
long ecc - CO2	2°	2°	2°	8°	-118°
long ecc - $d^{13}C$	164°	163°	166°	-110°	-123°
long ecc - CaCO3	6°	6°	7°	-40°	-11°

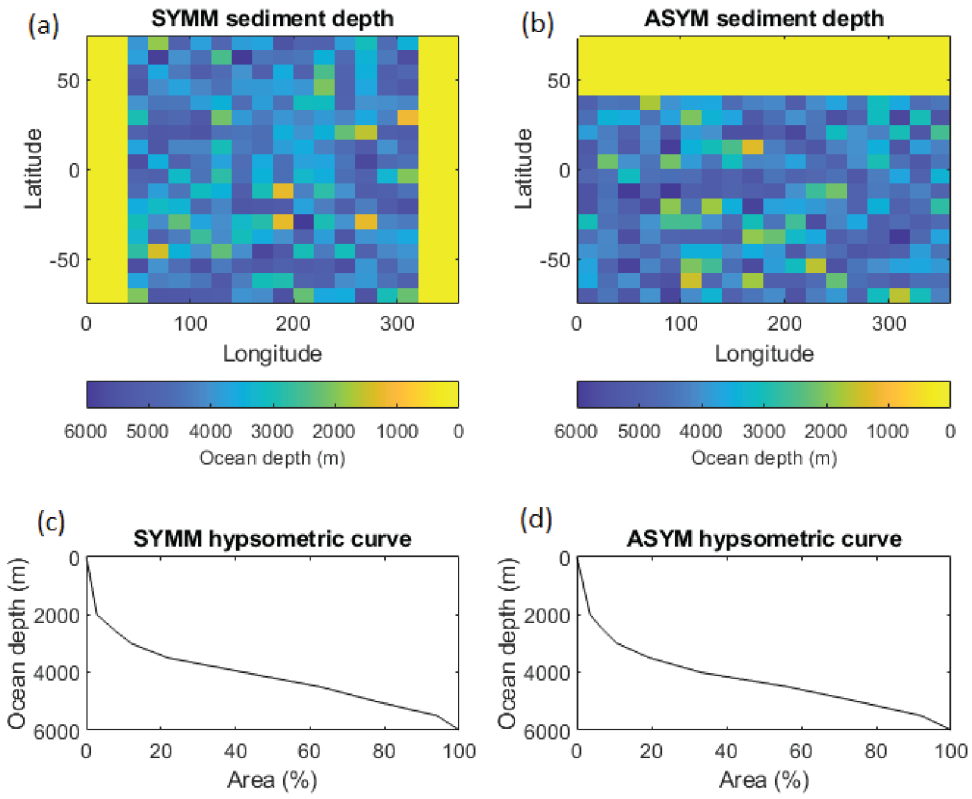

Figure B.1: Ocean depth of SYMM and ASYM. A latitude-longitude ocean sediment depth grid for (a) SYMM and (b) ASYM. Bright yellow colors indicate land masses. The hypsometric curve for (c) SYMM and (d) ASYM ocean sediments showing the cumulative distribution of ocean sediment depth generated with 'muffingen' v0.9.25 (DOI: 10.5281/zenodo.5130677)

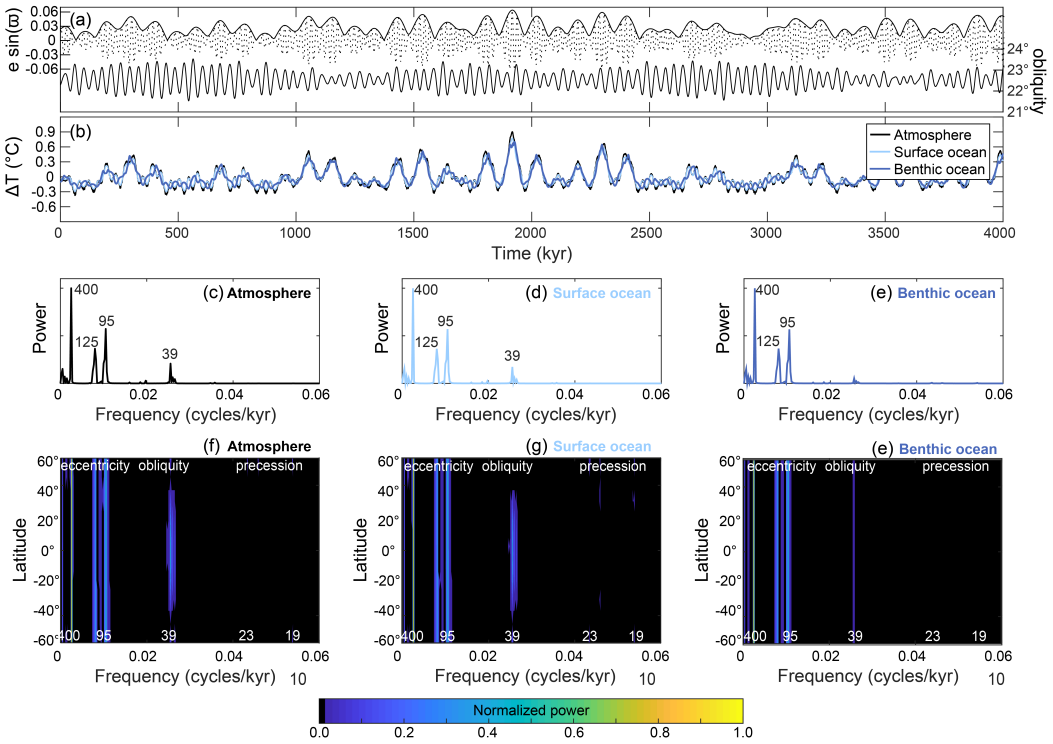

Figure B.2: Astronomical climate evolution in SYMM of Exp.0. (a) The eccentricity, obliquity, and the precession index (e sin(ω)) used to calculate the daily mean insolation across four million years of cGENIE simulation. (b) The simulated change in the global annual mean temperature in the atmosphere (black), surface (light blue), and deep ocean (dark blue) with their respective normalized power spectra in panels (c-e) calculated using the Fast Fourier Transform. Each value near a spectral peak indicates the associated period of the cycle in kyr. The power spectra of temperature in the (f) atmosphere, (g) surface, and (h) deep ocean are shown for each latitude.

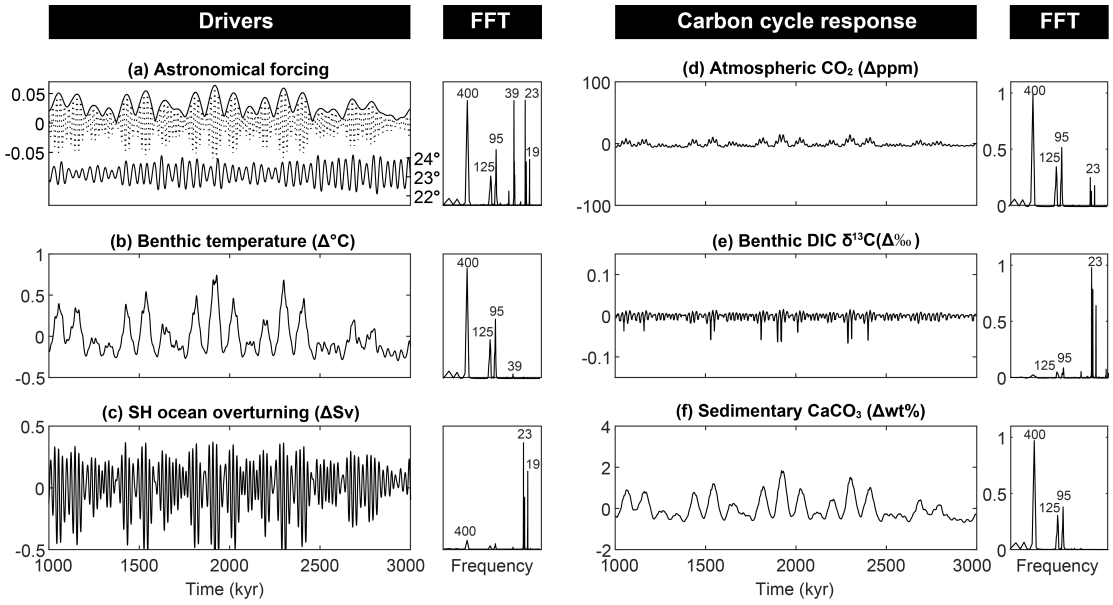

Figure B.3: Exp.1, ocean circulation and CO_2 solubility feedbacks in SYMM. (a) Astronomical forcing parameters (eccentricity, obliquity (in degrees), and precession index (e $\sin(\omega)$)) and their Fast Fourier Transform (FFT) normalized to the highest individual power. (b) Change in benthic ocean temperature. (c) Change in the maximum Southern Hemisphere ocean overturning strength, defined by the maximum overturning strength reached in the SH across all ocean depth levels. (d) Change in atmospheric CO_2. (e) Change in benthic DIC δ^{13}C. (f) Change in wt% $CaCO_3$. All variables are annual global mean values and are accompanied by their respective FFTs, normalized to the peak with maximum power.

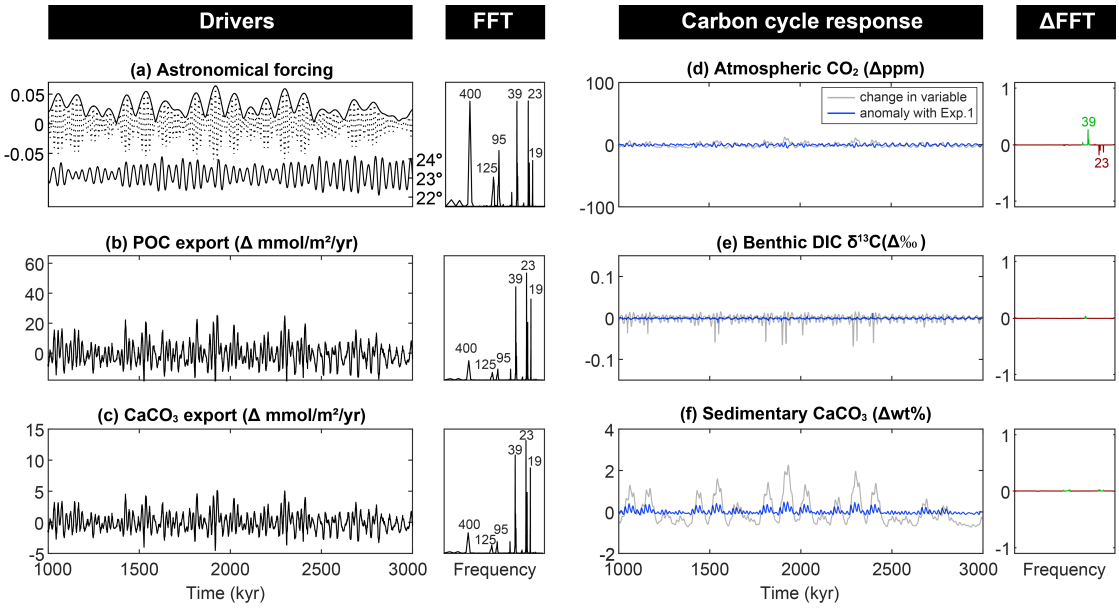

Figure B.4: Exp.2, marine surface productivity feedback in SYMM. (a) Astronomical forcing parameters (as per Figure B.3a). (b) Change in the export of particulate organic carbon (POC). (c) Change in the export of $CaCO_3$. (d) Change in atmospheric CO_2. (e) Change in benthic DIC $\delta^{13}C$. (f) Change in wt% $CaCO_3$. All variables are annual global mean values and are accompanied by their respective FFTs, normalized to the peak with maximum power. In blue, the values are plotted as anomalies with the previous experiment and depict the change driven by the marine productivity feedback only. Likewise, the FFTs are plotted as anomalies. A positive (green) value on the y-axis indicates an increase in relative power and a negative (red) value indicates a decrease in relative power compared to the previous experiment.

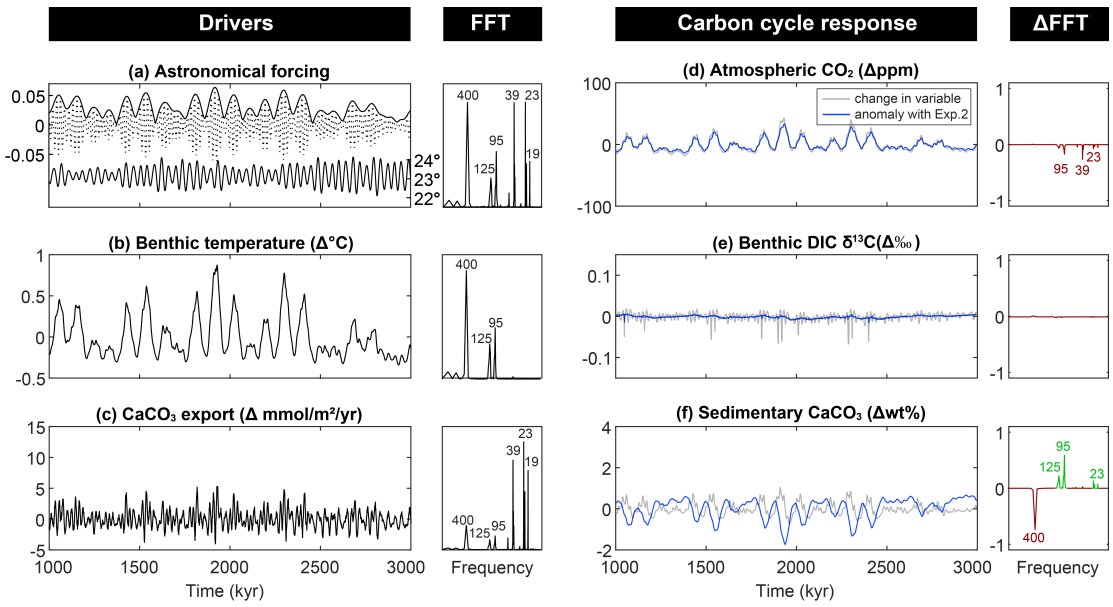

Figure B.5: Exp.3, deep marine CaCO3 feedback in SYMM. (a) Astronomical forcing parameters (as per Figure B.3a). (b) Change in benthic ocean temperature. (c) Change in the export of $CaCO_3$. (d) Change in atmospheric CO_2. (e) Change in benthic DIC $\delta^{13}C$. (f) Change in wt% $CaCO_3$. All variables are annual global mean values and are accompanied by their respective FFTs, normalized to the peak with maximum power. In blue, the values are plotted as anomalies with the previous experiment and depict the change driven by the marine $CaCO_3$ feedback only. Likewise, the FFTs are plotted as anomalies. A positive (green) value on the y-axis indicates an increase in relative power and a negative (red) value indicates a decrease in relative power compared to the previous experiment.

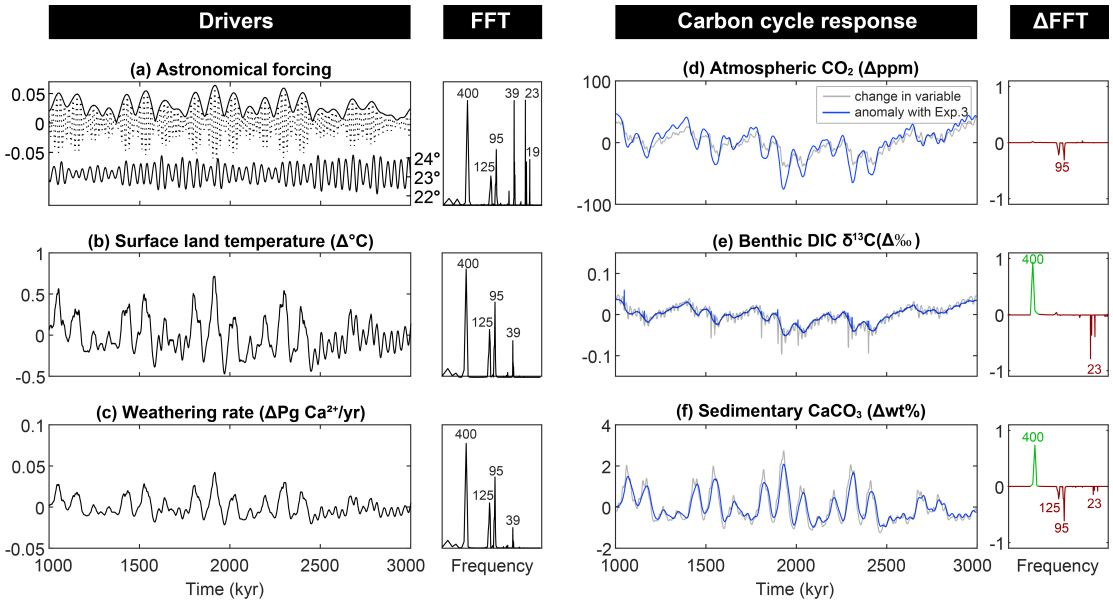

Figure B.6: Exp.4, terrestrial rock weathering feedback in SYMM. (a) Astronomical forcing parameters (as per Figure B.3a). (b) Change in surface land temperature. (c) Change in the rate of terrestrial weathering. (d) Change in atmospheric CO_2. (e) Change in benthic DIC $\delta^{13}C$. (f) Change in wt% $CaCO_3$. All variables are annual global mean values and are accompanied by their respective FFTs, normalized to the peak with maximum power. In blue, the values are plotted as anomalies with the previous experiment and depict the change driven by the terrestrial weathering feedback only. Likewise, the FFTs are plotted as anomalies. A positive (green) value on the y-axis indicates an increase in relative power and a negative (red) value indicates a decrease in relative power compared to the previous experiment.

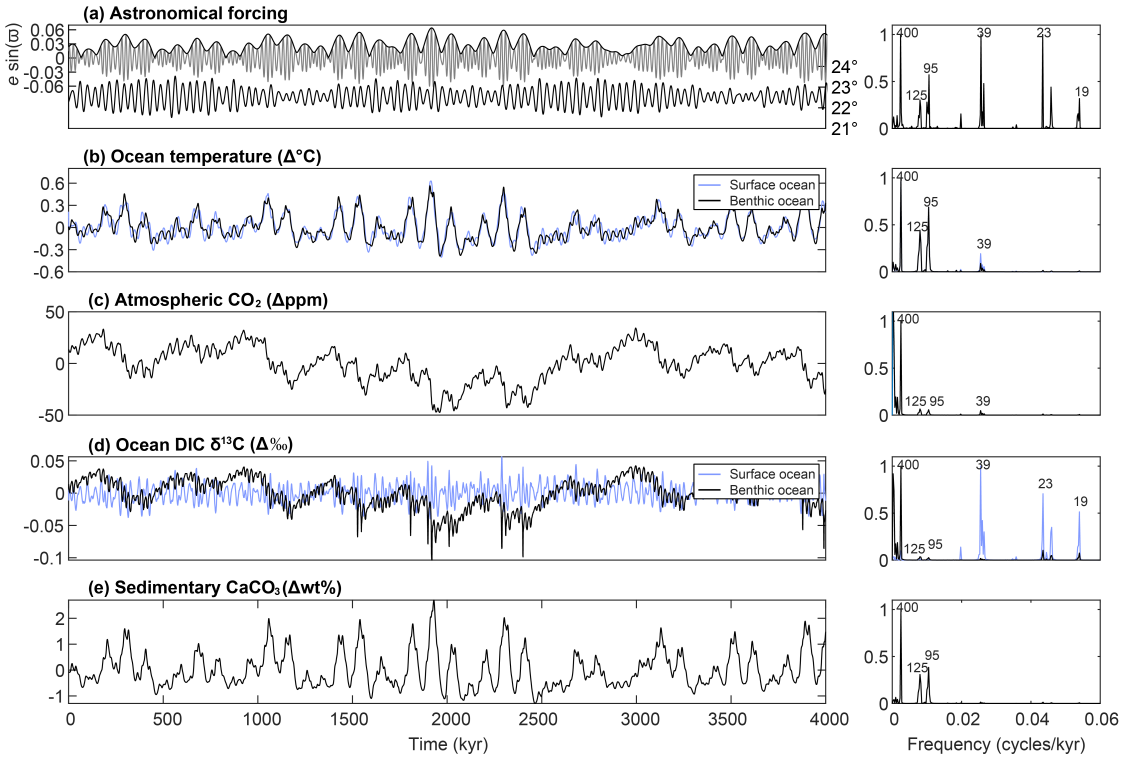

Figure B.7: Cumulative astronomical impact of SYMM simulations. (a) Astronomical forcing parameters (as per Figure B.3a). (b) Annual global mean temperature change in the benthic (black) and surface (blue) ocean. (c) Annual global mean pCO_2 change. (d) Annual global mean DIC $\delta^{13}C$ change in the benthic (black) and surface (blue) ocean. (e) Global mean sedimentary $CaCO_3$ change. All variables are accompanied by their respective FFTs, normalized to the peak with maximum power. The combined impact of all four climate-carbon feedbacks on atmospheric, ocean, and sedimentary reservoirs.

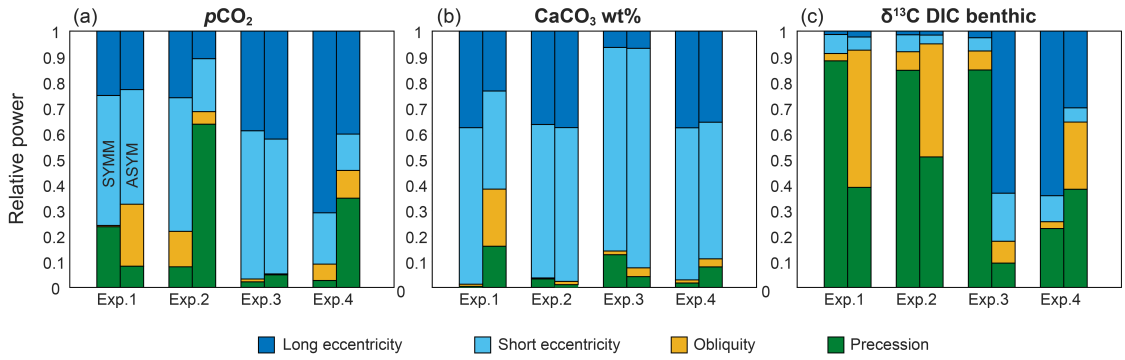

Figure B.8: Relative spectral power of astronomical elements. The relative spectral power of the long (267-500 kyr) and short (78-154 kyr) eccentricity, obliquity (36-41 kyr), and precession (18-24 kyr) cycles in the simulated (a) $p\mathrm{CO}_2$, (b) marine CaCO_3, and (c) DIC $\delta^{13}\mathrm{C}$ in the four experimental designs of Exp.1, Exp.2, Exp.3, and Exp.4. Left bars are results from the SYMM simulations and right bars are ASYM results.

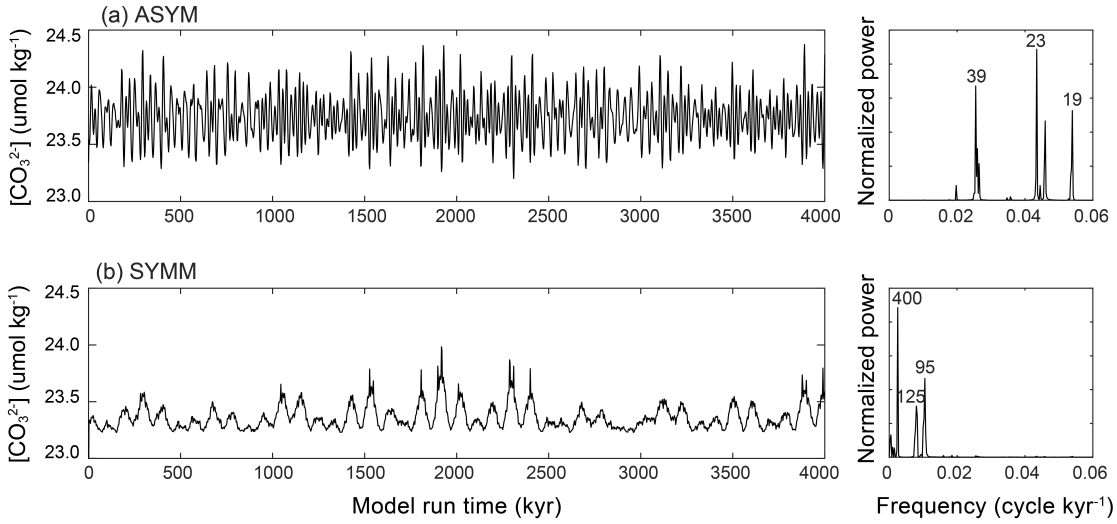

Figure B.9: Benthic carbonate ion concentrations. The change in carbonate ion concentration ($[\mathrm{CO}_3^{2-}]$) as a result of astronomically induced changes in ocean temperature, circulation, and ocean solubility (Exp.1) for (a) ASYM and (b) SYMM with their respective FFT power spectra normalized to the peak with maximum power.

Appendix C

Supplementary Information:

Chapter 5

The obliquity model described in Laskar, Joutel, and Boudin (1993) is applied for the integration of Earth's obliquity (ϵ) and precession (p_A) over time for each of the stable dynamical n-body simulations in Horner et al. (2020). The obliquity model follows the following equations based on the rigid Earth theory of Kinoshita (1977).

$$\begin{aligned} \frac{dp_A}{dt} &= R(\epsilon) - \cot\,\epsilon[A(p,q)\sin\,p_A + B(p,q)\cos\,p_A] - 2C(p,q) - p_g \\ \frac{d\epsilon}{dt} &= -B(p,q)\sin\,p_A + A(p,q)\cos\,p_A \end{aligned} \tag{C.1}$$

$$
\begin{aligned}
A(p,q) &= \frac{2}{\sqrt{1-p^2-q^2}}(\dot{q} + p(q\dot{p} - p\dot{q})) \\
B(p,q) &= \frac{2}{\sqrt{1-p^2-q^2}}(\dot{p} - q(q\dot{p} - p\dot{q})) \\
C(p,q) &= (q\dot{p} - p\dot{q})
\end{aligned}
\tag{C.2}
$$

$$
\begin{aligned}
R(\epsilon) =& \frac{3k^2 m_M}{a_M^3 \nu}\frac{C-A}{C} \\
&\times \left[(M_0 - M_2/2)\cos\,\epsilon + M_1\frac{\cos\,2\epsilon}{\sin\,\epsilon} - M_3\frac{m_M}{m_E+m_M}\frac{n_M^2}{\nu n_\Omega}\frac{C-A}{C}(6\cos^2\epsilon - 1)\right] \\
&+ \frac{3k^2 m_\odot}{a_\odot^3 \nu}\frac{C-A}{C}[S_0\cos\,\epsilon]
\end{aligned}
\tag{C.3}
$$

where p = $\sin(i/2)\sin(\Omega)$ and q = $\sin(i/2)\cos(\Omega)$. Numerical values for each parameter are given in Laskar, Joutel, and Boudin (1993). All parameters are set as their original values that were used to reconstruct the rotational evolution of our modern Earth for direct comparability between cycles experienced by modern Earth and the alternative Earth-like planets simulated in this study.

Several tests are performed to verify the results. First, the simulation most comparable to the modern Solar System, with Jupiter at 5.2 au and an eccentricity of 0.05, is compared to the existing (La93) astronomical solution. Both amplitudes and power spectra of precession and obliquity cycles match with the La93 (Laskar, Joutel, & Boudin, 1993) solution (Figure C.1ab). Secondly, we test the sensitivity to the initial obliquity angle for the modern. Initial values of ϵ_0=23°, ϵ_0=30°, ϵ_0=40°, ϵ_0=50°, ϵ_0=60° are used for integra-

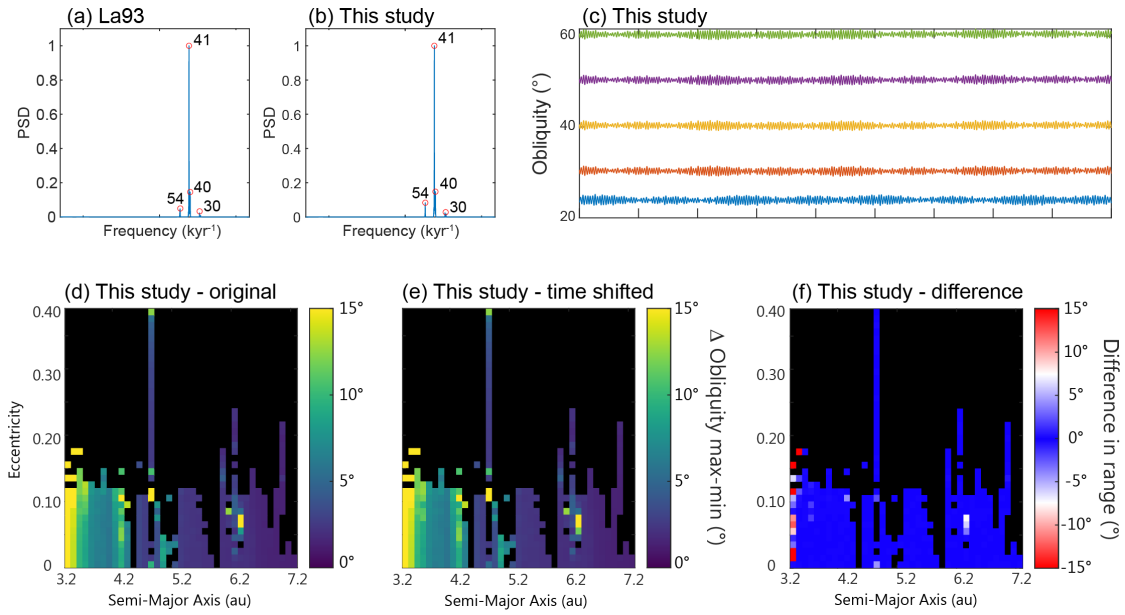

Figure C.1: Testing the obliquity model. (a) Fast Fourier power spectrum of the La93 astronomical solution. (b) Fast Fourier power spectrum of the simulation in this study most comparable to the Solar system configuration. (c) Obliquity model output for initial obliquity values of 23°, 30°, 40°, 50°, 60° for the modern Solar system configuration. (d) The maximum variation in the obliquity (in degrees) of an Earth-like planet under different planetary architectures, i.e. Figure 5.6a in low resolution (40×40 simulations across the full parameter space). (e) As Figure C.1d but input signal shifted in time by 100 year to demonstrate sensitivity to initial conditions. (f) Difference in maximum obliquity variation between C.1e and C.1d.

tion. Despite the very different simulated mean obliquity, the amplitudes and main periods remain unchanged (Figure C.1c).

Some simulations display an initial drift in obliquity across the first few years (e.g. Figure 5.7a). To verify that this drift does not result from sensitivity of the model equations to small deviations, we run sensitivity tests for a small sub-sample (40×40) of simulations in which the input signal is slightly offset. For instance, the original input signal has a time step of 1000 year, i.e. t = 0, 1000, 2000, etc. In the sensitivity runs, the input signal is shifted by 100 years, i.e. t = 100, 1100, 2100, etc. The differences at the

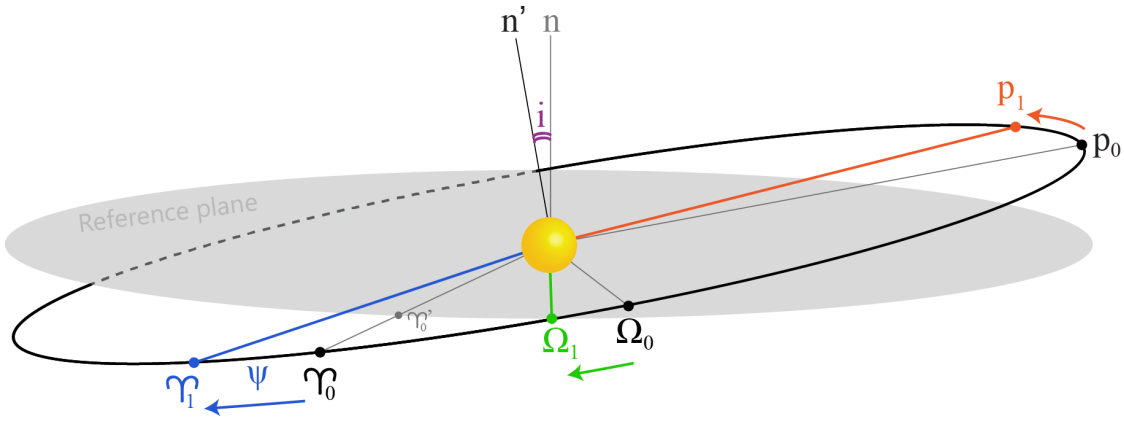

Figure C.2: Schematic depiction of the relative positions of the ascending node (Ω_0 and Ω_1), perihelion (p_0 and p_1), and the moving vernal equinox (Υ_0 and Υ_1) at two sequential points in time, controlled by the clockwise movement of axial precession (Ψ) on the Earth-like planet. Their relative direction of movement is indicated with arrows. N-body simulations provide the angle (longitude) of the ascending node relative to a reference point (Υ'_0) on the reference plane with orbit normal (n). The reference point is the first point of Aries during the year 2000. The orbital inclination (i) is the angle between the plane of reference and orbital plane with normal (n').

start of the simulations that show an initial drift are negligible and confirm the transient nature of the first few thousands of years while the planet adjusts to the new conditions. To prevent the transient drift at the start of the simulation from distorting the results of the amplitude calculations, the first million year is removed from the analysis when extracting the maximum obliquity amplitude (Figure 5.6). The sensitivity test also reveals that the model is sensitive to the initial conditions (Figure C.1d-f). Whilst the majority of simulations in the low-resolution parameter space appear to have a low sensitivity to initial conditions in terms of the maximum obliquity variation, those regions where the Jupiter-like companion is close to 3.2 au display a greater deviation between the two sensitivity simulations and should be interpreted with caution.